UNIVERSITY OF TRENTO

Doctoral School in Civil, Environmental and Mechanical Engineering

Curriculum 3. Modelling and Simulation

Giovanni Bordiga

Homogenization of periodic lattice materials for wave propagation, localization, and bifurcation

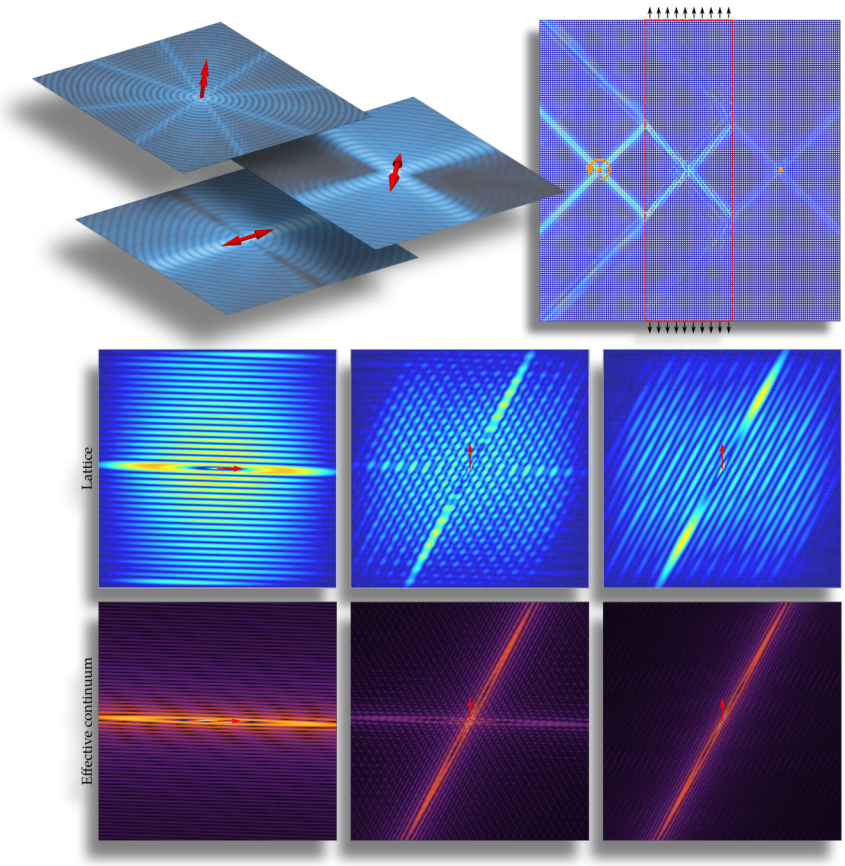

2020 - Doctoral thesis

University of Trento
Doctoral School in Civil, Environmental and Mechanical Engineering
http://web.unitn.it/en/dricam
Via Mesiano 77, I-38123 Trento
Tel. +39 0461 282670 / 2611 - *dicamphd@unitn.it*

University of Trento

Doctoral Thesis

Homogenization of periodic lattice materials for wave propagation, localization, and bifurcation

Author
Giovanni Bordiga

Supervisors
Prof. Andrea Piccolroaz
Prof. Davide Bigoni

Modelling and Simulation – XXXII cycle 2016/2019

Solid and Structural Mechanics Group (SSMG)
Department of Civil, Environmental, and Mechanical Engineering (DICAM)

April 17, 2020

To my mother,
for her love and courage

To my father,
for his love and kindness

To my sister,
for her love and strength

Declaration of Authorship

I, Giovanni Bordiga, declare that this thesis titled, "Homogenization of periodic lattice materials for wave propagation, localization, and bifurcation" and the work presented in it are my own. I confirm that:

- This work was done wholly or mainly while in candidature for a research degree at this University.
- Where any part of this thesis has previously been submitted for a degree or any other qualification at this University or any other institution, this has been clearly stated.
- Where I have consulted the published work of others, this is always clearly attributed.
- Where I have quoted from the work of others, the source is always given. With the exception of such quotations, this thesis is entirely my own work.
- I have acknowledged all main sources of help.
- Where the thesis is based on work done by myself jointly with others, I have made clear exactly what was done by others and what I have contributed myself.

Signed: _____

Date: _____

Acknowledgements

The guidance and encouragement that I have received from my advisors Prof. Andrea Piccolroaz and Prof. Davide Bigoni allowed me to enjoy a fruitful and productive PhD experience. I am grateful to them for being my mentors. I am also thankful to all the members of the *Solid and Structural Mechanics Group*, for making the group a collaborative and stimulating environment.

A special thanks goes to all the inhabitants of the *Fifth Floor* and the *Independent Reign of Soppalco*, for having welcomed me to this joyful land and warmly accompanied during the cheerful as well as less cheerful moments. Thanks to Alessandro, Gabriel, Marco, Gianluca, Luca, and Andrea for the uncountably many compelling discussions and 'scientific' dinners. An additional thanks goes to Gianluca for being able to uncontrollably multiply the number of bifurcations in a discussion and thus explore unimaginable scenarios and surprising perspectives of a problem. In this regard, Ale and Marco deserve an additional thanks for trying to bring back Gian from Mars with useful products of the mental exploration. Thanks a lot also to HF Luca (LPA), without you this story would be *much* shorter to tell, keep rocking! Andrea thank you so much, for your generous help and for your friendship. And thanks to all the people who have made this journey more pleasant: Daniele, Gabriele, David, Luigi, Diego, Diana, Costanza, Alice, Riccardo, Matteo, Mattia, Piotr, Lakshminath (LK), Moritz, Ilaria, Elena, Rossella, Daniele. Put simply, the PhD would not have been the same without all of you.

Finally, I am immensely indebted to my family for the unconditional support and constant encouragement that allowed me to overcome the tough moments and serenely pursue my path.

Financial support from the ERC Advanced Grant "Instabilities and non-local multiscale modelling of materials" ERC-2013-ADG-340561-INSTABILITIES (2014-2019) is gratefully acknowledged.

"A hundred times every day I remind myself that my inner and outer life depends on the labors of other men, living and dead, and that I must exert myself in order to give in the same measure as I have received and am still receiving."

Albert Einstein

UNIVERSITY OF TRENTO

Abstract

Department of Civil, Environmental, and Mechanical Engineering (DICAM)

Modelling and Simulation

Homogenization of periodic lattice materials for wave propagation, localization, and bifurcation

by Giovanni Bordiga

The static and dynamic response of lattice materials is investigated to disclose and control the connection between microstructure and effective behavior. The analytical methods developed in the thesis aim at providing a new understanding of material instabilities and strain localizations as well as effective tools for controlling wave propagation in lattice structures.

The time-harmonic dynamics of arbitrary beam lattices, deforming flexurally and axially in a plane, is formulated analytically to analyze the influence of the mechanical parameters on the dispersion properties of the spectrum of Floquet-Bloch waves. Several forms of dynamic localizations are shown to occur for in-plane wave propagation of grid-like elastic lattices. It is demonstrated that lattices of rods, despite being 'simple' structures, can exhibit a completely different channeled response depending on the characteristics of the forcing source (i.e. frequency and direction) as well as on the slenderness of the elastic links. It is also shown how the lattice parameters can be tuned to attain specific dispersion properties, such as flat bands and sharp Dirac cones.

In the research field of material instabilities, a key result proposed in this thesis is the development of both static and dynamic homogenization methods capable of accounting for second-order effects in the macroscopic response of prestressed lattices. These methods, the former based on an incremental strain-energy equivalence and the latter based on the asymptotic analysis of lattice waves, allow the identification of the incremental constitutive operator capturing the macroscopic incremental response of arbitrary lattice configurations. The homogenization framework has allowed the systematic analysis of prestress-induced phenomena on the incremental response of both the lattice structure and its 'effective' elastic solid, which in turn has enabled the identification of the complex interplay between microstructure, prestress, loss of ellipticity (shear band formation) and short-wavelength bifurcations.

Potential new applications for the control of wave propagation are also shown to be possible by leveraging the inclusion of second-order terms in the incremental dynamics. In particular, the tunability of the prestress state in a square lattice structure has been exploited to obtain dynamic interfaces with designable transmission properties. The interface can be introduced in a material domain by selectively prestressing the desired set of ligaments and the prestress level can be tuned to achieve total reflection, negative refraction, and wave channeling.

The obtained results open new possibilities for the realization of engineered materials endowed with a desired constitutive response, as well as to enable the identification of novel dynamic material instabilities.

Published papers

The main results presented in this thesis are summarized in the following papers:

1. G. Bordiga, L. Cabras, D. Bigoni, and A. Piccolroaz. "Free and Forced Wave Propagation in a Rayleigh-Beam Grid: Flat Bands, Dirac Cones, and Vibration Localization vs Isotropization". In: *Int. J. Solids Struct.* 161 (2019), pp. 64–81. DOI: 10.1016/j.ijsolstr.2018.11.007

2. G. Bordiga, L. Cabras, A. Piccolroaz, and D. Bigoni. "Prestress Tuning of Negative Refraction and Wave Channeling from Flexural Sources". In: *Appl. Phys. Lett.* 114.4 (2019), p. 041901. DOI: 10.1063/1.5084258

3. G. Bordiga, L. Cabras, A. Piccolroaz, and D. Bigoni. "Incremental Constitutive Tensors and Strain Localization for Prestressed Elastic Lattices: Part I – Quasi-static Response". In: *J. Mech. Phys. Solids* (2020). arXiv: 2001.02096 [physics.class-ph]. *(under review)*

4. G. Bordiga, L. Cabras, A. Piccolroaz, and D. Bigoni. "Incremental Constitutive Tensors and Strain Localization for Prestressed Elastic Lattices: Part II – Incremental Dynamics". In: *J. Mech. Phys. Solids* (2020). arXiv: 2001.02151 [physics.class-ph]. *(under review)*

Contents

List of Figures

List of Tables

1 Introduction

The mechanical design of materials at their microstructural level is becoming the new frontier for the creation of materials with unprecedented capabilities. This new approach has led to a series of successful results, as for instance, the realization of architected materials exhibiting extreme mechanical features such as foldability, energy absorption, dynamic isolation, and wave channeling [5–14], which are even enhanced by reconfigurability, tunability, and programmability [15–17]. A key component of this progress is the advancement in the modelling of the physical relationships between material 'substructure' and 'effective' macroscopic behavior, provided by the development of homogenization theories [18–23].

Within this context, the present thesis aims at investigating the connection between material microstructure and material response, at both macro and micro scale, in terms of dynamic characteristics, material instabilities, and localization phenomena, occurring in a class of composite materials endowed with a reticulated periodic structure (so-called 'lattices'). The statics and dynamics of these composites is addressed by adopting the structural model of the elastic rod to represent interactions at the material scale. This idealization will be shown to be highly effective for obtaining *analytical* results capturing the static and dynamic behavior of heterogeneous materials, and thus enabling the efficient analysis of the influence of microstructural parameters, without requiring the expensive parametric computations typically needed in three-dimensional continuum formulations.

The resulting theoretical and numerical analysis has three main ramifications: (i) the investigation of the influence of structural variables on low and high frequency response of lattice materials; (ii) the identification of new ways of tuning the response of structured materials for the realization of adaptable dynamical interfaces; (iii) the modelling of the relationships between material structure, stress state, and material instabilities, as well as their influence on the 'effective' macroscopic response.

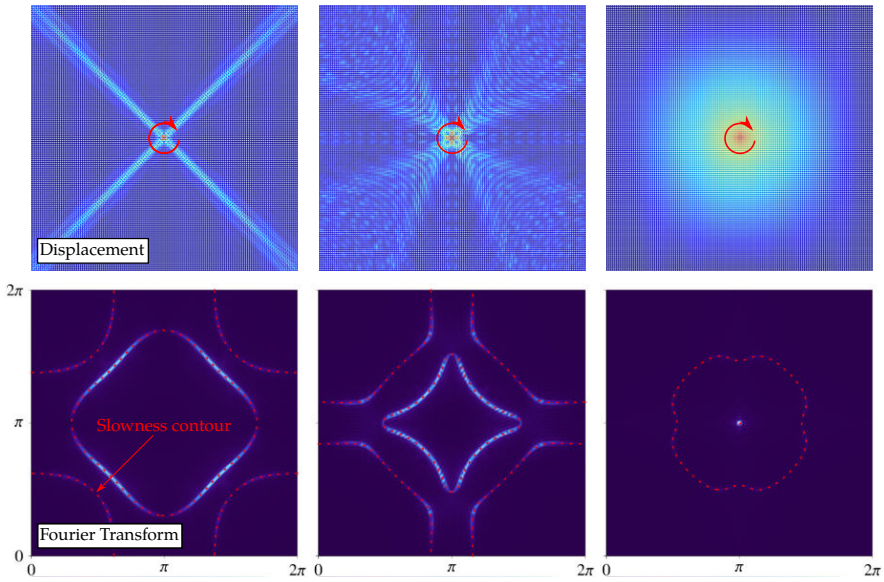

Fig. 1.1. Dynamic localization and progressive 'isotropization' (from left to right), occurring during the forced wave propagation of a grid lattice of elastic Rayleigh beams (deforming in the plane). Displacement field (upper parts) and corresponding Fourier transform (lower parts) are shown as generated by a couple (of axis orthogonal to the lattice plane) pulsating at different frequency (increasing from left to right). In the right column, the forcing source excites exclusively the Bloch wave characterized by a pure 'rotational' standing wave, hence leading to a resonant mode with a circular wavefront. Further details are provided in Chapter 2 (see Figs. 2.12–2.15).

The modelling of the dynamic features of vector wave propagation in lattice materials is first addressed in Chapter 2, with an exploratory analysis of in-plane vibrations of a grid of elastic beams. The eigenvalue problem for free wave propagation is formulated analytically for a rectangular grid of elastic rods with distributed mass and endowed with rotational inertia (so-called 'Rayleigh beams'). The analytic formulation allows the investigation of the influence of the mechanical parameters on the dispersion properties of the spectrum of Floquet-Bloch waves, whose characteristics are visualized by the computation of the dispersion relation and waveforms. Due to the coupling between axial and transverse displacements, the dispersion relation is found to be strongly dependent on the slenderness of the beams. This effect is exploited to show how the lattice parameters can be tuned to attain specific dispersion properties, such as flat bands and sharp Dirac cones [24]. The effect of the rotational inertia, namely the lowering of the propagation frequencies as well as the 'sharpening' of the double-root points, is highlighted by comparing results obtained adopting the Rayleigh model vs the standard Euler-Bernoulli.

The computation of waveforms corresponding to propagating modes and standing waves reveals valuable information about possible resonance

phenomena under forced vibrations. The case of dynamic loading is analyzed by means of a finite-size computational model of the lattice structure where the beams are discretized using finite elements. As the focus of the investigation is the material response, the numerical simulations are performed adopting a perfectly matched layer (PML) along the boundaries of the domain in order to simulate an infinite lattice and thus avoid boundary disturbances[1]. Results spanning low-to-high frequency regimes are compared to the simpler problem of lattice subject to out-of-plane motion [25], demonstrating that a wider range of *dynamic localizations* is possible for in-plane deformation, due to the complex interplay between axial and flexural waves (see Fig. 1.1). It is shown that a simple grid of beams can switch between several forms of wave localizations and even exhibit surprising *'isotropizations'* depending on both the frequency and direction of the pulsating load (both in-plane forces and out-of-plane couples are considered).

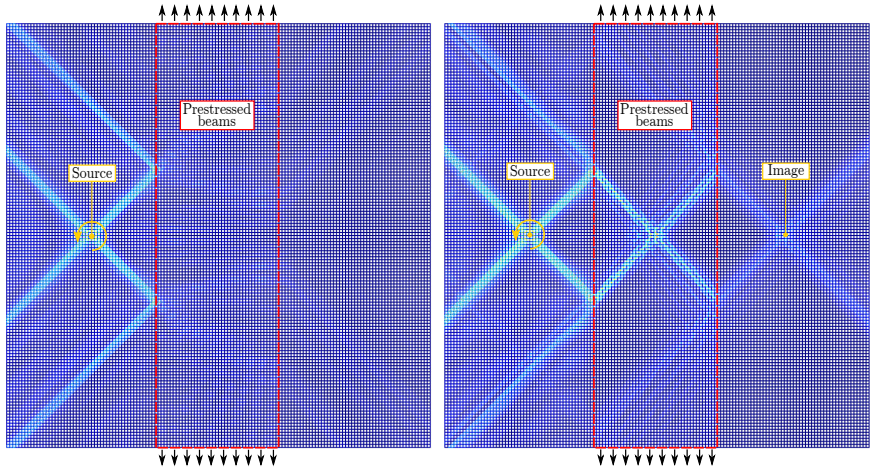

Fig. 1.2. Dynamic interfaces are realized by introducing prestressed layers in a lattice (deformed in the plane where elastic rods suffer bending and axial strain) where the prestress can be tuned to achieve the desired effect. A punctual time-harmonic excitation, in the form of a couple (with axis normal to the lattice plane), is applied to a lattice material, so that the layer of prestressed rods can be tuned to obtain the total reflection of the incident channeled wave (left) or to obtain negative refraction inside the interface (right). In the latter case, the negative refraction is exploited to realize a flat lens, so that the image of the forcing source is reconstructed on the opposite side. Further details are provided in Chapter 3 (see Fig. 3.2 and 3.3).

This study on the dynamics of lattice materials stimulated the idea of harnessing wave localizations in order to manipulate the propagation of mechanical signals in a material domain. To this purpose, an additional mechanical parameter, the *axial preload* (or prestress) of the elastic rods, is introduced in Chapter 3, where the problem of incremental wave propagation is enriched by the geometric second-order contribution of the prestress

[1]For any given frequency, the outgoing waves can be completely absorbed at the boundary by tuning the damping in the PML, so that reflection is not generated in the interior domain.

state. The key point is that, if a prestress is applied in such a way that the local distortion of the lattice structure is negligible, material interfaces can be introduced in an 'ambient lattice' by selectively prestressing a desired set of rods. The prestress level can then be tuned to achieve desired transmission properties at given working frequencies. The advantage of leveraging states of prestress is that the dynamic characteristics of the interface can be altered *without* requiring structural modification in the ambient material, thus the system can be easily reconfigured for multiple applications.

In order to demonstrate the potential new applications that can be achieved in the control of wave propagation, different configurations of prestress states are introduced in a square lattice structure to obtain dynamic interfaces exhibiting total reflection, negative refraction, focussing, and wave guiding effects. Two examples are reported in Fig. 1.2, where the response induced in the ambient lattice by a pulsating moment is controlled by preloading a vertical layer of rods. On the left part of the figure, the preload is selected to produce a purely reflective interface, while on the right part, *without* changing the working frequency but by increasing the preload, the interface is shown to effectively behave as a material with a negative refractive index, thus allowing the reconstruction of the image of the source on the opposite side of the layer. This realizes the elastodynamic counterpart of the optical effect known as *flat lensing* [26].

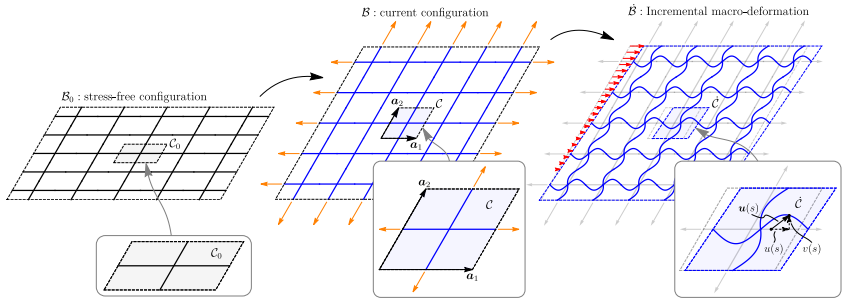

Fig. 1.3. The response of a lattice of elastic rods is defined with reference to a relative Lagrangian setting where the current prestressed configuration is assumed as reference for the determination of the incremental response. A periodic two-dimensional lattice of (axially and flexurally deformable) elastic rods is considered prestressed from the stress-free configuration $\mathcal{B}_0$ (left) by means of a purely axial loading state. The prestressed configuration $\mathcal{B}$ (center) can be represented as the tessellation of a single unit cell along the vectors of the direct basis $\{\boldsymbol{a}_1, \boldsymbol{a}_2\}$. Upon the current prestressed configuration, the response of the lattice to a macroscopic incremental deformation gradient (right) identifies the response of the 'effective' continuum.

Other prestress-induced phenomena of paramount relevance for the understanding of the 'effective' material response are *material instabilities*, which are the main subject of Chapter 4 and 5. Instabilities such as shear banding and strain localizations are well-known phenomena from the point of view of continuum mechanics, but less is known about how these can emerge from and are affected by the microstructural organization of the

material. This is mostly due to the phenomenological character of the constitutive laws usually employed in the modelling at the continuum scale. Therefore, in order to relate *quantitatively* the macroscopic response of a prestressed material to the internal state of its constituents, proper homogenization methods have to be devised.

In Chapter 4, a static strain-energy-based homogenization is developed for prestressed lattices, capable of incorporating second-order mechanical effects in the incremental macroscopic response. Building upon the work of Triantafyllidis [18, 19, 27–30] and Ponte Castañeda [20, 31–38], the homogenization method is formulated for arbitrary lattice geometries made of elastic rods which are considered subject to arbitrarily large nonlinear axial deformations and whose incremental response is derived analytically from the large deformation beam theory. By means of a relative Lagrangian description (see Fig 1.3), the incremental response of the prestressed lattice to the application of an arbitrary macroscopic incremental displacement gradient is evaluated analytically. The 'effective' continuum material is then identified through the incremental strain-energy matching between the lattice and the continuum, which provides the homogenized *current prestress state* as well as the *incremental constitutive operator* relating the incremental nominal stress to the incremental deformation gradient.

The method is employed to obtain the analytical expression for the *incremental constitutive tensor* of the 'effective' continuum for a wide family of lattices, covering several classes of anisotropy: isotropic, cubic, orthotropic, and complete anisotropy as well. Leveraging the analytic result, failure of ellipticity of the incremental macroscopic response is systematically analyzed as a function of the lattice parameters and compared to the loss of stability of the lattice which is computed by spanning over all possible wavelength bifurcations. This allows the identification of the lattice structural parameters affecting the *critical* type of bifurcation so to discriminate the lattice configurations reaching failure of ellipticity for the 'effective' continuum (corresponding to bifurcations of infinite-wavelength, so-called 'macroscopic') from the ones exhibiting short-wavelength bifurcations (called 'local' or 'microscopic' instabilities).

'Macro' and 'micro' bifurcations are investigated via a Green's function-based perturbative approach [39] to disclose the incremental response of the lattice material and its 'effective' continuum when statically perturbed close to the bifurcation threshold. Two examples of this analysis are reported in Fig 1.4, where two rhombic grid lattices (orthotropic on the left and anisotropic on the right) are prestressed to bring the 'effective' material close to the elliptic boundary and then perturbed by the application of a static self-equilibrated dipole. The maps of incremental displacements of the lattice (upper part) demonstrate that the emergence of strain localization bands is correctly predicted by the response of the homogenized solid (lower part). Moreover, the analytic result for the 'effective' continuum enables the tunability of this extreme material response, as the inclination and the number of localization bands can be designed by tuning the mechanical parameters of the underlying lattice structure.

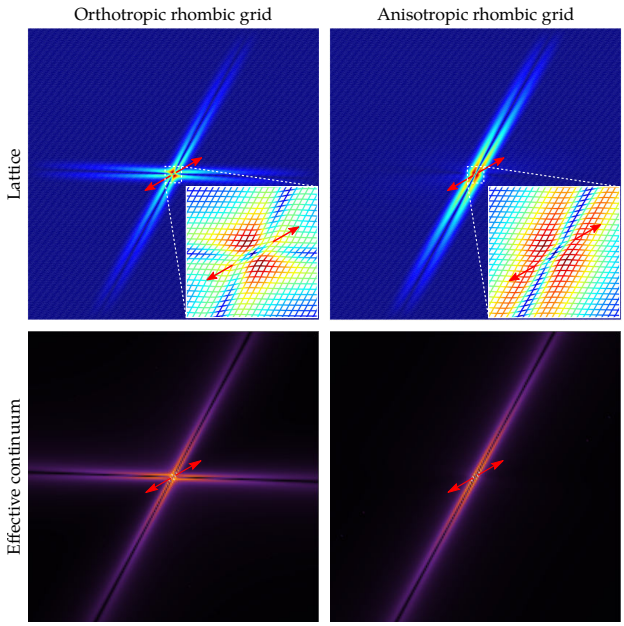

Fig. 1.4. Examples of static strain localizations in anisotropic lattices made up of flexurally and axially deformable elastic rods, prestressed close to failure of strong ellipticity of the homogenized material. Two periodic lattices with a rhombic grid structure correspond to 'effective' continuum materials, which are brought close to failure of strong ellipticity by means of an in-plane state of prestress. Both the lattice and its 'effective' material display an incremental response characterized by strain localization bands, which are revealed as the response to an applied perturbation (here in the form of a static self-equilibrated dipole, see the case of dynamic excitation in Fig. 1.5). The good agreement between the actual response of the lattice structure (upper part computed via f.e.m.) and the behavior of the 'effective' solid obtained via homogenization (lower part computed via Green's function) demonstrates that the stability analysis of the homogenized material allows the determination of the correct number of localization bands and their inclination. Further details are provided in Chapter 4 (see Figs. 4.10–4.13).

The static homogenization outlined in Chapter 4 is generalized in Chapter 5 to the dynamics of incremental waves propagating in prestressed lattices. A dynamic homogenization technique is developed by analyzing the asymptotic response of a lattice of elastic rods deforming in the plane and subject to incremental waves in the low-frequency regime. By extending recent results on beam lattices [40] to the incremental dynamics of prestressed lattices, it is shown that the asymptotics of the Floquet-Bloch spectrum on the acoustic branches is characterized by linear dispersion and uniform wave modulation. The result is derived without restrictions on the rods' constitutive law and without neglecting the rotational inertia of the rods' cross section. In contrast to the static homogenization, it is shown that the dynamic approach provides directly the *acoustic tensor* of the 'effective' continuum, which proves that the failure of ellipticity (i.e. the singularity of the acoustic tensor) *coincides* with the condition of macro-bifurcation of the lattice (i.e. a bifurcation of infinite wavelength). It is also shown how

both 'macro' and 'micro' bifurcations occurring in the lattice have a clear dynamic interpretation in terms of degeneracies of the dispersion relation as a function of the prestress state.

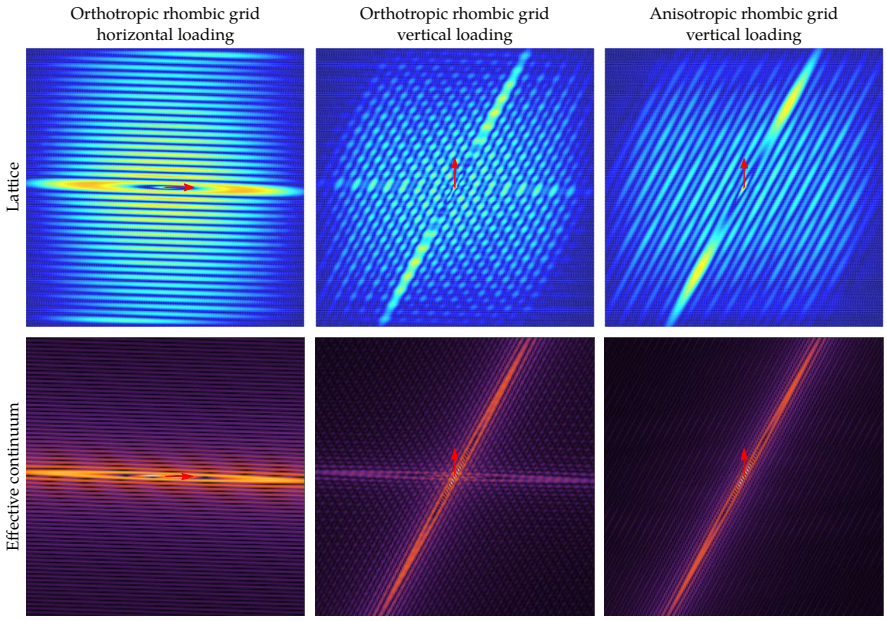

Fig. 1.5. Examples of dynamic localization occurring in prestressed lattice made up of flexurally and axially deformable elastic rods, prestressed close to failure of strong ellipticity of the homogenized material. When a dynamic perturbation is applied to such materials (here in the form of a pulsating force, see the case of static loading in Fig. 1.4), the incremental response is characterized by the propagation of almost parallel plane waves propagating outward from the forcing source and having a wavefront inclination dictated by the direction of ellipticity loss. Depending on the loading direction and the material anisotropy, the lattice response (upper part computed via f.e.m.) exhibits a single or multiple localization, both correctly predicted by the time-harmonic Green's function (lower part) of the 'effective' solid obtained via homogenization. Further details are provided in Chapter 5 (see Figs. 5.9–5.17).

The response of the family of lattices considered in Chapter 4 is analyzed in the time-harmonic regime by introducing a pulsating concentrated force as an incremental perturbation to the prestressed material. Some examples of the results are reported in Fig. 1.5, demonstrating an excellent agreement between the lattice response and the time-harmonic Green's function of the homogenized material. The lattice-continuum comparison is also conducted in the Fourier space, by computing the Fourier transform of the lattice response and superimposing it to the slowness contour of both the lattice and the continuum, so to assess the spectrum of Bloch waves excited by the load. The comparison demonstrates that, as the material lies inside the strong elliptic domain, the 'effective' continuum is an accurate representation of the lattice behavior, while the nonlinear dispersion of the lattice

may become important, even at low frequency, only in the neighborhood of the elliptic boundary.

2

Free and forced wave propagation in Rayleigh-beam grids

In-plane wave propagation in a periodic rectangular frame structure, which includes axial and flexural deformation, the latter enhanced with rotational inertia (so-called 'Rayleigh beams'), is analyzed both with a Floquet-Bloch exact formulation for free oscillations and with a numerical treatment (developed with PML absorbing boundary conditions) for forced vibrations (including Fourier representation and energy flux evaluations), induced by a concentrated force or moment. A complex interplay is observed between axial and flexural vibrations (not found in the common idealization of out-of-plane motion), giving rise to several forms of vibration localization: 'X-', 'cross-' and 'star-' shaped, and channel propagation. These localizations are triggered by several factors, including rotational inertia and slenderness of the beams and the type of forcing source (concentrated force or moment). Although the considered grid of beams introduces an orthotropy in the mechanical response, a surprising 'isotropization' of the vibration is observed at special frequencies. Moreover, rotational inertia is shown to 'sharpen' degeneracies related to Dirac cones (which become more pronounced when the aspect ratio of the grid is increased), while the slenderness can be tuned to achieve a perfectly flat band in the dispersion diagram. The obtained results can be exploited in the realization of metamaterials designed to filter waves during propagation.

2.1 Introduction

Research on metamaterials (employed to guide and control elastic waves for applications in microstructured devices [9, 10, 41–45] and earthquake resistant structures [46–50]) has focused a strong research effort on time-harmonic vibrations of periodic beam networks. These networks can be analyzed via Floquet-Bloch analysis for free vibrations of an infinite domain (which can be either 'exact', when performed with a symbolic computation program [51] or approximated, when solved numerically [52]), or using the f.e. methodology for forced vibrations of finite-size structures [25].

Several topologies, vibration conditions and beam models have been considered for wave propagation in two-dimensional lattices, namely, hexagonal, triangular, and square honeycombs, re-entrant and Kagomé lattices [53, 54], subject to out-of-plane motion with [25, 55, 56] or without [57] rotational inertia (the so-called 'Rayleigh correction', introducing a bound to the phase and group velocity of a beam [58, 59]).

Forced vibrations of grid of beams has been considered for a two-dimensional mass/spring periodic structure [60], while asymptotic approximations of lattice Green's functions have been given [61, 62], close to standing wave frequencies, with the purpose of revealing the directional anisotropy in two and three-dimensional periodic lattices.

Although in-plane vibrations of a rectangular grid of Rayleigh (axially and flexurally deformable) beams may be considered a mature research field, for which the governing equations and the solution techniques are well-known, many interesting features still remain to be explored. This exploration is provided in the present work, where an exact Floquet-Bloch analysis is performed and complemented with a numerical treatment of the forced vibrations induced by the application of a concentrated force or moment, including presentation of the Fourier transform and energy flow (treated in [63] for free vibrations). It is shown that (i) aspect ratio of the grid, (ii) slenderness, and (iii) rotational inertia of the beams decide the emergence of several forms of highly-localized waveforms, namely, 'channel propagation', 'X-', 'cross-', 'star-' shaped vibration modes. Moreover, these mechanical properties of the grid can be designed to obtain flat bands and degeneracies related to Dirac cones in the dispersion diagram and directional anisotropy or, surprisingly, dynamic 'isotropization', for which waves propagate in a square lattice with the polar symmetry characterizing propagation in an isotropic medium.

The presented results open the way to the design of vibrating devices with engineered properties, to tune the frequency response of the structure.

2.2 In-plane Floquet-Bloch waves in a rectangular grid of beams

An infinite lattice of Rayleigh beams is considered, periodically arranged in a rectangular geometry as shown in Fig. 2.1a, together with the unit cell, Fig. 2.1b. The beams are rigidly joined together, so that the angle between the beams at every nodal point is preserved. Moreover, the usual assumptions of the linear elasticity theory are adopted, including beam unshearability, small-amplitude of vibrations and absence of damping.

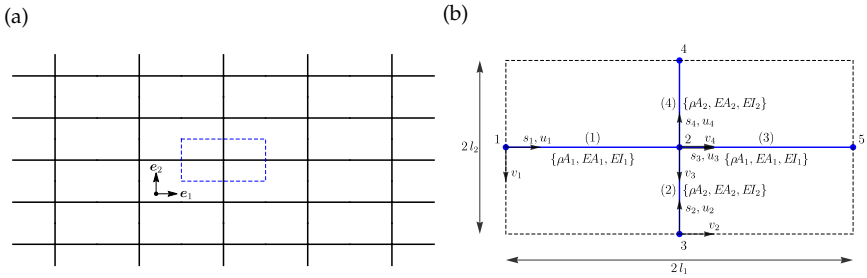

Fig. 2.1. Geometry of the grid-beam structure, made up of elements which may deform extensionally and in bending (a) and the relevant unit cell, where the local reference system is shown (b).

Each beam is assumed to be axially extensible and flexible, so that the equations governing the time-harmonic (in-plane) response are

$$\begin{aligned} EA\,\frac{\partial^2 u(s)}{\partial s^2} + \rho A\,\omega^2 u(s) = 0\,, \\ EI\,\frac{\partial^4 v(s)}{\partial s^4} + \rho I\,\omega^2 \frac{\partial^2 v(s)}{\partial s^2} - \rho A\,\omega^2 v(s) = 0\,, \end{aligned} \tag{2.1}$$

where ρ is the mass density, E the Young modulus, A and I are respectively the area and the second moment of inertia of the beam's cross-section, and ω is the angular frequency of the time-harmonic vibration. The axial and transverse displacements are denote with $u(s)$ and $v(s)$, respectively, where s is the local axial coordinate, Fig. 2.1b. By setting $\xi = s/l$, with l being the length of the beam, Eqs. (2.1) can be cast in the following dimensionless form

$$u''(\xi) + \tilde{\omega}^2 u(\xi) = 0, \qquad v''''(\xi) + \tilde{\omega}^2 v''(\xi) - \frac{\lambda^2}{4}\,\tilde{\omega}^2 v(\xi) = 0, \tag{2.2}$$

where $\tilde{\omega} = \omega\, l\sqrt{\rho/E}$ is a non-dimensional angular frequency, $\lambda = 2\,l\sqrt{A/I}$ represents the slenderness of the beam, and the prime denotes differentiation with respect to ξ.

The general solution of Eqs. (2.2) is sought in the form

$$u(\xi) = \sum_{j=1}^{2} C_j e^{i\,\eta_j(\tilde{\omega})\,\xi}, \qquad v(\xi) = \sum_{j=1}^{4} D_j e^{i\,\gamma_j(\tilde{\omega},\lambda)\,\xi}, \tag{2.3}$$

where the C_j and D_j denote 6 complex constants, while the η_j and γ_j are characteristic roots

$$\eta_{1,2}(\tilde{\omega}) = \pm\tilde{\omega}, \qquad \gamma_{1,2,3,4}(\tilde{\omega},\lambda) = \pm\sqrt{\frac{\tilde{\omega}}{2}\left(\tilde{\omega} \pm \sqrt{\lambda^2+\tilde{\omega}^2}\right)}. \tag{2.4}$$

With the local coordinates shown in Fig. 2.1b, the displacement field on each beam of the unit cell is

$$\begin{gathered} u_p(\xi_p) = \sum_{q=1}^{2} C_{pq} e^{i\,\eta_q(\tilde{\omega}_p)\,\xi_p}\,, \quad v_p(\xi_p) = \sum_{q=1}^{4} D_{pq} e^{i\,\gamma_q(\tilde{\omega}_p,\,\lambda_p)\,\xi_p}\,, \\ \xi_p = s_p/l_p\,, \quad \forall\, p \in \{1,\dots,4\}\,, \end{gathered} \tag{2.5}$$

where the 24 undetermined constants, C_{pq} and D_{pq}, can be found by imposing kinematic compatibility and equilibrium conditions at the central junction, plus the Floquet-Bloch boundary conditions between corresponding sides of the unit cell.

Assuming for simplicity the elastic modulus E and the mass density ρ to be equal in all the beams, by choosing the following dimensionless variables

$$\begin{gathered} \tilde{\omega}_1 = \omega\, l_1\sqrt{\rho/E}, \quad \lambda_1 = 2\,l_1\sqrt{A_1/I_1}, \quad \lambda_2 = 2\,l_2\sqrt{A_2/I_2}, \\ \alpha = l_1/l_2, \quad \chi = A_1/A_2, \end{gathered} \tag{2.6}$$

the linear system governing the time-harmonic oscillations of the lattice is defined as follows.

- Compatibility of displacements and rotations at the central node of the unit cell

$$\begin{array}{lll} v_1(1) = v_3(0), & v_2(1) = v_4(0), & v_1(1) = -u_2(1), \\ u_1(1) = u_3(0), & u_2(1) = u_4(0), & v_2(1) = u_1(1), \\ v_1'(1) = \alpha\, v_2'(1), & \alpha\, v_2'(1) = v_3'(0), & v_3'(0) = \alpha\, v_4'(0), \end{array} \tag{2.7}$$

- equilibrium of the central node

$$
\begin{aligned}
u_3'(0) - u_1'(1) - \frac{4\,\alpha}{\chi\lambda_2^2}\,v_4'''(0) - \frac{4}{\chi\alpha\lambda_2^2}\,\tilde{\omega}_1^2\,v_4'(0) + \\
+ \frac{4\,\alpha}{\chi\lambda_2^2}\,v_2'''(1) + \frac{4}{\chi\alpha\lambda_2^2}\tilde{\omega}_1^2\,v_2'(1) = 0\,, \\
u_4'(0) - u_2'(1) - \frac{4\,\chi}{\alpha\lambda_1^2}\,v_1'''(1) - \frac{4\,\chi}{\alpha\lambda_1^2}\tilde{\omega}_1^2\,v_1'(1) + \\
+ \frac{4\,\chi}{\alpha\lambda_1^2}\,v_3'''(0) + \frac{4\,\chi}{\alpha\lambda_1^2}\tilde{\omega}_1^2\,v_3'(0) = 0\,, \\
v_3''(0) + \frac{\lambda_1^2}{\chi\lambda_2^2}\,v_4''(0) - v_1''(1) - \frac{\lambda_1^2}{\chi\lambda_2^2}\,v_2''(1) = 0\,,
\end{aligned}
\tag{2.8}
$$

- Floquet-Bloch boundary conditions

$$
\begin{aligned}
u_3(1) &= u_1(0)\,e^{i\,K_1}, \\
v_3(1) &= v_1(0)\,e^{i\,K_1}, \\
v_3'(1) &= v_1'(0)\,e^{i\,K_1}, \\
u_3'(1) &= u_1'(0)\,e^{i\,K_1}, \\
v_3'''(1) + \tilde{\omega}_1^2\,v_3'(1) &= (v_1'''(0) + \tilde{\omega}_1^2\,v_1'(0))\,e^{i\,K_1}, \\
v_3''(1) &= v_1''(0)\,e^{i\,K_1}, \\
u_4(1) &= u_2(0)\,e^{i\,K_2/\alpha}, \\
v_4(1) &= v_2(0)\,e^{i\,K_2/\alpha}, \\
v_4'(1) &= v_2'(0)\,e^{i\,K_2/\alpha} \\
u_4'(1) &= u_2'(0)\,e^{i\,K_2/\alpha}, \\
v_4'''(1) + \frac{\tilde{\omega}_1^2}{\alpha^2}\,v_4'(1) &= \left(v_2'''(0) + \frac{\tilde{\omega}_1^2}{\alpha^2}\,v_2'(0)\right)\,e^{i\,K_2/\alpha}, \\
v_4''(1) &= v_2''(0)\,e^{i\,K_2/\alpha},
\end{aligned}
\tag{2.9}
$$

  where K_1 and K_2 are dimensionless components of the Bloch wave vector $\boldsymbol{k} = k_1\boldsymbol{e}_1 + k_2\boldsymbol{e}_2$, namely, $K_1 = k_1 2l_1$, $K_2 = k_2 2l_1$.

Eqs. (2.7)–(2.9) provide the complete set of equations governing the propagation of in-plane Floquet-Bloch waves for an infinite and periodic Rayleigh beam lattice. The governing equations for the corresponding Euler-Bernoulli approximation can be easily obtained by neglecting the rotational inertia terms, $\rho I_1 = \rho I_2 = 0$, and by retaining only the low-frequency term of the flexural characteristic roots γ_j, i.e. $\gamma_{1,2,3,4} = \pm\sqrt{\pm\tilde{\omega}\lambda/2}$.

2.3 Dispersion properties and Bloch waveforms

2.3.1 Dispersion equation

A substitution of representation (2.5) into the boundary conditions (2.7)–(2.9) leads to an algebraic homogeneous linear system of the type

$$\boldsymbol{A}(\tilde{\omega}_1, \boldsymbol{K}, \lambda_1, \lambda_2, \alpha, \chi)\, \boldsymbol{c} = \boldsymbol{0}, \tag{2.10}$$

where $\boldsymbol{A}$ is a 24×24 complex matrix, function of the dimensionless angular frequency $\tilde{\omega}_1$ and wave vector $\boldsymbol{K}$, slenderness λ_1 and λ_2, aspect ratio α and geometric ratio χ. Vector $\boldsymbol{c}$ collects the 24 complex constants, C_{pq} and D_{pq}, appearing in the displacement field, Eqs. (2.5).

Introducing the following normalization

$$\Omega = \frac{4l_1^2\omega}{\pi^2\sqrt{EI_1/(\rho A_1)}} = \frac{2\lambda_1\tilde{\omega}_1}{\pi^2}, \tag{2.11}$$

where the angular frequency ω has been made dimensionless through division by the first flexural natural frequency of a simply supported Euler-Bernoulli beam, the non-trivial solutions of the system (2.10) are found when the matrix $\boldsymbol{A}$ is rank-deficient

$$\det \boldsymbol{A}(\Omega, \boldsymbol{K}, \lambda_1, \lambda_2, \alpha, \chi) = 0, \tag{2.12}$$

which is the *dispersion equation*, implicitly defining the relation between the angular frequency Ω and the wave vector $\boldsymbol{K}$, namely, the so-called *dispersion relation*. Furthermore, for each point of the $\{\Omega, \boldsymbol{K}\}$-space satisfying Eq. (2.12), the corresponding eigenvector $\boldsymbol{c}(\Omega, \boldsymbol{K})$ can be computed from (2.10).

Hence, the propagation of Floquet-Bloch waves is governed by the eigenvalue problem (2.10), where the *eigenfrequencies* are determined by the dispersion relation $\Omega(\boldsymbol{K})$, periodic with period $[0, 2\pi] \times [0, 2\pi\alpha]$, and the *eigenmodes* (or waveforms) are defined by the eigenvectors $\boldsymbol{c}(\Omega, \boldsymbol{K})$, to be inserted into Eqs. (2.5).

2.3.2 Dispersion surfaces: Euler-Bernoulli vs Rayleigh

Dispersion surfaces are provided for the Euler-Bernoulli as well as the Rayleigh lattices, with an emphasis on the effects of both the rotational inertia and the slenderness of the beams. To this end, a lattice made up of beams of equal characteristics, except the length, is addressed, $\chi = 1$, $I_1 = I_2$. A square grid, $\alpha = 1$, $\lambda_1 = \lambda_2 = \lambda = 5$, and a rectangular, $\alpha = 2$, $\lambda_1 = 2\lambda_2 = 10$, are considered. Results are reported in Figs. 2.2 and 2.4a for a square and in Fig. 2.4b for a rectangular grid.

The dispersion surfaces shown in the figures are complemented by the band diagrams reported in Figs. 2.3 and 2.5, relative to the paths Γ–X–Y–Γ

and Γ–*X*–*Y*–*Z*–Γ reported in the Figs. 2.2 and 2.4b, permitting the appreciation of details which remain undetected from the dispersion surfaces.

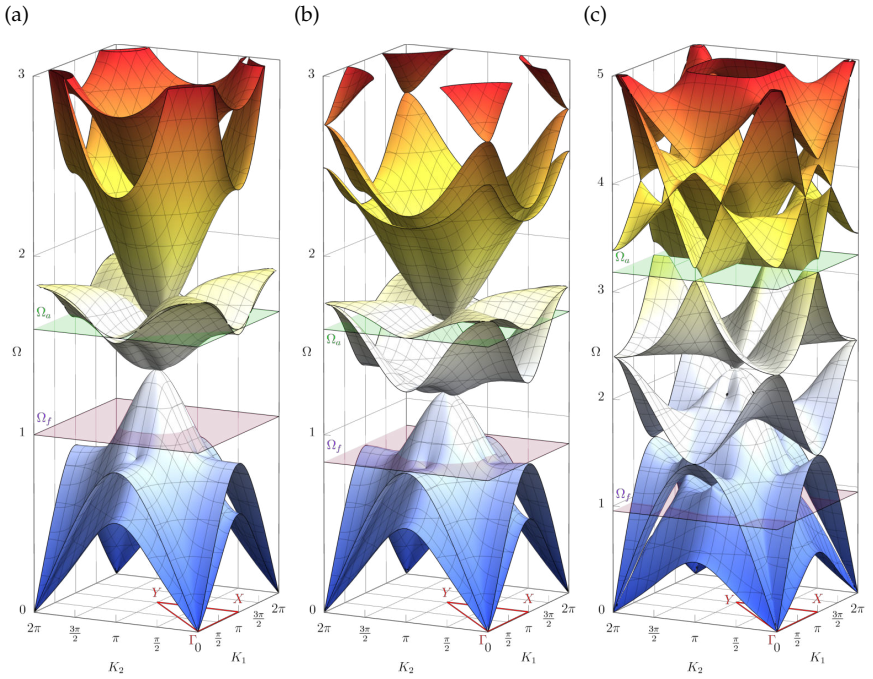

Fig. 2.2. The effect of rotational inertia (becoming important at high frequency) is evidenced by the differences between the dispersion surfaces for a square lattice made up of Euler-Bernoulli (a) and Rayleigh (b) beams, both relative to a slenderness $\lambda = 5$. The influence of the slenderness (already evident at low frequency) may be appreciated by comparing the case $\lambda = 5$ (b) with the case $\lambda = 10$ (c). The green and pink horizontal planes denote two first natural frequencies of a double-pinned beam, namely, Ω_f corresponds to the flexural vibration and identifies the stationary point of the lowest dispersion surface (occurring at $\{K_1, K_2\} = \{\pi, \pi\}$). Ω_a corresponds to the axial vibration and identifies the set of stationary points of the fourth and fifth surface located respectively at $K_1 = \pi$, $\forall K_2$ and $K_2 = \pi$, $\forall K_1$. The band diagrams corresponding to the path Γ–*X*–*Y*–Γ sketched in the figure are reported in Fig. 2.3.

The dispersion surfaces reported in Figs. 2.2 and 2.4 have been marked with the following two particular frequencies (respectively with a pink and green plane)

$$\Omega_j^f = \frac{\lambda_1}{\sqrt{\pi^2 + \lambda_j^2}} \frac{l_1}{l_j}, \qquad \Omega_j^a = \frac{\lambda_1}{\pi} \frac{l_1}{l_j}, \qquad \forall\, j \in \{1, 2\} \tag{2.13}$$

which are the lowest natural frequencies of, respectively, the flexural and axial mode of a double-pinned Rayleigh beam. It is worth noting that

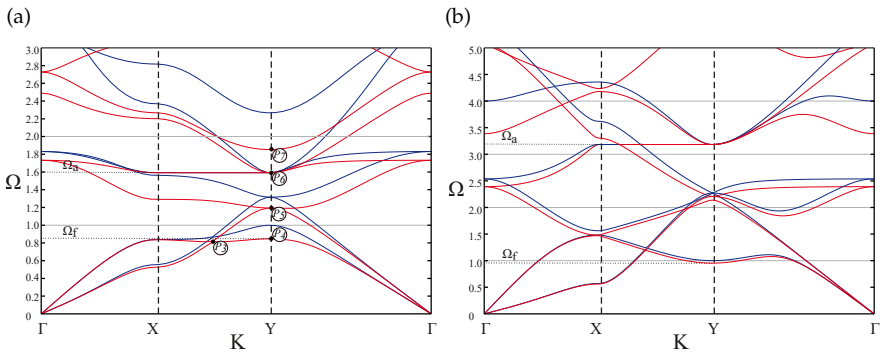

Fig. 2.3. A lowering of the dispersion frequency induced by the rotational inertia is visible in the band diagrams for a square lattice made up of Euler-Bernoulli (blue curves) and Rayleigh beams (red curves), with slenderness $\lambda = 5$ (a) and $\lambda = 10$ (b). The labels P_i (marked also in Fig. 2.6, see also Table 2.1) denote the points where the corresponding waveforms have been computed and shown in Figs. 2.8–2.10. Note that Ω_f always corresponds to the vertex of the first dispersion surface, denoted by P_4, whereas Ω_a corresponds to the flat band, denoted by P_6. Furthermore, the rotational inertia leaves the flat band at $\Omega = \Omega_a$ unaltered along the $X-Y$ path, due to the fact that purely axial vibrations occur. The diagrams have been evaluated along the boundary of the first irreducible Brillouin zone (path Γ–X–Y–Γ sketched in Fig. 2.2).

Ω_j^f is always lower than Ω_j^a, and that, in the particular case of the Euler-Bernoulli model, the dimensionless natural frequencies become $\Omega_1^f = 1$ and $\Omega_2^f = \alpha\lambda_1/\lambda_2$.

The beam slenderness (which measures the relative importance between flexural and axial deformations along the beams in the grid) is expected to play an important role in the in-plane wave propagation and thus in the dispersion relation $\Omega(K_1, K_2)$. This is in fact a consequence of the compatibility and equilibrium equations to be satisfied at the central node, Eqs. (2.7)–(2.8), which produce a coupling between axial and transverse displacements along the beams, simply absent in the case of out-of-plane motion [25]. The influence of the slenderness can be easily appreciated by comparing results reported in Fig. 2.2b with those reported in Fig. 2.2c, relative to a slenderness $\lambda = 5$ in the former figure and $\lambda = 10$ in the latter. Note that, these values have been selected to highlight differences in the model response, even if the structural hypothesis of beam unshearability looses validity at small values of slenderness. It can be for instance noticed that the second and third dispersion surfaces are strongly separated by an increase of stiffness.

Rotational inertia produces a lowering of the propagation frequency, so that for any fixed value of slenderness, each dispersion surface of the Rayleigh beam lattice is *lower* than the corresponding surface for Euler-Bernoulli (compare Fig. 2.2a to Fig. 2.2b and see Fig. 2.3), so that a seventh surface enters the frequency response in Fig. 2.2b.

Moreover, a separation is observed between the dispersion surfaces, except at low frequency, the so-called 'acoustic branches', where it is known that the two Rayleigh and Euler-Bernoulli models predict the same response.

An interesting feature emerging from the dispersion surfaces is the presence of sets of points independent of the rotational inertia, so that their position remains the same for both beam models. These points can be seen by comparing the fourth surface in Fig. 2.2a and 2.2b, where it can be noticed that the points corresponding to $K_1 = \pi,\ \forall K_2$ or $K_2 = \pi,\ \forall K_1$ are located at the same frequency $\Omega_a = \lambda/\pi$ in both figures (highlighted with an horizontal green plane), which is the frequency corresponding to the first *axial* mode of vibration of a double-pinned beam. Here the dispersion relation is stationary, so that the corresponding waveforms has a null group velocity, and, in fact (see Section 2.3.3), these waves do not involve flexion, so that the joints of the entire lattice remain fixed.

A flattening of the fourth dispersion surface, giving rise to an *infinite set of standing waves propagating at the same frequency with an arbitrary wave vector*, can be produced through a tuning of slenderness for both the Euler-Bernoulli and Rayleigh beam models. This can be deduced by noting the reversal in the curvature of the fourth dispersion surface relative to $\lambda = 5$ (Fig. 2.2b) compared to that relative to $\lambda = 10$ (Fig. 2.2c), suggesting the existence of a flat surface for an intermediate value of slenderness. Indeed the flat surface is present when the first flexural and axial mode of a double-clamped beam have the same natural frequency, which, for the Rayleigh model, occurs for a value of λ satisfying the following equation

$$\left[\cos(2\,\gamma_1(\tilde{\omega},\lambda))\cosh\left(\frac{\tilde{\omega}\lambda}{\gamma_1(\tilde{\omega},\lambda)}\right)+ \right. \\ \left. +\frac{\tilde{\omega}}{\lambda}\sin(2\,\gamma_1(\tilde{\omega},\lambda))\sinh\left(\frac{\tilde{\omega}\lambda}{\gamma_1(\tilde{\omega},\lambda)}\right)-1\right]_{\tilde{\omega}=\pi/2}=0, \quad (2.14)$$

where

$$\gamma_1(\tilde{\omega},\lambda)=\sqrt{\tilde{\omega}\left(\tilde{\omega}+\sqrt{\lambda^2+\tilde{\omega}^2}\right)/2}.$$

A numerical solution of Eq. (2.14) (in the interval $5 \le \lambda \le 10$) yields $\lambda \approx 6.192$. For this value of slenderness, the dispersion surfaces and the band diagram reported respectively in Figs. 2.4a and 2.5a show the presence of a flat dispersion surface. Note in particular that at the point Y (i.e. $K_1 = K_2 = \pi$) a triple root of the dispersion equation exists, corresponding to the intersection between the fourth, fifth and sixth dispersion surfaces.

The aspect ratio ($\alpha = l_1/l_2$) **of the rectangular lattice** has an important effect on the vibrational characteristics of the grid. In particular, Figs. 2.4b and 2.5b pertain to a Rayleigh beam with $\alpha = 2, \lambda_1 = 2\lambda_2 = 10$ and these results can be compared to those reported in Figs. 2.2b, 2.2c and 2.3. Besides

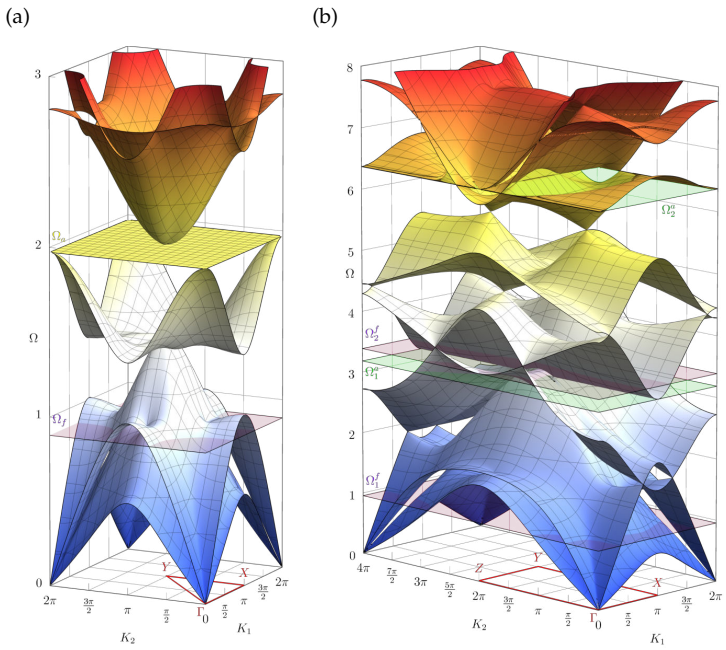

Fig. 2.4. A completely flat band of the fourth dispersion surface is produced in a Rayleigh beam square lattice at the slenderness $\lambda = 6.192$, so that an infinite set of standing waves propagate at the same frequency $\Omega = 1.971$, part (a). Dirac cones are clearly visible in the dispersion surfaces of a rectangular lattice with contrasting slenderness with $\lambda_1 = 10$ and $\lambda_2 = 5$, part (b). Note that the frequencies Ω_f and Ω_a found for the square lattice (Figs. 2.2b and 2.2c) are now split in the four frequencies $\Omega^f_{1,2}$ and $\Omega^a_{1,2}$. The band diagrams corresponding to the paths Γ–*X*–*Y*–Γ and Γ–*X*–*Y*–*Z*–Γ sketched in the figure are reported in Fig. 2.5.

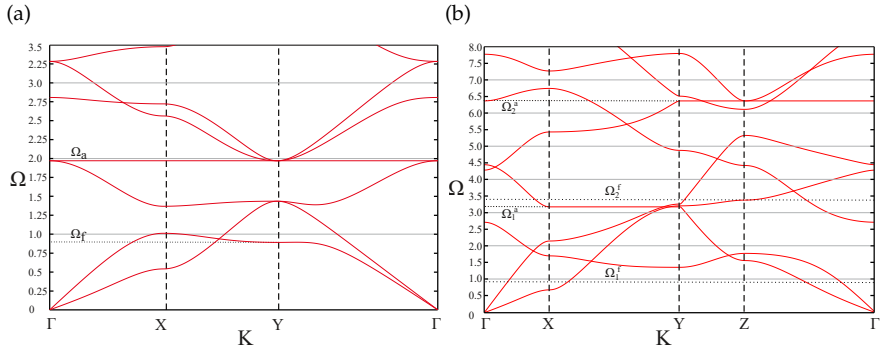

Fig. 2.5. The band diagrams relative to the paths Γ–*X*–*Y*–Γ and Γ–*X*–*Y*–*Z*–Γ sketched in Fig. 2.4 show: (a) the perfectly flat band occurring at the slenderness $\lambda = 6.192$ in a Rayleigh square lattice; (b) the Dirac cones (particularly evident in the fourth and fifth band) present in a rectangular lattice with slenderness contrast $\lambda_1 = 10$, $\lambda_2 = 5$.

the fact that the surfaces are different, two aspects can be noticed: (i) that

the two frequencies Ω_a and Ω_f split into the four $\Omega^a_{1,2}$ and $\Omega^f_{1,2}$ and (ii) that Dirac cones become clearly visible [24, 25].

Several singularities and Dirac cones connect the complex multiple dispersion surfaces in Figs. 2.2 and 2.4, but Dirac cones become particularly evident in the rectangular grid, Fig. 2.4b. At these singular points the dispersion relation may become non-smooth.

2.3.3 Slowness contours, Dirac cones, and standing waves

Detailed features of the individual dispersion surfaces are analyzed by computing their level sets, also referred to as *slowness contours*. As these contours provide valuable information on the kind of anisotropy to be expected in the time-harmonic response of the lattice, their analysis allows us to identify the frequency regimes corresponding to different dynamic behaviours. In fact, this tool has already been proved to be successful at predicting the preferential directions of the forced vibrations for the out-of-plane problem [25].

As discussed in the previous section, the in-plane wave propagation problem involves more complex dispersion characteristics than the out-of-plane, due to the coupling between the axial and flexural beam vibrations. Furthermore, the vectorial nature of the problem allows the application of different types of in-plane concentrated loads, namely two orthogonal point forces and a concentrated bending moment, and hence the shape of the slowness contours alone cannot provide a comprehensive description of the forced lattice vibrations. Therefore, a complete investigation of the lattice vibration properties, involves determination of the following aspects:

(i) identification of frequency ranges displaying the non-convexity of the slowness contours, for possible detection of negative refraction;

(ii) computation of waveforms corresponding to double roots and standing waves, as connected to resonance under forced vibrations;

(iii) identification of waveforms evidencing a purely extensional or flexural response, corresponding to vibration modes of a finite-length beam.

For the Rayleigh beam model and the two values of slenderness, $\lambda = 5$ and 10, the slowness contours of the first five dispersion surfaces have been computed and reported in Figs. 2.6 and 2.7, complemented by the corresponding 3d views. Along the contours pertaining to $\lambda = 5$, points are marked (labeled $P_1, P_2, \ldots$), for which the corresponding waveforms are shown in Figs. 2.8–2.10. The numerical values of the coordinates of these points are provided in Table 2.1; in addition, the same points have also been indicated in Fig. 2.3a.

The first property that clearly emerges from the shape of the contours is the cubic symmetry in the quasi-static (low-frequency) response, inherited by the symmetry of the square grid itself. In particular, considering the two lowest surfaces (Figs. 2.6f and 2.6g or 2.7f and 2.7g) in the neighbourhood of

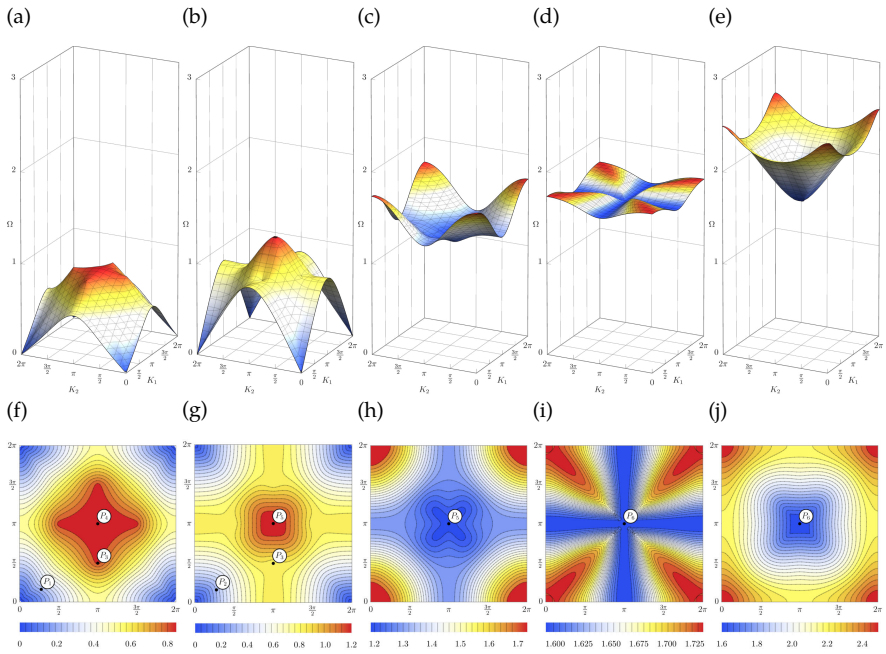

Fig. 2.6. The cubic anisotropy is evident from the slowness contours (f)–(j) associated to the dispersion surfaces (a)–(e), for a square grid of Rayleigh beams with slenderness $\lambda = 5$. The labels P_i (marked also in Fig. 2.3a, see also Table 2.1) denote the points where the corresponding waveforms have been computed and shown in Figs. 2.8–2.10. Linear dispersion at low frequency is visible in the acoustic branches (the first two dispersion surfaces), while the dispersion relation becomes nonlinear at high frequency and the isofrequency contours dramatically change and display several double-root points such as the four Dirac cones (one of them is labelled P_3) connecting the first two surfaces as well as the stationary points connecting the second and the third (P_5) or the fourth and fifth surface (P_6).

Point	K_1	K_2	Ω	Disp. Surface
P_1	$\sqrt{3}/2$	$1/2$	0.230	1^{st}
P_2	$\sqrt{3}/2$	$1/2$	0.325	2^{nd}
P_3	π	1.555	0.812	$1^{\text{st}} - 2^{\text{nd}}$
P_4	π	π	$\Omega_f \approx 0.8467$	1^{st}
P_5	π	π	1.193	$2^{\text{nd}} - 3^{\text{rd}}$
P_6	π	π	$\Omega_a \approx 1.592$	$4^{\text{th}} - 5^{\text{th}}$
P_7	π	π	1.853	6^{th}

Table 2.1. Location (in the $\{K_1, K_2, \Omega\}$-space) of the points on the dispersion surfaces (for a Rayleigh beam lattice with slenderness $\lambda = 5$) at which the corresponding waveforms have been computed and reported in Figs. 2.8–2.10. The points are also marked in Figs. 2.3a and 2.6. Note that points corresponding to double roots connect two surfaces.

$\{K_1, K_2\} = \{0, 0\}$, the contours perfectly match the linear dispersion of the acoustic branches of a classical Cauchy continuum endowed with a cubic

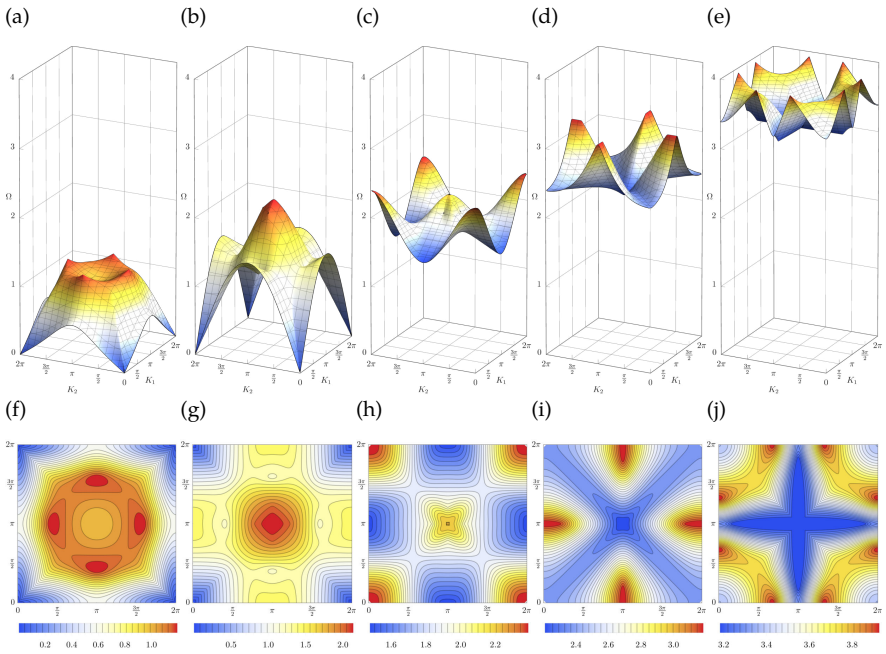

Fig. 2.7. The cubic anisotropy, occurring at all frequencies, is evident from the slowness contours (f)–(j) and associated dispersion surfaces (a)–(e), for a square grid of Rayleigh beams with slenderness $\lambda = 10$.

material symmetry. It is in fact recalled that the effective elastic parameters (Young modulus E^*, Poisson's ratio ν^*, shear modulus G^*, and mass density ρ^*) of a 2d continuum equivalent to a square beam grid are [64]

$$E^* = EA/(2l_1), \qquad \nu^* = 0, \qquad G^* = 6EI/(2l_1)^3, \qquad \rho^* = 2\rho A/(2l_1),$$

so that the velocities of the pressure and shear waves propagating in the effective continuum are

$$v_{p,0^\circ} = \sqrt{\frac{E^*}{\rho^*}}, \qquad v_{s,0^\circ} = \sqrt{\frac{G^*}{\rho^*}},$$

in the direction parallel to the principal axes and

$$v_{p,45^\circ} = \sqrt{\frac{(1+\nu^*)E^* + 2G^*}{2\rho^*}}, \qquad v_{s,45^\circ} = \sqrt{\frac{(1-\nu^*)E^*}{2\rho^*}}$$

in the direction inclined at 45° with respect to the principal axes (which, for a cubic material, are the only directions corresponding to de-coupling of pressure and shear waves).

On the first two low-frequency branches (where the wavelength of the

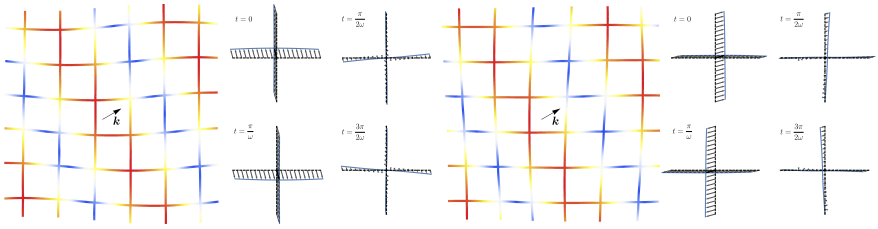

(a) Waveform at $P_1 : \{K_1, K_2, \Omega\} = \{\frac{\sqrt{3}}{2}, \frac{1}{2}, 0.230\}$.

(b) Waveform at $P_2 : \{K_1, K_2, \Omega\} = \{\frac{\sqrt{3}}{2}, \frac{1}{2}, 0.325\}$.

Fig. 2.8. Low-frequency (long-wavelength) waveforms for a square Rayleigh beam grid, computed on the acoustic branches (the two lowest dispersion surfaces). The locations of the corresponding points P_i on the dispersion surfaces are represented in Figs. 2.6f and 2.6g.

propagating waves is much larger than the size of the lattice unit cell), the structured medium is expected to exhibit a continuum-like dynamic response, displaying cubic anisotropy. This behaviour is clearly demonstrated by the associated waveforms shown in Fig. 2.8, where it can be noticed from the insets showing the unit cell that the modulation of the Floquet-Bloch wave is essentially uniform. Moreover, the comparison between Fig. 2.8a and 2.8b shows that the anisotropy induces a sort of 'mixing' of the 'shear' and 'pressure' waves as the amplitudes are neither parallel nor orthogonal to the wave vector, in agreement with the cubic symmetry.

As we consider higher frequencies, the dispersion becomes nonlinear and the geometry of the slowness contours changes dramatically. Non-convex slowness contours are evident in the proximity of the top of the first dispersion surface, displaying two orthogonal preferential directions inclined at 45° with respect to the orientation of the beams (see Fig. 2.6f). This non-convex pattern occurs again on the third surface, but with different preferential directions, which are now aligned parallel to the beams of the lattice (see Fig. 2.6h).

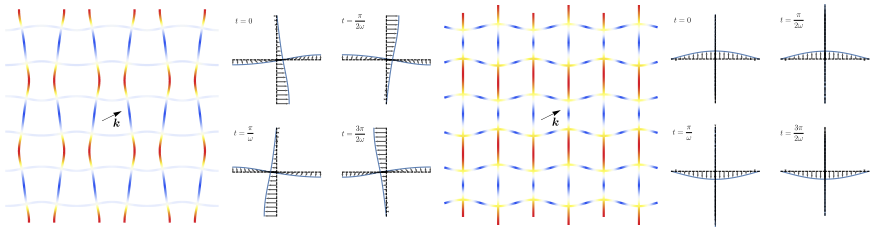

(a) 1st waveform at $P_3 : \{K_1, K_2, \Omega\} = \{\pi, 1.555, 0.812\}$.

(b) 2nd waveform at $P_3 : \{K_1, K_2, \Omega\} = \{\pi, 1.555, 0.812\}$.

Fig. 2.9. Waveforms in a square grid of Rayleigh beams at the Dirac vertex, which connects the first and the second dispersion surface. Both waves propagate vertically, but are standing horizontally and, in particular, the vertical beams transmit pure flexural vibrations (a) and pure axial waves (b).

The peculiarities of the high-frequency dynamics can be associated not only to the features of the slowness contours, but also to the actual waveforms corresponding to double roots, Dirac cones, and standing waves. In this regard, the Dirac vertex is considered, which is present at the point $P_3: \{K_1, K_2, \Omega\} = \{\pi, 1.555, 0.812\}$ connecting the two lowest dispersion surfaces. The two waveforms related to this double root are depicted in Fig. 2.9, where it can be seen that both waves *propagate vertically, but are standing horizontally*, so that they highlight the difference between the phase velocity and the group velocity of Floquet-Bloch waves. Specifically, a better understanding of these waves can be obtained by considering the motion of horizontal and vertical beams separately: the latter beams (Fig. 2.9a) are subject to purely flexural vibrations, so that the junctions do not displace vertically, while in the waveform shown in Fig. 2.9b these beams undergo a purely axial motion. On the other hand, the dynamics of horizontal beams is characterized by nodal points (where displacement remains constantly null), which in the waveform reported in Fig. 2.9b are located at the midpoint of the beams for both the axial and flexural waves, while in Fig. 2.9a the nodes of the transverse and the axial displacement are located at the junctions and at the midpoints, respectively. Due to the cubic symmetry, three Dirac points analogous to that considered above are present for the same frequency at the Bloch vectors $\{K_1, K_2\} = \{\pi, \pi \pm (\pi - 1.555)\}$ and $\{K_1, K_2\} = \{\pi \pm (\pi - 1.555), \pi\}$ (see Figs. 2.6f and 2.6g).

It is important to observe that the Dirac points are very different from those occurring for out-of-plane vibrations, where triple roots are found whose waveforms are purely standing waves [25]. In contrast, the in-plane vibrations associated to the Dirac vertex exhibit what can be called '*unidirectional propagation*', as the waves propagate along one direction but are standing along the other.

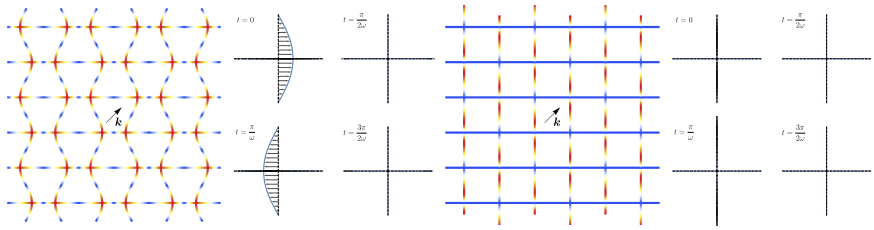

(a) Waveform at $P_5: \{K_1, K_2, \Omega\} = \{\pi, \pi, 1.193\}$. (b) Waveform at $P_6: \{K_1, K_2, \Omega\} = \{\pi, \pi, 1.592\}$.

Fig. 2.10. Standing waves occurring in a square grid of Rayleigh beams, corresponding to the double root connecting the second to the third (a) and the fourth to the fifth (b) dispersion surface. The vertical beams are subject to a purely flexural deformation while the horizontal beams exhibit pure axial vibrations, so that nodal points are located at the midpoints of beams (a). The waveform (b) occurs at a frequency $\Omega = \Omega_a = \lambda/\pi$, corresponding to the first axial vibration mode of a double-clamped beam. The motion of horizontal and vertical beams are completely decoupled and nodal lines are clearly visible. Due to symmetry, the companion waveforms analogous to (a) and (b) can also propagate at the same frequencies, with reversed roles of the horizontal and vertical beams.

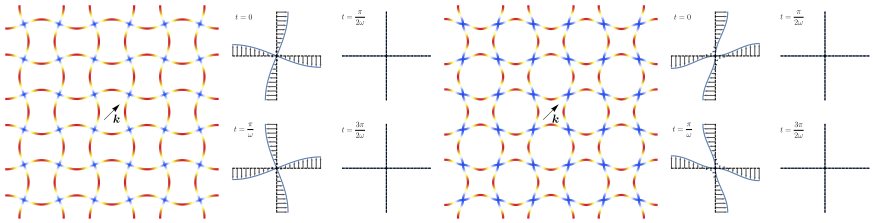

(a) Waveform at $P_4 : \{K_1, K_2, \Omega\} = \{\pi, \pi, 0.847\}$. (b) Waveform at $P_7 : \{K_1, K_2, \Omega\} = \{\pi, \pi, 1.853\}$.

Fig. 2.11. Purely flexural standing waves occurring in a square grid of Rayleigh beams on a stationary point of the first (a) and the sixth (b) dispersion surface, at a frequency corresponding to the first flexural mode of a simply supported (a) and a double-clamped (b) Rayleigh beam. Nodal points are located at the junctions for both cases, but these joints may have a rotational motion (a), as opposed to the situation where they are totally fixed (b).

At the points P_5 and P_6, two double roots are found, where the dispersion surfaces do not present a cone-like geometry, rather they seem to exhibit stationary points which would imply the presence of standing waves. This is confirmed by the corresponding pairs of waveforms computed at these points and in fact revealing sets of nodal points distributed along the two orthogonal directions (Fig. 2.10). In particular, the two eigenmodes corresponding to P_5 (Fig. 2.10a) are characterized by a peculiar combination of a purely flexural motion along one set of beams and a purely extensional deformation along the orthogonal set, with nodal points located at the beams' midpoints. On the other hand, the waveforms corresponding to P_6 (Fig. 2.10b) involve only purely axial standing waves along one direction and nodal lines along the other, so that the junctions remain fixed and the lattice vibrates with a frequency $\Omega = \Omega_a = \lambda/\pi$, corresponding to the first axial mode of a double-clamped beam.

Purely flexural standing waves are found at the points P_4 and P_7 where, respectively, the first and sixth branches of the dispersion relation become stationary. The corresponding waveforms, represented in Fig. 2.11, show nodal points at the junctions, so that each beam oscillates according to the first flexural vibration mode of a double-pinned beam in Fig. 2.11a, or of a double-clamped beam in Fig. 2.11b.

The above-reported investigation will be useful in the next section for the interpretation and prediction of the lattice dynamics induced by a time-harmonic point load.

2.4 Forced vibration of a grid of Rayleigh beams

The relation between the dynamic response of a grid of Rayleigh beams and the Floquet-Bloch analysis performed in the previous section can be investigated through the analysis of the vibrations induced by a time-harmonic source (a concentrated force or moment) in a lattice of infinite extent. To this purpose, a square grid of Rayleigh beams is numerically solved using

the Comsol Multiphysics® f.e.m. program in the frequency response mode. A square finite-size computational window with $(N-1)\times(N-1)$ unit cells is considered, where $N = 161$ is the number of nodes in each direction, with a perfectly matched layer (PML) along the boundaries, to simulate an infinite lattice. By tuning the damping in the boundary layers, the outgoing waves can be completely absorbed, so that reflection is not generated in the interior domain. The physical parameters for the numerical computations are chosen to be identical to those used in the previous Section 2.3.

Since the in-plane problem is vectorial, different types of loading are considered, namely a concentrated in-plane (the vector defining the moment is orthogonal to the plane of the grid) moment and a concentrated in-plane force, applied to the central junction. For a given loading and a given dimensionless angular frequency Ω, the complex displacement field, with components $u = u_R + iu_I$ and $v = v_R + iv_I$, is computed. The results are plotted in terms of the total displacement associated to the real parts, $\delta_R(x, y, \Omega) = \sqrt{u_R^2 + v_R^2}$. For the sake of brevity, the total displacement associated to the imaginary parts $\delta_I(x, y, \Omega) = \sqrt{u_I^2 + v_I^2}$ is omitted.

The numerical simulations are complemented with a Fourier analysis of the nodal displacements, with the purpose of providing a clear connection between the forced response of the Rayleigh beam lattice and the Floquet-Bloch analysis performed in the previous sections.

For a given dimensionless angular frequency Ω, the two-dimensional fast Fourier transform is applied to the nodal displacement field, $u_{pq} = u(x_p, y_q)$ and $v_{pq} = v(x_p, y_q)$, where (x_p, y_q) are the coordinates of the (pq)-node in the grid. This gives the transformed fields $U_{rs} = \mathcal{F}[u_{pq}]$ and $V_{rs} = \mathcal{F}[v_{pq}]$, where the transform is defined as follows

$$\begin{aligned} X_{rs} = \mathcal{F}[x_{pq}] &= \frac{1}{N^2}\sum_{p=1}^{N}\sum_{q=1}^{N} x_{pq} e^{-\frac{2\pi i}{N}(p-1)(r-1)} e^{-\frac{2\pi i}{N}(q-1)(s-1)} \\ &= \frac{1}{N^2}\sum_{p=1}^{N}\sum_{q=1}^{N} x_{pq} e^{-i(p-1)K_1} e^{-i(q-1)K_2} = X(K_1, K_2), \\ &\qquad\qquad \forall\, r, s \in \{1, \ldots, N\} \end{aligned} \tag{2.15}$$

in which $K_1 = \frac{2\pi}{N}(r-1)$ and $K_2 = \frac{2\pi}{N}(s-1)$ are the components of the dimensionless wave vector appearing in Eq. (2.9).

The fast Fourier transform provides the spectrum of Bloch plane waves composing the forced dynamic response of the beam grid. Specifically, $|U(K_1, K_2)|$ and $|V(K_1, K_2)|$ are the amplitudes of a plane wave with wave vector $\{K_1, K_2\}$, such that the physical displacement field can be represented as the superposition of all the N^2 plane waves of the spectrum. For each numerical simulation performed at a given frequency, the density plot of the quantity $\sqrt{|U|^2+|V|^2}$ is reported superimposed to the slowness contour computed at the same frequency with the Floquet-Bloch technique.

2.4.1 Pulsating moment: wave localization and 'isotropization'

A grid of Rayleigh beams is investigated when forced by a time-harmonic concentrated moment, acting at a node and pulsating at a given dimensionless angular frequency Ω, in the range of frequencies analyzed in Section 2.3. The results are reported in Figs. 2.12–2.15 in terms of the total displacement associated to the real parts, δ_R. Each numerical simulation is accompanied by the Fourier transform of the complex displacement field, shown in the lower part of the figure, where a red dotted line indicates the slowness contours obtained with the Floquet-Bloch analysis at the considered frequency Ω (see Fig. 2.6).

Three different frequency intervals are investigated, namely: a low frequency regime, from $\Omega = 0$ up to the vertex P_4 of the first dispersion surface, at $\Omega_f = 0.8467$ (results are reported in Figs. 2.12 and 2.13); an intermediate frequency regime, between the points P_4 and P_6, at $\Omega_a = 1.5915$, where the propagation of axial waves prevails (results are reported in Fig. 2.14); and finally a high frequency regime from the point P_6 up to higher frequencies (results are reported in Fig. 2.15). The transition between the low and the intermediate frequency regimes deserves a special attention, because here the first dispersion surface shows a stationary point (point P_4, being either a maximum or a minimum, depending on the slenderness ratio). This frequency corresponds to the resonant mode occurring at $\Omega_f = 0.8467$ and represented by the pure flexural standing wave in Fig. 2.11a, so that three different frequencies close to this point are investigated (results are reported in Fig. 2.13).

The results of the numerical simulations for the low-frequency regime $\Omega \in (0, \Omega_f = 0.8467)$ are reported in Fig. 2.12. For a given frequency Ω in this range, two dispersion surfaces are always intersected. The Fourier transform of the nodal displacements of the forced lattice, shown in the lower part of the figure, displays the spectrum of Bloch plane waves composing the dynamic response, which nicely corresponds to the slowness contours (red dotted lines) obtained through the Floquet-Bloch analysis in Section 2.3. The long-wavelength regime for $\Omega = 0.025$ is shown in Fig. 2.12a, where the wave pattern with square wavefronts is typical of a material with cubic symmetry. Increasing the frequency up to $\Omega = 0.65$, the dynamic response exhibits a strong localization along two preferential directions at $\pm 45°$ with respect to the horizontal axis, Fig. 2.12b. The corresponding Fourier transform, reported in Fig. 2.12e, clearly highlights the excited Bloch waves, among the ones predicted by the slowness contours at the same frequency (red dotted lines). It is evident that the applied pulsating moment excites waves along the two inclined preferential directions, whereas waves with the 'isotropic' shape corresponding to the rounded slowness contour are not generated. Approaching the stationary point of the first dispersion surface (point P_4 in Fig. 2.6), at the frequency $\Omega = 0.8$, a less marked but still visible diagonal localization is observed, together with a propagation along the principal axes of the lattice, see Fig. 2.12c. Note that, while the slowness contour

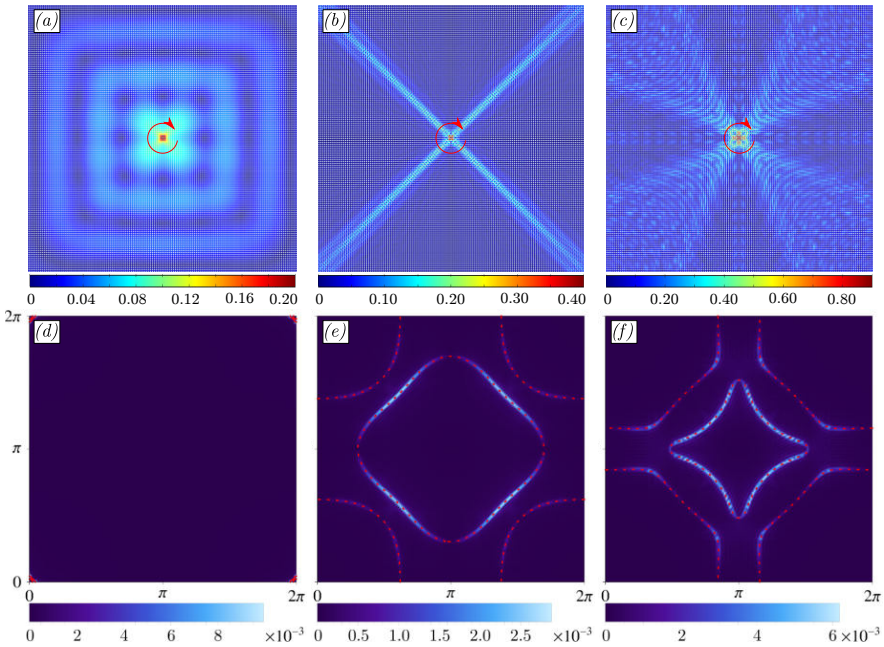

Fig. 2.12. Total displacement field (upper part, a-b-c) and corresponding Fourier transform (lower part, d-e-f) during vibrations of a Rayleigh grid of beams excited by a time-harmonic concentrated moment (applied out-of-plane in a low-frequency interval, $0 < \Omega < \Omega_f = 0.8467$). The slowness contour evaluated from the Floquet-Bloch analysis is superimposed in red spots. (a) and (d), $\Omega = 0.025$, at low frequency the wave pattern is typical of a continuous material with cubic anisotropy (note that the slowness contour and the Bloch spectrum are confined at the corners of the lower figure). (b) and (e), $\Omega = 0.65$, a strong vibration localization along directions inclined at ±45°. (c) and (f), $\Omega = 0.8$ the inner cross-shaped slowness contour is the most excited by the applied load; however, its re-entrant curved edges lead to a fan of preferential directions, developing around the lines inclined at ±45°.

is convex in Fig. 2.12 (e), it becomes concave in part (f). The re-entrant curved edges lead to a fan of preferential propagation directions around lines inclined at ±45°. The appearance of Bloch waves corresponding to the second slowness contour justifies the weak propagation along the principal axes.

In the proximity of the stationary point of the first dispersion surface (occurring at $\Omega_f = 0.8467$), a sudden change in the response of the lattice is observed, so that a narrow range of frequencies is analyzed and reported in Fig. 2.13. Part (a) of this figure shows the displacement field for a pulsating moment with frequency $\Omega = 0.83628$, where the applied moment excites mostly Bloch waves corresponding to the inner diamond-shaped slowness contour visible in Fig. 2.13d. Waves with squared wavefront are produced, while the two preferential directions inclined at ±45° still remain visible. Immediately below the stationary point of the first dispersion surface, at $\Omega = 0.8455$, the wave pattern becomes similar to the response of an isotropic material. Indeed, at this frequency, the inner slowness contour shrinks and

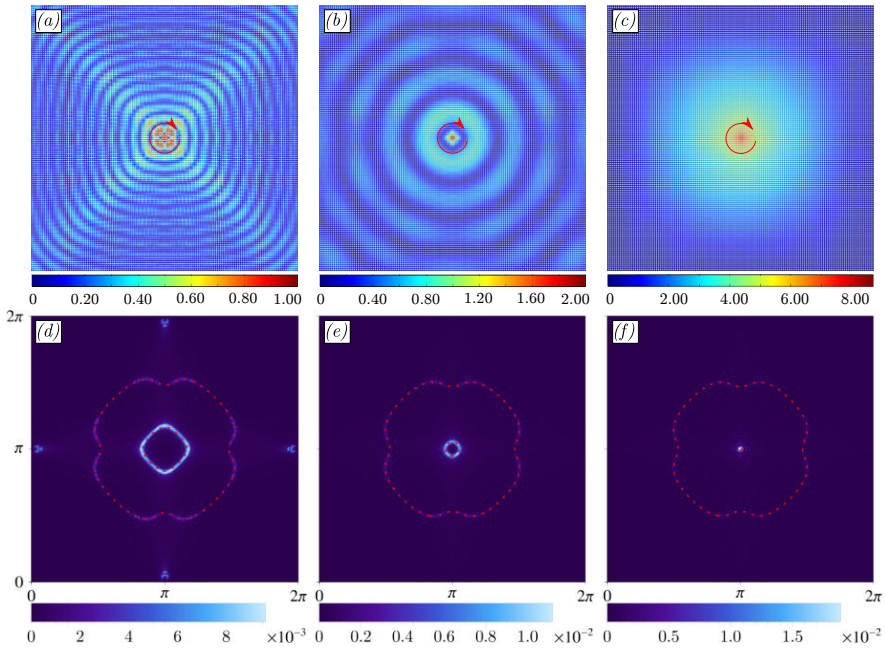

Fig. 2.13. Total displacement field (upper part, a-b-c) and corresponding Fourier transform (lower part, d-e-f) during vibrations of a Rayleigh grid of beams excited by a time-harmonic concentrated moment (applied out-of-plane at frequencies near the stationary point P_4 in Fig. 2.6, $\Omega_f = 0.8467$, of the first dispersion surface). The slowness contour evaluated from the Floquet-Bloch analysis is superimposed in red spots. (a) and (d), $\Omega = 0.83628$, the inner diamond-shaped slowness contour is excited by the applied load, producing waves with squared wavefront; two preferential vibration directions inclined at $\pm 45°$ are still visible. (b) and (e), $\Omega = 0.8455$, at a frequency very close to the resonant point P_4, the inner slowness contour shrinks to a little circle and the waves assume an almost circular wavefront when close to the source, while these assume an octagonal shape far away from the source. (c) and (f), $\Omega_f = 0.8467$, at the resonant frequency the inner slowness contour shrinks to a point, the corresponding evanescent waveform is typical of a resonant mode. Note that, as the resonant frequency Ω_f is approached, the lattice response exhibits a remarkable 'isotropization' with wavefronts becoming circular.

becomes almost circular, Fig. 2.13e; correspondingly, the waves produced by the applied moment show an almost circular wavefront, when they are close to the source, while they assume an *octagonal shape*, when far away from the source and present a increased wavelength, when compared to the lower frequencies. At the stationary point of the first dispersion surface, corresponding to the frequency $\Omega_f = 0.8467$, the total displacement field δ_R, reported in Fig. 2.13c, shows an evanescent wave pattern, typical of a resonant mode, so that the inner slowness contour reduces to a point, Fig. 2.13f. The Bloch eigenmode corresponding to this point is identified through the Floquet-Bloch analysis (Section 2.3) as a purely flexural standing wave, in which the junctions of the grid exhibit a pure rotational motion, Fig. 2.11a, which explains the observed resonant wave pattern. This peculiar

response of the dynamic lattice, occurring close to the stationary point of the frequency surface, shows a surprisingly 'isotropization' effect, for which waves propagate in a square lattice with a polar symmetry resembling the symmetry observed in an isotropic medium. This is due to the fact that the stationary point represents a maximum for the dispersion surface, so that the slowness contours become circular in the neighborhood of this point. Additionally, the applied load (a concentrated moment) excites with its polar symmetry exactly the Bloch waves associated with the inner circular isofrequency contour.

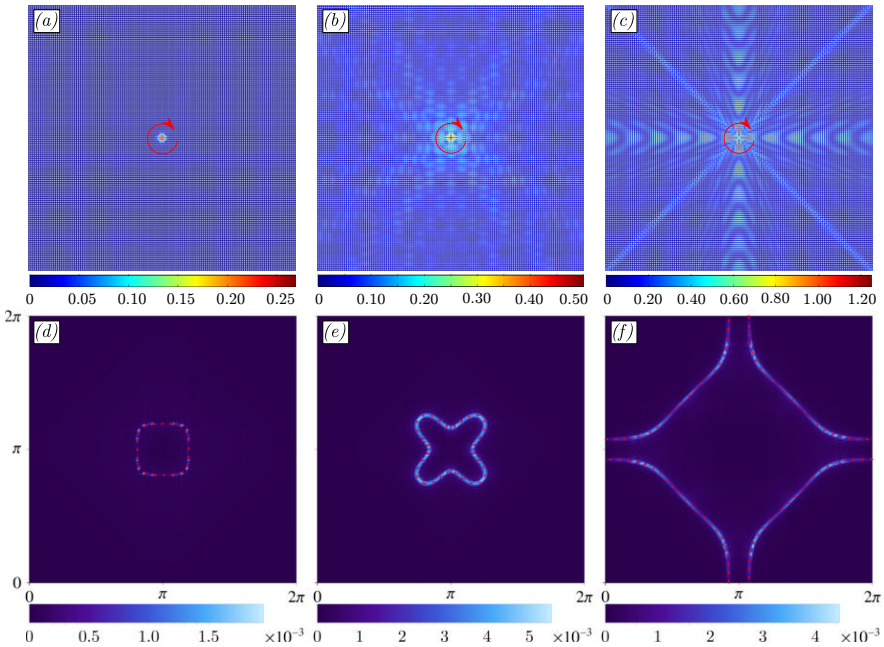

Fig. 2.14. Total displacement field (upper part, a-b-c) and corresponding Fourier transform (lower part, d-e-f) during vibrations of a Rayleigh grid of beams excited by a time-harmonic concentrated moment (applied out-of-plane in an intermediate frequency regime $\Omega_f = 0.8467 < \Omega < \Omega_a = 1.5915$, where only one dispersion surface is intersected). The slowness contour evaluated from the Floquet-Bloch analysis is superimposed in red spots. (a) and (d), $\Omega = 1.1$, the applied concentrated moment does not produce any visible wave propagation. (b) and (e), $\Omega = 1.21$, the Bloch waves of an 'X-shaped' slowness contour are almost uniformly excited, giving rise to several preferential directions inclined around the directions ±45°. (c) and (f), $\Omega = 1.3$, the preferential vibration directions are vertical, horizontal and inclined ±45°.

Fig. 2.14 shows the dynamic response of the lattice in the intermediate frequency regime, between the stationary point of the first dispersion curve, $\Omega_f = 0.8467$, and the fourth dispersion surface, $\Omega_a = 1.5915$. For $\Omega = 1.10$ the slowness contour intersects the second dispersion surface. The total displacement field δ_R, reported in Fig. 2.14a, shows an evanescent waveform prevailing at this frequency. The corresponding Fourier transform, Fig. 2.14d, confirms that the applied moment excites only weakly Bloch

waves. At the lower part of the third dispersion surface, for $\Omega = 1.21$, the displacement field shows a waveform with several preferential directions inclined at ±45°, Fig. 2.14b. This pattern is in agreement with the corresponding 'X-shaped' slowness contour shown in Fig. 2.14e. At $\Omega = 1.3$, Fig. 2.14c, localization is observed along preferential directions inclined at ±45°, together with a characteristic 'herringbone' pattern along the principal axes of the lattice (0°/90°), in agreement with the Bloch waves excited at this frequency, Fig. 2.14f.

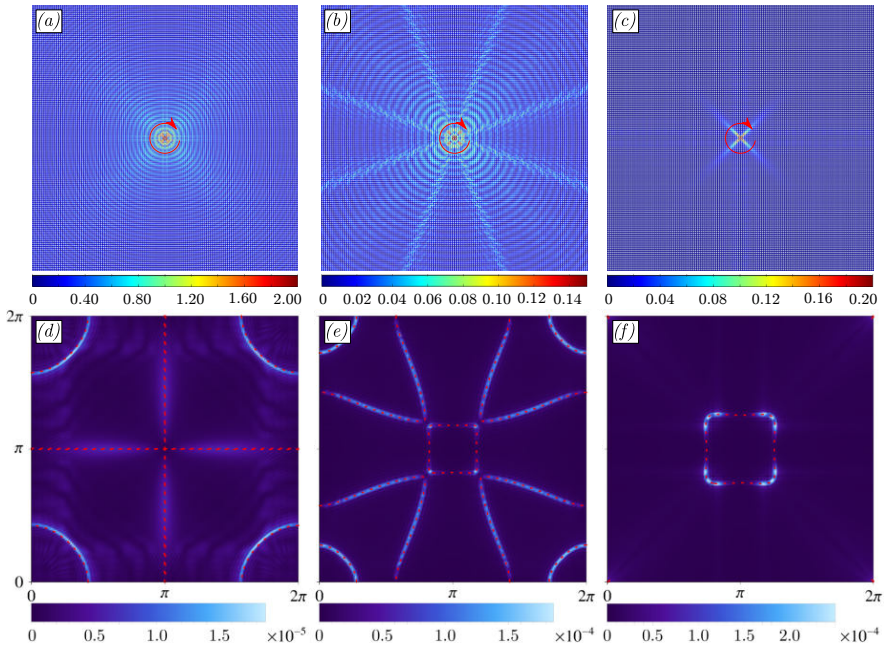

Fig. 2.15. Total displacement field (upper part, a-b-c) and corresponding Fourier transform (lower part, d-e-f) during vibrations of a Rayleigh grid of beams excited by a time-harmonic concentrated moment (applied out-of-plane in a high-frequency interval, $\Omega \geq \Omega_a = 1.5915$). The slowness contour evaluated from the Floquet-Bloch analysis is superimposed in red spots. (a) and (d), $\Omega_a = 1.5915$, since the applied concentrated moment cannot excite axial waves, the associated cross-like slowness contour is not highlighted in the Fourier transform, so that almost isotropic waves are generated, which are associated to the rounded slowness contour. (b) and (e), $\Omega = 1.67$, the slowness contours have a complex geometry, including square and rounded segments, together with eight symmetrically distributed branches; the corresponding waveform shows eight preferential directions with rounded wavefronts. (c) and (f), $\Omega = 1.7326$, a strong vibration localization along directions inclined at ±45° is clearly visible, also highlighted by the corresponding Fourier transform.

The dynamic response of the lattice in the high frequency regime, is reported in Fig. 2.15, starting from the troughs of the fourth dispersion surface at the frequency $\Omega_a = 1.5915$. In this regime the Floquet-Bloch analysis predicts the propagation of axial waves along the ligaments of the lattice , Fig. 2.10b. At the frequency $\Omega_a = 1.5915$, corresponding to the troughs of the fourth dispersion surface, the dynamic response of the lattice shows

almost circular wavefronts with only a weak preferential direction of propagation inclined at ±45°, Fig. 2.15a. The corresponding Fourier transform, Fig. 2.15d, highlights that the excited Bloch waves correspond to points of the third dispersion surface, having almost circular slowness contours. This wave pattern can be deduced from the Floquet-Bloch analysis because the vibration eigenmodes pertaining to the troughs (associated with the cross-like slowness contour) consist of purely extensional standing waves, Fig. 2.10b, which cannot be excited by a time-harmonic moment, so that an almost isotropic wave propagation prevails, associated with the rounded slowness contours. At $\Omega = 1.67$ the wave pattern reported in Fig. 2.15b shows four fans (spanning an angle of 45°) of preferential directions with rounded wavefronts. This waveform is the result of the complex geometry of the slowness contours, as illustrated in Fig. 2.15e, which includes square and rounded contours together with eight symmetrically distributed branches. Finally, at the frequency $\Omega = 1.7326$, an unexpected strong localization is observed, along directions inclined at ±45°, Fig. 2.15c. Here the slowness contours would predict preferential directions along the principal axes of the lattice (0°/90°), but the Fourier transform reported in Fig. 2.15f shows that the excited Bloch waves correspond to the corners of the squared slowness contour, which explains the observed preferential vibration directions.

2.4.2 Pulsating force: vibration channeling

The dynamic response is analyzed of a square grid of Rayleigh beams (with $\lambda = 5$) subject to a time-harmonic in-plane force (with different inclinations: horizontal or at 45°) applied to a node. Total displacement fields (upper parts, a-b-c) and corresponding Fourier transform (lower parts, d-e-f) are reported in Figs. 2.16–2.18, together with the slowness contours evaluated from the Floquet-Bloch analysis, superimposed with red spots to facilitate comparisons.

For the frequency $\Omega = 0.65$, the total displacement field δ_R, reported in Fig. 2.16a, looks different when compared to the displacement produced by a nodal moment (Fig. 2.12b). In particular, in addition to preferential propagation directions inclined at ±45°, which produce an 'X-shaped' vibration localization, other directions of propagation emerge, exhibiting a distinctive 'herringbone' wave pattern along the horizontal axis. A comparison between Figs. 2.16 (a) and (d) and Fig. 2.12 (b) and (e) (all pertaining to the same frequency $\Omega = 0.65$) shows the presence in the case of the concentrated force of Bloch waves corresponding to the second dispersion surface with rounded slowness contour, a circumstance which explains the propagation in directions other than ±45°.

Increasing the dimensionless angular frequency to $\Omega = 1.10$, waves are localized along the horizontal axis, as illustrated in Fig. 2.16b. For an higher frequency, $\Omega = 1.273$, a behaviour peculiar of the Rayleigh beam lattice is observed, namely, the propagation becomes strongly localized in the direction perpendicular to the direction of the applied force, as clearly shown in Fig. 2.16c. Although the slowness contour at this frequency has an almost

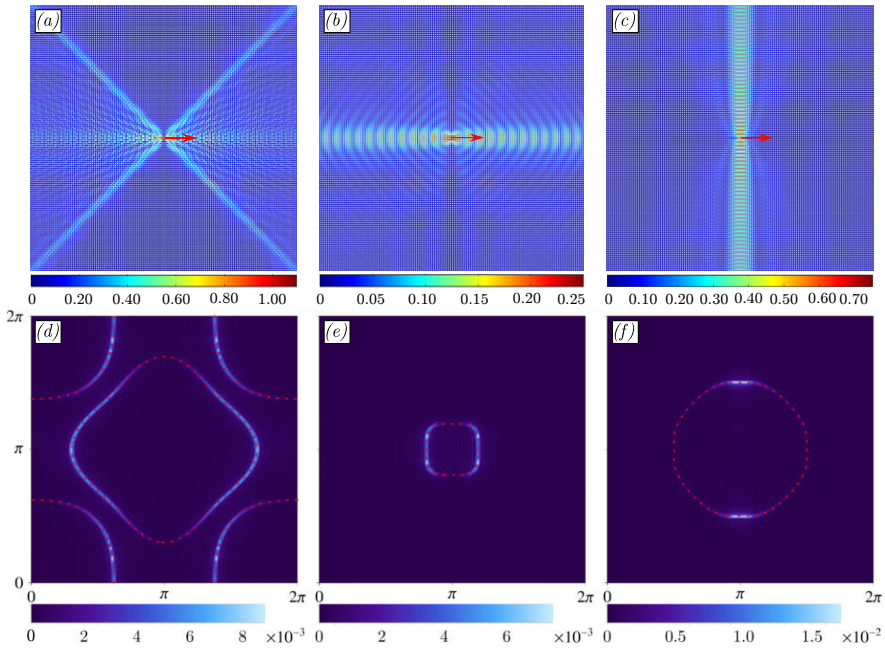

Fig. 2.16. Total displacement field (upper part, a-b-c) and corresponding Fourier transform (lower part, d-e-f) during vibrations of a Rayleigh grid of beams excited by a horizontal time-harmonic concentrated force (applied in the plane in the frequency interval $0 < \Omega < \Omega_a = 1.5915$). The slowness contour evaluated from the Floquet-Bloch analysis is superimposed in red spots. (a) and (d), $\Omega = 0.65$, an 'X-shaped' localization of vibrations around two preferential directions inclined at ±45°; waves propagate within the left and right sectors, while waves are not visible in the upper and lower sectors. (b) and (e), $\Omega = 1.10$, waves possess a rhombus-shaped wavefront and an amplitude localized along the horizontal axis. (c) and (f), $\Omega = 1.273$, waves are strongly localized along the vertical direction (orthogonal to the force).

circular shape, the Fourier transform, Fig. 2.16f, highlights that the activated Bloch waves are localized at the ends of the vertical diameter, which explains the observed strong localization.

Effects related to the directionality of the pulsating force can be appreciated through a comparison between Fig. 2.16 and Fig. 2.17, where the frequency-dependent interaction is visible between the vibration patterns produced by the two in-plane components of the pulsating force. For instance, for $\Omega = 0.65$ the wave pattern produced by a point force inclined at 45° with respect to the horizontal axis (Fig. 2.17a) is characterized by a strong localization along the preferential direction at −45°, whereas the preferential direction at +45°, present when the force is horizontal (Fig. 2.16a), disappears. Rapidly decaying waves are also visible along vertical and horizontal directions. At the frequency $\Omega = 1.10$, the rhombus-shaped wavefronts visible in Fig. 2.16b are not affected by the inclination of the load, but the combination of the two force components generates a wave pattern characterized by an absence of propagation in the second and fourth quadrant and, at the

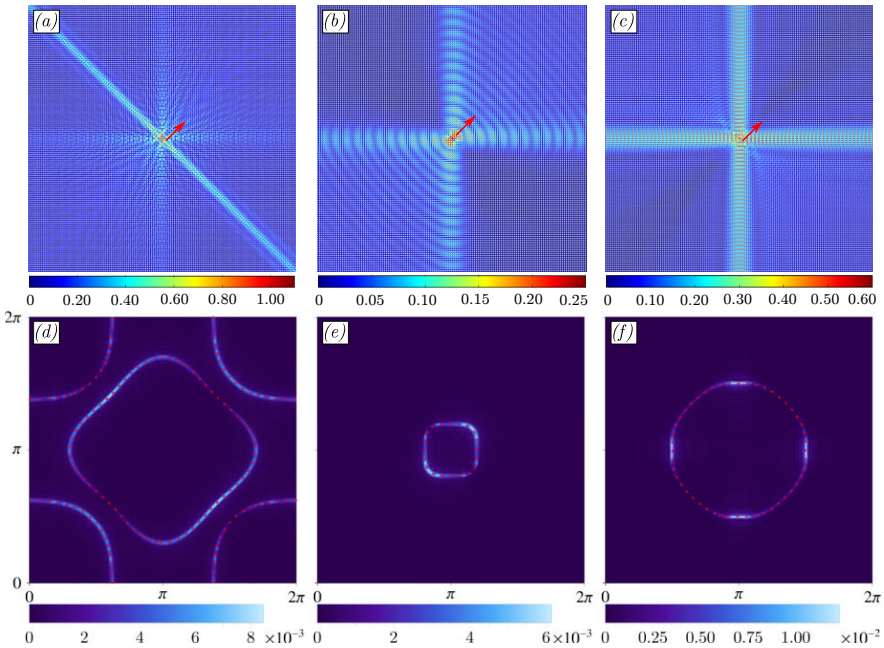

Fig. 2.17. Total displacement field (upper part, a-b-c) and corresponding Fourier transform (lower part, d-e-f) during vibrations of a Rayleigh grid of beams excited by a time-harmonic concentrated force (inclined at 45° and applied in the plane in the frequency interval $0 < \Omega < \Omega_a = 1.5915$). The slowness contour evaluated from the Floquet-Bloch analysis is superimposed in red spots. (a) and (d), $\Omega = 0.65$, waves are strongly localized along preferential directions inclined at −45° (perpendicular to the applied force); rapidly decaying waves are also visible along vertical and horizontal directions (b) and (e), $\Omega = 1.10$, waves propagate within the first and third quadrant with vertical and horizontal preferential directions. (c) and (f), $\Omega = 1.273$, a symmetrical cross-shaped wave localization is visible, where waves propagate within the second and fourth quadrant.

same time, by an amplification of the response in first and third quadrant (see Fig. 2.17b). A comparison between Figs. 2.16c and 2.17c, at $\Omega = 1.273$, shows that the total displacement field δ_R produced by the inclined load displays a prevalent propagation in the second and fourth quadrant, while a negligible response is observed in the first and third quadrant.

At the frequency $\Omega = \Omega_a = 1.5915$, corresponding to the troughs of the fourth dispersion surface, the dynamic response of the lattice to a nodal force is drastically different from that generated by a nodal moment (compare Fig. 2.15a to Fig. 2.18a). While an activation of Bloch waves in the third dispersion surface with rounded slowness contour (Fig. 2.15a and d) are observed for an applied moment, a nodal force generates axial waves involving only the horizontal and/or (depending on the direction of the force) the vertical beams connected to the junction where the force is applied. This extremely localized wave pattern is linked to the 'cross-shaped' slowness contour, as shown by the Fourier transform in Fig. 2.18d.

Finally, the dynamic behaviour of the beam grid, when a time-harmonic

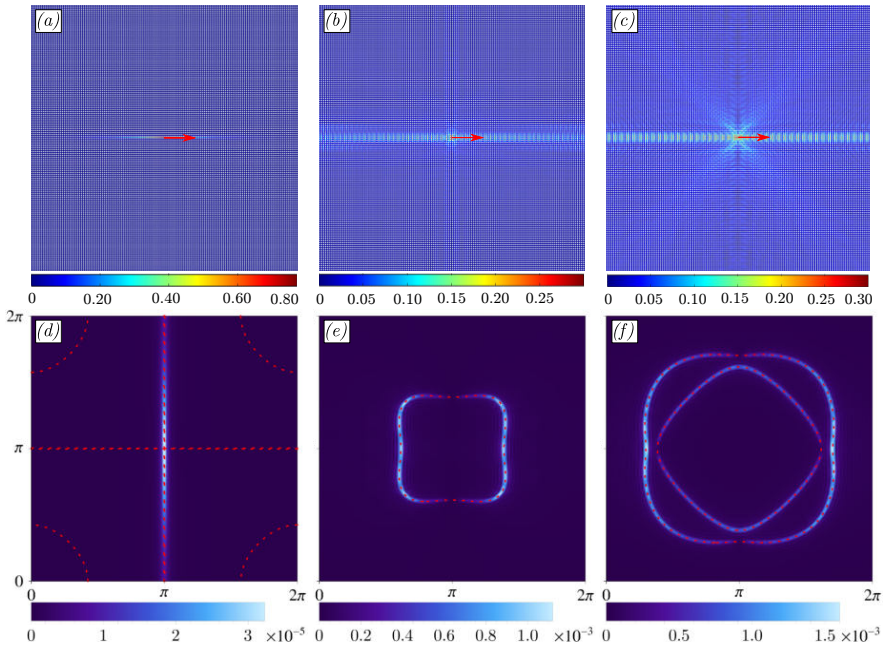

Fig. 2.18. Total displacement field (upper part, a-b-c) and corresponding Fourier transform (lower part, d-e-f) during vibrations of a Rayleigh grid of beams excited by a horizontal time-harmonic concentrated force (applied in the plane in a high-frequency regime, $\Omega \geq \Omega_a = 1.5915$). The slowness contour evaluated from the Floquet-Bloch analysis is superimposed in red spots. (a) and (d), $\Omega_a = 1.5915$, an extremely localized wave pattern is visible, which involves only horizontal beams. (b) and (e), $\Omega = 1.85$, waves localized along the horizontal axis are visible. (c) and (f), $\Omega = 2.10$, combination of a prevalent horizontal localization associated to the activation of the outer contour and an 'X-shaped' wave pattern produced by the Bloch waves belonging to the inner slowness contour.

nodal force is applied, pulsating at high frequency, $\Omega = 1.85$, is reported in Fig. 2.18b. At this frequency, the slowness contour has a squared shape similar to that of Fig. 2.16e at $\Omega = 1.10$. Correspondingly, also the wave pattern is similar, showing an horizontal preferential vibration direction. When the frequency increases to the value $\Omega = 2.10$, Fig. 2.18c, the displacement becomes strongly localized in the horizontal direction, while rapidly-decaying vibrations emerge with inclination ±45°.

2.4.3 Energy flow

The data obtained from the numerical simulations presented in the previous section are now analyzed to investigate the dynamic anisotropy of the beam grid in terms of the *energy flow* through the lattice produced by the pulsating load. This aspect can be of significant interest for the control of wave propagation and energy channeling in metamaterials.

With the purpose of constructing a 2d vector field representation of the energy flow propagating through the beams of the lattice, the flow along

a single beam is derived. Denoting with s the local coordinate measured along the beam and increasing in the direction of the unit vector $\boldsymbol{t}$, the conservation of energy for an arbitrary part of a beam in an integral form writes

$$\frac{d}{dt}\int_{s_1}^{s_2}(\mathcal{T}(s,t)+\mathcal{E}(s,t))\,ds = (\Re\boldsymbol{a}_{\boldsymbol{t}}(s,t)\cdot\Re\dot{\boldsymbol{u}}(s,t))\Big|_{s=s_1}^{s=s_2}+h(t), \quad \forall s_1, s_2, \tag{2.16}$$

where $\mathcal{T}$ and $\mathcal{E}$ are, respectively, the kinetic and elastic energy densities (functions of the coordinate s and of the time t), while $\boldsymbol{a}_{\boldsymbol{t}}$ is the vector collecting the internal forces acting on the cross-section with unit normal $\boldsymbol{t}$, $\dot{\boldsymbol{u}}$ collects the corresponding velocities and h accounts for energy sources (for instance the power of external loads) and dissipation (for instance viscous damping) present along the interval (s_1, s_2) of the beam. The complex representation of the displacement field is used, so that the $\Re$ operator is needed.

In the absence of energy sources and dissipations, Eq. (2.16) expresses the balance between the rate of variation of the energy stored and the power done by the internal forces acting at the ends of any beam interval. This power is expressed through the scalar product $\Re\boldsymbol{a}_{\boldsymbol{t}}\cdot\Re\dot{\boldsymbol{u}}$, regardless of the structural model employed for the beam and it can be represented in an orthonormal basis $\{\boldsymbol{t}, \boldsymbol{n}, \boldsymbol{e}_3\}$ as follows

$$\begin{aligned}\Re\boldsymbol{a}_{\boldsymbol{t}}\cdot\Re\dot{\boldsymbol{u}} &= \Re(N\,\boldsymbol{t}+V\,\boldsymbol{n}+M\,\boldsymbol{e}_3)\cdot\Re(\dot{u}_t\,\boldsymbol{t}+\dot{u}_n\,\boldsymbol{n}+\dot{\varphi}\,\boldsymbol{e}_3),\\ &= \Re N\,\Re\dot{u}_t+\Re V\,\Re\dot{u}_n+\Re M\,\Re\dot{\varphi},\end{aligned} \tag{2.17}$$

where N, V and M are, respectively, the axial force, the shear force and the bending moment, while the axial, transverse and rotational velocities are denoted as $\dot{u}_t$, $\dot{u}_n$ and $\dot{\varphi}$. As expression (2.17) defines the instantaneous energy flux flowing in the $-\boldsymbol{t}$ direction, the *instantaneous energy flow* on a single beam is defined as

$$\boldsymbol{q}(s,t) = -(\Re N\,\Re\dot{u}_t+\Re V\,\Re\dot{u}_n+\Re M\,\Re\dot{\varphi})\,\boldsymbol{t}, \tag{2.18}$$

where the dependence on coordinate s and the time t is now highlighted.

For time-harmonic response of the beam lattice, it is convenient to evaluate the time average of the energy flow (2.18) over one period of oscillation, so that the 'effective' energy transmitted is obtained. A well-known result of complex variable calculus [65] yields

$$\langle\boldsymbol{q}(s,t)\rangle = -\boldsymbol{t}\,\frac{\omega}{2\pi}\int_0^{2\pi/\omega}\Re\boldsymbol{a}_{\boldsymbol{t}}\cdot\Re\dot{\boldsymbol{u}}\,dt = -\frac{1}{2}\Re(\boldsymbol{a}_{\boldsymbol{t}}\cdot\dot{\boldsymbol{u}}^*)\,\boldsymbol{t}, \tag{2.19}$$

where the symbol * denotes the complex conjugate and $\langle\,\rangle$ the time average operator. Furthermore, it is worth noting that, for time-harmonic motion, the time average of the energy flow is also constant in s when applied loads and dissipation are absent, $h = 0$, a property which can be easily obtained

by localizing Eq. (2.16)

$$\frac{\partial}{\partial t}(\mathcal{T}(s,t)+\mathcal{E}(s,t)) = -\frac{\partial}{\partial s}(\boldsymbol{q}(s,t)\cdot\boldsymbol{t}), \tag{2.20}$$

and then averaging on time both sides to obtain

$$\left\langle \frac{\partial}{\partial t}(\mathcal{T}+\mathcal{E}) \right\rangle = \frac{\omega}{2\pi}(\mathcal{T}+\mathcal{E})\Big|_{t=0}^{t=2\pi/\omega} = 0,$$

(where the left-hand side vanishes due to the time-harmonic assumption), so that

$$\frac{\partial}{\partial s}(\langle \boldsymbol{q}(s,t)\rangle \cdot \boldsymbol{t}) = 0, \tag{2.21}$$

which proves the average energy flow to be independent of s and therefore to coincide with its mean value $\langle \boldsymbol{q} \rangle$.

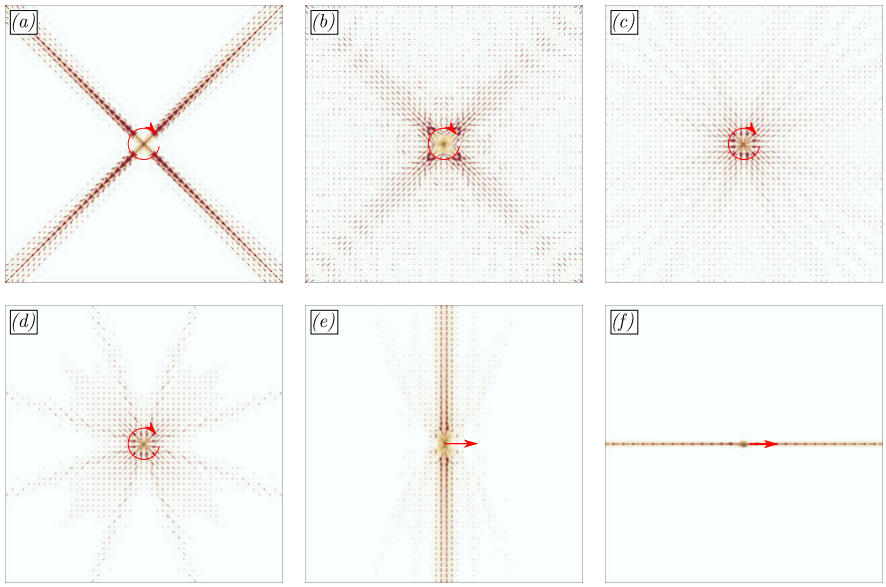

Fig. 2.19. Different forms of vibration localization visible on the vectorial representation (the figure with the associated displacement field is reported in parenthesis) of the energy flow produced by a pulsating concentrated moment at the frequencies: (a) $\Omega = 0.65$ (Fig. 2.12b); (b) $\Omega = 0.8363$ (Fig. 2.13a); (c) $\Omega = 1.5915$, (Fig. 2.15a); (d) $\Omega = 1.67$, (Fig. 2.15b); by an horizontal force at (e) $\Omega = 1.273$ (Fig. 2.16c); and by a horizontal force at (f) $\Omega = 1.5915$ (Fig. 2.18a).

Eq. (2.19) can be computed on each beam of the grid, thus providing the vector field of the energy flow, given in Fig. 2.19 for the cases of an applied concentrated moment or force, which is considered in the previous two sections. Moreover, the outgoing flux Q across a circular path (of radius r

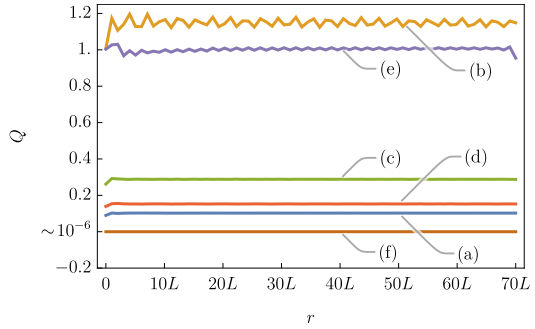

Fig. 2.20. Outgoing energy flux Q across a circular path centred at the loading point. The numerical computation shows that Q is independent of the radius r ($L = 2l_1$ is the length of the beams), apart from weak oscillations due to the spatial discretization of the fem analysis. This result represents a verification of the accuracy of the numerical solutions obtained in Section 2.4.1 and 2.4.2. Labels (a)–(f) refer to the corresponding energy flow vector plots reported in Fig 2.19.

and outward unit normal $\boldsymbol{n}$), centered at the loading point,

$$Q(r) = \int_0^{2\pi} \langle \boldsymbol{q} \rangle \cdot \boldsymbol{n}\, r\, d\theta, \tag{2.22}$$

is reported in Fig. 2.20. As the energy conservation requires the flux Q to be independent of the radius, this independence is used to verify the accuracy of the simulations as well as to compare the amount of mechanical power absorbed by the lattice for different frequencies and loads.

The comparison between the vectorial representations reported in Fig. 2.19 and the corresponding displacement fields (referenced in the captions) clearly shows that the directions of the energy flow are in nice agreement with the wave patterns computed in the previous sections. Indeed, the numerical computations confirm that the mechanical energy (in the absence of dissipation) systematically flows along the directions of the group velocity vectors, which are locally orthogonal to the slowness contours (see also [63]).

Considering the case of concentrated moment, the symmetry of the load produces a peculiar rotational symmetry in the directions of propagation of the energy, exhibiting different degrees of localization, which depend on the frequency. Comparing, for instance, Fig. 2.19a and 2.19d, the energy flows along four and eight radial preferential directions, respectively, and in both cases the intensity of the flow decreases with the distance from the load due to the corresponding increase of the length of the wavefront.

Figs. 2.19b and 2.19c show that the anisotropy of the energy flow is less significant at the frequencies $\Omega = 0.8363$ and $\Omega = 1.5915$, where, in fact, the Fourier transforms indicate the prevalence of wave vectors corresponding to almost circular slowness contours (Figs. 2.13d and 2.15d).

The case of applied force (Figs. 2.19e and 2.19f) differs strongly from the

case of applied moment, as the in-plane load breaks the rotational symmetry. This is clearly evident in Figs. 2.19e, where the pulsating horizontal force induces an energy flow propagating in the vertical direction, forming two symmetric 'triangular' streams of decaying intensity. Another interesting effect emerges at the frequency of the axial waves $\Omega = \Omega_a = \lambda/\pi \approx 1.5915$, for which the energy transmitted by the force exhibits an extremely localized unidirectional propagation, as shown in Fig. 2.19f, where the force is applied horizontally and the energy flows along a strongly localized 'channel' without attenuation.

2.5 Concluding remarks

Localization of vibration in various complex forms ('channels' or 'X-', 'cross-', 'star-' shaped narrow modes), anisotropic – but also isotropic – wave propagation, and Dirac cones and flat bands in the dispersion surfaces have been shown to be possible at various frequencies, through Floquet-Bloch exact treatment and numerical analysis of a rectangular grid of Rayleigh elastic beams with diffused mass. In particular, a surprising 'isotropization' of the moment-induced wave pattern has been demonstrated to occur at the frequency corresponding to the stationary point of the first dispersion surface. The presented results demonstrate that these effects can be designed by tuning the aspect ratio of the grid, the slenderness and the rotational inertia of the beams. Therefore, additive manufacturing technologies can in principle be used to produce microstructured materials with engineered vibrational properties.

3

Prestress tuning of negative refraction and wave channeling

The quest for wave channeling and manipulation has driven a strong research effort on topological and architected materials, capable of propagating localized electromagnetical or mechanical signals. With reference to an elastic structural grid, which elements can sustain both axial and flexural deformations, it is shown that material interfaces can be created with structural properties tuned by prestress states to achieve total reflection, negative refraction, and strongly localized signal channeling. The achievement of a flat lens and localized modes is demonstrated and tunability of the system allows these properties to hold for a broad range of wavelengths. An ingredient to obtain these effects is the use, suggested here and never attempted before, of concentrated pulsating moments. The important aspect of the proposed method is that states of prestress can be easily removed or changed to tune with continuity the propagational characteristics of the medium, so that a new use of vibration channeling and manipulation is envisaged for elastic materials.

3.1 Introduction

The possibility of channeling, trapping, and controlling waves opens new possibilities such as cloaking of a part of a body, or achieving total reflection and negative refraction, effects which prelude the realization of flat lens, able to overcome the diffraction limits through superlensing effects [26, 66–68]. Negative refraction in elastic lattices has been obtained for a plane wave [25, 55, 56, 69, 70] (and experimentally confirmed [71–73]), while only

in electromagnetism [74] and in elastic plates under flexure [75] pulsating sources have been considered so far.

Edge waves and trapped modes have been demonstrated, but their realization involves the use of gyroscopic systems [9, 11, 76], piezoelectric elements [77], topological materials [17] or structures inducing floppy modes [78, 79]. Recently topologically protected edge waves for plates subject to flexure have been demonstrated [80].

A route to achieve wide frequency bandwidth for the above-mentioned dynamical effects is tunability of the mechanical properties, representing a crucial ingredient in the development of metamaterials or architected materials, so that the wave propagation can be changed and manipulated, according to different needs, for instance in a way that an interface may be occasionally made permeable to mechanical disturbances or changed to realize total reflection or otherwise to allow negative refraction. Tunability has been addressed with reconfigurable origami materials [15], connectivity [9], piezoelectric effects [77], or, finally, prestress [81–83]. This latter technique can simply be implemented by applying forces to a structure prior to wave propagation, which results strongly influenced, as the dynamics of musical instruments clearly show. Forces can be readily applied and removed, so that tunability can be easily and quickly obtained.

Prestress is shown in this article to govern flexural and axial waves propagation in an elastic square grid of beams, so that axial forces can be applied to a set of beams arranged in a layer inside an infinite lattice of beams not subject to prestress. For a certain level of prestress (always assumed tensile to avoid buckling), the layer is shown to completely reflect waves, while waves are transmitted for a different prestress level and may display negative refraction and focusing. Moreover, narrow layers of prestressed elements give rise to highly localized trapped modes, showing strongly focused propagation.

3.2 Time-harmonic vibration of a lattice of axially and flexurally deformable beams

An infinite square lattice of elastic Rayleigh beams [59] (both axially and flexurally deformable and of length L) is assumed, where layers are subject to a prestress, induced by axial forces P, acting on a set of rods (Fig. 3.1a). The prestressed layer defines a 'structured interface', with a width chosen as $40L$. The slenderness $\lambda = L/r$ (where r is the radius of gyration of the beam's cross-section) of each beam is assumed equal to 15 and the lattice is analyzed for time-harmonic vibration, with angular frequency ω, so that introducing a dimensionless local coordinate $\xi = s/L$, the equations governing the dynamics of the lattice in terms of axial and transverse displacements, u and

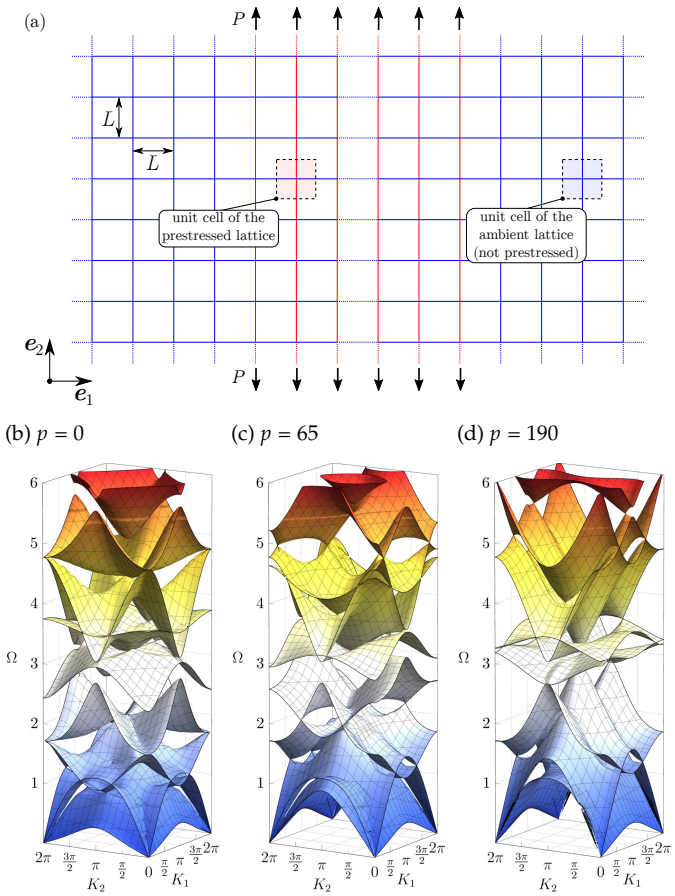

Fig. 3.1. (a) Geometry of the beam grid lattice and the prestressed layer. The vertical beams marked in red are subject to the axial prestress P, so that a tunable interface is realized. The dispersion surfaces of the ambient lattice (not prestressed) and of the prestressed lattice are reported in parts (b), (c), and (d), showing the strong effect of the prestress (made dimensionless as $p = PL^2/EI$).

v, are

$$u''(\xi) + \Omega^2\, u(\xi) = 0\,, \tag{3.1}$$

$$v''''(\xi) + (\Omega^2 - p)\, v''(\xi) - \lambda^2\, \Omega^2\, v(\xi) = 0\,, \tag{3.2}$$

where $\Omega = \omega\, L\sqrt{\rho/E}$ and $p = PL^2/EI$ are the dimensionless angular frequency and axial prestress, respectively (ρ is the mass density, E the Young modulus, I the second moment of the cross section's area and the prime denotes differentiation with respect to ξ).

An exact Floquet-Bloch analysis guides the determination of the level of prestress to tune desired dynamic responses of the lattice, for instance, achieving the total reflection of a wave, or its negative refraction, when

the wave impinges on an interface separating the lattice without prestress from the prestressed layer. In particular, the prestress level is determined using the slowness contours, obtained from the dispersion equation, of the periodic homogeneous lattice without and with prestress (dispersion surfaces as influenced by the prestress p are shown in Fig. 3.1b–d). Special attention has been paid to eliminate the possibility of buckling, by selecting a *tensile* prestress (even though effects similar to those shown in the following can be obtained for compressive prestress, or changing the slenderness of a layer of rods, an option presented in the Section A).

The eigenvalue problem governing wave propagation in the periodic grid can be easily formulated as follows (see also [1] for details). On each beam of the unit cell, the solution of eqs. (3.1) and (3.2) can be expressed in terms of a linear combination of complex exponentials, $u(\xi) = C\, e^{i\,\eta\,\xi}$ and $v(\xi) = D\, e^{i\,\gamma\,\xi}$, where the characteristic roots are

$$\eta_{1,2} = \pm\Omega\,,$$
$$\gamma_{1,2,3,4} = \pm\sqrt{\frac{1}{2}\left(\Omega^2 - p \pm \sqrt{4\lambda^2\Omega^2 + (\Omega^2 - p)^2}\right)}\,.$$

Then, the solution of the unit cell is constrained by imposing the junction and equilibrium conditions at the central joint and the Bloch-Floquet boundary conditions between corresponding sides of the unit cell for: (i) axial and flexural displacements, (ii) rotation, (iii) internal moment, (iv) axial and shear forces.

A homogeneous linear system of equations governing the propagation of Floquet-Bloch waves is found in the form

$$\boldsymbol{A}(\Omega, \boldsymbol{K}, p, \lambda)\, \boldsymbol{c} = \boldsymbol{0}\,, \tag{3.3}$$

where $\boldsymbol{A}(\Omega, \boldsymbol{K}, p, \lambda)$ is a 24×24 complex matrix, function of the angular frequency Ω and the wave vector $\boldsymbol{K}$, of dimensionless components K_1 and K_2 (obtained from multiplication of the Bloch wave vector, $\boldsymbol{k} = k_1\boldsymbol{e}_1 + k_2\boldsymbol{e}_2$, by L), as well as the prestress parameter p and the slenderness λ. Finally, vector $\boldsymbol{c}$ defines the waveform as it collects the 24 complex constants that multiply the exponential functions appearing in the displacement fields. As the system (3.3) is homogeneous, all non-trivial solutions are found when the matrix $\boldsymbol{A}(\Omega, \boldsymbol{K})$ becomes singular, a condition providing the dispersion equation. The latter equation has been solved numerically in order to identify the influence of the axial prestress on the structure of the dispersion surfaces (see Fig. 3.1b, c, and d) and consequently to tune the prestress parameter p.

3.3 Tunable transmission properties of prestressed interfaces

Two forcing sources have been considered to demonstrate the effects related to the presence of an interface separating elastic beams unloaded from beams pre-loaded with an axial force.

The first dynamic excitation is a plane wave generated and propagated in the grid using the following technique. In a first step, by means of Eq. (3.3) a single Floquet-Bloch wave is calculated for an infinite square grid of beams not subject to prestress. In a second step, the just calculated displacements are applied on a finite portion of the boundary of a square region, which contains layers of prestressed elastic beams and is enclosed within PML boundary conditions (the damping parameter is tuned to prevent reflection at the boundary). Propagation in the latter square region is analyzed via finite elements using COMSOL Multiphysics® in the frequency response mode. The rotational inertia term of the Rayleigh model is implemented by modifying the moment equation of the standard Euler-Bernoulli elements [55]. The second dynamic excitation is a concentrated time-harmonic moment (of out-of-plane axis) applied to a junction of the beam network (where the prestress is absent), adjacent to the boundary of the prestressed structured interface.

In the following applications, the frequency levels have been selected to provide a slowness contour of the ambient lattice (not prestressed) characterized by almost perfectly straight edges, in order to favor a strongly localized forced response [1, 57].

3.3.1 Total reflection

A total reflection is shown in Fig. 3.2a of a plane wave (inclined at 45° and propagating at the frequency $\Omega = 3.10$) against an interface with prestressed vertical elements subject to a tensile load of $p = 65$. This value of prestress (and those assumed in the following) is very high, so that in a practical implementation of the concept presented in this paper, a nonlinear material with a tangent stiffness modulus strongly decreasing with strain has to be used (strictly speaking, only the tangent modulus at the prescribed prestress level enters in the formulation).

The black and green arrows denote the group velocity of the incident wave $\boldsymbol{v}^{\mathrm{gr}}_{\mathrm{inc}}$ and of the reflected wave $\boldsymbol{v}^{\mathrm{gr}}_{\mathrm{refl}}$, respectively, while the slowness contour of the lattice is shown in the inset without (marked green) and with (marked red) prestress. With reference to the inset, the propagation direction of the incident plane wave, with fronts perpendicular to vector $\boldsymbol{K}$, is defined by the gradient of the dispersion relation at the point A, i.e. the group velocity of the incident wave $\boldsymbol{v}^{\mathrm{gr}}_{\mathrm{inc}}$ (black arrow) in the lattice without prestress. Using the conservation of the component of $\boldsymbol{K}$ parallel to the interface ($K_{\parallel} = K_2$), the gradient at point B determines the group velocity of the reflected wave $\boldsymbol{v}^{\mathrm{gr}}_{\mathrm{refl}}$ (green arrow). The directions of $\boldsymbol{v}^{\mathrm{gr}}_{\mathrm{inc}}$ and

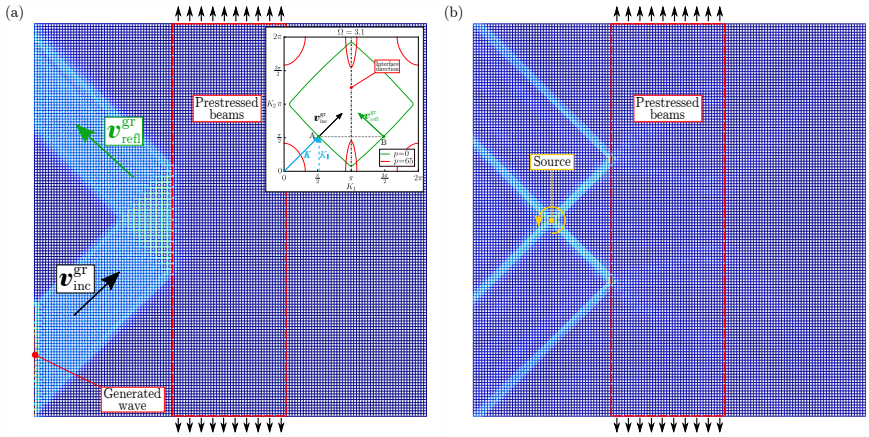

Fig. 3.2. Total reflection on a layer of prestressed ($p = 65$) elastic rods, at a frequency $\Omega = 3.10$ of: (a) a plane wave incident at 45° and (b) a channeled wave pattern generated by a pulsating concentrated moment. The black and green arrows in part (a) denote the group velocities $v^{\mathrm{gr}}_{\mathrm{inc}}$ and $v^{\mathrm{gr}}_{\mathrm{refl}}$, respectively, and the inset shows the slowness contours for the lattice without (green) and with (red) prestress, respectively.

$v^{\mathrm{gr}}_{\mathrm{refl}}$ highlight the total reflection, also marked by the fact that the slowness contour of the interface (red) is not intersected by the projection of the vector $\boldsymbol{K}$ along the direction of the interface.

Channeling of the signal generated by a pulsating concentrated moment (of out-of-plane axis) is shown in Fig. 3.2b. The source, vibrating at $\Omega = 3.10$, is applied near the same interface used for Fig. 3.2a and defining a prestressed layer, so that total reflection is again observed, but now obtained for the wide Bloch spectrum generated by the pulsating moment.

3.3.2 Negative refraction and flat lensing

Tuning the prestress to $p = 190$ in the geometry already analyzed for total reflection, now negative refraction is observed (Fig. 3.3a), so that a part of the incident wave continues to be reflected and another part crosses the interface with a strongly negative angle of refraction. In particular, the black, the green and the red arrows denote the group velocity of the incident $v^{\mathrm{gr}}_{\mathrm{inc}}$, of the reflected $v^{\mathrm{gr}}_{\mathrm{refl}}$ and of the refracted $v^{\mathrm{gr}}_{\mathrm{refr}}$ waves, respectively. The inset shows that the green slowness contour remains the same as that of the grid without prestress, while the red contour is now modified by the higher value of prestress p. The level of prestress is tuned to obtain a significant change of the group velocity direction between the ambient lattice and the prestressed grid. The gradient at point B determines the group velocity $v^{\mathrm{gr}}_{\mathrm{refl}}$ (green arrow), while the gradient at point C the group velocity of the refracted wave $v^{\mathrm{gr}}_{\mathrm{refr}}$ (red arrow). The strong negative refraction follows from the scalar product $v^{\mathrm{gr}}_{\mathrm{inc}} \cdot v^{\mathrm{gr}}_{\mathrm{refr}} \approx 0$.

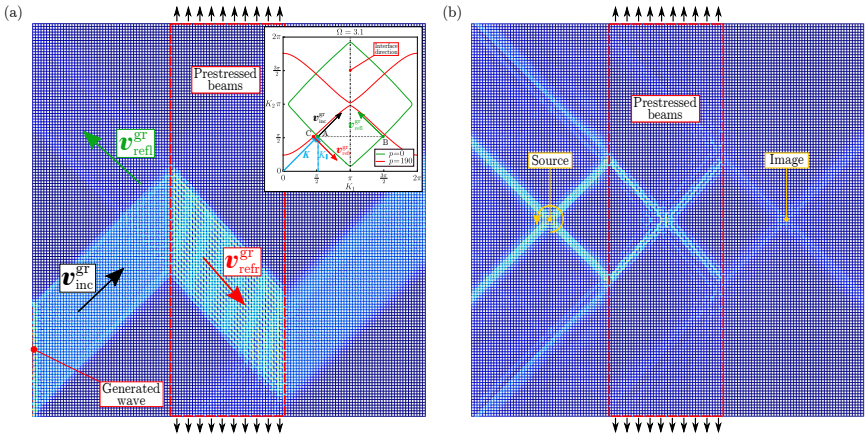

Fig. 3.3. Negative refraction inside a layer of highly prestressed, $p = 190$, beams (a), producing a flat lens (b). In part (a) a plane wave is incident at 45° on the interface at the frequency $\Omega = 3.10$ and the black, green and red arrows denote the group velocities v^{gr}_{inc}, v^{gr}_{refl} and v^{gr}_{refr}, respectively. The inset shows the slowness contours for the periodic lattice without (green) and with (red) prestress, respectively. In part (b) a channeled wave pattern is generated by a pulsating concentrated moment and the corresponding image is reconstructed through a flat lens interface.

Using the negative refraction achieved with the prestressed interface, it is possible to transform the layer of prestressed beams into a flat lens [26, 66, 69, 70], as demonstrated by the wave focusing, forming an image evident in Fig. 3.3b, where a channeled wave pattern generated by the pulsating concentrated bending moment is reported.

It is worth noting that the designed interface is capable of refracting most of the Bloch spectrum activated by the pulsating moment and therefore reflecting only a small part of the incident signal. Furthermore, as a consequence of the simplicity of the tuning obtained through prestress of some beams, the transmission properties of the interface can be easily changed, so that the response can switch from a pure reflection (Fig. 3.2b) to a flat lens effect (Fig. 3.3b). This provides much more flexibility for applications in dynamics than solutions requiring structural modifications of the material [69, 72, 84–87].

3.3.3 Trapping and focussing of a signal

Taking advantage of the interplay between the mechanical properties of the lattice subject or not to prestress, it is possible to introduce a band of prestressed beams inside an homogeneous lattice in such a way to generate complex paths to be followed by a trapped wave generated by a concentrated bending moment applied inside the path.

An 'S-shaped' trapped wave is shown in Fig. 3.4a, which propagates at frequency $\Omega = 5.65$ inside a channel delimited by two narrow layers of prestressed beams ($p = 190$), an expedient which realizes a simple method

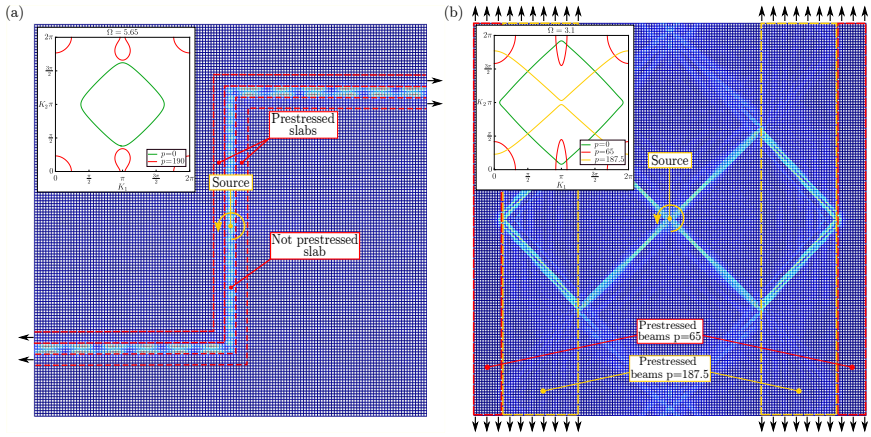

Fig. 3.4. (a) Trapping of a wave generated by a concentrated bending moment, pulsating at the frequency $\Omega = 5.65$, inside a channel delimited by two narrow layers of prestressed beams ($p = 190$) aligned parallel to the desired propagation path. (b) The combination of two layers of beams at different level of prestress ($p = 65$ and $p = 187.5$) generates a complex channeled wave pattern with negative refraction and focussing effect ($\Omega = 3.10$).

to spatially control the energy transmission along any desired path [88]. Again, since the effect is prestress-induced, it provides a valuable alternative to other methods of channeling dynamic signals (e.g. leveraging edge-waves in gyroscopic systems [9, 11, 76] and topological materials [17] or embedding piezoelectric elements in elastic lattices [77]).

Finally, it is worth mentioning that layers of beams subject to different prestress levels can be introduced to obtain complicated effects. For instance, a complex channeled wave pattern showing negative refraction and focussing effects is shown in Fig. 3.4b, as obtained by the combination of two layers of prestressed beams at different values of force ($p = 65$ and $p = 187.5$). This double-layer interface is designed to first bend the signal (through the negative refraction occurring at the first prestressed layer $p = 187.5$) and then to focus it on the reflective prestressed layer ($p = 65$). The second interface totally reflects the signal towards the first one, which in turn directs it, with a negative angle of refraction, towards the original source, where the signal is concentrated exactly where it is generated. Only a small part of the original signal is lost in the passage through the first interface due to partial reflection. As the thickness of these layers can be easily adjusted, the point of focussing can be effectively engineered as a function of distance from the forcing source.

3.4 Concluding remark

In summary, we have demonstrated that prestress represents a simple way to tune the mechanical properties of an elastic grid of (axially and flexurally deformable) beams, so that the response to wave propagation of a totally

reflective interface can be changed so to leave the signal refracting through the interface with a negative angle. Moreover, the prestress can be used to localize wave propagation into narrow layers inside a material, to mimic edge wave propagation in topological materials, or to trap energy inside thin channels. The wave manipulation tool proposed in this study benefits from the fact that the signal is generated by a moment source and the obtained dynamical properties work correctly for a wide range of wavelengths.

4

Bifurcation and strain localization in prestressed lattices: static response

A lattice of elastic rods organized in a parallelepiped geometry can be axially loaded up to an arbitrary amount without distortion and then be subject to incremental displacements. Using quasi-static homogenization theory, this lattice can be made equivalent to a prestressed elastic solid subject to incremental deformation, in such a way to obtain extremely localized mechanical responses. These responses can be analyzed with reference to a mechanical model which can, *in principle*, be realized, so that features such as for instance shear bands inclination, or emergence of a single shear band, or competition between micro (occurring in the lattice but not in the equivalent solid) and macro (present in both the lattice and the equivalent continuum) instabilities become all designable features. The analysis of localizations is performed using a Green's function-based perturbative approach to highlight the correspondence between micromechanics of the composite and homogenized response of the equivalent solid. The presented results, limited to quasi-static behaviour, provide a new understanding of strain localization in a continuum and open new possibilities for the realization and experimentation of materials exhibiting these extreme mechanical behaviours. Dynamic homogenization and vibrational localization are deferred to Chapter 5 of this study.

4.1 Introduction

Shear banding and strain localizations, usually found to emerge before failure of materials, are typically accompanied by large plastic deformation,

damage, and possibly fracture. Mechanical features of shear bands strongly depend on the tested material, so that for instance shear bands are normally inclined (to the direction of tensile stress) less in rocks than in metals. As a consequence, from the modelling point of view, the analysis of these material instabilities is complicated by the fact that (complex and often phenomenological) elastoplastic constitutive laws are to be used for a material which has to be brought through and beyond several bifurcation thresholds (corresponding for instance to surface instability or cavitation), before encountering shear band formation, the latter typically complicated by the simultaneous emergence of elastic unloading zones adjacent to zones of intense plastic loading. From the experimental point of view, samples have to be brought to failure, so that experiments cannot be repeated on the same sample and the material forming the latter cannot be easily changed to analyzed different instability manifestations, for instance in such a way to alter the shear band inclination.

Imagine now a material in which shear banding and other instabilities may occur well inside the elastic range and far from failure. A material that can be designed to produce shear bands with a desired inclination, or in which shear bands are the first instability occurring at increasing stress, or in which the anisotropy (not imperfections) allows the formation of only one shear band. Imagine that this material would be characterized by rigorously determined elastic constitutive laws (thus avoiding complications such as the double branch of the incremental constitutive laws of plasticity) and would be, at least in principle, a material realizable (for instance via 3d printing technology) and testable in laboratory conditions. This material would be ideal not only to *theoretically* analyze instabilities, but also to *practically* realize the 'architected materials' which are preconized to yield extreme mechanical properties such as foldability, channelled response, and surface effects [6, 7, 15]. The crucial step towards the definition of a class of these materials was made by Triantafyllidis [18, 19, 27–30] and Ponte Castañeda [20, 31–38], who laid down a general framework for the homogenization of elastic composites and for the analysis of bifurcation and strain localization in these materials. In particular, (i) they showed how to realize an elastic material displaying a prestress-sensitive incremental response, exactly how it is *postulated* for nonlinear elastic solids subject to incremental deformation, and (ii) provided a new understanding of strain localization phenomena, showing that a global bifurcation of a lattice structure corresponds to a loss of ellipticity of the equivalent continuum, while the latter is unaffected by a local bifurcation occurring in the composite.

The aim of the present work is to extend the mentioned findings to lattices of elastic rods of arbitrary geometry and subject to nonlinear axial deformation of the elements, so to explore shear band formation and localization by applying a perturbative approach [89], both to the lattice and to the equivalent continuum. In particular, a lattice of elastic rods organized in a parallelepiped network is an example of a composite which may be arbitrarily preloaded without introducing grid distortion, so that rigorous homogenization results show how a prestressed composite material can react

to incremental displacements as an equivalent elastic continuum. A quasi-static approach to homogenization, based on a strain energy equivalence between the lattice and the continuum, is developed to analyze a generic lattice[1], so that it becomes possible to obtain the infinite-body Green's function for the homogenized solid and compare the response of this solid to an applied concentrated force with the behaviour of the lattice at various levels of preload. This comparison reveals, first of all, the excellent quality of the homogenization approach (so that the incremental displacement fields found in the lattice and in the homogenized material are practically coincident) and highlights the features of shear banding, so that this instability is on the one hand given a clear interpretation in terms of structural global instability of the lattice and on the other sharply discriminated from local instabilities in the composite, which remain undetected in the continuum. Examples of such instabilities, 'invisible' in the equivalent material, are provided, which exhibit an 'explosive' character, so that extend from a punctual perturbation to the whole lattice.

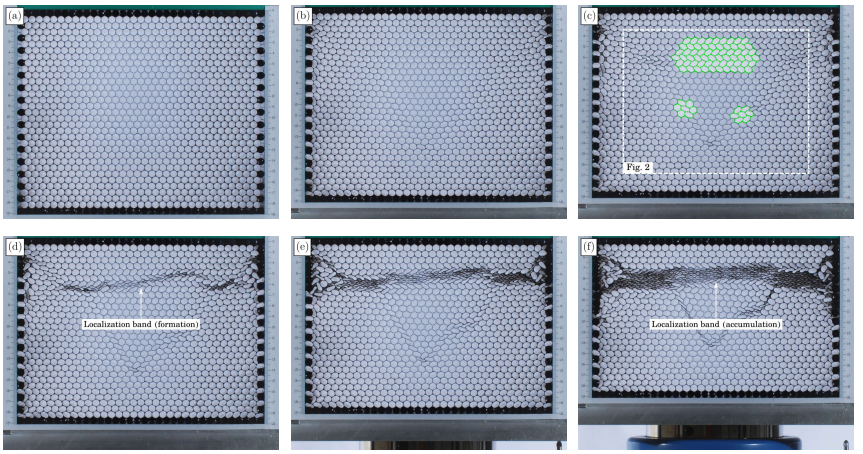

Fig. 4.1. Emergence of a periodic micro-bifurcation (ovalization of the straws' cross sections, part c), subsequent strain localization (collapse of the straws' cross sections, part d), and final strain accumulation (parts e and f) during uniaxial deformation of an initially (parts a and b) hexagonal packing of drinking straws.

An example of local instability, undetected in the homogenized material, but revealed through the analysis of the microstructure, is provided in Fig. 4.1, where photos of experiments (performed at the Instabilities Lab of the University of Trento) are shown in which a package of drinking straws, initially in a regular hexagonal disposition, is subject to an overall uniaxial strain. The unloaded configuration (Fig. 4.1a) is not particularly different from the configuration subject to a light loading (Fig. 4.1b). An increase of the loading yields a micro-bifurcation in terms of a periodic ovalization

[1]For the geometries investigated in [19] our homogenization approach provides exactly the same results. Moreover, the energy equivalence provides the same results that will be derived in Chapter 5 using a Floquet-Bloch dynamic approach.

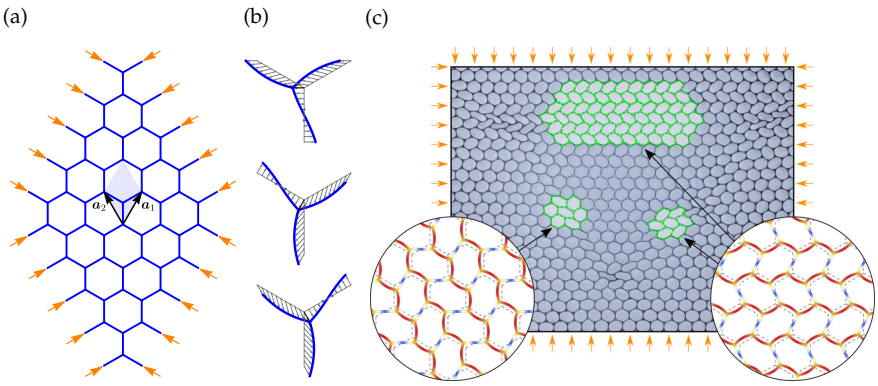

Fig. 4.2. The micro-bifurcation mode emerging during the uniaxial deformation of the package of drinking straws shown in Fig. 4.1 is modelled (with the tools provided in this chapter) as the micro-buckling of an honeycomb lattice of elastic rods, isotropically loaded with compressive forces. The equilibrium of the honeycomb structure (a) bifurcates displaying three critical modes (b), which induces a periodic ovalization pattern, explaining the regular and diffuse buckled zones in the array of drinking straws (c).

of the straws' cross sections (Fig. 4.1c), while at higher load strain localization occurs (in terms of collapse of the cross sections, Fig. 4.1d), with subsequent strain band accumulation (Figs. 4.1e and 4.1f). The periodic ovalization is perfectly captured by a bifurcation analysis of the hexagonal rods' grid (Fig. 4.2) subject to isotropic compression and displaying a periodic bifurcation mode which is compared with a detail of the photo shown in Fig. 4.1c.[2]

Homogenization is shown to provide a tool to select the geometry and loading of a lattice in a way to produce an equivalent solid with arbitrary incremental anisotropy, so that the shear band inclination, or the emergence of a singular shear band can be designed. The results that will be presented also demonstrate how lattice models of heterogeneous materials can be highly effective to obtain analytical expressions for homogenized properties, thus allowing an efficient analysis of the influence of the microstructural parameters. This is a clear advantage over continuum formulations of composites, where analytical results can only be obtained for simple geometries and loading configurations (as for instance in the case of laminated solids [29, 30, 90]). Several new features are found, including a 'super-sensitivity' of the localization direction to the preload state and the conditions in which a perfect correspondence between the lattice and the continuum occurs (so that the discrete system and the equivalent solid share all the same bifurcation modes). The microscopic features found for the strain localization are shown to share remarkable similarities with the localized failure patterns observed in honeycombs (as Fig. 4.1 demonstrates), foams and wood [91–

[2]The bifurcation occurs at an axial load in the grid (that was analytically calculated to be $-\arccos^2(-1/3)EJ/l^2 \approx -3.6EJ/l^2$) smaller than the load corresponding to loss of ellipticity in the equivalent material (which was calculated through the homogenization scheme presented in this chapter to be $\approx -7.014EJ/l^2$).

94], while the highly localized deformation bands emerging at macroscopic loss of ellipticity are reminiscent of the failure modes observed in balsa wood [95].

This chapter is organized as follows. The derivation of the incremental equilibrium is presented in Section 2 for a lattice of elastic rods organized in an arbitrary periodic geometry, while the homogenization is developed in Section 3, providing the incremental constitutive tensor of the effective Cauchy continuum. The stability of lattice structure and its relation with the strong ellipticity of the equivalent solid is given in Section 4, while examples and comparisons with the perturbative approach are presented in Sections 5 and 6, where the analysis is specialized to a grid of elastic rods arbitrarily inclined and equipped with diagonal springs.

Results presented in this chapter are restricted to quasi-static behaviour, while the important case of dynamic homogenization (with the Floquet-Bloch technique) and dynamic shear banding is deferred to Chapter 5 of this study.

4.2 Incremental response of lattices of axially preloaded elastic rods

A two-dimensional periodic lattice of elastic rods, deformable in the plane both axially and flexurally, is considered, in which all structural members are axially prestressed from an unloaded reference configuration $\mathcal{B}_0$. The prestress is assumed to be produced by dead loading acting at infinity, while body forces in the lattice are excluded for simplicity. It is assumed that the preload not only satisfies equilibrium, but also preserves periodicity and leaves the structure free of flexure. The prestressed configuration $\mathcal{B}$ is periodic along two linearly independent vectors $\{\boldsymbol{a}_1, \boldsymbol{a}_2\}$, defining the direct basis of the lattice, so that the structure can be constructed from a single unit cell $\mathcal{C}$, assumed to be composed of N_b nonlinear elastic rods with Euler-Bernoulli incremental kinematics, as sketched in Fig. 4.3.

By considering in-plane flexural and axial incremental deformations, the incremental displacement field of the k–th rod in a given unit cell is defined by the vector field (Fig. 4.3)

$$\boldsymbol{u}_k(s_k) = \{u_k(s_k), v_k(s_k)\}^\intercal, \qquad \forall k \in \{1, ..., N_b\}, \tag{4.1}$$

where s_k is the coordinate along the k–th rod, $u_k(s_k)$ and $v_k(s_k)$ are the axial and transverse incremental displacements. The incremental rotation of the rod's cross-section $\theta_k(s_k)$ is assumed to satisfy the unshearability condition of the Euler-Bernoulli kinematics, namely, $\theta_k(s_k) = v_k'(s_k)$.

4.2.1 Analytic solution for the prestressed elastic rod

The incremental equilibrium equations for an elastic rod obeying Euler-Bernoulli kinematics and prestressed with an axial load P (assumed positive

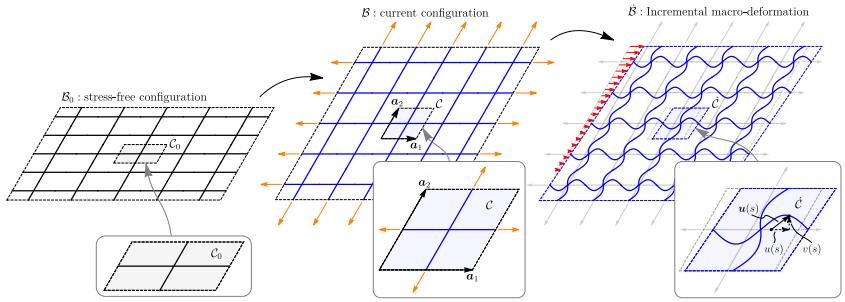

Fig. 4.3. A periodic two-dimensional lattice of (axially and flexurally deformable) elastic rods is considered prestressed from the stress-free configuration $\mathcal{B}_0$ (left) by means of a purely axial loading state. The prestressed configuration $\mathcal{B}$ (center) can be represented as the tessellation of a single unit cell along the vectors of the direct basis $\{\boldsymbol{a}_1, \boldsymbol{a}_2\}$. Upon the current prestressed configuration, the incremental response (right) is defined by the incremental displacement field of each rod $\boldsymbol{u}(s)$, here decomposed in an axial and transverse component, $u(s)$ and $v(s)$.

in tension) and pre-stretched by $\lambda_0 > 0$, are the following

$$A(\lambda_0)\, u''(s) = 0\,, \tag{4.2a}$$
$$B(\lambda_0)\, v''''(s) - P(\lambda_0)\, v''(s) = 0\,, \tag{4.2b}$$

where $A(\lambda_0)$ and $B(\lambda_0)$ are the *current* axial and bending stiffnesses, respectively, and $s \in (0, l)$ with l being the *current* length of the rod. It is worth noting that the current axial and bending stiffnesses are, in general, function of the current pre-stretch λ_0, which in turn depends on the axial load P. In fact, Eqs. (4.2) govern the incremental equilibrium of an axially pre-stretched rod, and their analytic derivation, accompanied with the evaluation of $A(\lambda_0)$ and $B(\lambda_0)$ from given strain-energy functions, is deferred to Appendix C. In the following, the parameters $A(\lambda_0)$ and $B(\lambda_0)$ will simply be denoted as A and B, and treated as independent quantities for generality. The specific example in which the rods composing the lattice are made up of a Mooney-Rivlin elastic incompressible material is explicitly reported in Appendix C.

Eqs. (4.2) is a system of linear ODEs for the functions $u(s)$ and $v(s)$. As the system is fully decoupled, the solution is easily obtained in the form

$$u(s) = C_1^u + C_2^u\, s\,, \qquad v(s) = C_1^v\, e^{-\beta s} + C_2^v\, e^{\beta s} + C_3^v\, s + C_4^v\,, \tag{4.3}$$

where $\{C_1^u, C_2^u, C_1^v, \ldots, C_4^v\}$ are 6 arbitrary complex constants and $\beta = \sqrt{P/B}$.

4.2.2 Exact shape functions and stiffness matrix

For a rod of length l, the following nomenclature can be introduced

$$\begin{aligned} u(0) &= u_1\,, \quad v(0) = v_1\,, \quad \theta(0) = \theta_1\,, \\ u(l) &= u_2\,, \quad v(l) = v_2\,, \quad \theta(l) = \theta_2\,, \end{aligned} \tag{4.4}$$

so that the vector $\boldsymbol{q} = \{u_1, v_1, \theta_1, u_2, v_2, \theta_2\}^\intercal$ now collects the degrees of freedom of the rod expressed in terms of end displacements. Solving the conditions (4.4) for the constants $\{C_1^u, C_2^u, C_1^v, ..., C_4^v\}^\intercal$ allows the solution (4.3) to be rewritten as

$$\boldsymbol{u}(s) = \boldsymbol{N}(s;P)\,\boldsymbol{q}\,, \tag{4.5}$$

which is now a linear function of the nodal displacements $\boldsymbol{q}$. The 2×6 matrix $\boldsymbol{N}(s;P)$ acts as a matrix of prestress-dependent 'shape functions' and therefore the representation (4.5) can also be considered as the definition of a 'finite element' endowed with shape functions built from the exact solution. Moreover, these shape functions reduce to the solution holding true in the absence of prestress, because in the limit

$$\lim_{P\to 0} \boldsymbol{N}(s;P) = \begin{bmatrix} 1-\frac{s}{l} & 0 & 0 & \frac{s}{l} & 0 & 0 \\ 0 & \frac{(l-s)^2(l+2s)}{l^3} & \frac{(l-s)^2 s}{l^2} & 0 & \frac{(3l-2s)s^2}{l^3} & \frac{s^2(s-l)}{l^2} \end{bmatrix},$$

the usual shape functions (linear and Hermitian for axial and flexural displacements, respectively) are retrieved.

By employing Eq. (4.5), the incremental stiffness matrix of a prestressed rod can be computed, so that for the k-th rod the elastic strain energy is given by

$$\begin{aligned} \mathcal{E}_k &= \frac{1}{2}\int_0^{l_k} \left(A_k\, u_k'(s_k)^2 + B_k\, v_k''(s_k)^2\right)\, ds_k \\ &= \frac{1}{2}\,\boldsymbol{q}_k^\intercal \left(\int_0^{l_k} \boldsymbol{B}_k(s_k;P_k)^\intercal\, \boldsymbol{E}_k\, \boldsymbol{B}_k(s_k;P_k)\, ds_k\right) \boldsymbol{q}_k\,, \end{aligned} \tag{4.6}$$

where $\boldsymbol{E}_k$ is a matrix collecting the stiffness terms, while $\boldsymbol{B}_k(s_k;P)$ is the strain-displacement matrix, defined as follows

$$\boldsymbol{E}_k = \begin{bmatrix} A_k & 0 \\ 0 & B_k \end{bmatrix}, \qquad \boldsymbol{B}_k(s_k;P_k) = \begin{bmatrix} \frac{\partial}{\partial s_k} & 0 \\ 0 & \frac{\partial^2}{\partial s_k^2} \end{bmatrix} \boldsymbol{N}_k(s_k;P_k)\,.$$

The 'geometric' contribution of the axial prestress is now included in the potential energy (details are provided in Appendix C),

$$\mathcal{V}_k^g = \frac{1}{2}P_k \int_0^{l_k} v_k'(s_k)^2\, ds_k = \frac{1}{2}\,\boldsymbol{q}_k^\intercal \left(P_k \int_0^{l_k} \boldsymbol{b}_k(s_k;P_k)^\intercal\, \boldsymbol{b}_k(s_k;P_k)\, ds_k\right) \boldsymbol{q}_k\,, \tag{4.7}$$

where $\boldsymbol{b}_k(s_k;P_k) = \begin{bmatrix} 0 & \frac{\partial}{\partial s_k} \end{bmatrix} \boldsymbol{N}_k(s_k;P_k)$ is a vector collecting the derivatives of the shape functions describing the transverse displacement v. A combination of Eqs. (4.6) and (4.7), yields the potential energy for the k-th rod in the form

$$\mathcal{V}_k = \mathcal{E}_k + \mathcal{V}_k^g\,. \tag{4.8}$$

Note that, as the equilibrium equations for the rods have been linearized

around an axially pre-loaded configuration, the potential (4.8) represents the incremental potential energy with respect to the current configuration. See the Appendix C for details on the derivation of Eqs. (4.6)–(4.8).

From Eqs. (4.6), (4.7) and (4.8) the prestress-dependent stiffness matrix is defined as

$$\boldsymbol{K}_k(P_k) = \int_0^{l_k} \boldsymbol{B}_k(s_k;P_k)^\intercal \boldsymbol{E}_k \boldsymbol{B}_k(s_k;P_k)\, ds_k + P_k \int_0^{l_k} \boldsymbol{b}_k(s_k;P_k)^\intercal \boldsymbol{b}_k(s_k;P_k)\, ds_k,$$

so that

$$\boldsymbol{K}_k = \begin{bmatrix} \frac{A_k}{l_k} & 0 & 0 & -\frac{A_k}{l_k} & 0 & 0 \\ 0 & \frac{12B_k}{l_k^3}\varphi_1(p_k) & \frac{6B_k}{l_k^2}\varphi_2(p_k) & 0 & -\frac{12B_k}{l_k^3}\varphi_1(p_k) & \frac{6B_k}{l_k^2}\varphi_2(p_k) \\ 0 & \frac{6B_k}{l_k^2}\varphi_2(p_k) & \frac{4B_k}{l_k}\varphi_3(p_k) & 0 & -\frac{6B_k}{l_k^2}\varphi_2(p_k) & \frac{2B_k}{l_k}\varphi_4(p_k) \\ -\frac{A_k}{l_k} & 0 & 0 & \frac{A_k}{l_k} & 0 & 0 \\ 0 & -\frac{12B_k}{l_k^3}\varphi_1(p_k) & -\frac{6B_k}{l_k^2}\varphi_2(p_k) & 0 & \frac{12B_k}{l_k^3}\varphi_1(p_k) & -\frac{6B_k}{l_k^2}\varphi_2(p_k) \\ 0 & \frac{6B_k}{l_k^2}\varphi_2(p_k) & \frac{2B_k}{l_k}\varphi_4(p_k) & 0 & -\frac{6B_k}{l_k^2}\varphi_2(p_k) & \frac{4B_k}{l_k}\varphi_3(p_k) \end{bmatrix},$$

where the φ_j are functions of the non-dimensional measure of prestress $p_k = P_k l_k^2/B_k$ given by

$$\begin{aligned} \varphi_1(p_k) &= \frac{p_k^{3/2}}{12\left(\sqrt{p_k} - 2\tanh\left(\sqrt{p_k}/2\right)\right)}, \\ \varphi_2(p_k) &= \frac{p_k}{6\sqrt{p_k}\coth\left(\sqrt{p_k}/2\right) - 12}, \\ \varphi_3(p_k) &= \frac{p_k\cosh\left(\sqrt{p_k}\right) - \sqrt{p_k}\sinh\left(\sqrt{p_k}\right)}{4\sqrt{p_k}\sinh\left(\sqrt{p_k}\right) - 8\cosh\left(\sqrt{p_k}\right) + 8}, \\ \varphi_4(p_k) &= \frac{\sqrt{p_k}\left(\sinh\left(\sqrt{p_k}\right) - \sqrt{p_k}\right)}{\left(4\sqrt{p_k}\coth\left(\sqrt{p_k}/2\right) - 8\right)\sinh^2\left(\sqrt{p_k}/2\right)}. \end{aligned}$$

Note that the stiffness matrix representative of the lattice reduces, in the limit of vanishing prestress (or unitary pre-stretch $\lambda_{0k} = 1$), to the usual stiffness matrix of an Euler-Bernoulli beam with Hermitian shape functions, so that

$$\lim_{p\to 0} \varphi_j(p) = 1, \quad \forall j \in \{1,\dots,4\}.$$

4.2.3 Incremental equilibrium of the lattice of elastic rods

The current configuration of the lattice unit cell is subject, on the boundary, to the nominal internal *incremental* actions and *incremental* displacements transmitted by the rest of the lattice. Therefore, the incremental potential

energy of the cell can be evaluated through a direct summation of all contributions from the rods, equation (4.8), over the set of structural elements present inside the cell, plus the incremental work done on the unit cell boundary by the internal actions $\boldsymbol{f}$,

$$\mathcal{V}(\boldsymbol{q}) = \sum_{k=1}^{N_b} \mathcal{V}_k(\boldsymbol{C}_k \boldsymbol{q}) - \boldsymbol{f} \cdot \boldsymbol{q} \,, \tag{4.9}$$

where $\boldsymbol{q}$ is the vector collecting the degrees of freedom of the unit cell, $\boldsymbol{C}_k$ is the connectivity matrix of the k-th rod, such that $\boldsymbol{q}_k = \boldsymbol{C}_k \boldsymbol{q}$, and $\boldsymbol{f}$ is the vector collecting the *generalized* (incremental and nominal) internal actions (including bending moments) at the nodes of the unit cell.

The (referential) incremental equilibrium equations (in the absence of body forces) are therefore obtained from the stationarity of the potential energy (4.9) yielding

$$\boldsymbol{K}(\boldsymbol{P})\, \boldsymbol{q} = \boldsymbol{f} \,, \tag{4.10}$$

where

$$\boldsymbol{K}(\boldsymbol{P}) = \frac{\partial^2}{\partial \boldsymbol{q} \partial \boldsymbol{q}} \sum_{k=1}^{N_b} \mathcal{V}_k(\boldsymbol{C}_k \boldsymbol{q}) \tag{4.11}$$

is the symmetric (as derived from a potential) stiffness matrix of the unit cell, function of the vector $\boldsymbol{P} = \{P_1, \dots, P_{N_b}\}$ collecting the axial prestress of the rods. The dimension of the system (4.10) is $3N_j$ where N_j is the number of nodes in the unit cell.

4.3 Incremental response of the effective Cauchy continuum

As the preloaded configuration of the lattice is assumed to be spatially periodic, the homogenized incremental response of an equivalent prestressed elastic solid can be defined by computing the average strain-energy density, associated to an incremental displacement field (defined for the j-th node by the displacement and rotation components, respectively, $\boldsymbol{q}_u^{(j)} = \{u^{(j)}, v^{(j)}\}^\intercal$ and $\boldsymbol{q}_\theta^{(j)} = \{\theta^{(j)}\}$) which obeys the Cauchy-Born hypothesis [96–98]. The latter, for a single unit cell, prescribes that the displacement of the lattice nodes be decomposed into the sum of an affine incremental deformation (ruled by a second-order tensor $\boldsymbol{L}$) and a periodic field (defined by a displacement $\tilde{\boldsymbol{q}}_u^{(j)}$ and a rotational $\tilde{\boldsymbol{q}}_\theta^{(j)}$ component) as

$$\boldsymbol{q}_u^{(j)} = \tilde{\boldsymbol{q}}_u^{(j)} + \boldsymbol{L}\, \boldsymbol{x}_j \,, \qquad \boldsymbol{q}_\theta^{(j)} = \tilde{\boldsymbol{q}}_\theta^{(j)} \,, \qquad \forall j \in \{1, \dots, N_j\} \tag{4.12}$$

where $\boldsymbol{x}_j$ is the position of the j-th node.

The periodic term $\tilde{\boldsymbol{q}}$ satisfies $\tilde{\boldsymbol{q}}^{(p)} = \tilde{\boldsymbol{q}}^{(q)}$ for all $\{p, q\}$ such that $\boldsymbol{x}_q - \boldsymbol{x}_p = n_j \boldsymbol{a}_j$ (with $n_j \in \{0, 1\}$), and can be expressed in terms of its independent

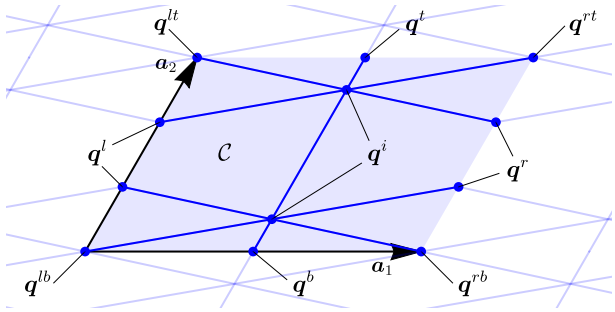

Fig. 4.4. The vector $\boldsymbol{q}$ collects the degrees of freedom of the unit cell. In order to impose the periodic boundary conditions required by the Cauchy-Born hypothesis (4.12) (or the quasi-periodic boundary conditions required by the Floquet-Bloch hypothesis (4.28) that will be used in the bifurcation analysis), $\boldsymbol{q}$ is partitioned between sets of inner nodes $\boldsymbol{q}^i$, boundary nodes located at corners $\{\boldsymbol{q}^{lb}, \boldsymbol{q}^{lt}, \boldsymbol{q}^{rb}, \boldsymbol{q}^{rt}\}$, and boundary nodes on the edges $\{\boldsymbol{q}^l, \boldsymbol{q}^b, \boldsymbol{q}^r, \boldsymbol{q}^t\}$. The corresponding vector of incremental internal nominal actions $\boldsymbol{f}$ is partitioned in the same way.

components through a partition of the degrees of freedom, made in accordance with the location of the nodes present inside the unit cell (see Fig. 4.4), as

$$\tilde{\boldsymbol{q}} = \begin{Bmatrix} \tilde{\boldsymbol{q}}^i \\ \tilde{\boldsymbol{q}}^l \\ \tilde{\boldsymbol{q}}^b \\ \tilde{\boldsymbol{q}}^{lb} \\ \tilde{\boldsymbol{q}}^r \\ \tilde{\boldsymbol{q}}^t \\ \tilde{\boldsymbol{q}}^{rb} \\ \tilde{\boldsymbol{q}}^{lt} \\ \tilde{\boldsymbol{q}}^{rt} \end{Bmatrix} = \begin{bmatrix} \boldsymbol{I} & \boldsymbol{0} & \boldsymbol{0} & \boldsymbol{0} \\ \boldsymbol{0} & \boldsymbol{I} & \boldsymbol{0} & \boldsymbol{0} \\ \boldsymbol{0} & \boldsymbol{0} & \boldsymbol{I} & \boldsymbol{0} \\ \boldsymbol{0} & \boldsymbol{0} & \boldsymbol{0} & \boldsymbol{I} \\ \boldsymbol{0} & \boldsymbol{I} & \boldsymbol{0} & \boldsymbol{0} \\ \boldsymbol{0} & \boldsymbol{0} & \boldsymbol{I} & \boldsymbol{0} \\ \boldsymbol{0} & \boldsymbol{0} & \boldsymbol{0} & \boldsymbol{I} \\ \boldsymbol{0} & \boldsymbol{0} & \boldsymbol{0} & \boldsymbol{I} \\ \boldsymbol{0} & \boldsymbol{0} & \boldsymbol{0} & \boldsymbol{I} \end{bmatrix} \begin{Bmatrix} \tilde{\boldsymbol{q}}^i \\ \tilde{\boldsymbol{q}}^l \\ \tilde{\boldsymbol{q}}^b \\ \tilde{\boldsymbol{q}}^{lb} \end{Bmatrix}, \tag{4.13a}$$

which may succinctly be rewritten as

$$\tilde{\boldsymbol{q}} = \boldsymbol{Z}_0 \, \tilde{\boldsymbol{q}}^* \,, \tag{4.13b}$$

where $\boldsymbol{Z}_0$ and $\tilde{\boldsymbol{q}}^*$ are defined according to Eq. (4.13a). The vector $\tilde{\boldsymbol{q}}$ in Eq. (4.13a) has been partitioned to highlight the inner and boundary nodes according to the notation introduced in Fig. 4.4. The same partitioning is also used for the vectors $\boldsymbol{q}$ and $\boldsymbol{f}$.

In order to enforce the Cauchy-Born conditions into the equations of incremental equilibrium (4.10), it is convenient to rewrite Eq. (4.12) as

$$\boldsymbol{q}(\tilde{\boldsymbol{q}}^*, \boldsymbol{L}) = \boldsymbol{Z}_0 \, \tilde{\boldsymbol{q}}^* + \hat{\boldsymbol{q}}(\boldsymbol{L}), \tag{4.14}$$

where the affine part of the deformation $\hat{\boldsymbol{q}}(\boldsymbol{L})$ is a vector-valued function linear in $\boldsymbol{L}$ and such that

$$\hat{\boldsymbol{q}}(\boldsymbol{L})_u^{(j)} = \boldsymbol{L}\, \boldsymbol{x}_j \,, \qquad \hat{\boldsymbol{q}}(\boldsymbol{L})_\theta^{(j)} = \boldsymbol{0} \,, \qquad \forall j \in \{1, \dots, N_j\},$$

where the same notation introduced with Eq. (4.12) has been used do that the subscript u (subscript θ) denotes displacement (rotations) components.

Note that, since the lattice is subject to a non-vanishing prestress state, the macroscopic incremental deformation gradient defined by $\boldsymbol{L}$ must be an arbitrary second-order tensor and *not constrained to be symmetric* (as it happens in the absence of prestress [33, 97, 98]). As explained in the next section, this unsymmetry is essential for the correct evaluation of the incremental fourth-order tensor defining the effective continuum, 'macroscopically equivalent' to the lattice.

4.3.1 Incremental constitutive tensor for the equivalent continuum

Before introducing the homogenization technique, it is important to recall that, as shown in Section 4.2, the equilibrium equations for the lattice are (i) obtained in the context of a linearized theory, and (ii) referred to a prestressed reference configuration, therefore, the unknown 'equivalent' continuum has to be formulated in the context of the incremental theory of nonlinear elasticity by means of a relative Lagrangian description [99]. As a consequence, the response of the effective material is defined by an *incremental constitutive law* in the form

$$\dot{\boldsymbol{S}} = \mathbb{C}[\boldsymbol{L}]\,, \tag{4.15}$$

relating the increment of the first Piola-Kirchhoff stress $\dot{\boldsymbol{S}}$ to the gradient of incremental displacement $\boldsymbol{L}$, through the elasticity tensor $\mathbb{C}$. The most general form for the constitutive tensor $\mathbb{C}$ is

$$\mathbb{C} = \mathbb{E} + \boldsymbol{I} \boxtimes \boldsymbol{T} \qquad \text{in components} \qquad \mathbb{C}_{ijkl} = \mathbb{E}_{ijkl} + \delta_{ik} T_{jl}\,, \tag{4.16}$$

where δ_{ik} is the Kronecker delta, $\boldsymbol{T}$ is the Cauchy stress, defining the *prestress*, and $\mathbb{E}$ is a fourth-order elastic tensor, endowed with all usual (left and right minor and major) symmetries

$$\mathbb{E}_{ijkl} = \mathbb{E}_{jikl} = \mathbb{E}_{ijlk} = \mathbb{E}_{klij}\,, \tag{4.17}$$

so that $\mathbb{C}$ lacks the minor symmetries but has the major symmetry. The symmetries of $\mathbb{C}$ explain the reason why the full incremental deformation gradient $\boldsymbol{L}$, and *not* only its symmetric part, appears in the Cauchy-Born hypothesis (4.12) of the lattice. Moreover, Eq. (4.16) shows that $\boldsymbol{L}$ can be restricted to be symmetric *only in the absence of prestress*, $\boldsymbol{T} = \boldsymbol{0}$.

The incremental strain-energy density for the prestressed continuum is referred to the prestressed configuration and can be expressed in terms of a second-order expansion with respect to the incremental deformation gradient $\boldsymbol{L}$ as follows

$$\mathcal{W}(\boldsymbol{L}) = \underbrace{\boldsymbol{T}\cdot\boldsymbol{L}}_{\mathcal{W}_1(\boldsymbol{L})} + \underbrace{\mathbb{C}[\boldsymbol{L}]\cdot\boldsymbol{L}/2}_{\mathcal{W}_2(\boldsymbol{L})}\,, \tag{4.18}$$

where the first-order increment $\mathcal{W}_1(\boldsymbol{L})$ accounts for the work expended by the current prestress state $\boldsymbol{T}$ (due to the relative Lagrangian description the first Piola-Kirchhoff stress coincides with the Cauchy stress), while the second-order term $\mathcal{W}_2(\boldsymbol{L})$ is the strain-energy density associated with the incremental first Piola-Kirchhoff stress given by Eq. (4.15).

It is also worth noting that taking the second gradient of the incremental energy density (4.18) with respect to $\boldsymbol{L}$ yields the constitutive fourth-order tensor $\mathbb{C}$ relating the stress increment to the incremental displacement gradient, while the first gradient provides, when evaluated at $\boldsymbol{L} = \boldsymbol{0}$, the prestress $\boldsymbol{T}$. The latter property will be used to dissect the effect of prestress in the homogenized response of the lattice.

4.3.2 First and second-order matching of the incremental strain-energy density

The homogenization of the lattice response is based on the equivalence between the average incremental strain-energy associated to a *macroscopic* incremental displacement gradient applied to the lattice and the incremental strain-energy density of the effective elastic material subject to the same deformation. In the classical homogenization theory, this condition is known as *macro-homogeneity* condition, or Hill-Mandel theorem, [33, 97, 100, 101], which provides the link between the microscopic and macroscopic scale.

In the following, the macro-homogeneity condition is enforced to obtain the incremental energy density (4.18) that matches the effective behaviour of the prestressed lattice at first- $\mathcal{W}_1(\boldsymbol{L})$ and at second- $\mathcal{W}_2(\boldsymbol{L})$ order. Thus, the homogenization scheme is based on the following steps:

(i) An incremental deformation gradient $\boldsymbol{L}$ is considered, so that the incremental energy density for the unknown equivalent continuum is defined by Eq. (4.18);

(ii) following the Cauchy-Born hypothesis, Eq. (4.14), the incremental displacement field for the lattice is prescribed by the given tensor $\boldsymbol{L}$ and the periodic vector $\tilde{\boldsymbol{q}}^*$ necessary to enforce the equilibrium of the lattice;

(iii) with the solution of the lattice in terms of $\boldsymbol{L}$ (the periodic vector $\tilde{\boldsymbol{q}}^*$ becomes in solution a function of $\boldsymbol{L}$) the incremental energy density is calculated for the lattice;

(iv) the two incremental energy densities in the continuum and in the lattice are matched, so to obtain the parameters defining the equivalent solid.

Determination of the periodic displacement field for the lattice. By substituting condition (4.14) into Eqs. (4.10) and pre-multiplying by $\boldsymbol{Z}_0^\intercal$, the incremental equilibrium becomes

$$\boldsymbol{Z}_0^\intercal \boldsymbol{K}(\boldsymbol{P})\, \boldsymbol{Z}_0\, \tilde{\boldsymbol{q}}^* + \boldsymbol{Z}_0^\intercal \boldsymbol{K}(\boldsymbol{P})\, \hat{\boldsymbol{q}}(\boldsymbol{L}) = \boldsymbol{Z}_0^\intercal \boldsymbol{f}\,, \tag{4.19}$$

where the right-hand side can be written more explicitly using the partitioning introduced in Fig. 4.4 as

$$\boldsymbol{Z}_0^\intercal \boldsymbol{f} = \begin{Bmatrix} \boldsymbol{f}^i \\ \boldsymbol{f}^l + \boldsymbol{f}^r \\ \boldsymbol{f}^b + \boldsymbol{f}^t \\ \boldsymbol{f}^{lb} + \boldsymbol{f}^{rb} + \boldsymbol{f}^{lt} + \boldsymbol{f}^{rt} \end{Bmatrix}.$$

The fact that the only non-vanishing forces are assumed to be the internal actions transmitted at the unit cell boundary by the neighboring cells implies $\boldsymbol{f}^i = \boldsymbol{0}$. Moreover, as the displacement field satisfying the Cauchy-Born hypothesis generates *internal* forces in the infinite lattice that are *periodic* along the direct basis $\{\boldsymbol{a}_1, \boldsymbol{a}_2\}$, any single unit cell is subject to *external* boundary forces that are *anti-periodic*. Consequently $\boldsymbol{f}^l = -\boldsymbol{f}^r$, $\boldsymbol{f}^b = -\boldsymbol{f}^t$ and $\boldsymbol{f}^{lb} = -\boldsymbol{f}^{rb} - \boldsymbol{f}^{lt} - \boldsymbol{f}^{rt}$, so that the term $\boldsymbol{Z}_0^\intercal \boldsymbol{f}$ vanishes and Eq. (4.19) becomes

$$\boldsymbol{Z}_0^\intercal \boldsymbol{K}(\boldsymbol{P})\, \boldsymbol{Z}_0\, \tilde{\boldsymbol{q}}^* = -\boldsymbol{Z}_0^\intercal \boldsymbol{K}(\boldsymbol{P})\, \hat{\boldsymbol{q}}(\boldsymbol{L})\,. \tag{4.20}$$

The solution of the linear system (4.20) provides the incremental strain $\tilde{\boldsymbol{q}}^*$ internal to the lattice for every given $\boldsymbol{L}$. As a consequence of the linearity of $\hat{\boldsymbol{q}}(\boldsymbol{L})$, the solution $\tilde{\boldsymbol{q}}^*(\boldsymbol{L})$ is, in turn, linear in $\boldsymbol{L}$.

A few considerations have to be made about the solvability of the system (4.20). In fact, it is easy to show that the matrix $\boldsymbol{Z}_0^\intercal \boldsymbol{K}(\boldsymbol{P})\, \boldsymbol{Z}_0$ is always singular, regardless of the specific lattice structure under consideration. This is proved by considering a vector $\tilde{\boldsymbol{q}}^* = \boldsymbol{t}$ defining a pure rigid-body translation and observing that $\boldsymbol{K}(\boldsymbol{P})\, \boldsymbol{Z}_0\, \boldsymbol{t} = \boldsymbol{0}$, which, in turn, implies that the dimension of the nullspace of $\boldsymbol{Z}_0^\intercal \boldsymbol{K}(\boldsymbol{P})\, \boldsymbol{Z}_0$ is *at least* 2, as two linearly independent rigid-body translations exist for a 2d lattice. Any other deformation mode, possibly contained in $\ker(\boldsymbol{Z}_0^\intercal \boldsymbol{K}(\boldsymbol{P})\, \boldsymbol{Z}_0)$, is therefore a zero-energy mode (called also with the pictoresque name 'floppy mode' [78, 102]). These modes are excluded in the following analysis to ensure solvability of system (4.20), so that $\ker(\boldsymbol{Z}_0^\intercal \boldsymbol{K}(\boldsymbol{P})\, \boldsymbol{Z}_0)$ contains *only* two (in the present 2d formulation) rigid-body translations. This exclusion does not affect generality, as the analysis of floppy modes can always be recovered in the limit of vanishing stiffness of appropriate structural elements. Note also that sometimes floppy modes can be eliminated or introduced simply playing with the prestress state (which may induce stiffening or softening [103, 104]).

Having excluded floppy modes and observing that the right-hand side of Eq. (4.20) is orthogonal to $\ker(\boldsymbol{Z}_0^\intercal \boldsymbol{K}(\boldsymbol{P})\, \boldsymbol{Z}_0)$,

$$\boldsymbol{t} \cdot \boldsymbol{Z}_0^\intercal \boldsymbol{K}(\boldsymbol{P})\, \hat{\boldsymbol{q}}(\boldsymbol{L}) = 0,$$

for all rigid-body translations $\boldsymbol{t}$, the solution $\tilde{\boldsymbol{q}}^*(\boldsymbol{L})$ can be determined.

Match of the second-order incremental strain-energy density and determination of the incremental constitutive tensor. The solution of the linear system (4.20) allows the incremental displacement (4.14) to be expressed only in terms of the macroscopic displacement gradient $\boldsymbol{L}$ as $\boldsymbol{q}(\tilde{\boldsymbol{q}}^*(\boldsymbol{L}), \boldsymbol{L})$.

Therefore, the second-order incremental strain-energy stored in a single unit cell of the lattice undergoing a macroscopic strain can be evaluated as follows

$$\mathcal{E}(\boldsymbol{L}) = \frac{1}{2}\, \boldsymbol{q}(\tilde{\boldsymbol{q}}^*(\boldsymbol{L}), \boldsymbol{L}) \cdot \boldsymbol{K}(\boldsymbol{P})\, \boldsymbol{q}(\tilde{\boldsymbol{q}}^*(\boldsymbol{L}), \boldsymbol{L})\,, \tag{4.21}$$

which is a quadratic form in $\boldsymbol{L}$, because $\boldsymbol{q}(\tilde{\boldsymbol{q}}^*(\boldsymbol{L}), \boldsymbol{L})$ is linear in $\boldsymbol{L}$. By equating the second-order strain-energy density of the continuum $\mathcal{W}_2(\boldsymbol{L}) = \mathbb{C}[\boldsymbol{L}] \cdot \boldsymbol{L}/2$ to the average energy of the lattice (4.21), the following equivalence condition is obtained

$$\underbrace{\frac{1}{2}\, \mathbb{C}[\boldsymbol{L}] \cdot \boldsymbol{L}}_{\text{Continuum}} = \underbrace{\frac{1}{|C|}\, \mathcal{E}(\boldsymbol{L})}_{\text{Lattice}}\,, \tag{4.22}$$

where $|C|$ is the area of the unit cell.

Finally, the second gradient of (4.22) with respect to $\boldsymbol{L}$ yields the incremental constitutive tensor for the effective Cauchy material, equivalent to the lattice, in the form

$$\mathbb{C} = \frac{1}{|C|}\, \frac{\partial^2 \mathcal{E}(\boldsymbol{L})}{\partial \boldsymbol{L}\, \partial \boldsymbol{L}} = \frac{1}{2|C|}\, \frac{\partial^2}{\partial \boldsymbol{L}\, \partial \boldsymbol{L}} \Big[\boldsymbol{q}(\tilde{\boldsymbol{q}}^*(\boldsymbol{L}), \boldsymbol{L}) \cdot \boldsymbol{K}(\boldsymbol{P})\, \boldsymbol{q}(\tilde{\boldsymbol{q}}^*(\boldsymbol{L}), \boldsymbol{L}) \Big]\,, \tag{4.23}$$

which becomes now an *explicit function of the prestress state*, as well as of all the mechanical parameters defining the lattice.

Match of the first-order incremental strain-energy density and homogenization of the prestress state. So far, the incremental constitutive tensor $\mathbb{C}$ of a continuum equivalent to a prestressed elastic lattice, Eq. (4.23), has been obtained through homogenization. It is important now to 'dissect' from $\mathbb{C}$ the effect of the prestress $\boldsymbol{T}$ and, as a consequence, to obtain the tensor $\mathbb{E}$.

It will be shown below that the current prestress state $\boldsymbol{T}$ of the homogenized material can be directly linked to the prestress state $\boldsymbol{P} = \{P_1, ..., P_{N_b}\}$ of the lattice. In fact, by observing that (4.22) represents the *second-order* incremental strain energy, equal to $\mathcal{W}_2(\boldsymbol{L}) = \dot{\boldsymbol{S}}(\boldsymbol{L}) \cdot \boldsymbol{L}/2$, an equivalence analogous to (4.22) can be obtained considering the *first-order* increment of the strain energy, $\mathcal{W}_1(\boldsymbol{L}) = \boldsymbol{T} \cdot \boldsymbol{L}$. Thus, the first-order term can be identified as the *average work done by the prestress state* $\boldsymbol{P}$ *during the lattice deformation* $\boldsymbol{q}(\tilde{\boldsymbol{q}}^*(\boldsymbol{L}), \boldsymbol{L})$ *induced by* $\boldsymbol{L}$ so that the following equivalence can be stated

$$\underbrace{\boldsymbol{T} \cdot \boldsymbol{L}}_{\text{Continuum}} = \underbrace{\frac{1}{|C|}\, \boldsymbol{f}_{\boldsymbol{P}} \cdot \boldsymbol{q}(\tilde{\boldsymbol{q}}^*(\boldsymbol{L}), \boldsymbol{L})}_{\text{Lattice}}\,, \tag{4.24}$$

where the vector $\boldsymbol{f}_{\boldsymbol{P}}$ collects the forces that emerge at the nodes of the unit cell and are in equilibrium with the axial preload of the elastic rods $\boldsymbol{P}$ *in the current configuration assumed as reference*. As a consequence, the forces $\boldsymbol{f}_{\boldsymbol{P}}$ are independent of $\boldsymbol{L}$ and linear in $\boldsymbol{P}$.

Equation (4.24) requires that the work done by axial loads $\boldsymbol{f_P}$ for nodal displacements $\boldsymbol{q}$ associated to a skew-symmetric velocity gradient $\boldsymbol{L} = \boldsymbol{W}$ be zero, namely

$$\boldsymbol{f_P} \cdot \boldsymbol{q}(\tilde{\boldsymbol{q}}^*(\boldsymbol{W}), \boldsymbol{W}) = 0\,. \tag{4.25}$$

This statement is a direct consequence of the principle of virtual work for rigid body incremental motions, because $\boldsymbol{q}(\tilde{\boldsymbol{q}}^*(\boldsymbol{W}), \boldsymbol{W})$ represents an incremental rotation of the lattice and $\boldsymbol{f_P}$ satisfies equilibrium. Hence, taking into account the property (4.25), the homogenized prestress $\boldsymbol{T}$ can be obtained as the gradient of the equivalence condition (4.24) with respect to the symmetric part of $\boldsymbol{L}$, denoted as $\boldsymbol{D}$,

$$\boldsymbol{T} = \frac{1}{|C|}\,\frac{\partial}{\partial \boldsymbol{D}}\Big[\boldsymbol{f_P} \cdot \boldsymbol{q}(\tilde{\boldsymbol{q}}^*(\boldsymbol{D}), \boldsymbol{D})\Big]\,. \tag{4.26}$$

4.4 Stability of prestressed lattices of elastic rods, strong ellipticity, and ellipticity of the effective continuum

Lattice bifurcations are governed by the value of the preload $\boldsymbol{P}$ and they can exhibit deformation modes with different wavelength. When the wavelength becomes infinite, a 'global bifurcation' occurs. While in the homogenization procedure periodic conditions are used, the systematic investigation of bifurcations occurring in the lattice can be conducted by complementing the incremental equilibrium of the lattice (4.10) with Floquet-Bloch boundary conditions, which involve displacement fields of arbitrary wavelength [98].

Denoting the wave vector as $\boldsymbol{k} \in \mathbb{R}^2$ and applying Bloch's theorem (see [1, 52] for details), Eq. (4.10) becomes

$$\boldsymbol{Z}(\boldsymbol{k})^{\mathsf{H}}\boldsymbol{K}(\boldsymbol{P})\,\boldsymbol{Z}(\boldsymbol{k})\,\boldsymbol{q}^* = \boldsymbol{0}\,, \tag{4.27}$$

where symbol $^{\mathsf{H}}$ denotes the complex conjugate transpose operation and the matrix-valued function $\boldsymbol{Z}(\boldsymbol{k})$ generalizes $\boldsymbol{Z}_0$ in Eq. (4.13) as

$$\boldsymbol{q} = \begin{Bmatrix} \boldsymbol{q}^i \\ \boldsymbol{q}^l \\ \boldsymbol{q}^b \\ \boldsymbol{q}^{lb} \\ \boldsymbol{q}^r \\ \boldsymbol{q}^t \\ \boldsymbol{q}^{rb} \\ \boldsymbol{q}^{lt} \\ \boldsymbol{q}^{rt} \end{Bmatrix} = \begin{bmatrix} \boldsymbol{I} & \boldsymbol{0} & \boldsymbol{0} & \boldsymbol{0} \\ \boldsymbol{0} & \boldsymbol{I} & \boldsymbol{0} & \boldsymbol{0} \\ \boldsymbol{0} & \boldsymbol{0} & \boldsymbol{I} & \boldsymbol{0} \\ \boldsymbol{0} & \boldsymbol{0} & \boldsymbol{0} & \boldsymbol{I} \\ \boldsymbol{0} & z_1\boldsymbol{I} & \boldsymbol{0} & \boldsymbol{0} \\ \boldsymbol{0} & \boldsymbol{0} & z_2\boldsymbol{I} & \boldsymbol{0} \\ \boldsymbol{0} & \boldsymbol{0} & \boldsymbol{0} & z_1\boldsymbol{I} \\ \boldsymbol{0} & \boldsymbol{0} & \boldsymbol{0} & z_2\boldsymbol{I} \\ \boldsymbol{0} & \boldsymbol{0} & \boldsymbol{0} & z_1 z_2\boldsymbol{I} \end{bmatrix} \begin{Bmatrix} \boldsymbol{q}^i \\ \boldsymbol{q}^l \\ \boldsymbol{q}^b \\ \boldsymbol{q}^{lb} \end{Bmatrix}, \quad \boldsymbol{q} = \boldsymbol{Z}(\boldsymbol{k})\,\boldsymbol{q}^*\,, \tag{4.28}$$

in which $z_j = e^{i\,\boldsymbol{k}\cdot\boldsymbol{a}_j} \quad \forall j \in \{1, 2\}$.

Note that conditions (4.28) represents the generalization of Eq. (4.13) to displacement fields of arbitrary wavelengths, in fact $\boldsymbol{Z}(\boldsymbol{0}) = \boldsymbol{Z}_0$, therefore they allow bifurcations of arbitrary wavelength to be detected and not only those occurring at the long-wavelength limit, $\|\boldsymbol{k}\| \to 0$.

For a given $\boldsymbol{k}$, the associated preload state $\boldsymbol{P}$ leading to a bifurcation can be obtained by searching for non-trivial solutions of the incremental equilibrium (4.27). Hence, by introducing the notation $\boldsymbol{K}^*(\boldsymbol{P},\boldsymbol{k}) = \boldsymbol{Z}(\boldsymbol{k})^{\mathsf{H}}\boldsymbol{K}(\boldsymbol{P})\,\boldsymbol{Z}(\boldsymbol{k})$, a bifurcation becomes possible when

$$\det \boldsymbol{K}^*(\boldsymbol{P},\boldsymbol{k}) = 0\,. \tag{4.29}$$

It is worth noting that the matrix $\boldsymbol{K}^*(\boldsymbol{P},\boldsymbol{k})$ is Hermitian, $\boldsymbol{K}^*(\boldsymbol{P},\boldsymbol{k}) = \boldsymbol{K}^*(\boldsymbol{P},\boldsymbol{k})^{\mathsf{H}}$, which implies that the determinant (4.29) is always real. Moreover, the periodicity of $\boldsymbol{Z}(\boldsymbol{k})$ implies that this determinant is periodic in the $\boldsymbol{k}$-space with period $[0,2\pi]\times[0,2\pi]$ in the basis $\{\boldsymbol{b}_1,\boldsymbol{b}_2\}$ reciprocal to $\{\boldsymbol{a}_1,\boldsymbol{a}_2\}$, so that $\boldsymbol{b}_i\cdot\boldsymbol{a}_j = \delta_{ij}$.

In order to construct the *stability domain* of a lattice, the *critical* (in other words first) bifurcation needs to be selected by solving Eq. (4.29) for the smallest preload spanning over all possible wavelengths. Specifically, by introducing the unit vector $\hat{\boldsymbol{P}}$, which singles out a direction in the preload space, the prestress state is defined as $\gamma\hat{\boldsymbol{P}}$ for a radial loading, so that the critical bifurcation corresponds to the value γ_{B} defined as

$$\gamma_{\mathrm{B}} = \inf_{\gamma\geq 0}\left\{\gamma \;\middle|\; \det \boldsymbol{K}^*(\gamma\hat{\boldsymbol{P}},\ \eta_1\boldsymbol{b}_1+\eta_2\boldsymbol{b}_2) = 0\,,\ 0<\eta_1<2\pi\,,\ 0<\eta_2<2\pi\right\}. \tag{4.30}$$

where the periodicity of $\boldsymbol{K}^*(\boldsymbol{P},\boldsymbol{k})$ is used to conveniently restrict to one period the search for the infimum over the $\boldsymbol{k}$-space. It is worth noting that for a vanishing wave vector, Eq. (4.29) is always satisfied regardless of the preload state, because the nullspace of $\boldsymbol{K}^*(\boldsymbol{P},\boldsymbol{0})$ always contains rigid-body translations. These trivial solutions clearly need to be excluded.

Strong ellipticity enforces uniqueness of the incremental problem of a homogeneous and homogeneously deformed material subject to prescribed incremental displacement on the whole boundary [105] and corresponds to the positive definiteness of the acoustic tensor (associated to the incremental constitutive tensor $\mathbb{C}$) defined with reference to every unit vectors $\boldsymbol{n}$ and $\boldsymbol{g}$ as

$$\boldsymbol{A}^{(\mathbb{C})}(\boldsymbol{n})\,\boldsymbol{g} = \mathbb{C}[\boldsymbol{g}\otimes\boldsymbol{n}]\,\boldsymbol{n}\,. \tag{4.31}$$

When the prestress state is null and except in the case of an extreme material, where the stiffness of the rods becomes vanishing small [106], the homogenized material response is strong elliptic, which in turn implies ellipticity.

Failure of ellipticity corresponds to macro (or global) instabilities, where the bifurcation is characterized by a wavelength long when compared to the period of the lattice structure, which models a localization of deformation

in the equivalent continuum. The homogenized material is elliptic (E) as long as the the acoustic tensor $\boldsymbol{A}^{(\mathbb{C})}(\boldsymbol{n})$ is non-singular for every pair of unit vectors $\boldsymbol{n}$ and $\boldsymbol{g}$, namely,

$$\boldsymbol{A}^{(\mathbb{C})}(\boldsymbol{n})\,\boldsymbol{g} \neq \boldsymbol{0}\,. \tag{4.32}$$

When the acoustic tensor becomes singular, a localization of deformation may occur corresponding to a dyad $\boldsymbol{g} \otimes \boldsymbol{n}$. The localization is called 'shear band' in the special case $\boldsymbol{g} \cdot \boldsymbol{n} = 0$, or 'compaction band' or 'splitting mode' when $\boldsymbol{g} \cdot \boldsymbol{n} = \pm 1$.

It is assumed that the elastic lattice under consideration is equivalent, at null prestress, to a strong elliptic elastic solid, characterized by a constitutive tensor which is function of the prestress $\boldsymbol{T}$, in turn through the axial preload $\boldsymbol{P}$ in the elastic rods, equation (4.26), namely, $\boldsymbol{A}^{(\mathbb{C})}(\boldsymbol{P}, \boldsymbol{n})$. Therefore, using again the previously defined unit vector $\hat{\boldsymbol{P}}$ and with reference to an infinite material (or to a material with prescribed displacement on the whole boundary) bifurcations are excluded as long as the response remains strong elliptic, while failure of this condition is simultaneous to failure of ellipticity, which occurs at the value γ_{E} defined as

$$\gamma_{\mathrm{E}} = \min_{\gamma \geq 0} \left\{ \gamma \,\middle|\, \min_{\boldsymbol{n}, \|\boldsymbol{n}\|=1} \left[\det \boldsymbol{A}^{(\mathbb{C})}(\gamma \hat{\boldsymbol{P}}, \boldsymbol{n}) \right] = 0 \right\}. \tag{4.33}$$

Relation between bifurcations in the lattice and in the effective continuum is that failure of ellipticity of the latter corresponds to long-wavelength bifurcations of the former, $\|\boldsymbol{k}\| \to 0$, while *all* bifurcations are scanned through equation (4.30), a circumstance which implies $\gamma_{\mathrm{B}} \leq \gamma_{\mathrm{E}}$. Moreover, whenever $\gamma_{\mathrm{B}} < \gamma_{\mathrm{E}}$ *the bifurcation occurs at microscopic level and is not detectable in the homogenized material, which can still be strong elliptic* [18, 19, 36].

4.5 Incremental constitutive operator, failure of ellipticity and micro-bifurcation for a specific elastic lattice

The geometry of the current, prestressed configuration of a preloaded lattice, selected to apply the previously developed formalism, is sketched in Fig. 4.5 and is composed of a rhombic grid (of side l) of elastic rods, inclined at an angle α, and characterized by the following non-dimensional parameters and $A_2 = A_1 = A$, $\Lambda_1 = l\sqrt{A/B_1}$, $\Lambda_2 = l\sqrt{A/B_2}$, where the subscript 1 and 2 are relative to the horizontal and inclined rods, as depicted in Fig. 4.5b. The direct basis of the periodic structure is denoted by the pair of vectors $\{\boldsymbol{a}_1, \boldsymbol{a}_2\}$ whose representation with respect to the basis $\{\boldsymbol{e}_1, \boldsymbol{e}_2\}$ (see Fig. 4.5a) is

$$\boldsymbol{a}_1 = l\,\boldsymbol{e}_1\,, \qquad \boldsymbol{a}_2 = l\,(\boldsymbol{e}_1 \cos\alpha + \boldsymbol{e}_2 \sin\alpha)\,,$$

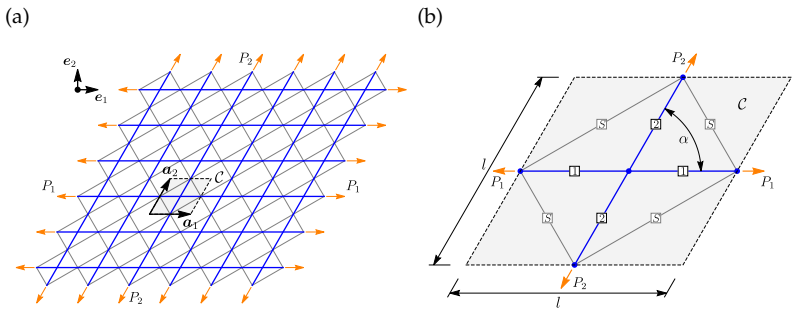

Fig. 4.5. Current configuration of a rhombic lattice of preloaded elastic rods (a), with the associated unit cell C (b). The direct basis of the lattice is denoted by the pair of vectors $\{\boldsymbol{a}_1, \boldsymbol{a}_2\}$ (a). Labels 1, 2, and S denote the horizontal rods, the inclined rods, and the diagonal springs, respectively (b). The spring stiffness, the axial and flexural rigidity of the rods, the preloads P_1 and P_2, as well as the grid angle α can all be varied to investigate different incremental responses.

while the reciprocal basis $\{\boldsymbol{b}_1, \boldsymbol{b}_2\}$ is defined as $\boldsymbol{a}_i \cdot \boldsymbol{b}_j = \delta_{ij}$, so that

$$\boldsymbol{b}_1 = (\boldsymbol{e}_1 - \boldsymbol{e}_2 \cot\alpha)/l\,, \qquad \boldsymbol{b}_2 = \boldsymbol{e}_2 \csc\alpha/l\,,$$

and the wave vector can be written as $\boldsymbol{k} = \eta_1 \boldsymbol{b}_1 + \eta_2 \boldsymbol{b}_2$, with $\eta_{1,2}$ being dimensionless components. The resulting 'skewed' grid is also considered stiffened by a diagonal bracing realized by linear springs[3] connecting the midpoints of the horizontal and inclined rods, as sketched in Fig. 4.5b. The stiffness of the springs is assumed constant $k_S = \kappa A/l$, with κ being a dimensionless measure of stiffness.

In the configuration shown in Fig. 4.5, the lattice is subject to a preload state defined by the axial forces P_1 and P_2, made dimensionless respectively as $p_1 = P_1 l^2/B_1$ and $p_2 = P_2 l^2/B_2$, so that a lattice is defined by the parameter set $\{\alpha, \Lambda_1, \Lambda_2, \kappa, p_1, p_2\}$. Note also that the considered lattice structure includes as a particular case that of a rectangular grid, analyzed in [19].

4.5.1 Incremental constitutive tensor of the equivalent continuum

The homogenization technique outlined in Section 4.3 for prestressed lattices of arbitrary geometry can be directly applied to the grid of elastic rods shown in Fig. 4.5. The incremental constitutive tensor is computed via Eq. (4.23)

[3] These springs can be seen as added after the lattice has been deformed or as deformed together with the lattice. In the former case further assumptions need not be introduced, while in the latter, the effects of the preload on the springs has to be neglected in the interest of simplicity. The diagonal springs are used in this example to show that microscopic instabilities may occur before macroscopic.

and made dimensionless as follows

$$\mathbb{C} = \frac{A}{l}\,\bar{\mathbb{C}}(\underbrace{p_1,\ p_2}_{\text{prestress}},\underbrace{\Lambda_1,\ \phi,\ \kappa,\ \alpha}_{\text{microstructure}})\,, \tag{4.34a}$$

where $\phi = B_2/B_1$ (note that $\Lambda_2 = \Lambda_1/\sqrt{\phi}$), and the non-dimensional tensor-valued function $\bar{\mathbb{C}}(p_1, p_2, \Lambda_1, \phi, \kappa, \alpha)$ can be decomposed as

$$\bar{\mathbb{C}}(p_1, p_2, \Lambda_1, \phi, \kappa, \alpha) = \bar{\mathbb{C}}^{\mathrm{G}}(p_1, p_2, \Lambda_1, \phi, \alpha) + \bar{\mathbb{C}}^{\mathrm{S}}(\kappa, \alpha)\,, \tag{4.34b}$$

with $\bar{\mathbb{C}}^{\mathrm{G}}$ and $\bar{\mathbb{C}}^{\mathrm{S}}$ being, respectively, the contribution of the rod's grid and the diagonal springs. The full expression for the components of $\bar{\mathbb{C}}^{\mathrm{G}}$ and $\bar{\mathbb{C}}^{\mathrm{S}}$ with respect to the basis $\{\boldsymbol{e}_1, \boldsymbol{e}_2\}$ (sketched in Fig. 4.5a) is the following (components that have to be equal by symmetry are not reported)

$$\begin{aligned}
\bar{\mathbb{C}}^{\mathrm{G}}_{1111} &= \frac{1}{2d\sin\alpha}\left(\sinh\left(\frac{\sqrt{p_2}}{2}\right)\left(\sqrt{p_1}p_2\phi\cosh\left(\frac{\sqrt{p_1}}{2}\right)\left(\cos(4\alpha)\left(\Lambda_1^2-p_2\phi\right)+4\Lambda_1^2\cos(2\alpha)+11\Lambda_1^2+p_2\phi\right)\right.\right.\\
&\quad -2\sinh\left(\frac{\sqrt{p_1}}{2}\right)\left(\cos(4\alpha)\left(\Lambda_1^2\left(p_1+p_2\phi\right)-p_2^2\phi^2\right)+\Lambda_1^2\left(p_1+p_2\phi\right)\left(4\cos(2\alpha)+11\right)+p_2^2\phi^2\right)\\
&\quad \left.\left.+p_1\sqrt{p_2}\sinh\left(\frac{\sqrt{p_1}}{2}\right)\cosh\left(\frac{\sqrt{p_2}}{2}\right)\left(\cos(4\alpha)\left(\Lambda_1^2-p_2\phi\right)+4\Lambda_1^2\cos(2\alpha)+11\Lambda_1^2+p_2\phi\right)\right),\\
\bar{\mathbb{C}}^{\mathrm{G}}_{1122} &= \frac{4\sin\alpha\cos^2\alpha}{d}\left(\sinh\left(\frac{\sqrt{p_2}}{2}\right)\left(\sqrt{p_1}p_2\phi\cosh\left(\frac{\sqrt{p_1}}{2}\right)\left(\Lambda_1^2-p_2\phi\right)\right.\right.\\
&\quad \left.\left.-2\sinh\left(\frac{\sqrt{p_1}}{2}\right)\left(\Lambda_1^2\left(p_1+p_2\phi\right)-p_2^2\phi^2\right)\right)+p_1\sqrt{p_2}\sinh\left(\frac{\sqrt{p_1}}{2}\right)\cosh\left(\frac{\sqrt{p_2}}{2}\right)\left(\Lambda_1^2-p_2\phi\right)\right),\\
\bar{\mathbb{C}}^{\mathrm{G}}_{1112} &= \frac{-2\cos\alpha}{d}\left(\sinh\left(\frac{\sqrt{p_2}}{2}\right)\left(2\sinh\left(\frac{\sqrt{p_1}}{2}\right)\left(\cos(2\alpha)\left(\Lambda_1^2\left(p_1+p_2\phi\right)-p_2^2\phi^2\right)+\Lambda_1^2\left(p_1+p_2\phi\right)+p_2^2\phi^2\right)\right.\right.\\
&\quad \left.-\sqrt{p_1}p_2\phi\cosh\left(\frac{\sqrt{p_1}}{2}\right)\left(\cos(2\alpha)\left(\Lambda_1^2-p_2\phi\right)+\Lambda_1^2+p_2\phi\right)\right)\\
&\quad \left.+p_1\sqrt{p_2}\sinh\left(\frac{\sqrt{p_1}}{2}\right)\cosh\left(\frac{\sqrt{p_2}}{2}\right)\left(\cos(2\alpha)\left(p_2\phi-\Lambda_1^2\right)-\Lambda_1^2-p_2\phi\right)\right),\\
\bar{\mathbb{C}}^{\mathrm{G}}_{1121} &= \frac{4\cos\alpha}{d}\left(\sinh\left(\frac{\sqrt{p_2}}{2}\right)\left(2\sinh\left(\frac{\sqrt{p_1}}{2}\right)\left(p_1p_2\phi-\cos^2\alpha\left(\Lambda_1^2\left(p_1+p_2\phi\right)-p_2^2\phi^2\right)\right)\right.\right.\\
&\quad \left.+\sqrt{p_1}p_2\phi\cos^2\alpha\cosh\left(\frac{\sqrt{p_1}}{2}\right)\left(\Lambda_1^2-p_2\phi\right)\right)\\
&\quad \left.+p_1\sqrt{p_2}\cos^2\alpha\sinh\left(\frac{\sqrt{p_1}}{2}\right)\cosh\left(\frac{\sqrt{p_2}}{2}\right)\left(\Lambda_1^2-p_2\phi\right)\right),\\
\bar{\mathbb{C}}^{\mathrm{G}}_{2222} &= \frac{2\sin\alpha}{d}\left(\sinh\left(\frac{\sqrt{p_2}}{2}\right)\left(\sqrt{p_1}p_2\phi\cosh\left(\frac{\sqrt{p_1}}{2}\right)\left(\cos(2\alpha)\left(p_2\phi-\Lambda_1^2\right)+\Lambda_1^2+p_2\phi\right)\right.\right.\\
&\quad \left.-2\sinh\left(\frac{\sqrt{p_1}}{2}\right)\left(-\cos(2\alpha)\left(\Lambda_1^2\left(p_1+p_2\phi\right)-p_2^2\phi^2\right)+\Lambda_1^2\left(p_1+p_2\phi\right)+p_2^2\phi^2\right)\right)\\
&\quad \left.+p_1\sqrt{p_2}\sinh\left(\frac{\sqrt{p_1}}{2}\right)\cosh\left(\frac{\sqrt{p_2}}{2}\right)\left(\cos(2\alpha)\left(p_2\phi-\Lambda_1^2\right)+\Lambda_1^2+p_2\phi\right)\right),
\end{aligned}$$

$$\bar{\mathbb{C}}^{\mathrm{G}}_{2212} = \frac{4\sin^2\alpha\cos\alpha}{d}\left(\sinh\left(\frac{\sqrt{p_2}}{2}\right)\left(\sqrt{p_1}p_2\phi\cosh\left(\frac{\sqrt{p_1}}{2}\right)\left(\Lambda_1^2 - p_2\phi\right)\right.\right.$$
$$\left. - 2\sinh\left(\frac{\sqrt{p_1}}{2}\right)\left(\Lambda_1^2\left(p_1+p_2\phi\right) - p_2^2\phi^2\right)\right) + p_1\sqrt{p_2}\sinh\left(\frac{\sqrt{p_1}}{2}\right)\cosh\left(\frac{\sqrt{p_2}}{2}\right)\left(\Lambda_1^2 - p_2\phi\right)\Big),$$

$$\bar{\mathbb{C}}^{\mathrm{G}}_{2221} = \frac{2\cos\alpha}{d}\left(\sinh\left(\frac{\sqrt{p_2}}{2}\right)\left(\sqrt{p_1}p_2\phi\cosh\left(\frac{\sqrt{p_1}}{2}\right)\left(\cos(2\alpha)\left(p_2\phi - \Lambda_1^2\right) + \Lambda_1^2 + p_2\phi\right)\right.\right.$$
$$- 2\sinh\left(\frac{\sqrt{p_1}}{2}\right)\left(-\cos(2\alpha)\left(\Lambda_1^2\left(p_1+p_2\phi\right) - p_2^2\phi^2\right) + \Lambda_1^2\left(p_1+p_2\phi\right) + p_2\phi\left(2p_1+p_2\phi\right)\right)\Big)$$
$$\left. + p_1\sqrt{p_2}\sinh\left(\frac{\sqrt{p_1}}{2}\right)\cosh\left(\frac{\sqrt{p_2}}{2}\right)\left(\cos(2\alpha)\left(p_2\phi - \Lambda_1^2\right) + \Lambda_1^2 + p_2\phi\right)\right),$$

$$\bar{\mathbb{C}}^{\mathrm{G}}_{1212}$$
$$= \frac{-2\sin\alpha}{d}\left(\sinh\left(\frac{\sqrt{p_2}}{2}\right)\left(2\sinh\left(\frac{\sqrt{p_1}}{2}\right)\left(\cos(2\alpha)\left(\Lambda_1^2\left(p_1+p_2\phi\right) - p_2^2\phi^2\right) + \Lambda_1^2\left(p_1+p_2\phi\right) + p_2^2\phi^2\right)\right.\right.$$
$$\left. - \sqrt{p_1}p_2\phi\cosh\left(\frac{\sqrt{p_1}}{2}\right)\left(\cos(2\alpha)\left(\Lambda_1^2 - p_2\phi\right) + \Lambda_1^2 + p_2\phi\right)\right)$$
$$\left. + p_1\sqrt{p_2}\sinh\left(\frac{\sqrt{p_1}}{2}\right)\cosh\left(\frac{\sqrt{p_2}}{2}\right)\left(\cos(2\alpha)\left(p_2\phi - \Lambda_1^2\right) - \Lambda_1^2 - p_2\phi\right)\right),$$

$$\bar{\mathbb{C}}^{\mathrm{G}}_{1221} = \frac{-4\sin\alpha}{d}\left(\sinh\left(\frac{\sqrt{p_2}}{2}\right)\left(2\sinh\left(\frac{\sqrt{p_1}}{2}\right)\left(\cos^2\alpha\left(\Lambda_1^2\left(p_1+p_2\phi\right) - p_2^2\phi^2\right) - p_1p_2\phi\right)\right.\right.$$
$$\left. + \sqrt{p_1}p_2\phi\cos^2\alpha\cosh\left(\frac{\sqrt{p_1}}{2}\right)\left(p_2\phi - \Lambda_1^2\right)\right)$$
$$\left. + p_1\sqrt{p_2}\cos^2\alpha\sinh\left(\frac{\sqrt{p_1}}{2}\right)\cosh\left(\frac{\sqrt{p_2}}{2}\right)\left(p_2\phi - \Lambda_1^2\right)\right),$$

$$\bar{\mathbb{C}}^{\mathrm{G}}_{2121} = \frac{p_1\sqrt{p_2}}{d}\sinh\left(\frac{\sqrt{p_1}}{2}\right)\cosh\left(\frac{\sqrt{p_2}}{2}\right)\left(\sin\alpha\left(\Lambda_1^2 - 5p_2\phi\right) + \sin(3\alpha)\left(\Lambda_1^2 - p_2\phi\right)\right.$$
$$\left. + 4\csc(\alpha)\left(p_1+p_2\phi\right)\right)$$
$$- 2\sin\alpha\sinh\left(\frac{\sqrt{p_2}}{2}\right)\left(2\sinh\left(\frac{\sqrt{p_1}}{2}\right)\left(\cos(2\alpha)\left(\Lambda_1^2\left(p_1+p_2\phi\right) - p_2^2\phi^2\right)\right.\right.$$
$$\left. + 2\csc^2(\alpha)\left(p_1+p_2\phi\right)^2 + \Lambda_1^2\left(p_1+p_2\phi\right) - p_2\phi\left(4p_1+3p_2\phi\right)\right)$$
$$\left. - \sqrt{p_1}p_2\phi\cosh\left(\frac{\sqrt{p_1}}{2}\right)\left(\cos(2\alpha)\left(\Lambda_1^2 - p_2\phi\right) + 2\csc^2(\alpha)\left(p_1+p_2\phi\right) + \left(\Lambda_1^2 - 3p_2\phi\right)\right)\right),$$

where

$$d = e^{-\frac{1}{2}\left(\sqrt{p_1}+\sqrt{p_2}\right)}\Lambda_1^2\left(\left(e^{\sqrt{p_1}}\left(\sqrt{p_1}-2\right)+\sqrt{p_1}+2\right)\left(e^{\sqrt{p_2}}-1\right)p_2\phi - 2\left(e^{\sqrt{p_1}}-1\right)p_1\left(e^{\sqrt{p_2}}-1\right)\right.$$
$$\left. + \left(e^{\sqrt{p_1}}-1\right)p_1\left(e^{\sqrt{p_2}}+1\right)\sqrt{p_2}\right).$$

The constitutive tensor ruling the effect of diagonal springs can be written as

$$\bar{\mathbb{C}}^{\mathrm{S}}_{1111} = \kappa\frac{5+3\cos(2\alpha)}{4\sin\alpha},$$
$$\bar{\mathbb{C}}^{\mathrm{S}}_{1112} = \bar{\mathbb{C}}^{\mathrm{S}}_{1121} = \bar{\mathbb{C}}^{\mathrm{S}}_{1211} = \bar{\mathbb{C}}^{\mathrm{S}}_{1121} = \bar{\mathbb{C}}^{\mathrm{S}}_{2111} = \kappa\cos\alpha,$$
$$\bar{\mathbb{C}}^{\mathrm{S}}_{1122} = \bar{\mathbb{C}}^{\mathrm{S}}_{2211} = \bar{\mathbb{C}}^{\mathrm{S}}_{1212} = \bar{\mathbb{C}}^{\mathrm{S}}_{1221} = \bar{\mathbb{C}}^{\mathrm{S}}_{2112} = \bar{\mathbb{C}}^{\mathrm{S}}_{2121} = \bar{\mathbb{C}}^{\mathrm{S}}_{2222} = \frac{1}{2}\kappa\sin\alpha,$$
$$\bar{\mathbb{C}}^{\mathrm{S}}_{1222} = \bar{\mathbb{C}}^{\mathrm{S}}_{2122} = \bar{\mathbb{C}}^{\mathrm{S}}_{2212} = \bar{\mathbb{C}}^{\mathrm{S}}_{2221} = 0.$$

4.5.2 Prestress tensor of the equivalent continuum

The prestress tensor $\boldsymbol{T}$, equivalent in the continuum to the preload forces $\boldsymbol{P}$ in the elastic lattice, can be either calculated using equation (4.26) or, directly, by computing the average normal and tangential tractions along the faces with unit normal $\boldsymbol{e}_1$ and $\boldsymbol{e}_2$. With reference to Fig. 4.5b the following expression is obtained

$$\boldsymbol{T} = \left(\frac{P_1}{l\sin\alpha} + \frac{P_2\cos^2\alpha}{l\sin\alpha}\right)\boldsymbol{e}_1\otimes\boldsymbol{e}_1 + \\ + \frac{P_2\cos\alpha}{l}(\boldsymbol{e}_1\otimes\boldsymbol{e}_2 + \boldsymbol{e}_2\otimes\boldsymbol{e}_1) + \frac{P_2\sin\alpha}{l}\boldsymbol{e}_2\otimes\boldsymbol{e}_2\,. \quad (4.35)$$

4.5.3 Loss of ellipticity vs micro-bifurcation

With reference to the lattice sketched in Fig. 4.5b, the value of the prestress state, which is critical for bifurcation of the grid is determined by employing conditions (4.33) and (4.30), and computing numerically the prestress multipliers γ_{E} and γ_{B}. Results are presented as *uniqueness domains* in the non-dimensional prestress space $\{p_1, p_2\}$ by fixing the set of geometrical and mechanical parameters $\{\alpha, \Lambda_1, \Lambda_2, \kappa\}$. The boundary of the stability domain identifies the 'critical', namely, the first bifurcation of the incremental equilibrium of the lattice.

The dependence on α, Λ_1, Λ_2, κ has been analyzed by considering two grid configurations that will be referred to as the *orthotropic grid*, with equal slenderness $\Lambda_1 = \Lambda_2 = 10$, and the *anisotropic grid*, characterized by different slenderness values, $\Lambda_1 = 7$ and $\Lambda_2 = 15$. For each lattice, the influence of the rods' inclination is explored by setting $\alpha = \pi/2, \pi/3, \pi/4, \pi/6$, while the stiffness of the springs is investigated in the range $\kappa \in [0, 1]$. In this way, the influence of the diagonal bracing on the critical bifurcation mode is analyzed.

To investigate both macroscopic (infinite wavelength) and microscopic (finite wavelength) bifurcations, results for the orthotropic grid with $\alpha = \pi/2$ are reported in Fig. 4.6, where critical bifurcation loads p_1 and p_2 are reported for the cases in which diagonal springs are absent ($\kappa = 0$, Fig. 4.6a, b, c) and for a spring stiffness $\kappa = 0.2$ (Fig. 4.6d, e, f).

The uniqueness domains (Fig. 4.6a and 4.6d) have been computed by solving equation (4.30) for radial loading paths in the non-dimensional load space $\{p_1, p_2\}$. To clarify the results of this computation, two critical boundaries are reported, one with a continuous line and the other with a continuous-dotted line, referring to bifurcations of long (infinite) and 'shortest possible' wavelength, respectively. The former occurs when the infimum of (4.30) is attained at $\boldsymbol{k} = \boldsymbol{0}$, while the latter refers to the infimum computed on the boundary of the reciprocal unit cell, $\eta_{1,2} = \pm\pi$[4]. The location of the infimum can be visualized, by fixing the loading direction as

[4]Note that all the possible wavelengths have been considered in the computation of the stability domain (as expressed by Eq. (4.30)), but in Fig. 4.6a and 4.6d the critical wave vectors

$\boldsymbol{p} = \gamma\,\hat{\boldsymbol{p}}$, and then by numerically computing the bifurcation surface defined as $\det \boldsymbol{K}^*(\gamma\hat{\boldsymbol{p}},\ \eta_1\boldsymbol{b}_1 + \eta_2\boldsymbol{b}_2) = 0$ in the space $\{\eta_1, \eta_2, \gamma\}$. Two radial paths are considered in Fig. 4.6a and 4.6d, namely, equibiaxial $\hat{\boldsymbol{p}} = \{-1/\sqrt{2}, -1/\sqrt{2}\}$ and uniaxial $\hat{\boldsymbol{p}} = \{-1, 0\}$ compression (red dashed lines), and the corresponding bifurcation surfaces are reported in Fig. 4.6b, c and Fig. 4.6e, f, respectively.

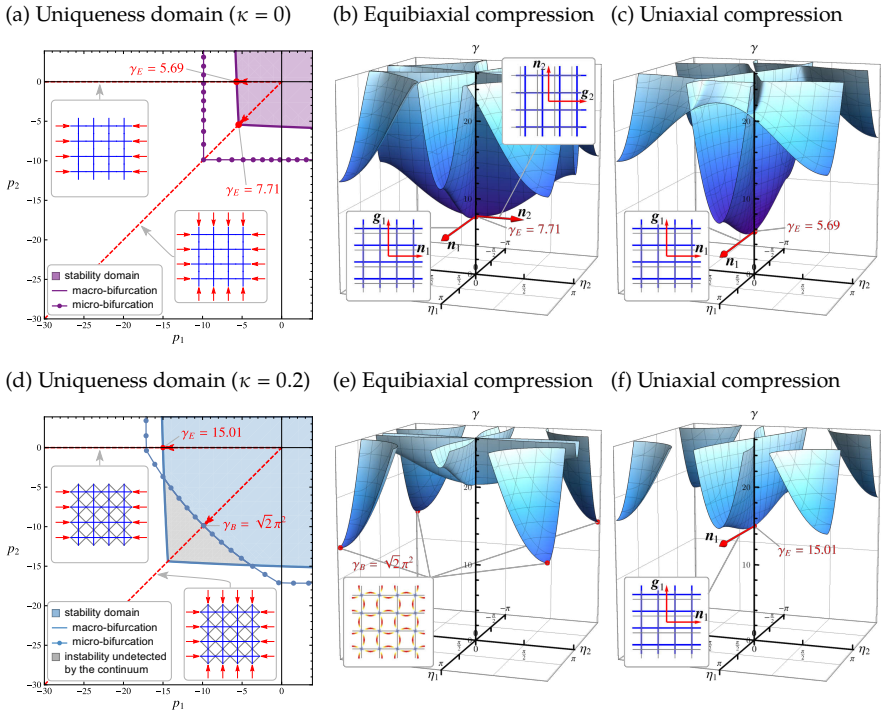

Fig. 4.6. (a) and (d): Uniqueness/stability domains in the loading space $\{p_1, p_2\}$ for a square grid (with equal slenderness of the rods $\Lambda_1 = \Lambda_2 = 10$), when diagonal springs are absent (upper part) and present (with spring stiffness $\kappa = 0.2$, lower part). A continuous (a dotted) contour represents the occurrence of macro (of micro) bifurcations, so that the shaded regions correspond to strong ellipticity and uniqueness for the equivalent continuum. In the absence of diagonal springs, macro-instabilities, corresponding to ellipticity loss, prevail and always occur before micro bifurcations, while when the diagonal springs are considered, the situation is more complex so that one or the other instability may be critical. (b, c) and (e, f): with reference to two specific radial loading paths of equibiaxial and uniaxial compression, shown as red dashed lines in (a) and (d), the bifurcation surfaces evidence the solutions for failure of ellipticity in terms of critical dyads $\boldsymbol{n} \otimes \boldsymbol{g}$.

In the absence of diagonal springs, Fig. 4.6a reports the uniqueness domain, corresponding to strong ellipticity in the solid equivalent to the lattice, showing that (for every loading direction $\hat{\boldsymbol{p}}$) a macro-bifurcation, in other words an ellipticity loss (referred to the dyad $\boldsymbol{n} \otimes \boldsymbol{g}$), is always reached

$\boldsymbol{k}$ have been found to either be at the origin ($\boldsymbol{k} = \boldsymbol{0}$) or on the boundary of the reciprocal unit cell (shortest wavelengths).

before micro-bifurcation. The latter represents a structural instability for the lattice that cannot be detected in the equivalent continuum.

For the two radial loading paths shown in Fig. 4.6a, the bifurcation surfaces Figs. 4.6b,c, show that the minimum values of the load multiplier γ are attained at $\{\eta_1, \eta_2\} = \{0, 0\}$, which corresponds to a macro-bifurcation for the lattice (associated to an infinite wavelength mode), so that the critical prestress multipliers $\gamma_E = 7.71$ and $\gamma_E = 5.69$ lie on the border of ellipticity loss. The two bifurcations correspond respectively to two orthogonal modes and a single mode.

The presence of diagonal springs complicates the situation as reported in Fig. 4.6d. In this case the uniqueness/stability domains show that micro-bifurcations may sometimes occur within the region of strong ellipticity, which is for instance the case of equibiaxial compression (radial path inclined at 45°) and not the case of uniaxial compression (horizontal radial path). In fact, when the diagonal springs are present, for equibiaxial compression a critical micro-bifurcation occurs, so that Fig. 4.6e shows that the minimum value of the load multiplier, $\gamma_B = \sqrt{2}\pi^2$, is attained at four points, $\{\eta_1, \eta_2\} = \{\pm\pi, \pm\pi\}$, all associated to a bifurcation mode with a finite wavelength, as shown in the inset. For uniaxial compression, Fig. 4.6f, a macro-bifurcation of the grid, in other words a loss of ellipticity, occurs at $\gamma_E = 15.01$ and the tangent to the bifurcation surface at the origin singles out the infinite-wavelength bifurcation mode (shown in the inset and appearing as a rigid translation).

Further results on uniqueness domains for the orthotropic and the anisotropic grid are reported in Figs. 4.7 and 4.8, respectively. The strong ellipticity boundary (corresponding to macro-bifurcation) in the equivalent solid is denoted with a continuous line, while the circular markers identify the boundary of the uniqueness/stability region for micro bifurcations, which remain undetected in the equivalent solid. Moreover, critical bifurcation modes have been reported in insets of Figs. 4.7 and 4.8, which refer to some specific points on the stability boundary (labelled as B_1, B_2, B_3 in the former figure and B_4, B_5, B_6, B_7, B_8 in the latter). The critical loads and the critical wave vectors for each bifurcation mode are reported in Table 4.1.

From Figs. 4.7 and 4.8 the following features can be highlighted.

- For the orthotropic grid the strong ellipticity boundary is symmetric with respect to the bisector defined by the condition $p_1 = p_2$, which is the principal direction of orthotropy for the grid when $\Lambda_1 = \Lambda_2$ (a symmetry which is broken for the anisotropic grid);

- For every value of the grid angle α, the effect of the diagonal springs essentially consists in an enlargement of the strong ellipticity region (see the arrow in Fig. 4.8 denoting increasing values of stiffness κ);

- The stiffening induced by increasing the spring stiffness κ is much more effective for nearly orthogonal grids ($\alpha \approx \pi/2$) than for small values of inclination α (compare Fig. 4.7a to Fig. 4.7d and Fig. 4.8a to Fig. 4.8d);

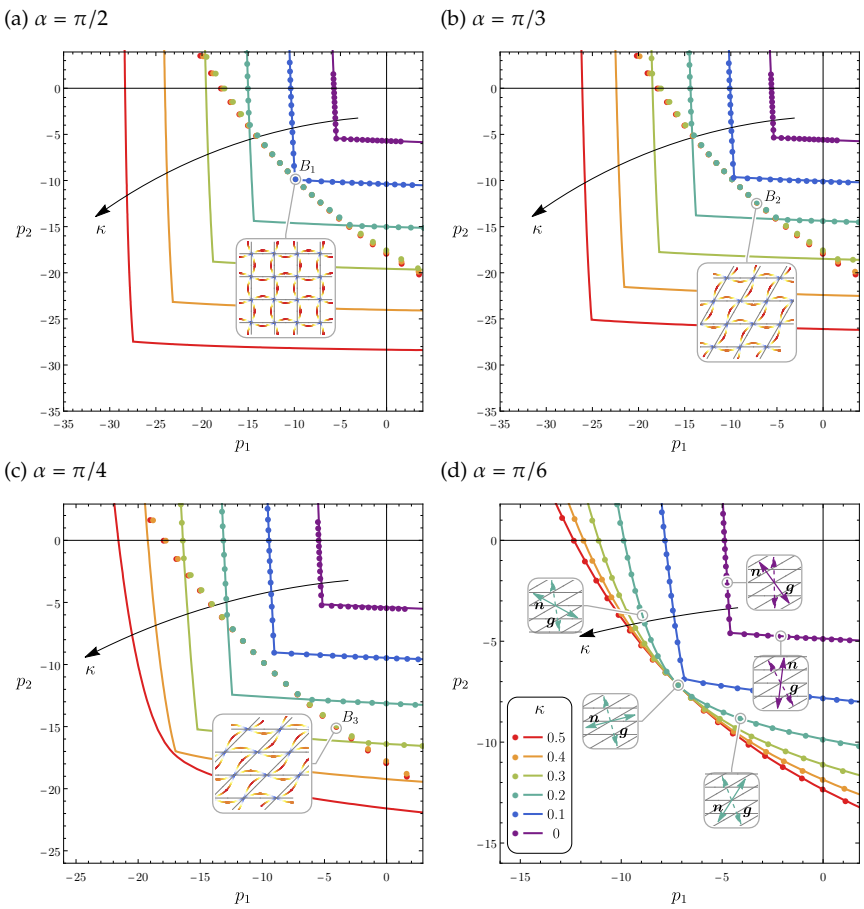

Fig. 4.7. Strong ellipticity domains (corresponding to macro-bifurcations, continuous lines) and uniqueness domains for micro-bifurcation (circular markers) for an orthotropic lattice of prestressed elastic rods with $\Lambda_1 = \Lambda_2 = 10$, at different rod angles α and stiffness κ of the diagonal springs. Points B_1, B_2, B_3 on the stability boundaries have been selected for the computation of the associated critical bifurcation mode (shown in the insets). Table 4.1 collects the critical loads and the critical wave vectors for each bifurcation mode. At small grid angles, for instance the reported value of $\alpha = \pi/6$, failure of ellipticity coincides with micro-bifurcation in the lattice, so that the bifurcation mode is always characterized by an infinite wavelength. For these grid configurations, the direction of ellipticity loss exhibits a *'super-sensitivity'* with respect to the load directionality, shown in the insets of part (d), reporting the critical dyads $\boldsymbol{n} \otimes \boldsymbol{g}$ for failure of ellipticity.

- For every value of the spring stiffness κ, the deviation from orthogonality of the grid always reduces the size of the strong ellipticity region, so that the largest strong ellipticity region is attained for $\alpha = \pi/2$.

From the mathematical point of view, the $\{p_1, p_2\}$-space can be classified by evaluating the roots associated to the symbol of the equilibrium operator $\mathrm{div}\,\mathbb{C}[\mathrm{grad}(\bullet)]$, so that the elliptic, parabolic, and hyperbolic regimes can be determined. Results of this classification are reported in Appendix B, where

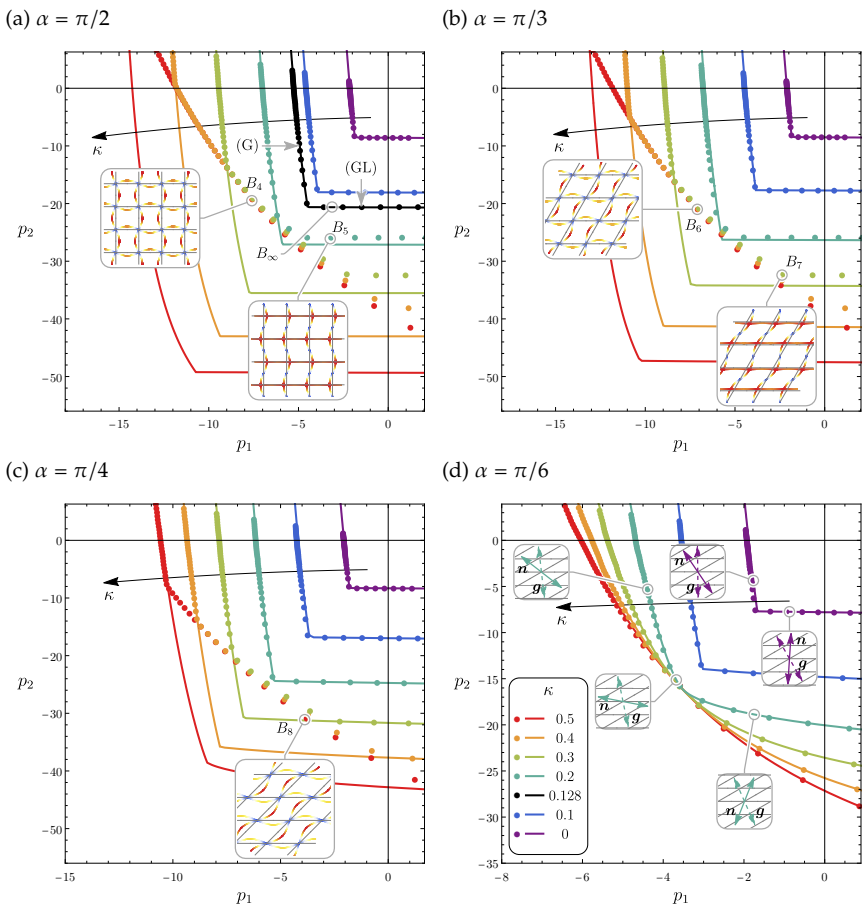

Fig. 4.8. As for Fig. 4.7, except that $\Lambda_1 = 7$, $\Lambda_2 = 15$ and that the points on the stability boundary for which the critical bifurcation modes have been computed are labeled B_4, B_5, B_6, B_7, B_8. Note also that, the typical microscopic bifurcation modes of the anisotropic grid exhibit widely different deformations dictated by the prestress direction (see insets in parts a, b, c corresponding to points labeled B_4, B_5, B_6, B_7, B_8 and compare for instance mode B_4 to B_5 or B_6 to B_7).

a few grid configurations have been considered.

The stability boundaries (circular markers in Fig. 4.7 and 4.8), evidence the following characteristics.

- At small values of spring stiffness κ, the first bifurcation is always global, so that *the strong ellipticity and the stability boundaries coincide independently of the prestress direction*; a feature visible for $\kappa = 0, 0.1$ (purple and blue) in Fig. 4.7a and Fig. 4.8a);

- An increase in the spring stiffness κ leads to a first bifurcation of local type (the critical mode is characterized by a finite wavelength), *so that the stability region lies inside the elliptic boundary;*

Label	Λ_1	Λ_2	α	κ	p_1	p_2	$\boldsymbol{k}_{\text{cr}}$
B_1	10	10	$\pi/2$	0.2	$-\pi^2$	$-\pi^2$	$\pi\boldsymbol{b}_1 + \pi\boldsymbol{b}_2$
B_2	10	10	$\pi/3$	0.3	−7.16	−12.40	$\pi\boldsymbol{b}_1 + \pi\boldsymbol{b}_2$
B_3	10	10	$\pi/4$	0.7	−4.05	−15.13	$\pi\boldsymbol{b}_1 + \pi\boldsymbol{b}_2$
B_4	7	15	$\pi/2$	0.4	−7.72	−18.64	$\pi\boldsymbol{b}_1 + \pi\boldsymbol{b}_2$
B_5	7	15	$\pi/2$	0.2	−3.41	−25.91	$\pi\boldsymbol{b}_2$
B_6	7	15	$\pi/3$	0.3	−6.98	−20.93	$\pi\boldsymbol{b}_1 + \pi\boldsymbol{b}_2$
B_7	7	15	$\pi/3$	0.3	−2.12	−32.40	$\pi\boldsymbol{b}_2$
B_8	7	15	$\pi/4$	0.5	−4.00	−30.37	$\pi\boldsymbol{b}_1 + \pi\boldsymbol{b}_2$
B_∞	7	15	$\pi/2$	0.128	−3.44	−20.62	$\eta_2\boldsymbol{b}_2\ \forall\eta_2$

Table 4.1. Critical bifurcation modes $\boldsymbol{k}_{\text{cr}}$ for several configurations of the orthotropic ($\Lambda_1 = \Lambda_2 = 10$) and anisotropic ($\Lambda_1 = 7$, $\Lambda_2 = 15$) lattice. Plots of the corresponding deformation fields are reported as insets in Figs. 4.7 and 4.8.

- Fig. 4.7d and Fig. 4.8d show that, at sufficiently small values of grid angle (for instance at $\alpha = \pi/6$), *failure of strong ellipticity dictates the first bifurcation independently of the stiffness of the diagonal springs* (see circular markers of the stability boundary overlapping with the elliptic boundary);

- The typical *microscopic bifurcation modes of the orthotropic grid are characterized by a pure rotational deformation of the junctions of the grid* (see insets in Fig. 4.7a, b, c corresponding to the points labeled as B_1, B_2, B_3);

- Typical *microscopic bifurcation modes of the anisotropic grid exhibit widely different deformations dictated by the prestress direction* (see insets in Fig. 4.8a, b, c corresponding to points labeled B_4, B_5, B_6, B_7, B_8 and compare for instance mode B_4 to B_5 or B_6 to B_7).

- A bifurcation always occurs for every lattice geometry at an equibiaxial load $\{p_1, p_2\} = \{-\pi^2, -\pi^2\}$ (point B_1 in Fig. 4.7a) regardless of the values of Λ_1, Λ_2, κ, and α. This bifurcation can be explained by the fact that the normalized load $Pl^2/B = -\pi^2$ corresponds to the buckling load of a simply supported Euler-Bernoulli beam, and thus, when all the rods of an arbitrary grid are prestressed at this level, a purely flexural buckling mode becomes available (shown in the inset of Fig. 4.7a).

Despite the complex influence of the geometrical and mechanical parameters on the stability of the prestressed lattice, two important 'transitions' characterize the nature of the first bifurcation, namely:

(i) a *macro-to-micro* transition of the critical bifurcation mode occurs at increasing stiffness of the diagonal springs κ;

(ii) a *micro-to-macro* transition of the critical bifurcation mode occurs at decreasing the rod's inclination α.

The above transitions will be exploited in Section 4.6 to investigate the static response induced by a concentrated force applied to a lattice preloaded closely to a bifurcation (both global and local bifurcations will be considered).

4.5.4 A single localization band with a highly tunable inclination

A remarkable characteristic is associated to the micro-to-macro bifurcation transition obtained at decreasing angle α, namely, a *super-sensitivity of the localization band normal, represented by the unit vector* $\boldsymbol{n}$*, with respect to the state of pre-load, while the localization mode* $\boldsymbol{g}$ *results only weakly affected*.

For instance, at $\alpha = \pi/6$ and sufficiently high spring stiffness κ, the insets in Figs. 4.7d and 4.8d show that the relative inclinations between the localization band normal $\boldsymbol{n}$ and the localization mode $\boldsymbol{g}$ strongly vary as a function of the load state in the lattice.

When the spring stiffness vanishes, $\kappa = 0$, the localization band is essentially set by the grid inclination as it is almost perfectly aligned parallel to the inclinations 0 and $\pi/6$, so that failure of ellipticity occurs in a direction $\boldsymbol{n}$ that is almost orthogonal to the rods. On the contrary, at $\kappa = 0.2$ a single localization band occurs, whose inclination strongly depends on the load directionality and is essentially unrelated to the underlying grid pattern (shown in the insets corresponding to $\kappa = 0.2$ in Figs. 4.7d and 4.8d). *The super-sensitivity of the localization direction provides an enhanced tunability of the macroscopic localization pattern by means of a simple modification of the load applied to the lattice*.

It is worth noting that the localization direction can also be designed by constructing a lattice with a suitable value of rods' angle α, but this approach would not be easily reconfigurable, as the structure geometry has to be defined in advance.

4.5.5 Infinite set of bifurcation wavelengths in a lattice: perfect equivalence with the continuum

Loss of ellipticity in a solid occurs at modes of all (namely, infinite,) wavelengths, while the corresponding condition in the lattice *usually* is that bifurcation occurs only in a mode involving an infinite wavelength. In this sense the equivalent continuous body has a response differing from the lattice, a circumstance which may be expected as a consequence of the homogenization procedure, which is applied to a discrete lattice.

Surprisingly, it is shown in the following that special conditions can be found in which the lattice bifurcates similarly to the equivalent continuum, by displaying infinite modes, covering every wavelength. In this case a *perfect equivalence between the bifurcation in the lattice structure and failure of ellipticity in the effective continuum occurs*.

For a square grid (with $\alpha = \pi/2$, $\Lambda_1 = 7$, and $\Lambda_2 = 15$), the perfect equivalence was obtained at a fixed value of load by varying the stiffness of

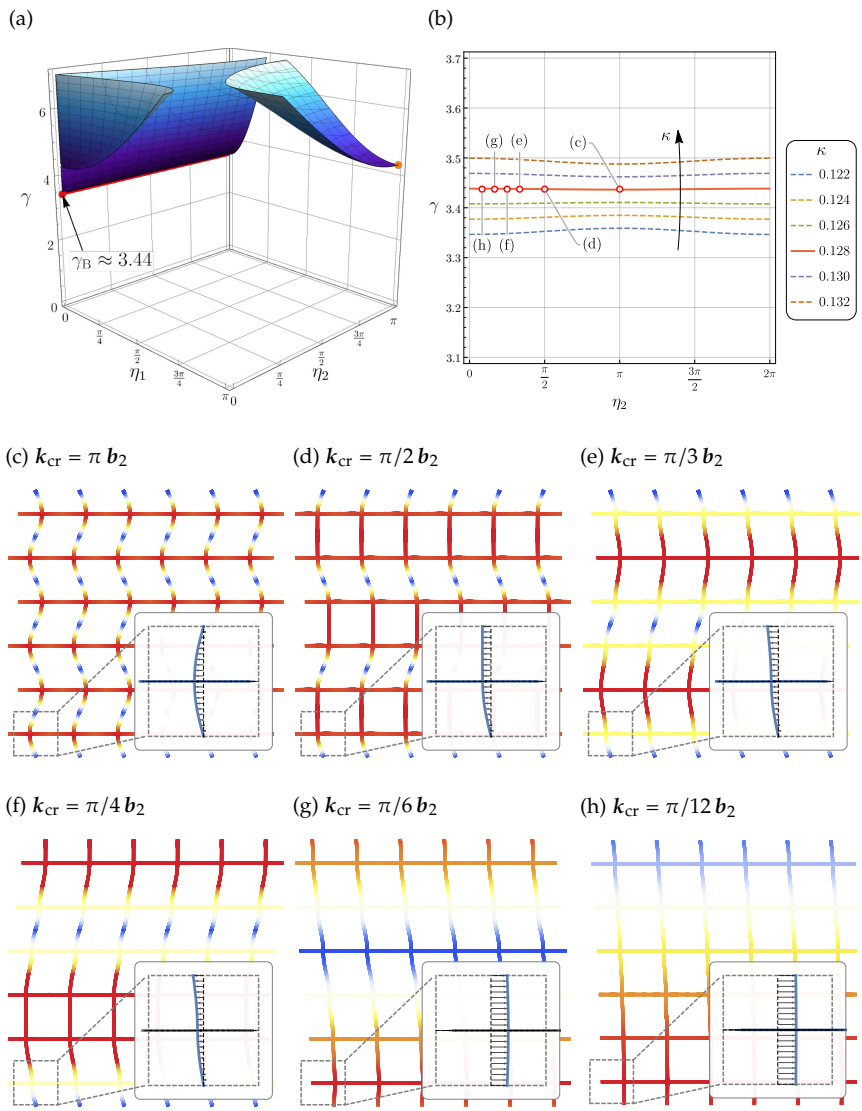

Fig. 4.9. Conditions showing a perfect equivalence between the lattice and the corresponding continuum, so that when the latter looses ellipticity, the former exhibits bifurcation occurring with infinite modes covering all wavelengths, a situation which is revealed by the flat line (highlighted in red) in the bifurcation diagram (part a). The perfect equivalence is obtained through accurate tuning of the stiffness of the diagonal springs ($\kappa \approx 0.128$ for a square grid with $\Lambda_1 = 7$ and $\Lambda_2 = 15$ and a loading $\{p_1, p_2\} \approx 3.44\{-1, -6\}$). Part (b) represents a section of the bifurcation surface at $\eta_1 = 0$ detailing the flat minimum of the curve occurring at $\kappa \approx 0.128$. Parts (c)–(h) present selected bifurcation modes documenting a transition at increasing wavelength of the bifurcation modes from a local bifurcation (c) to a shear-band-type instability (h).

the diagonal springs κ, thus obtaining $\kappa \approx 0.128$. This value was calculated by numerically solving equation (4.30) between $\kappa = 0.1$ and $\kappa = 0.2$, because

these two values pinpoint the threshold of separation between macro and micro bifurcation. For these values of the lattice parameters and loads the bifurcation mode is unique and involves only the infinite wavelength (macro bifurcation) along the curved boundary denoted as (G) in Fig. 4.8a, while on the boundary denoted as (GL) in the same figure *an infinite number of bifurcation modes of arbitrary wavelength is present for every critical loading state*, as detailed for the point B_∞ in Fig. 4.9.

Fig. 4.9a reports the three-dimensional plot in the space $\{\eta_1, \eta_2, \gamma\}$ satisfying the bifurcation condition [of vanishing of the determinant in Eq. (4.30)] where γ is the loading multiplier for $\{p_1, p_2\} = \gamma\{-1, -6\}$, so that the critical value γ_B leading to bifurcation is highlighted as a red line marking the minimum of the bifurcation surface. A section of this surface at $\eta_1 = 0$ is reported in Fig. 4.9b to show the dependence of the critical multiplier on the stiffness κ, so that for $\kappa < 0.128$ the critical wave vector is $\boldsymbol{k}_{cr} = 0$ (macro instability), while for $\kappa > 0.128$ the critical wave vector is $\boldsymbol{k}_{cr} = \pi\, \boldsymbol{b}_2$ (micro instability), and for $\kappa = 0.128$ every wave vector of the form $\boldsymbol{k}_{cr} = \eta_2\, \boldsymbol{b}_2$ (with arbitrary η_2) identifies a different bifurcation mode occurring at the same load multiplier $\gamma_B \approx 3.44$. Within this infinite set of bifurcation modes, a few bifurcation modes (see the labelled points on the red contour of Fig. 4.9b) are reported in order to show the transition of the bifurcation mode from a local bifurcation (Fig. 4.9c) to a global shear-band type instability (Fig. 4.9h).

4.6 Macroscopic and microscopic localizations via perturbative approach

The correlation between the incremental response of the lattice and of the equivalent solid is now investigated close to the conditions of instability using the 'perturbative approach' introduced in [89]. Following this approach, the response of the lattice to an applied static concentrated load (in terms of a force or a force dipole) is numerically evaluated via finite elements (using the commercial code COMSOL Multiphysics®) and compared to the response of the equivalent solid by computing the Green's function associated to the operator div $\mathbb{C}$[grad(•)].

The two-dimensional Green's tensor $\mathcal{G}$ needed to perturb the equivalent material and corresponding to a Dirac delta function centred at $\boldsymbol{x} = \boldsymbol{0}$ is [99]

$$\mathcal{G}(\hat{\boldsymbol{x}}) = -\frac{1}{4\pi^2} \oint_{|\boldsymbol{n}|=1} \left(\boldsymbol{A}^{(\mathbb{C})}(\boldsymbol{n})\right)^{-1} \log|\hat{\boldsymbol{x}} \cdot \boldsymbol{n}|\,, \tag{4.36}$$

where the position vector $\boldsymbol{x}$ has been made dimensionless through division by the rod's length l, so that $\hat{\boldsymbol{x}} = \boldsymbol{x}/l$. Note that $\mathcal{G} = \mathcal{G}^\intercal$ due to the symmetry of the acoustic tensor.

Numerical simulations are performed to analyze the lattice by considering a finite square computational domain of width $350l$, where l is discretized in 10 finite elements with cubic shape functions. The selected mesh has been defined by performing a number of simulations with three different

mesh refinements, namely 5, 10, and 20 elements for l, and then adopting 10 elements, as 20 provided no significant improvement, but substantial computational burden. As the numerical simulations are meant to be compared to the infinite-body Green's function, the size of the domain has been calibrated in order to minimize boundary disturbances with clamped conditions at the four edges of the square domain. The governing equation for the prestressed Euler-Bernoulli rod, Eq. (4.2b), used in the finite element scheme has been implemented by modifying the bending moment contribution with an additional geometric term representing the load multiplied by the transverse displacement of the rod.

The investigation presented below will reveal that:

(i) The localization of deformation connected to macro bifurcation in the lattice and to failure of ellipticity in the equivalent solid are strictly similar;

(ii) The lattice response close to a micro bifurcation evidences a *'microscopic' type of localization*, which remains completely undetected in the homogenized material.

These two different mechanical behaviours are analyzed by exploiting the macro-to-micro transition of the first bifurcation mode, which is controlled by the increase in the stiffness of the diagonal springs of the lattice considered in Section 4.5. The grid is subject now to an equibiaxial compression loading. Hence, in Section 4.6.1 the lattice is considered in the absence of diagonal springs ($\kappa = 0$), while in Section 4.6.2 the lattice is reinforced with a springs' stiffness $\kappa = 0.4$.

4.6.1 Macroscopic bifurcations on the verge of ellipticity loss

The lattice configurations selected for the following analysis are reported in Table 4.2, together with the values of the preload $\boldsymbol{p}_{\mathrm{E}}$ corresponding to loss of ellipticity in the equivalent continuum (obtained by numerically solving equation (4.33) assuming a radial path $\boldsymbol{p} = \{p_1, p_1\}$) or, in other words, to a macro bifurcation in the lattice. As explained in the previous section, the stiffness of the diagonal springs is set to zero in order to ensure that a macroscopic bifurcation is critical. The table reports also the inclination θ_{cr} of the normal $\boldsymbol{n}$ to the localization band, defined as $\boldsymbol{n}_{\mathrm{E}} = \boldsymbol{e}_1 \cos\theta_{\mathrm{cr}} + \boldsymbol{e}_2 \sin\theta_{\mathrm{cr}}$.

A comparison is presented between the response of the lattice loaded with a concentrated force dipole and a dipole Green's function of the effective solid, in terms of maps of incremental displacements. The results are presented as contour plots in Figs. 4.10–4.13, where the color scale has been conveniently normalized according to the norm of the computed displacement field. In the upper part of the figures, results pertaining to the discrete lattice structure are presented, while, in the lower part, results are relative to the equivalent continuum, obtained via homogenization. The figures from

Geometry	*Rods slenderness*	*Symmetry*	$\boldsymbol{p}_{\mathrm{E}}$	θ_{cr}
Square	$\Lambda_1 = \Lambda_2 = 10$	Cubic	$-5.434\,\{1,1\}$	$0°, 90°$
$(\alpha = \pi/2)$	$\Lambda_1 = 7,\ \Lambda_2 = 15$	Orthotropic	$-2.071\,\{1,1\}$	$0°$
Rhombus	$\Lambda_1 = \Lambda_2 = 10$	Orthotropic	$-5.345\,\{1,1\}$	$88.2°, 151.8°$
$(\alpha = \pi/3)$	$\Lambda_1 = 7,\ \Lambda_2 = 15$	Anisotropic	$-2.043\,\{1,1\}$	$151.4°$

Table 4.2. Equibiaxial compression loads $\boldsymbol{p}_{\mathrm{E}}$ and inclinations θ_{cr} of $\boldsymbol{n}_{\mathrm{E}}$ corresponding to failure of ellipticity in the equivalent material, corresponding to a macro-bifurcation in the lattice, for different grid configurations (see Fig. 4.5), in the absence of diagonal springs ($\kappa = 0$).

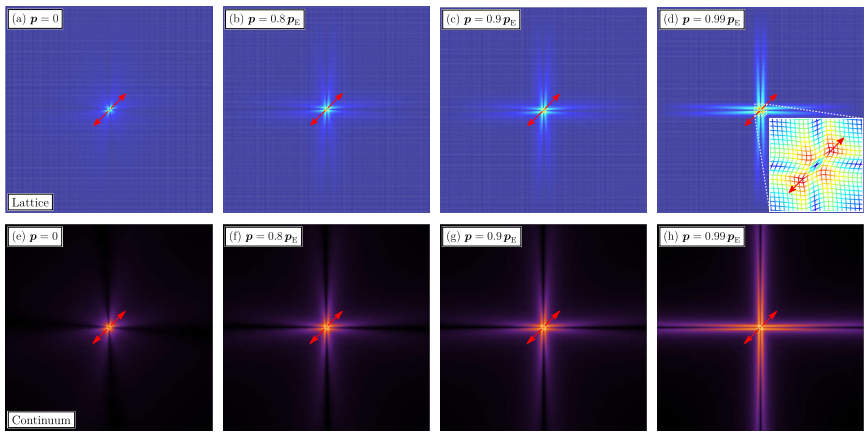

Fig. 4.10. Progressive emergence at increasing load of two orthogonal shear bands visible in the displacement field generated by a diagonal force dipole applied to a square lattice (with cubic symmetry, $\Lambda_1 = \Lambda_2 = 10$, upper part, a–d, simulated via f.e.m.) compared to the response of the homogenized continuum (lower part e–h). From left to right the load increases towards failure of strong ellipticity $\boldsymbol{p}_{\mathrm{E}}$. Shear bands are aligned parallel to the directions predicted at failure of ellipticity ($\theta_{\mathrm{cr}} = 0°, 90°$).

left to right correspond to the application of increasing preloads, which approach the strong ellipticity boundary in the equivalent solid in situations where failure of ellipticity corresponds also to the occurrence of a macro bifurcation of infinite wavelength. The part (d) of each figure ($\boldsymbol{p} = 0.99\boldsymbol{p}_{\mathrm{E}}$) also illustrates a magnification of the lattice response in the neighborhood of the loading zone, thus disclosing the microscopic deformation pattern associated to the extreme mechanical response of the material when close to elliptic boundary.

In the conditions analyzed in Figs. 4.10–4.13, the equivalent solid is found to be fully representative of the lattice structure, so that approaching failure of ellipticity the perturbative approach reveals, both in the continuum and in the real lattice, the formation of localized incremental deformation in the form of single or double localization bands. These can be horizontal, vertical or inclined. The correspondence between the behaviour of lattice and of the equivalent continuum is found to be excellent so that the maps

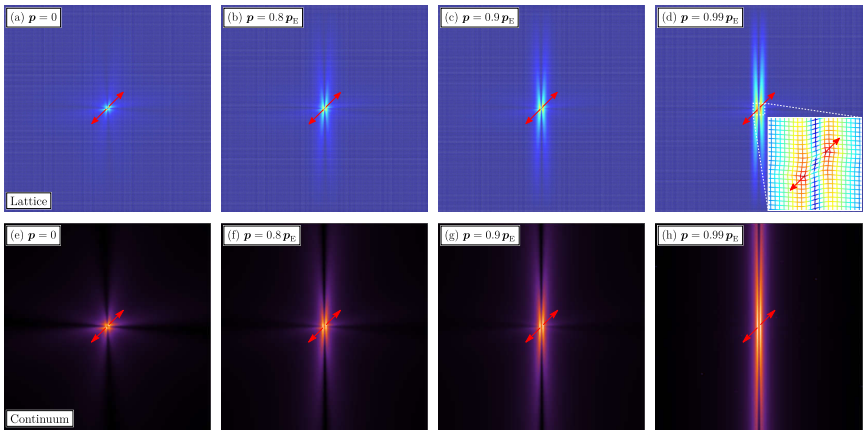

Fig. 4.11. As for Fig. 4.10, but for an orthotropic square lattice ($\Lambda_1 = 7,\ \Lambda_2 = 15$), where a single and vertical, $\theta_{cr} = 0°$, shear band forms.

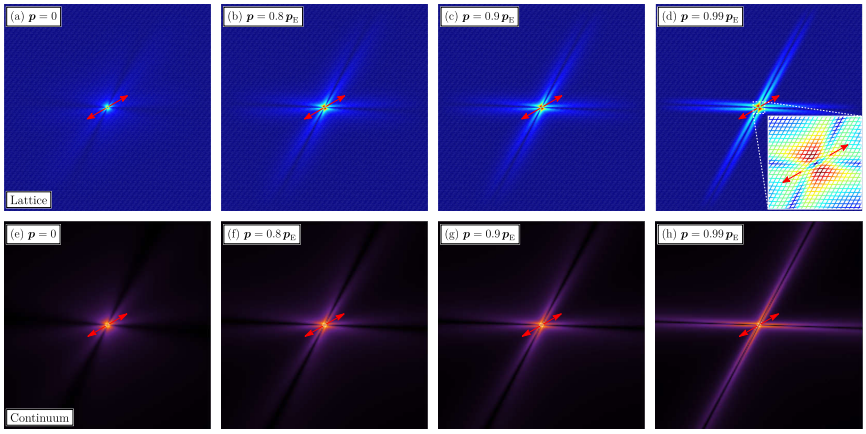

Fig. 4.12. As for Fig. 4.10, but for an orthotropic rhombic lattice ($\Lambda_1 = \Lambda_2 = 10$), where the two localization bands are inclined at angles $\theta_{cr} = 88.2°, 151.8°$.

reported in the upper part of the figures are practically identical to the corresponding maps in the lower part of the figures.

4.6.2 Microscopic bifurcations in the lattice and effects on the equivalent solid

Micro-bifurcations occurring when the equivalent solid is still in the strong ellipticity range are investigated in this section, with reference to an equibiaxially compressed square lattice with cubic symmetry $\Lambda_1 = \Lambda_2 = 10$ and diagonal springs of stiffness $\kappa = 0.4$. With the assumed spring stiffness, a microscopic bifurcation is critical, namely, it occurs when the equivalent solid is still in the strong elliptic domain.

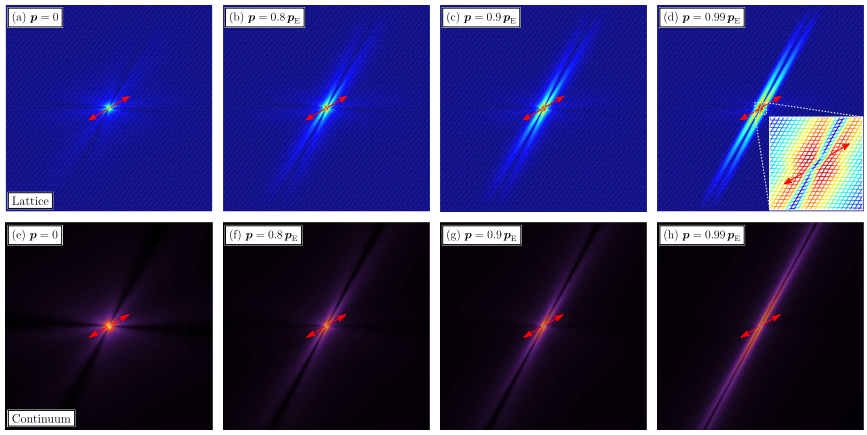

Fig. 4.13. As for Fig. 4.10, but for an anisotropic rhombic lattice ($\Lambda_1 = 7,\ \Lambda_2 = 15$), where a single localization band forms inclined at an angle $\theta_{\rm cr} = 151.4°$.

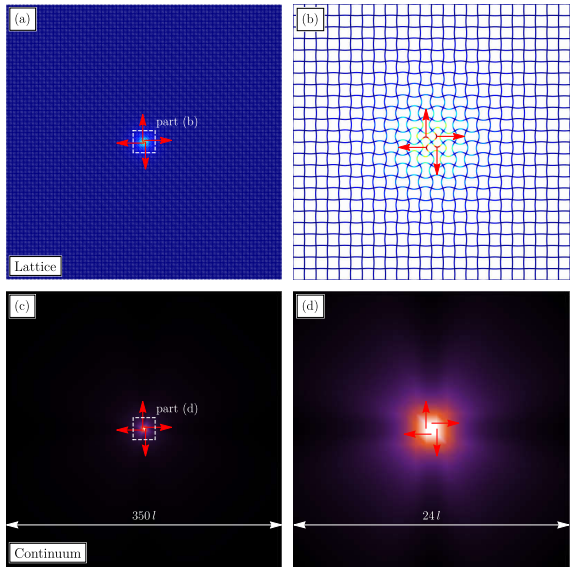

Fig. 4.14. Microscopic localization of the bifurcation mode evidenced in the incremental displacement map relative to a square lattice (cubic symmetry, $\Lambda_1 = \Lambda_2 = 10$, upper part) and in the equivalent continuum (lower part) at an equibiaxial compression load corresponding to bifurcation, $\boldsymbol{p}_{\rm B} = \{-\pi^2, -\pi^2\}$, under the action of a 'quadrupole' of forces applied at the midpoints of the rods. The quadrupole activates a highly localized 'rotational' bifurcation mode (labeled as in B_1 in Fig. 4.7a and Table 4.1), which leaves the lattice and the equivalent solid 'macroscopically' almost undeformed, while the *inter-node deformation is predominant* at the scale of the unit cell. The latter feature cannot be detected by the equivalent solid.

The incremental displacement maps in the lattice (*at* the critical load for micro-bifurcation) and in the equivalent continuum (still in the strong elliptic range) generated by the application of a force quadrupole are shown

in Fig. 4.14, where the upper parts (lower parts) refer to the lattice (to the continuum) and the parts on the right are a magnification of the zone around the quadrupole shown on the left.

The figure shows that the incremental response of the prestressed lattice is highly localized, so that only a strong magnification reveals buckling of the elastic rods. Even if the equivalent continuum is not at bifurcation, but still within the uniqueness/stability domain, the distribution of displacements in it somehow resembles that in the lattice, so that the homogenization is still representative of the response of the discrete structure, even though the *inter-node deformation* cannot be captured.

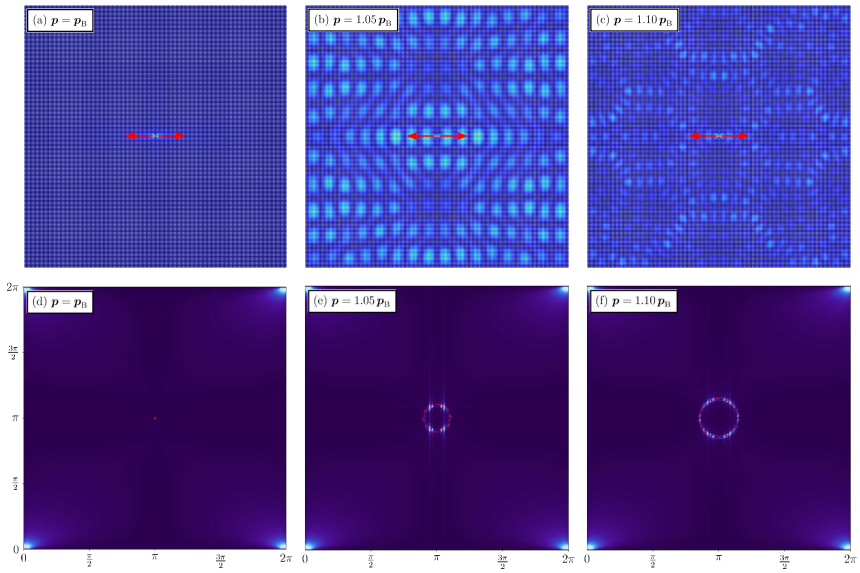

Fig. 4.15. Displacement map (a)–(c) and corresponding Fourier transform (d)–(f) showing the response of the lattice at a load corresponding to microscopic instability, $\boldsymbol{p} = \boldsymbol{p}_B$ and beyond, $\boldsymbol{p} = 1.05\boldsymbol{p}_B$, $1.10\boldsymbol{p}_B$. The slowness contour at null frequency, evaluated through the bifurcation condition is superimposed in red. While at the critical load the perturbation is so localized that results almost invisible, at higher loads an 'explosive' instability involving the whole lattice and extending up to the boundary of the domain is clearly observed.

The situation depicted in Fig. 4.14 completely changes when the lattice is loaded with forces beyond the critical value for micro bifurcation in the lattice, as shown in Fig. 4.15, only referred to the lattice loaded with a horizontal force dipole at different biaxial compression loadings (*at* the critical load $\boldsymbol{p} = \boldsymbol{p}_B$ for micro-buckling and beyond, namely, at $\boldsymbol{p} = 1.05\,\boldsymbol{p}_B$ and at $\boldsymbol{p} = 1.10\,\boldsymbol{p}_B$).

This figure shows displacement maps (upper part) and the corresponding Fourier transform (obtained via FFT of nodal displacements, lower part), with superimposed slowness contours corresponding to null frequency. The slowness contour (highlighted in red in the figure) was obtained from the

bifurcation condition, Eq. (4.29). The fact that the slowness contour is superimposed to the peaks of the transform (reported white in the figure), is a validation of the good correspondence between calculations performed via Floquet-Bloch and finite element simulations.

It can be concluded from Fig. 4.15 that, while at bifurcation load the incremental perturbation induced by the force dipole is practically so small and highly localized that results almost invisible, an 'explosive instability' is found in the lattice, which does not decay and extends to the whole domain occupied by the structure considered in the analysis. This is a special behaviour which remains unobserved in the equivalent continuum (still in the strong elliptic range) and cannot therefore be revealed through homogenization.

4.7 Conclusions

Homogenization of the incremental response of a lattice of elastic rods, axially pre-loaded to an arbitrary amount, has been shown to provide a superb tool for the design of cellular elastic materials of tunable properties and capable of extreme localized deformations. In particular, the perturbative approach to material instability reveals that strain localization in the composite is almost coincident with that occurring in the equivalent solid, which remains unaffected by micro bifurcations, possibly occurring in the lattice. However, the developed homogenization approach allows the exploration of geometries and stiffnesses of the composite in a way to inhibit or promote strain localization with respect to other micro instabilities. The vibrational properties of the lattice and the ability of the homogenization scheme to correctly capture them is a final crucial aspect in the design of cellular materials, that will be addressed in Chapter 5 of this study.

5

Bifurcation and strain localization in prestressed lattices: dynamic response

Floquet-Bloch wave asymptotics is used to homogenize the in-plane mechanical response of a lattice grid of elastic Rayleigh rods, possessing a distributed mass density together with a rotational inertia and subject to incremental dynamics, superimposed to a given state of axial loading of arbitrary magnitude. In contrast to the quasi-static energy match (addressed in Chapter 4 of the present study), the vibrational properties of the lattice are directly represented by the acoustic tensor of the equivalent solid, without passing through the constitutive tensor which is instead arrived via energy equivalency. The acoustic tensor is shown to result independent of the rods' rotational inertia and allows directly the analysis of strong ellipticity of the equivalent continuum, evidencing coincidence with macro-bifurcation in the lattice. On the other hand, the dynamics of micro-bifurcation corresponds to a vanishing frequency, at finite wavelength, of the lowest dispersion branch of the lattice. Dynamic homogenization reveals the structure of the acoustic branches close to ellipticity loss, and of forced vibrations (both in physical space and Fourier space) showing low-frequency wave localizations. A comparison between the strain localization occurring near ellipticity loss and the forced vibration of the lattice, both corresponding to the application of a concentrated pulsating force, shows that the homogenization technique allows an almost perfect representation of the lattice. Therefore, the presented results pave the way for the design of architected cellular materials to be used in applications where extreme deformation are involved.

5.1 Introduction

A lattice grid of axially-preloaded elastic rods, subject to in-plane incremental kinematics, has been shown (in Chapter 4 of this study, via quasi-static energy match with an equivalent continuum), to provide a way to the realization of a material evidencing macroscopic (strain localization) and microscopic (lattice buckling) instabilities within the elastic range. Such lattice represents an example of architected cellular material to be used for large strain applications where instabilities become a major issue. The latters are investigated in the present chapter within the dynamic range, thus employing an asymptotic homogenization based on the Floquet-Bloch wave technique, exploited to a level of generality never achieved so far. The vibrational properties of a cellular material are deeply affected by the emergence and development of localized signals, edge waves, and topologically protected modes [2, 10, 11, 76, 107, 108], an example being that reported in Fig. 5.1, where the dynamic emergence and propagation of discontinuity wavefronts (rectilinear and curvilinear) is shown in the so-called 'pinscreen', a material (made up of a perforated plate having each hole filled with a movable pin) on the verge of ellipticity loss.

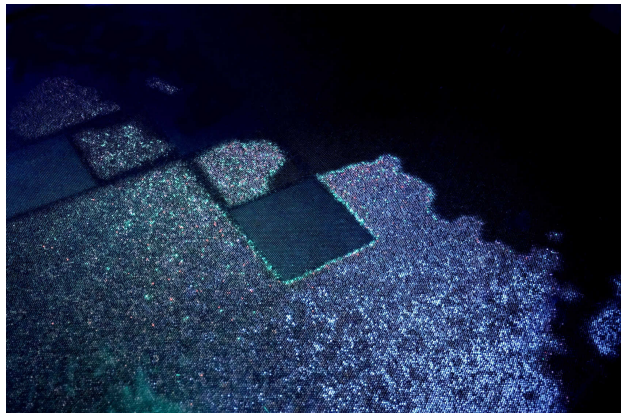

Fig. 5.1. Discontinuity wavefronts (some rectilinear, other curvilinear) forming during the (out-of-plane) dynamics of a periodic material (used as a toy, the so-called 'pinscreen', invented by W. Fleming), which works on the boundary of ellipticity loss (photo taken at the Exploratorium, San Francisco).

Homogenization techniques based on the asymptotic analysis of wave solutions dates back to Brillouin [65] and Born [96], and has received significant contributions in recent years when the case of random and periodic media has been considered [21–23, 40, 109–113] and also extended to the high-frequency regime [114–116]. With the exception of [40], these developments have been so far produced for the analysis of wave propagation in continuous materials, not in structures, so that their practical implementation required the systematic use of numerical techniques (typically

finite elements). It is shown in the this chapter that low-frequency effective properties can be derived analytically for lattices composed of rods (incrementally loaded in-plane) through a direct computation of the wave asymptotics[1]. Recent results on beam lattices [40] are here extended to the case of elastic lattices, axially stressed up to an arbitrary amount, whose incremental dynamics is derived without restrictions on the rods' constitutive law and without neglecting the rotational inertia of the rods' cross section. The low-frequency asymptotics of the lattice waves is shown to be governed by the spectral properties of the acoustic tensor associated to the effective solid and capturing the incremental response of the system.

While the final results coincide with those obtained via energy match, it is shown that Floquet-Bloch asymptotics leads directly to the acoustic tensor, not to the constitutive operator, of an equivalent, prestressed, solid. In this way, the correspondence between loss of ellipticity in the continuum and degeneracy of the acoustic properties in the lattice is *directly* demonstrated. Moreover, the elastic rods are characterized by an axial mass density, equipped with rotational inertia (the Rayleigh model [1, 55, 117]), so that it is possible to prove that the latter does not influence the vibrational properties, expressed by the acoustic tensor, of the equivalent continuum. The homogenization, obtained analytically, is exploited to investigate the lattice response near macro-instability threshold (coincident with the failure of strong ellipticity of the effective continuum), therefore unveiling microscopic features of lattice dynamics loaded up to the verge of shear band formation.

The response to the application of a pulsating concentrated force is finally analyzed in the spirit of [118] and [119], when applied both to the lattice (in the physical and Fourier spaces) and to the equivalent solid, with special detail on low-frequency wave localizations. The time-harmonic infinite-body Green's function (see [119]) of the effective solid is compared to the forced response of lattice obtained through the finite elements methodology, in which the application of PML boundary conditions to a finite grid simulates an infinite domain. The acoustic branches of the lattice structure and its continuum approximation are shown to be in almost perfect agreement, thus confirming that the lattice is an excellent candidate for the realization of architected cellular materials to be used to harness micro-buckling and strain localization, two features which can control the dynamic response of a structure with tunable functionality [5, 6].

This paper is organized as follows. The mathematical setting for incremental wave propagation is developed in Section 5.2 for an axially preloaded lattice of elastic rods, organized in an arbitrary periodic geometry. The asymptotic analysis of lattices waves is derived in Section 5.3, leading to the homogenization result that provides the acoustic tensor associated to the incremental effective Cauchy continuum. The developed homogenization scheme is applied in Section 5.4 to the same grid of elastic rods considered in Chapter 4, so that failure of ellipticity and micro-buckling are

[1]The mathematical setting is two-dimensional for simplicity, but the thee-dimensional extension is straightforward once the linearized dynamics of the rods is specified.

investigated now through the analysis of the dispersion characteristics of the lattice. In Section 5.5, the emergence and characterization of dynamic strain localization is presented by means of a perturbative approach (applied to the lattice and the effective continuum), which demonstrates how the *macroscopic* localization direction, as well as the number of localization bands, can effectively be designed through appropriate modifications of the *underling* lattice structure.

5.2 Incremental dynamics of preloaded lattices: governing equations

In this section, the governing equations for incremental wave propagation in an axially-preloaded lattice of elastic rods are formulated. These are obtained (i) by solving for time-harmonic vibrations the incremental dynamics of a single rod (derived in Appendix C), (ii) by using this solution to formulate the equations of motions of a single unit cell, and finally (iii) by applying the Bloch theorem to obtain the equations governing the incremental dynamics of the infinite lattice.

An infinite two-dimensional lattice structure is considered, composed of nonlinear elastic rods which are axially preloaded (or prestretched) from an unloaded reference configuration $\mathcal{B}_0$ to a preloaded configuration $\mathcal{B}$ used as reference in an updated Lagrangian formulation of incremental dynamics (Fig. 5.2).

By introducing a local coordinate s_k for each rod of a given unit cell, the *incremental* kinematics is described by means of the following fields

$$\boldsymbol{u}_k(s_k,t) = \{u_k(s_k,t), v_k(s_k,t)\}^\intercal, \qquad \forall k \in \{1,\dots,N_b\},$$

where N_b is the number of rods in the unit cell, and the two in-plane displacement components, respectively axial and transverse, are denoted by $u_k(s_k,t)$ and $v_k(s_k,t)$, while the rotation of the cross-section $\theta_k(s_k,t)$ is assumed to satisfy the unshearability condition $\theta_k(s_k,t) = v'(s_k,t)$[2]. Time-harmonic solutions are sought, so that, by introducing the circular frequency ω, the dependence on time t can be represented as

$$\boldsymbol{u}_k(s_k,t) = \hat{\boldsymbol{u}}_k(s_k)\, e^{-i\,\omega\, t} \qquad \forall k \in \{1,\dots,N_b\}, \tag{5.1}$$

where $\hat{\boldsymbol{u}}_k(s_k) = \{\hat{u}_k(s_k), \hat{v}_k(s_k)\}^\intercal$ are functions of the coordinate s_k only.

5.2.1 Bloch's theorem

Wave propagation in an infinite periodic elastic medium can effectively be analyzed through the application of Bloch theorem. Essentially, the theorem states that the time-harmonic solutions of the equations of motion possess a

[2]A dash will be used to denote differentiation with respect to the coordinate s_k.

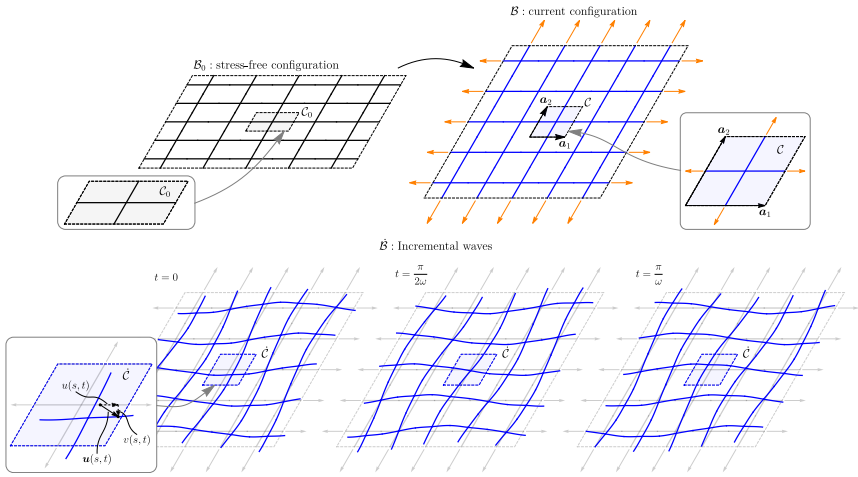

Fig. 5.2. A periodic two-dimensional lattice of (axially and flexurally deformable) elastic rods is considered, preloaded from the stress-free configuration $\mathcal{B}_0$ (upper part, on the left) by means of a pure axial loading state, transforming $\mathcal{B}_0$ to the current, preloaded configuration $\mathcal{B}$ (upper part, on the right). The latter configuration, used as reference in an updated Lagrangian description, can be represented as the tessellation of a single unit cell along the vectors of the direct basis $\{\boldsymbol{a}_1, \boldsymbol{a}_2\}$. The incremental dynamic response (lower part where an incremental deformation is shown at three different instants of time) is defined on $\mathcal{B}$ by the incremental displacement field of each rod $\boldsymbol{u}(s,t)$, here decomposed in an axial and transverse component, $u(s,t)$ and $v(s,t)$.

modulation in space having the same periodicity of the medium, a condition expressed by the following requirement[3]

$$\boldsymbol{u}(\boldsymbol{x},t) = \boldsymbol{\varphi}(\boldsymbol{x})\, e^{i\,(\boldsymbol{k}\cdot\boldsymbol{x}-\omega\, t)}\,, \tag{5.2a}$$

where $\boldsymbol{k}$ is the Bloch vector and the modulation $\boldsymbol{\varphi}(\boldsymbol{x})$ is periodic with respect to the direct basis, so that it satisfies

$$\boldsymbol{\varphi}(\boldsymbol{x} + n_j \boldsymbol{a}_j) = \boldsymbol{\varphi}(\boldsymbol{x}) \qquad \forall \{n_1, n_2\} \in \mathbb{Z}^2 \quad \forall \boldsymbol{x} \in \mathbb{R}^2\,.$$

Eq. (5.2a) can be equivalently expressed as

$$\boldsymbol{u}(\boldsymbol{x} + n_j \boldsymbol{a}_j, t) = \boldsymbol{u}(\boldsymbol{x}, t)\, e^{i\,\boldsymbol{k}\cdot(n_j \boldsymbol{a}_j)}\,. \tag{5.2b}$$

Note that, in the case of a lattice made up of rods, the waveform $\boldsymbol{\varphi}(\boldsymbol{x})$ (as well as the field $\boldsymbol{u}(\boldsymbol{x},t)$) is described by the displacement of the rods constituting the unit cell, and thus it is defined only for $\boldsymbol{x}$ corresponding to the location of the structural elements.

The importance of the Bloch's theorem lies in the fact that it allows the formulation of the dynamics of an infinite structure by complementing the equations of motion of a single unit cell with suitable boundary conditions.

[3]Note that an equation similar to Eq.(5.2b) holds also with the stress field replacing the displacement field.

These so-called Floquet-Bloch conditions enforce the periodicity of the lattice, by relating nodal displacements and forces on the boundary of the unit cell, according to the property expressed by Eq. (5.2b).

5.2.2 Time-harmonic solution of a preloaded elastic rod

The analytic solution is obtained for time-harmonic vibrations of a Rayleigh rod. In the framework of a linearized theory, the equations of motion governing the incremental dynamics of an axially pre-stretched Rayleigh rod are the following

$$\gamma(\lambda_0)\,\ddot{u}(s,t) - A(\lambda_0)\,u''(s,t) = 0\,, \tag{5.3a}$$

$$\gamma(\lambda_0)\,\ddot{v}(s,t) - \gamma_r(\lambda_0)\,\ddot{v}''(s,t) + B(\lambda_0)\,v''''(s,t) - P(\lambda_0)\,v''(s,t) = 0\,, \tag{5.3b}$$

where a superimposed dot denotes time differentiation, $\gamma(\lambda_0)$ is the *current* linear mass density, $\gamma_r(\lambda_0)$ is the *current* rotational inertia, λ_0 is the axial pre-stretch and $P(\lambda_0)$ the corresponding axial preload (assumed positive in tension), while $A(\lambda_0)$ and $B(\lambda_0)$ are, respectively, the *current* axial and bending stiffness. The analytic derivation of equations (5.3) is reported in Appendix C, where the formulation provided in Chapter 4 of this work is extended to the dynamic case. Moreover, the derivation of the current stiffnesses $A(\lambda_0)$ and $B(\lambda_0)$ from strain-energy functions, as well as the their identification for rods made up of an incompressible elastic material can be found in Appendix C. In the following, the parameters $\gamma(\lambda_0)$, $\gamma_r(\lambda_0)$, $A(\lambda_0)$, and $B(\lambda_0)$ will simply be denoted as, γ, γ_r, A, and B, and treated as independent quantities for generality.

The substitution of Eq. (5.1) into Eq. (5.3) leads to a system of linear ODEs for the functions $\hat{u}(s)$ and $\hat{v}(s)$. As the system is fully decoupled, the solution is easily obtained in the form

$$\hat{u}(s) = \sum_{j=1}^{2} C_j^u\, e^{i\,\beta_j^u\, s}\,, \qquad \hat{v}(s) = \sum_{j=1}^{4} C_j^v\, e^{i\,\beta_j^v\, s}\,, \tag{5.4}$$

where $\{C_1^u, C_2^u, C_1^v, \ldots, C_4^v\}$ are 6 arbitrary complex constants and the characteristic roots β_j^u and β_j^v are given by

$$\beta_{1,2}^u = \pm\frac{\tilde{\omega}}{l}\,, \quad \beta_{1,2,3,4}^v = \pm\frac{1}{l\sqrt{2}}\sqrt{-p + r\,\tilde{\omega}^2 \pm \sqrt{p^2 + (4\Lambda^2 - 2\,p\,r)\,\tilde{\omega}^2 + r^2\,\tilde{\omega}^4}}\,,$$

with l being the current length of the rod, $\tilde{\omega} = \omega\, l\sqrt{\gamma/A}$ the non-dimensional angular frequency, $p = Pl^2/B$ the non-dimensional preload, $\Lambda = l/\sqrt{B/A}$ the slenderness of the rod, and $r = \gamma_r A/(\gamma B)$ is the dimensionless rotational inertia.

5.2.3 Exact time-harmonic shape functions, mass and stiffness matrices

To facilitate the asymptotic expansion, it is instrumental to identify the 6 constants $\{C_1^u, C_2^u, C_1^v, ..., C_4^v\}^\intercal$, with the *degrees of freedom* at the rod's ends (i.e. its nodal displacements). This allows a dimensional reduction through a direct application of the compatibility conditions at the joints.

For any given rod of length l, the following notation for the nodal quantities is introduced

$$\begin{aligned} \hat{u}(0) = u_1\,, \quad \hat{v}(0) = v_1\,, \quad \hat{\theta}(0) = \theta_1\,, \\ \hat{u}(l) = u_2\,, \quad \hat{v}(l) = v_2\,, \quad \hat{\theta}(l) = \theta_2\,, \end{aligned} \tag{5.5}$$

so that collecting the degrees of freedom at the two ends of the rod in the vector $\hat{\boldsymbol{q}} = \{u_1, v_1, \theta_1, u_2, v_2, \theta_2\}^\intercal$ yields the solution of system (5.5) in the form

$$\hat{\boldsymbol{u}}(s) = \boldsymbol{N}(s;\omega,P)\,\hat{\boldsymbol{q}}\,, \quad \boldsymbol{u}(s,t) = \boldsymbol{N}(s;\omega,P)\,\boldsymbol{q}(t) = \boldsymbol{N}(s;\omega,P)\,\hat{\boldsymbol{q}}\,e^{-i\,\omega\,t}\,, \tag{5.6}$$

which is now a linear function of the nodal displacements $\boldsymbol{q}(t) = \hat{\boldsymbol{q}}\,e^{-i\,\omega\,t}$.

The 2-by-6 matrix $\boldsymbol{N}(s;\omega,P)$ acts as a matrix of frequency-dependent and preload-dependent 'shape functions' which is the *exact* functional basis in which the time-harmonic response of the rod can be represented. The representation (5.6) can also be considered as the definition of a 'finite element' endowed with shape functions built from the exact solution. Moreover, these time-harmonic shape functions reduce to the quasi-static solution when $\omega \to 0$ [so that for vanishing preload, in the limit $\lim_{\omega\to 0}\boldsymbol{N}(s;\omega,0)$ the usual shape functions for beam elements, employed for instance in [52], are recovered]. Note that, in the following, $\boldsymbol{N}(s;\omega,P)$ will simply be denoted as $\boldsymbol{N}(s;\omega)$, to simplify notation.

By employing Eq. (5.6), the exact mass and stiffness matrices of a rod under time-harmonic vibration can be computed. For the k-th rod the kinetic energy and the elastic strain energy are given by

$$\begin{aligned} \mathcal{T}_k &= \frac{1}{2}\int_0^{l_k} \gamma_k \left(\dot{u}_k(s_k,t)^2 + \dot{v}_k(s_k,t)^2\right) ds_k + \frac{1}{2}\int_0^{l_k} \gamma_{r,k}\dot{v}_k'(s_k,t)^2 ds_k \\ &= \frac{1}{2}\,\dot{\boldsymbol{q}}_k(t)^\intercal \left(\int_0^{l_k} \boldsymbol{N}_k(s_k;\omega)^\intercal \boldsymbol{J}_k\,\boldsymbol{N}_k(s_k;\omega) ds_k\right)\dot{\boldsymbol{q}}_k(t) + \\ &\qquad + \frac{1}{2}\,\dot{\boldsymbol{q}}_k(t)^\intercal \left(\int_0^{l_k} \gamma_{r,k}\,\boldsymbol{b}_k(s_k;\omega)^\intercal \boldsymbol{b}_k(s_k;\omega)\,ds_k\right)\dot{\boldsymbol{q}}_k(t)\,, \end{aligned} \tag{5.7a}$$

$$\begin{aligned} \mathcal{E}_k &= \frac{1}{2}\int_0^{l_k} \left(A_k\,u_k'(s_k,t)^2 + B_k\,v_k''(s_k,t)^2\right) ds_k \\ &= \frac{1}{2}\,\boldsymbol{q}_k(t)^\intercal \left(\int_0^{l_k} \boldsymbol{B}_k(s_k;\omega)^\intercal \boldsymbol{E}_k\,\boldsymbol{B}_k(s_k;\omega) ds_k\right)\boldsymbol{q}_k(t)\,, \end{aligned} \tag{5.7b}$$

where $\boldsymbol{J}_k$ and $\boldsymbol{E}_k$ are matrices collecting the inertia and stiffness terms, respectively, while $\boldsymbol{B}_k(s_k;\omega)$ is the strain-displacement matrix, which are defined as follows

$$\boldsymbol{J}_k = \begin{bmatrix} \gamma_k & 0 \\ 0 & \gamma_k \end{bmatrix}, \qquad \boldsymbol{E}_k = \begin{bmatrix} A_k & 0 \\ 0 & B_k \end{bmatrix}, \qquad \boldsymbol{B}_k(s_k;\omega) = \begin{bmatrix} \frac{\partial}{\partial s_k} & 0 \\ 0 & \frac{\partial^2}{\partial s_k^2} \end{bmatrix} \boldsymbol{N}_k(s_k;\omega)\,,$$

and $\boldsymbol{b}_k(s_k;\omega) = \begin{bmatrix} 0 & \frac{\partial}{\partial s_k} \end{bmatrix} \boldsymbol{N}_k(s_k;\omega)$ is a row vector containing the derivative of the shape functions corresponding to the transverse displacement v. Note that the kinetic energy (5.7a) accounts for translational as well as rotational inertia of the rod. In addition, the contribution of the axial preload can be included in the potential energy as (details are provided in Appendix C)

$$\begin{aligned} \mathcal{V}_k^g &= \frac{1}{2} P_k \int_0^{l_k} v_k'(s_k,t)^2 \, ds_k \\ &= \frac{1}{2}\, \boldsymbol{q}_k(t)^\intercal \left(P_k \int_0^{l_k} \boldsymbol{b}_k(s_k;\omega)^\intercal \boldsymbol{b}_k(s_k;\omega)\, ds_k \right) \boldsymbol{q}_k(t)\,. \end{aligned} \tag{5.8}$$

By combining Eqs. (5.7b) and (5.8), the potential energy of the k-th rod is denoted as

$$\mathcal{V}_k = \mathcal{E}_k + \mathcal{V}_k^g\,. \tag{5.9}$$

From Eqs. (5.7), (5.8) and (5.9) the frequency-dependent mass and stiffness matrices are naturally defined as

$$\begin{aligned} \boldsymbol{M}_k(\omega) = \int_0^{l_k} \boldsymbol{N}_k(s_k;\omega)^\intercal \boldsymbol{J}_k\, \boldsymbol{N}_k(s_k;\omega)\, ds_k + \\ + \int_0^{l_k} \gamma_{r,k}\, \boldsymbol{b}_k(s_k;\omega)^\intercal \boldsymbol{b}_k(s_k;\omega)\, ds_k\,, \end{aligned} \tag{5.10a}$$

$$\begin{aligned} \boldsymbol{K}_k(\omega) = \int_0^{l_k} \boldsymbol{B}_k(s_k;\omega)^\intercal \boldsymbol{E}_k\, \boldsymbol{B}_k(s_k;\omega)\, ds_k + \\ + P_k \int_0^{l_k} \boldsymbol{b}_k(s_k;\omega)^\intercal \boldsymbol{b}_k(s_k;\omega)\, ds_k\,. \end{aligned} \tag{5.10b}$$

The matrices for the quasi-static case can be obtained by evaluating the limit $\omega \to 0$. In particular, the quasi-static stiffness matrix $\lim_{\omega\to 0} \boldsymbol{K}_k(\omega)$ is found to be identical to that reported in Chapter 4, where it is used to formulate the incremental equilibrium and analyze the bifurcation of preloaded lattices.

5.2.4 Equations of motion for the isolated unit cell

As expressions (5.7)–(5.9) govern the *incremental* dynamics of a single rod, the kinetic and potential energies of a single unit cell can be obtained through

a summation of contributions from each rod

$$\mathcal{T} = \sum_{k=1}^{N_b} \mathcal{T}_k \,, \qquad \mathcal{V} = \sum_{k=1}^{N_b} \mathcal{V}_k \,,$$

and therefore the equations of motion for an isolated unit cell can be derived from Hamilton's principle applied to the Lagrangian

$$\mathcal{L}(\boldsymbol{q}, \dot{\boldsymbol{q}}) = \mathcal{T}(\dot{\boldsymbol{q}}) - \mathcal{V}(\boldsymbol{q}) + \mathcal{W}(\boldsymbol{q}) \,, \tag{5.11}$$

where $\boldsymbol{q}$ is the vector collecting all the degrees of freedom of the unit cell and $\mathcal{W}(\boldsymbol{q}) = \boldsymbol{f} \cdot \boldsymbol{q}$ is the *incremental* work done by the internal actions $\boldsymbol{f}$ acting on the boundary nodes.

The stationarity of the action associated to the Lagrangian (5.11) leads to the following Euler-Lagrange equations

$$\boldsymbol{M}(\omega)\, \ddot{\boldsymbol{q}}(t) + \boldsymbol{K}(\omega)\, \boldsymbol{q}(t) = \boldsymbol{f}(t) \,, \tag{5.12}$$

where $\boldsymbol{M}(\omega)$ and $\boldsymbol{K}(\omega)$ are, respectively, the mass and stiffness matrices of the unit cell. The global matrices can be easily obtained by assembling the local matrices expressed by Eqs. (5.10) for all the rods in the unit cell.

The assumption that the external action on the isolated unit cell is time-harmonic, $\boldsymbol{f}(t) = \hat{\boldsymbol{f}} e^{-i\,\omega\, t}$, allows a substitution of the time-harmonic response $\boldsymbol{q}(t) = \hat{\boldsymbol{q}}\, e^{-i\,\omega\, t}$, so to obtain the governing equation for the isolated unit cell

$$\boldsymbol{A}(\omega)\, \hat{\boldsymbol{q}} = \hat{\boldsymbol{f}} \,, \tag{5.13}$$

with the definition $\boldsymbol{A}(\omega) = -\omega^2 \boldsymbol{M}(\omega) + \boldsymbol{K}(\omega)$. Note that the dimension of the linear system (5.13) is $3N_j$, where N_j is the number of nodes of the unit cell.

5.2.5 Application of the Floquet-Bloch conditions

In order to describe the response of the infinite lattice, the governing equations of the isolated unit cell (5.13) have to be complemented with the Floquet-Bloch conditions. The application of these conditions to periodic beam lattices is well-known [52, 120] and is briefly summarized in the following.

(a)

As Eq. (5.2b) requires

$$\hat{\boldsymbol{q}}_q = \hat{\boldsymbol{q}}_p\, e^{i\, \boldsymbol{k}\cdot(\boldsymbol{x}_q - \boldsymbol{x}_p)} \,, \tag{5.14}$$

for all pairs of nodes $\{p, q\}$ such that $\boldsymbol{x}_q - \boldsymbol{x}_p$ is an integer, linear combination of the lattice vectors $\{\boldsymbol{a}_1, \boldsymbol{a}_2\}$, the relations to be imposed on the degrees of freedom of the unit cell derive directly from Eq. (5.2b), evaluated at $\boldsymbol{x} \in \partial C$

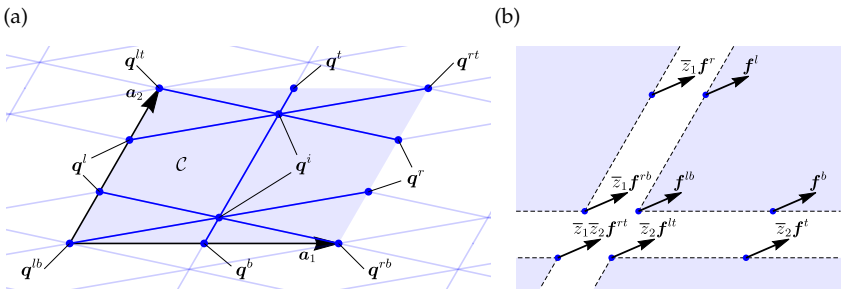

Fig. 5.3. In order to impose the appropriate Floquet-Bloch conditions required by Eq. (5.2b), vector $\boldsymbol{q}$ collecting the degrees of freedom of the unit cell is conveniently partitioned by distinguishing the sets of inner $\boldsymbol{q}^i$ and boundary nodes, both located at corners $\{\boldsymbol{q}^{lb}, \boldsymbol{q}^{lt}, \boldsymbol{q}^{rb}, \boldsymbol{q}^{rt}\}$ and on the edges $\{\boldsymbol{q}^l, \boldsymbol{q}^b, \boldsymbol{q}^r, \boldsymbol{q}^t\}$ (a). The corresponding force vector $\boldsymbol{f}$ is partitioned in the same way (b) and the forces acting on the boundary nodes have to satisfy equilibrium as well as the Floquet-Bloch conditions (the shift factor $z_j = e^{i\,\boldsymbol{k}\cdot\boldsymbol{a}_j}$ is simply a consequence of Eq. (5.2b)).

and for $n_j \in \{0, 1\}$, hence obtaining

$$\hat{\boldsymbol{q}} = \begin{Bmatrix} \hat{\boldsymbol{q}}^i \\ \hat{\boldsymbol{q}}^l \\ \hat{\boldsymbol{q}}^b \\ \hat{\boldsymbol{q}}^{lb} \\ \hat{\boldsymbol{q}}^r \\ \hat{\boldsymbol{q}}^t \\ \hat{\boldsymbol{q}}^{rb} \\ \hat{\boldsymbol{q}}^{lt} \\ \hat{\boldsymbol{q}}^{rt} \end{Bmatrix} = \begin{bmatrix} \boldsymbol{I} & \boldsymbol{0} & \boldsymbol{0} & \boldsymbol{0} \\ \boldsymbol{0} & \boldsymbol{I} & \boldsymbol{0} & \boldsymbol{0} \\ \boldsymbol{0} & \boldsymbol{0} & \boldsymbol{I} & \boldsymbol{0} \\ \boldsymbol{0} & \boldsymbol{0} & \boldsymbol{0} & \boldsymbol{I} \\ \boldsymbol{0} & z_1\boldsymbol{I} & \boldsymbol{0} & \boldsymbol{0} \\ \boldsymbol{0} & \boldsymbol{0} & z_2\boldsymbol{I} & \boldsymbol{0} \\ \boldsymbol{0} & \boldsymbol{0} & \boldsymbol{0} & z_1\boldsymbol{I} \\ \boldsymbol{0} & \boldsymbol{0} & \boldsymbol{0} & z_2\boldsymbol{I} \\ \boldsymbol{0} & \boldsymbol{0} & \boldsymbol{0} & z_1 z_2\boldsymbol{I} \end{bmatrix} \begin{Bmatrix} \hat{\boldsymbol{q}}^i \\ \hat{\boldsymbol{q}}^l \\ \hat{\boldsymbol{q}}^b \\ \hat{\boldsymbol{q}}^{lb} \end{Bmatrix}, \tag{5.15a}$$

succinctly written as

$$\hat{\boldsymbol{q}} = \boldsymbol{Z}(\boldsymbol{k})\,\hat{\boldsymbol{q}}^*\,, \tag{5.15b}$$

where $\boldsymbol{Z}(\boldsymbol{k})$ and $\hat{\boldsymbol{q}}^*$ are defined according to Eq. (5.15a), and $z_j = e^{i\,\boldsymbol{k}\cdot\boldsymbol{a}_j}$, with $j = 1, 2$. In Eq. (5.15a) the vector $\hat{\boldsymbol{q}}$ has been partitioned to denote the inner and boundary nodes according to the notation sketched in Fig. 5.3. The same partitioning is also introduced for the force vector $\hat{\boldsymbol{f}}$.

A substitution of Eqs. (5.15) into Eq. (5.13) provides

$$\boldsymbol{A}(\omega)\boldsymbol{Z}(\boldsymbol{k})\,\hat{\boldsymbol{q}}^* = \hat{\boldsymbol{f}}\,,$$

so that a left multiplication by $\boldsymbol{Z}(\boldsymbol{k})^{\mathsf{H}}$, where the superscript $^{\mathsf{H}}$ denotes the complex conjugate transpose operation[4], leads to the reduced system

$$\boldsymbol{Z}(\boldsymbol{k})^{\mathsf{H}}\boldsymbol{A}(\omega)\boldsymbol{Z}(\boldsymbol{k})\,\hat{\boldsymbol{q}}^* = \hat{\boldsymbol{f}}^*\,, \tag{5.16}$$

[4]The transpose of the conjugate of a matrix $\boldsymbol{M}$ is defined as $M^{\mathsf{H}}_{ij} = \overline{M}_{ji}$, where the bar denotes the complex conjugate.

where the following definition is introduced

$$\hat{\boldsymbol{f}}^* = \boldsymbol{Z}(k)^{\mathsf{H}}\hat{\boldsymbol{f}} = \begin{Bmatrix} \hat{\boldsymbol{f}}^i \\ \hat{\boldsymbol{f}}^l + \overline{z}_1\hat{\boldsymbol{f}}^r \\ \hat{\boldsymbol{f}}^b + \overline{z}_2\hat{\boldsymbol{f}}^t \\ \hat{\boldsymbol{f}}^{lb} + \overline{z}_1\hat{\boldsymbol{f}}^{rb} + \overline{z}_2\hat{\boldsymbol{f}}^{lt} + \overline{z}_1\overline{z}_2\hat{\boldsymbol{f}}^{rt} \end{Bmatrix} .$$

Note that the dimension of system (5.16) is smaller than the dimension of system (5.13). In fact, the imposition of the Floquet-Bloch conditions has permitted to express the equations of motion of the lattice only in terms of the reduced variables $\hat{\boldsymbol{q}}^*$ and $\hat{\boldsymbol{f}}^*$.

If external loads are not present in the infinite lattice (so that the boundary forces shown in Fig. 5.3b are purely internal actions), Eq. (5.2b) implies $\hat{\boldsymbol{f}}^* = \boldsymbol{0}$ and therefore the following system of equations is obtained, governing Floquet-Bloch wave propagation within the lattice

$$\boldsymbol{A}^*(\omega, \boldsymbol{k})\,\hat{\boldsymbol{q}}^* = \boldsymbol{0}\,, \tag{5.17}$$

where the matrix of the reduced system has been defined as $\boldsymbol{A}^*(\omega, \boldsymbol{k}) = \boldsymbol{Z}(\boldsymbol{k})^{\mathsf{H}}\boldsymbol{A}(\omega)\boldsymbol{Z}(\boldsymbol{k})$. Note that this matrix is non-symmetric, but for a conservative system is always Hermitian, so that $\boldsymbol{A}^*(\omega, \boldsymbol{k}) = \boldsymbol{A}^*(\omega, \boldsymbol{k})^{\mathsf{H}}$ and $\omega^2 \in \mathbb{R}$.

5.2.6 Generalized eigenvalue problem for the lattice dynamics

Eq. (5.17) defines a homogeneous linear system for the unknown vector $\hat{\boldsymbol{q}}^*$, in which the angular frequency ω and the wave vector $\boldsymbol{k}$ are for the moment undetermined.

It is important to note that the matrix-valued complex function $\boldsymbol{A}^*(\omega, \boldsymbol{k})$ depends on all the mechanical and geometrical parameters of the unit cell. Since Eq. (5.17) is homogeneous, all non-trivial solutions are obtained by imposing the condition

$$f(\omega, \boldsymbol{k}) = \det(\boldsymbol{A}^*(\omega, \boldsymbol{k})) = 0\,, \tag{5.18}$$

that defines, although implicitly, the dispersion relation, relating ω and $\boldsymbol{k}$ as $\omega(\boldsymbol{k})$. For every given wave vector $\boldsymbol{k}$ and for each of the corresponding roots $\omega(\boldsymbol{k})$ obtained from Eq. (5.18), the non-trivial solutions of Eq. (5.17) provide the modes of the Floquet-Bloch waves propagating through the lattice at each frequency. This means that the vector $\hat{\boldsymbol{q}}^*$ is an implicit function of ω and therefore of $\boldsymbol{k}$, so that the dependence on $\boldsymbol{k}$ can be made explicit so that Eq. 5.17 is rewritten as

$$\boldsymbol{A}^*(\omega(\boldsymbol{k}), \boldsymbol{k})\,\hat{\boldsymbol{q}}^*(\omega(\boldsymbol{k}), \boldsymbol{k}) = \boldsymbol{0}\,. \tag{5.19}$$

5.3 Incremental dynamics of preloaded lattices: asymptotic analysis

The scope of this section is the analysis of the low-frequency long-wavelength asymptotic behaviour of the lattice dynamics, which will enable the identification of the effective continuum material.

5.3.1 Wave propagation in a prestressed Cauchy continuum

Before introducing the homogenization technique, it is essential to recall here the fundamental equations governing incremental wave propagation in a prestressed hyperelastic continuum. An appropriate form of the equations for the prestressed continuum has to be selected, to result compatible with the formulation of the lattice dynamics introduced in Section 5.2. Specifically, it is observed that the equations of motion for the lattice are (i) obtained in the context of a linearized theory, and (ii) referred to a preloaded reference configuration, therefore, the dynamics of the unknown 'equivalent' continuum has to be formulated in the context of the incremental theory of nonlinear elasticity by means of a relative Lagrangian description [99]. This is based on *incremental constitutive laws* relating the increment of the first Piola-Kirchhoff stress $\dot{\boldsymbol{S}}$ to the incremental deformation gradient $\boldsymbol{L} = \operatorname{grad} \boldsymbol{u}$

$$\dot{\boldsymbol{S}} = \mathbb{C}[\boldsymbol{L}] \,, \tag{5.20}$$

through the elasticity tensor $\mathbb{C}$

$$\mathbb{C} = \mathbb{E} + \boldsymbol{I} \boxtimes \boldsymbol{T} \qquad \text{in components} \qquad \mathbb{C}_{ijkl} = \mathbb{E}_{ijkl} + \delta_{ik} T_{jl} \,, \tag{5.21}$$

where $\boldsymbol{T}$ is the Cauchy stress, defining here the *prestress*, and $\mathbb{E}$ is a fourth-order tensor endowed with the left and right minor symmetries and the major symmetry. Moreover, Eq. (5.21) implies that the number of unknown components of $\mathbb{C}$ is at most 9 for a 2d material and 27 for the 3d case.

In the absence of body forces, the incremental equations of motion for the continuum can be written in the usual form

$$\operatorname{Div} \dot{\boldsymbol{S}} = \rho_h \ddot{\boldsymbol{u}} \,, \tag{5.22}$$

where $\boldsymbol{u}$ is the incremental displacement field and $\rho_h > 0$ the mass density. Assuming the usual plane wave representation for incremental displacement, Eq. (5.22) leads to the following eigenvalue problem

$$\left(\boldsymbol{A}^{(\mathbb{C})}(\boldsymbol{k}) - \rho_h \, \omega_h^2 \boldsymbol{I} \right) \boldsymbol{a} = \boldsymbol{0} \,, \tag{5.23}$$

governing the wave propagation in a homogeneous Cauchy material whose acoustic tensor $\boldsymbol{A}^{(\mathbb{C})}(\boldsymbol{k})$ is defined with reference to the unit vector $\boldsymbol{k}$ as

$$A^{(\mathbb{C})}_{pr}(\boldsymbol{k}) = k_q \, \mathbb{C}_{pqrs} \, k_s \,.$$

The eigenvectors $\boldsymbol{a}$ represent the wave amplitudes, while the eigenvalues ω_h^2 are the roots of the characteristic equation

$$f_h(\omega_h, \boldsymbol{k}) = \det(\boldsymbol{A}^{(\mathbb{C})}(\boldsymbol{k}) - \rho_h\, \omega_h^2 \boldsymbol{I}) = 0\,. \tag{5.24}$$

Note that the subscript h differentiates $\omega_h(\boldsymbol{k})$ from $\omega(\boldsymbol{k})$, so that the former defines the angular frequency of a wave propagating through the equivalent homogeneous Cauchy continuum, while the latter the dispersion relation of the lattice.

5.3.2 Asymptotic expansion of Floquet-Bloch waves

A perturbation method is now developed for the equations governing wave propagation in a lattice made of prestressed elastic rods, through a generalization of the technique proposed by Born [96] for lattices involving only point-like mass interactions. A rigorous link is established between the low-frequency solutions of Eq. (5.19) and spectral characteristics of the equivalent continuum governed by Eq. (5.23).

The important point is that a wave propagating in an homogeneous Cauchy continuum can be seen as a special case of a Floquet-Bloch wave that is characterized by:

- a *linear dispersion relation*, so that writing $\boldsymbol{k} = \epsilon\, \boldsymbol{n}$ (with $\boldsymbol{n}$ being a unit vector), the following condition is obtained

$$\omega(\epsilon\, \boldsymbol{n}) = \omega_{\boldsymbol{n}}^{(1)}\, \epsilon\,, \tag{5.25}$$

  where $\omega_{\boldsymbol{n}}^{(1)}$ depends only on the direction $\boldsymbol{n}$;

- a *spatially uniform modulation*

$$\boldsymbol{\varphi}_k(\boldsymbol{x}) = \boldsymbol{a}(\boldsymbol{k})\,. \tag{5.26}$$

In general a periodic structured medium does *not* satisfy these properties for *every* wave vector $\boldsymbol{k}$, but its response can be analyzed about the point $\boldsymbol{k} = \boldsymbol{0}$ and compared with the constitutive equations of the continuum, Eqs. (5.25)–(5.26). In fact, the linear relation (5.25) can be considered as the first-order term in the asymptotic expansion of the dispersion relation $\omega(\epsilon\, \boldsymbol{n})$ centered at $\epsilon = 0$ (so that $\{\omega, \boldsymbol{k}\} = \boldsymbol{0}$) and along the direction $\boldsymbol{n}$ of the $\boldsymbol{k}$-space. This asymptotic expansion, truncated at the N-th term is

$$\omega(\epsilon\, \boldsymbol{n}) \sim \omega_{\boldsymbol{n}}^{(1)}\, \epsilon + \omega_{\boldsymbol{n}}^{(2)}\, \epsilon^2 + \ldots + \omega_{\boldsymbol{n}}^{(N)}\, \epsilon^N = \mathcal{S}_{\boldsymbol{n}}^N(\omega)(\epsilon)\,. \tag{5.27}$$

In the above expansion the $O(\epsilon^0)$ term vanishes because the point $\{\omega, \boldsymbol{k}\} = \boldsymbol{0}$ certainly satisfies the dispersion equation (5.18). This follows from the fact that, setting $\{\omega, \boldsymbol{k}\} = \boldsymbol{0}$, Eq. (5.19) becomes

$$\boldsymbol{A}^*(\boldsymbol{0})\, \hat{\boldsymbol{q}}^*(\boldsymbol{0}) = \boldsymbol{Z}(\boldsymbol{0})^{\mathsf{H}} \boldsymbol{K}(0) \boldsymbol{Z}(\boldsymbol{0})\, \hat{\boldsymbol{q}}^*(\boldsymbol{0}) = \boldsymbol{0}\,, \tag{5.28}$$

so that, since the matrix $\boldsymbol{Z}(\boldsymbol{0})$ prescribes *equal* displacements on corresponding sides of the unit cell (preventing rigid rotations), the only possible solutions $\hat{\boldsymbol{q}}^*(\boldsymbol{0})$ correspond to 2 rigid-body translations, which represent the nullspace of $\boldsymbol{K}(0)$ without rigid rotations. These rigid translations are essentially the limit of the eigenmodes $\boldsymbol{\varphi}_{\boldsymbol{k}}(\boldsymbol{x})$ for $\|\boldsymbol{k}\| \to 0$. Their derivation requires first the construction of the asymptotic expansion of $\boldsymbol{\varphi}_{\boldsymbol{k}}(\boldsymbol{x})$, in complete analogy to Eq. (5.27),

$$\boldsymbol{\varphi}_{\epsilon\,\boldsymbol{n}}(\boldsymbol{x}) \sim \boldsymbol{\varphi}_{\boldsymbol{n}}^{(0)}(\boldsymbol{x}) + \boldsymbol{\varphi}_{\boldsymbol{n}}^{(1)}(\boldsymbol{x})\,\epsilon + \boldsymbol{\varphi}_{\boldsymbol{n}}^{(2)}(\boldsymbol{x})\,\epsilon^2 + \ldots + \boldsymbol{\varphi}_{\boldsymbol{n}}^{(N)}(\boldsymbol{x})\,\epsilon^N = \mathcal{S}_{\boldsymbol{n}}^{N}(\boldsymbol{\varphi})(\epsilon)\,, \tag{5.29}$$

and then the computation of the limit $\epsilon \to 0$. As a result, the zeroth-order term of the waveform $\boldsymbol{\varphi}_{\boldsymbol{n}}^{(0)}$ is indeed *uniform* in space (independent of $\boldsymbol{x}$), and therefore the acoustic properties of the equivalent Cauchy continuum have to satisfy

$$\omega_h(\epsilon\,\boldsymbol{n}) = \omega_{\boldsymbol{n}}^{(1)}\,\epsilon\,, \tag{5.30a}$$

$$\boldsymbol{a}(\epsilon\,\boldsymbol{n}) = \boldsymbol{\varphi}_{\boldsymbol{n}}^{(0)} \qquad \forall \boldsymbol{n} \in \mathbb{R}^2\,, \tag{5.30b}$$

conditions which define an 'acoustic equivalence' between the lattice and the continuum.

An effective method to obtain the series expansions (5.27) and (5.29) is outlined in the following. As the waveform $\boldsymbol{\varphi}_{\boldsymbol{k}}(\boldsymbol{x})$ for a lattice made up of rods is governed by the vector of degrees of freedom $\hat{\boldsymbol{q}}^*$, solution of the eigenvalue problem (5.19), the expansion of $\hat{\boldsymbol{q}}^*(\omega(\boldsymbol{k}), \boldsymbol{k})$ is performed along an arbitrary direction $\boldsymbol{n}$ in the $\boldsymbol{k}$-space

$$\hat{\boldsymbol{q}}^*(\omega(\epsilon\,\boldsymbol{n}), \epsilon\,\boldsymbol{n}) \sim \hat{\boldsymbol{q}}_{\boldsymbol{n}}^{*(0)} + \hat{\boldsymbol{q}}_{\boldsymbol{n}}^{*(1)}\,\epsilon + \hat{\boldsymbol{q}}_{\boldsymbol{n}}^{*(2)}\,\epsilon^2 + \ldots\,, \tag{5.31}$$

so that the first term $\hat{\boldsymbol{q}}_{\boldsymbol{n}}^{*(0)}$ can be used to identify the left-hand side of Eq. (5.30b). To this end, the matrix $\boldsymbol{A}^*(\omega(\boldsymbol{k}), \boldsymbol{k})$ is expanded as

$$\boldsymbol{A}^*(\omega(\epsilon\,\boldsymbol{n}), \epsilon\,\boldsymbol{n}) \sim \boldsymbol{A}_{\boldsymbol{n}}^{*(0)} + \boldsymbol{A}_{\boldsymbol{n}}^{*(1)}\,\epsilon + \boldsymbol{A}_{\boldsymbol{n}}^{*(2)}\,\epsilon^2 + \ldots\,, \tag{5.32}$$

so that the eigenvalue problem (5.19) is rewritten through a substitution of the series representations (5.31) and (5.32) as

$$(\boldsymbol{A}_{\boldsymbol{n}}^{*(0)} + \boldsymbol{A}_{\boldsymbol{n}}^{*(1)}\,\epsilon + \boldsymbol{A}_{\boldsymbol{n}}^{*(2)}\,\epsilon^2 + \ldots)(\hat{\boldsymbol{q}}_{\boldsymbol{n}}^{*(0)} + \hat{\boldsymbol{q}}_{\boldsymbol{n}}^{*(1)}\,\epsilon + \hat{\boldsymbol{q}}_{\boldsymbol{n}}^{*(2)}\,\epsilon^2 + \ldots) = \boldsymbol{0}\,. \tag{5.33}$$

Since the dispersion relation $\omega(\boldsymbol{k})$ is formally inserted in the above expansions, Eq. (5.33) has to be satisfied for every value of ϵ, which means that the left-hand side has to vanish at every order in ϵ. Thus the following

sequence of linear systems is obtained

$$\begin{aligned}
&O(\epsilon^0): \quad \boldsymbol{A}_n^{*(0)}\,\hat{\boldsymbol{q}}_n^{*(0)} = \boldsymbol{0}\,,\\
&O(\epsilon^1): \quad \boldsymbol{A}_n^{*(0)}\,\hat{\boldsymbol{q}}_n^{*(1)} + \boldsymbol{A}_n^{*(1)}\,\hat{\boldsymbol{q}}_n^{*(0)} = \boldsymbol{0}\,,\\
&O(\epsilon^2): \quad \boldsymbol{A}_n^{*(0)}\,\hat{\boldsymbol{q}}_n^{*(2)} + \boldsymbol{A}_n^{*(1)}\,\hat{\boldsymbol{q}}_n^{*(1)} + \boldsymbol{A}_n^{*(2)}\,\hat{\boldsymbol{q}}_n^{*(0)} = \boldsymbol{0}\,,\\
&\quad\vdots \qquad\qquad\qquad\qquad \vdots\\
&O(\epsilon^j): \quad \boldsymbol{A}_n^{*(0)}\,\hat{\boldsymbol{q}}_n^{*(j)} + \sum_{h=1}^{j} \boldsymbol{A}_n^{*(h)}\,\hat{\boldsymbol{q}}_n^{*(j-h)} = \boldsymbol{0}, \qquad \forall j>0\,,
\end{aligned} \tag{5.34}$$

which has to be solved for the unknown vectors $\hat{\boldsymbol{q}}_n^{*(j)}$. It is clear that the computation of these vectors starts from the solution of the zeroth-order equation and then, sequentially, the higher-order terms are to be obtained. At the j-th order, the matrix of the linear system is $\boldsymbol{A}_n^{*(0)}$ and multiplies the unknown vector $\hat{\boldsymbol{q}}_n^{*(j)}$, so that the constant term (not involving the unknown $\hat{\boldsymbol{q}}_n^{*(j)}$) contains all the previously determined vectors $\{\hat{\boldsymbol{q}}_n^{*(0)}, \dots, \hat{\boldsymbol{q}}_n^{*(j-1)}\}$. Moreover, it is important to observe that the terms $\boldsymbol{A}_n^{*(j)}$ in the expansion (5.32) can be computed explicitly once the series $\mathcal{S}_n^N(\omega)(\epsilon)$ has been determined.

It is recalled that, as shown by Eq. (5.28), the matrix of each linear system $\boldsymbol{A}_n^{*(0)}$ is singular and it has a two-dimensional nullspace spanned by two linearly independent vectors, $\boldsymbol{t}_1$ and $\boldsymbol{t}_2$, which represent the two in-plane rigid-body translations.[5] Thus, every linear combination in the form

$$\hat{\boldsymbol{q}}_n^{*(0)} = \alpha_1 \boldsymbol{t}_1 + \alpha_2 \boldsymbol{t}_2, \qquad \forall\{\alpha_1,\alpha_2\}\in\mathbb{R}^2\,, \tag{5.35}$$

is a solution of the zeroth-order equation in (5.34). This implies that the matrix $\boldsymbol{A}_n^{*(0)}$ is not invertible, so that the solvability of the j-th linear system depends on the form of its right-hand side, which has to satisfy the following condition, known as the Fredholm alternative theorem

$$\left(\sum_{h=1}^{j} \boldsymbol{A}_n^{*(h)}\,\hat{\boldsymbol{q}}_n^{*(j-h)}\right)\cdot\boldsymbol{y} = 0, \qquad \forall \boldsymbol{y}\in\ker(\boldsymbol{A}_n^{*(0)}), \qquad \forall j>0\,, \tag{5.36}$$

or, equivalently, using Eq. (5.35), the condition

$$\left(\sum_{h=1}^{j} \boldsymbol{A}_n^{*(h)}\,\hat{\boldsymbol{q}}_n^{*(j-h)}\right)\cdot\boldsymbol{t}_1 = 0\,, \qquad \left(\sum_{h=1}^{j} \boldsymbol{A}_n^{*(h)}\,\hat{\boldsymbol{q}}_n^{*(j-h)}\right)\cdot\boldsymbol{t}_2 = 0, \qquad \forall j>0\,.$$

In principle, Eqs. (5.34) and (5.36) are sufficient to compute the series representations (5.31) and (5.27), thus making conditions (5.30) explicit.

[5] Since $\boldsymbol{t}_1$ and $\boldsymbol{t}_2$ describe two arbitrary rigid translations, $\boldsymbol{t}_1$ and $\boldsymbol{t}_2$ can be conveniently chosen as the rigid translations aligned parallel to $\boldsymbol{e}_1$ and $\boldsymbol{e}_2$, respectively.

5.3.3 The acoustic tensor for a lattice of elastic rods

The perturbation method outlined in Section 5.3.2 is general enough to provide, up to the desired order, the series representation of the acoustic properties of a preloaded lattice subject to incremental dynamics.

It will be proved in the following that it is always possible to employ the above-described perturbation technique to construct an eigenvalue problem governing the propagation of waves in a lattice (where elements are subject to both axial and flexural deformation) in the low-frequency and long-wavelength regime. In particular, this eigenvalue problem will possess the following properties:

(i) the eigenvalues identify the first-order term $\omega_{\boldsymbol{n}}^{(1)}$ of both acoustic branches of the dispersion relation;

(ii) the eigenvectors govern the zeroth-order term of the Floquet-Bloch waveform for both acoustic waves, through coefficients $\{\alpha_1, \alpha_2\}$ in the linear combination (5.35);

(iii) the algebraic structure of the problem is *exactly equivalent* to that governing wave propagation in a Cauchy material, Eq. (5.23).

The construction of the above eigenvalue problem allows the rigorous definition of the 'acoustic tensor for a lattice of elastic rods' and from the latter the identification of the elasticity tensor representing a material equivalent to the lattice. In fact, this eigenvalue problem defines eigenvalues and eigenvectors satisfying the conditions of acoustic equivalence, Eq. (5.30).

In order to construct the eigenvalue problem, the solution of the sequence of the linear systems (5.34) is pursued up to the order $O(\epsilon^2)$. The equations involve the following terms of the series (5.32)

$$\begin{aligned}
\boldsymbol{A}^{*(0)} &= \boldsymbol{Z}^{(0)\mathsf{H}} \boldsymbol{K}^{(0)} \boldsymbol{Z}^{(0)} \,, \\
\boldsymbol{A}_{\boldsymbol{n}}^{*(1)} &= \boldsymbol{Z}^{(0)\mathsf{H}} \boldsymbol{K}^{(0)} \boldsymbol{Z}_{\boldsymbol{n}}^{(1)} + \boldsymbol{Z}_{\boldsymbol{n}}^{(1)\mathsf{H}} \boldsymbol{K}^{(0)} \boldsymbol{Z}^{(0)} \,, \\
\boldsymbol{A}_{\boldsymbol{n}}^{*(2)} &= \boldsymbol{Z}_{\boldsymbol{n}}^{(1)\mathsf{H}} \boldsymbol{K}^{(0)} \boldsymbol{Z}_{\boldsymbol{n}}^{(1)} + \boldsymbol{Z}^{(0)\mathsf{H}} \boldsymbol{K}^{(0)} \boldsymbol{Z}_{\boldsymbol{n}}^{(2)} + \\
&\quad + \boldsymbol{Z}_{\boldsymbol{n}}^{(2)\mathsf{H}} \boldsymbol{K}^{(0)} \boldsymbol{Z}^{(0)} - \boldsymbol{Z}^{(0)\mathsf{H}} \boldsymbol{M}^{(0)} \boldsymbol{Z}^{(0)} \left(\omega_{\boldsymbol{n}}^{(1)}\right)^2 \,,
\end{aligned} \tag{5.37}$$

where a series expansion has been introduced for the matrices $\boldsymbol{K}(\omega(\epsilon\,\boldsymbol{n}))$, $\boldsymbol{M}(\omega(\epsilon\,\boldsymbol{n}))$ and $\boldsymbol{Z}(\epsilon\,\boldsymbol{n})$ as $\epsilon \to 0$. It is important to note that:

(i) up to the order $O(\epsilon^2)$, only the zeroth-order terms of the matrices $\boldsymbol{K}$ and $\boldsymbol{M}$ (which correspond to the quasi-static limit, $\boldsymbol{K}^{(0)} = \lim_{\omega\to 0} \boldsymbol{K}(\omega)$, $\boldsymbol{M}^{(0)} = \lim_{\omega\to 0} \boldsymbol{M}(\omega)$) are present;

(ii) the zeroth-order matrix $\boldsymbol{Z}^{(0)}$, and consequently $\boldsymbol{A}^{*(0)}$, is independent of the direction $\boldsymbol{n}$ (owing to continuity); while $\boldsymbol{A}_{\boldsymbol{n}}^{*(1)}$ is linear in $\boldsymbol{n}$, $\boldsymbol{A}_{\boldsymbol{n}}^{*(2)}$ is quadratic in $\boldsymbol{n}$;

(iii) the linear term $\omega_n^{(1)}$ starts to appear at order $O(\epsilon^2)$.

In the following, the first and second-order equation in the sequence of equations (5.34) are considered and their solvability conditions derived, Eq. (5.36). By means of Eq. (5.35), the first-order equation in the sequence (5.34) reads as

$$O(\epsilon^1): \quad \boldsymbol{A}^{*(0)}\,\hat{\boldsymbol{q}}_n^{*(1)} + \boldsymbol{A}_n^{*(1)}(\alpha_1\boldsymbol{t}_1 + \alpha_2\boldsymbol{t}_2) = \boldsymbol{0}\,, \tag{5.38}$$

and its solvabilty condition requires

$$\boldsymbol{t}_1 \cdot \boldsymbol{A}_n^{*(1)}(\alpha_1\boldsymbol{t}_1 + \alpha_2\boldsymbol{t}_2) = 0\,, \qquad \boldsymbol{t}_2 \cdot \boldsymbol{A}_n^{*(1)}(\alpha_1\boldsymbol{t}_1 + \alpha_2\boldsymbol{t}_2) = 0\,,$$

two conditions which are always satisfied. In fact, a use of Eq. $(5.37)_2$ yields

$$\boldsymbol{t}_j \cdot \boldsymbol{A}_n^{*(1)}\boldsymbol{t}_i = \boldsymbol{t}_j \cdot \left(\boldsymbol{Z}^{(0)\mathsf{H}}\boldsymbol{K}^{(0)}\boldsymbol{Z}_n^{(1)} + \boldsymbol{Z}_n^{(1)\mathsf{H}}\boldsymbol{K}^{(0)}\boldsymbol{Z}^{(0)}\right)\boldsymbol{t}_i\,,$$

a scalar product which vanishes because $\boldsymbol{Z}^{(0)}\boldsymbol{t}_i$ is a rigid-body translation, so that it cannot produce any stress, hence $\boldsymbol{K}^{(0)}\boldsymbol{Z}^{(0)}\boldsymbol{t}_i = \boldsymbol{0}$. Since Eq. (5.38) is always solvable, all its solutions can be expressed in the form

$$\hat{\boldsymbol{q}}_n^{*(1)} = \alpha_1\boldsymbol{t}_1'(\boldsymbol{n}) + \alpha_2\boldsymbol{t}_2'(\boldsymbol{n}) \qquad \forall\{\alpha_1,\alpha_2\} \in \mathbb{R}^2\,, \tag{5.39}$$

where $\boldsymbol{t}_1'$ and $\boldsymbol{t}_2'$ are the solutions of the following two linear systems

$$\boldsymbol{A}^{*(0)}\,\boldsymbol{t}_1'(\boldsymbol{n}) + \boldsymbol{A}_n^{*(1)}\boldsymbol{t}_1 = \boldsymbol{0}\,, \qquad \boldsymbol{A}^{*(0)}\,\boldsymbol{t}_2'(\boldsymbol{n}) + \boldsymbol{A}_n^{*(1)}\boldsymbol{t}_2 = \boldsymbol{0}\,.$$

Note that $\boldsymbol{t}_1'$ and $\boldsymbol{t}_2'$ are defined up to an arbitrary rigid-body translation.

By employing Eqs. (5.35) and (5.39), the linear system of order $O(\epsilon^2)$ reads as

$$O(\epsilon^2): \quad \boldsymbol{A}^{*(0)}\,\hat{\boldsymbol{q}}_n^{*(2)} = -\alpha_1(\boldsymbol{A}_n^{*(1)}\boldsymbol{t}_1'(\boldsymbol{n}) + \boldsymbol{A}_n^{*(2)}\boldsymbol{t}_1) - \alpha_2(\boldsymbol{A}_n^{*(1)}\boldsymbol{t}_2'(\boldsymbol{n}) + \boldsymbol{A}_n^{*(2)}\boldsymbol{t}_2)\,, \tag{5.40}$$

which (because $\boldsymbol{A}^{*(0)}$ is singular) admits a solution if and only if the right-hand side is orthogonal to both $\boldsymbol{t}_1$ and $\boldsymbol{t}_2$, namely

$$\begin{aligned}
&\alpha_1(\boldsymbol{A}_n^{*(1)}\boldsymbol{t}_1'(\boldsymbol{n}) + \boldsymbol{A}_n^{*(2)}\boldsymbol{t}_1)\cdot\boldsymbol{t}_1 + \alpha_2(\boldsymbol{A}_n^{*(1)}\boldsymbol{t}_2'(\boldsymbol{n}) + \boldsymbol{A}_n^{*(2)}\boldsymbol{t}_2)\cdot\boldsymbol{t}_1 = 0\,,\\
&\alpha_1(\boldsymbol{A}_n^{*(1)}\boldsymbol{t}_1'(\boldsymbol{n}) + \boldsymbol{A}_n^{*(2)}\boldsymbol{t}_1)\cdot\boldsymbol{t}_2 + \alpha_2(\boldsymbol{A}_n^{*(1)}\boldsymbol{t}_2'(\boldsymbol{n}) + \boldsymbol{A}_n^{*(2)}\boldsymbol{t}_2)\cdot\boldsymbol{t}_2 = 0\,,
\end{aligned}$$

that in matrix form can be written as[6]

$$\begin{bmatrix}
(\boldsymbol{A}_n^{*(1)}\boldsymbol{t}_1'(\boldsymbol{n}) + \boldsymbol{A}_n^{*(2)}\boldsymbol{t}_1)\cdot\boldsymbol{t}_1 & (\boldsymbol{A}_n^{*(1)}\boldsymbol{t}_2'(\boldsymbol{n}) + \boldsymbol{A}_n^{*(2)}\boldsymbol{t}_2)\cdot\boldsymbol{t}_1\\
(\boldsymbol{A}_n^{*(1)}\boldsymbol{t}_1'(\boldsymbol{n}) + \boldsymbol{A}_n^{*(2)}\boldsymbol{t}_1)\cdot\boldsymbol{t}_2 & (\boldsymbol{A}_n^{*(1)}\boldsymbol{t}_2'(\boldsymbol{n}) + \boldsymbol{A}_n^{*(2)}\boldsymbol{t}_2)\cdot\boldsymbol{t}_2
\end{bmatrix}
\begin{Bmatrix}\alpha_1\\ \alpha_2\end{Bmatrix} = \begin{Bmatrix}0\\ 0\end{Bmatrix}\,. \tag{5.41}$$

[6]Note that vectors $\boldsymbol{t}_j'(\boldsymbol{n})$ may contain an arbitrary rigid-body translation. This would apparently lead to a non-uniqueness in the form of Eq. (5.41), because the terms $\boldsymbol{t}_j \cdot \boldsymbol{A}_n^{*(1)}\boldsymbol{t}_i'(\boldsymbol{n})$ are present. This lack of uniqueness is only apparent, because $\boldsymbol{t}_j \cdot \boldsymbol{A}_n^{*(1)}\boldsymbol{t}_i = 0$.

Up to order $O(\epsilon^1)$ the coefficients $\{\alpha_1, \alpha_2\}$ and the linear term $\omega_n^{(1)}$ remain *completely arbitrary*, but now they have to satisfy the system (5.41) in order to make Eq. (5.40) solvable. In fact, the homogeneous system (5.41) represents an eigenvalue problem with eigenvectors $\{\alpha_1, \alpha_2\}$ and eigenvalues $\left(\omega_n^{(1)}\right)^2$. To see this more explicitly, expressions (5.37) can be substituted into Eq. (5.41) to obtain[7]

$$\overbrace{\begin{bmatrix} \boldsymbol{t}_1 \cdot \tilde{\boldsymbol{K}}_n^{(1)} \boldsymbol{t}_1 + \boldsymbol{t}_1'(\boldsymbol{n}) \cdot \tilde{\boldsymbol{K}}^{(0)} \boldsymbol{t}_1'(\boldsymbol{n}) & \boldsymbol{t}_2 \cdot \tilde{\boldsymbol{K}}_n^{(1)} \boldsymbol{t}_1 + \boldsymbol{t}_2'(\boldsymbol{n}) \cdot \tilde{\boldsymbol{K}}^{(0)} \boldsymbol{t}_1'(\boldsymbol{n}) \\ \boldsymbol{t}_1 \cdot \tilde{\boldsymbol{K}}_n^{(1)} \boldsymbol{t}_2 + \boldsymbol{t}_1'(\boldsymbol{n}) \cdot \tilde{\boldsymbol{K}}^{(0)} \boldsymbol{t}_2'(\boldsymbol{n}) & \boldsymbol{t}_2 \cdot \tilde{\boldsymbol{K}}_n^{(1)} \boldsymbol{t}_2 + \boldsymbol{t}_2'(\boldsymbol{n}) \cdot \tilde{\boldsymbol{K}}^{(0)} \boldsymbol{t}_2'(\boldsymbol{n}) \end{bmatrix}}^{\boldsymbol{\Xi}} \begin{Bmatrix} \alpha_1 \\ \alpha_2 \end{Bmatrix} + \underbrace{\left(\omega_n^{(1)}\right)^2 \begin{bmatrix} \boldsymbol{t}_1 \cdot \tilde{\boldsymbol{M}}^{(0)} \boldsymbol{t}_1 & \boldsymbol{t}_2 \cdot \tilde{\boldsymbol{M}}^{(0)} \boldsymbol{t}_1 \\ \boldsymbol{t}_1 \cdot \tilde{\boldsymbol{M}}^{(0)} \boldsymbol{t}_2 & \boldsymbol{t}_2 \cdot \tilde{\boldsymbol{M}}^{(0)} \boldsymbol{t}_2 \end{bmatrix}}_{\boldsymbol{\Gamma}} \begin{Bmatrix} \alpha_1 \\ \alpha_2 \end{Bmatrix} = \begin{Bmatrix} 0 \\ 0 \end{Bmatrix}, \tag{5.42}$$

with the following definitions

$$\tilde{\boldsymbol{K}}^{(0)} = \boldsymbol{Z}^{(0)\mathsf{H}} \boldsymbol{K}^{(0)} \boldsymbol{Z}^{(0)}, \quad \tilde{\boldsymbol{K}}_n^{(1)} = \boldsymbol{Z}_n^{(1)\mathsf{H}} \boldsymbol{K}^{(0)} \boldsymbol{Z}_n^{(1)}, \quad \tilde{\boldsymbol{M}}^{(0)} = \boldsymbol{Z}^{(0)\mathsf{H}} \boldsymbol{M}^{(0)} \boldsymbol{Z}^{(0)}.$$

Eq. (5.42) is an eigenvalue problem, and the following properties can be deduced:

(i) As the matrices $\tilde{\boldsymbol{K}}^{(0)}$, $\tilde{\boldsymbol{K}}_n^{(1)}$ and $\tilde{\boldsymbol{M}}^{(0)}$ are real and symmetric, also the matrices $\boldsymbol{\Xi}$ and $\boldsymbol{\Gamma}$ are real and symmetric, hence the eigenvalues $\left(\omega_n^{(1)}\right)^2$ are real;

(ii) Since $\boldsymbol{Z}^{(0)}$, $\boldsymbol{t}_1$ and $\boldsymbol{t}_2$ are independent of $\boldsymbol{n}$ and $\boldsymbol{Z}_n^{(1)}$, $\boldsymbol{t}_1'(\boldsymbol{n})$ and $\boldsymbol{t}_2'(\boldsymbol{n})$ are all linear in $\boldsymbol{n}$, each component of the 2-by-2 matrix $\boldsymbol{\Xi}$ is a quadratic form in $\boldsymbol{n}$;

(iii) The components of the 2-by-2 matrix $\boldsymbol{\Gamma}$ admit the following simplifications

$$\boldsymbol{t}_2 \cdot \tilde{\boldsymbol{M}}^{(0)} \boldsymbol{t}_1 = \boldsymbol{t}_1 \cdot \tilde{\boldsymbol{M}}^{(0)} \boldsymbol{t}_2 = 0, \quad \boldsymbol{t}_1 \cdot \tilde{\boldsymbol{M}}^{(0)} \boldsymbol{t}_1 = \boldsymbol{t}_2 \cdot \tilde{\boldsymbol{M}}^{(0)} \boldsymbol{t}_2 = \rho_h \, |C|,$$

where $\rho_h = \frac{1}{|C|} \sum_{k=1}^{N_b} \gamma_k \, l_k$ and $|C|$ are, respectively, the average mass density of the lattice and the area of the unit cell. Note that the matrix $\boldsymbol{\Gamma}$ contains only terms in the form $\boldsymbol{t}_i \cdot \tilde{\boldsymbol{M}}^{(0)} \boldsymbol{t}_j$, where $\boldsymbol{t}_i$ are rigid translations, and therefore *the rotational inertia of the rods plays no role* (recall the definition (5.10a)).

Finally the eigenvalue problem (5.42) can be written in the standard form

$$\left[\boldsymbol{A}^{(\mathrm{L})}(\boldsymbol{n}) - \rho_h \left(\omega_n^{(1)}\right)^2 \boldsymbol{I} \right] \boldsymbol{\alpha} = \boldsymbol{0}, \tag{5.43}$$

[7] The resulting expression has been simplified using again the property $\boldsymbol{K}^{(0)} \boldsymbol{Z}^{(0)} \boldsymbol{t}_i = \boldsymbol{0}$.

where $\boldsymbol{\alpha} = \{\alpha_1, \alpha_2\}^\intercal$ and tensor $\boldsymbol{A}^{(\mathrm{L})}(\boldsymbol{n})$ reads

$$\boldsymbol{A}^{(\mathrm{L})}(\boldsymbol{n}) = \frac{1}{|C|}\begin{bmatrix} \boldsymbol{t}_1 \cdot \tilde{\boldsymbol{K}}_{\boldsymbol{n}}^{(1)} \boldsymbol{t}_1 + \boldsymbol{t}_1'(\boldsymbol{n}) \cdot \tilde{\boldsymbol{K}}^{(0)} \boldsymbol{t}_1'(\boldsymbol{n}) & \boldsymbol{t}_2 \cdot \tilde{\boldsymbol{K}}_{\boldsymbol{n}}^{(1)} \boldsymbol{t}_1 + \boldsymbol{t}_2'(\boldsymbol{n}) \cdot \tilde{\boldsymbol{K}}^{(0)} \boldsymbol{t}_1'(\boldsymbol{n}) \\ \boldsymbol{t}_1 \cdot \tilde{\boldsymbol{K}}_{\boldsymbol{n}}^{(1)} \boldsymbol{t}_2 + \boldsymbol{t}_1'(\boldsymbol{n}) \cdot \tilde{\boldsymbol{K}}^{(0)} \boldsymbol{t}_2'(\boldsymbol{n}) & \boldsymbol{t}_2 \cdot \tilde{\boldsymbol{K}}_{\boldsymbol{n}}^{(1)} \boldsymbol{t}_2 + \boldsymbol{t}_2'(\boldsymbol{n}) \cdot \tilde{\boldsymbol{K}}^{(0)} \boldsymbol{t}_2'(\boldsymbol{n}) \end{bmatrix}. \tag{5.44}$$

It is important to note at this stage, that the eigenvalue problem (5.43) has exactly the same structure of Eq. (5.23). Furthermore, tensor $\boldsymbol{A}^{(\mathrm{L})}(\boldsymbol{n})$, the 'acoustic tensor of the lattice', uniquely defines the eigenvalues and eigenvectors appearing on the right-hand side of the equivalence conditions (5.30), so that $\omega_h = \omega_{\boldsymbol{n}}^{(1)}\epsilon$ and $\boldsymbol{a} = \boldsymbol{\varphi}_{\boldsymbol{n}}^{(0)} = \boldsymbol{\alpha}$. *This implies that the acoustic equivalence holds if and only if the 'acoustic tensor of the lattice' coincides with the acoustic tensor of the Cauchy material.* Therefore, the equivalent Cauchy continuum has to satisfy the acoustic equivalence condition (valid for every unit vector $\boldsymbol{n}$)

$$\boldsymbol{A}^{(\mathbb{C})}(\boldsymbol{n}) = \boldsymbol{A}^{(\mathrm{L})}(\boldsymbol{n}). \tag{5.45}$$

It is important to note that the equivalence condition has been obtained without introducing restrictive assumptions on the lattice structure, so that the homogenization method is completely general and *includes a generic state of axial preload acting on the lattice*. Moreover, the presented technique can easily be extended to three-dimensional lattices.

5.3.4 Identification of the incremental constitutive tensor equivalent to a preloaded lattice

The perturbation method developed in Section 5.3 leads to the determination of the acoustic tensor of an effective Cauchy continuum, equivalent to the low-frequency response of a preloaded lattice of rods. As the method is entirely based on the dynamics of the periodic medium, the acoustic tensor is obtained directly, without any prior computation of the effective constitutive tensor, which is instead traditional in standard energy-based homogenization techniques [97, 98, 121–123].

In this section the steps for retrieving the incremental (or 'tangent') constitutive tensor $\mathbb{C}$ are outlined from the acoustic tensor given by Eq. (5.45).

As the condition (5.45) has to hold for an arbitrary direction of propagation, it can equivalently be expressed by applying the Hessian with respect to $\boldsymbol{n}$ on both sides of Eq. (5.45) to obtain

$$\mathbb{C}_{ikjl} + \mathbb{C}_{iljk} = \frac{\partial^2 A_{ij}^{(\mathrm{L})}(\boldsymbol{n})}{\partial n_k \partial n_l}, \tag{5.46}$$

where the right-hand side can be regarded as a data defined by the lattice structure, namely, the Hessian of tensor (5.44). By considering the symmetry with respect to the $\{k, l\}$ indices, Eq. (5.46) provides a linear system of 54 equations in a three-dimensional setting or 12 equations in a two-dimensional setting, while the rank of the system is found to be 26 or 8, respectively. By recalling that the unknown tensor $\mathbb{C}$ has the form (5.21), it

is clear that, if the system is solvable, all but one of the unknown components of $\mathbb{C}$ can be determined as these are 27 for a three-dimensional lattice and 9 for a two-dimensional.

In order to solve for the identification, results obtained by Max Born [96] can now be generalized to prove that:

(i) the system is solvable when the equations of motions of the lattice satisfy the rotational invariance and

(ii) the solution is unique, except for the spherical part of the prestress (i.e. $\operatorname{tr}\boldsymbol{T}/3$ in 3d and $\operatorname{tr}\boldsymbol{T}/2$ in 2d) which remains undetermined for the system (5.46), but can be determined by matching the first-order incremental work introduced in Chapter 4.

5.4 Bifurcation and loss of ellipticity in a lattice of preloaded elastic rods

In order to demonstrate the effectiveness of the homogenization method developed in Section 5.3, the condition of loss of ellipticity for a preloaded two-dimensional grid lattice of elastic rods is derived and analyzed.

The geometry of the reference configuration is sketched in Fig. 5.4 and is composed of two sets of rods, inclined at an angle α and characterized by an axial stiffness $A_1 = A_2 = A$ and slenderness ratios $\Lambda_1 = l\sqrt{A/B_1}$, $\Lambda_2 = l\sqrt{A/B_2}$, where the subscripts 1 and 2 are relative to the horizontal and inclined rods, respectively. For simplicity, the linear mass density is assumed to be the same for both rods $\gamma_1 = \gamma_2 = \gamma$, while the rotational inertia contribution has been shown in Section 5.3.3 to be negligible for the homogenization result. The resulting grid of rods is also considered

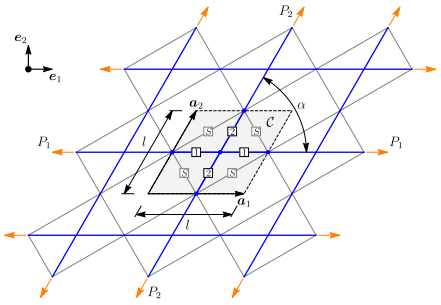

Fig. 5.4. Current configuration of a rhombic lattice of preloaded elastic rods, with the associated unit cell C highlighted. The direct basis for the lattice is denoted by the pair of vectors $\{\boldsymbol{a}_1, \boldsymbol{a}_2\}$. Labels 1, 2, and S denote the horizontal rods, the inclined rods, and the diagonal springs, respectively. The stiffness of inclined springs, the axial and flexural rigidity of the rods, the preloads P_1 and P_2, as well as the grid angle α can all be varied to investigate different incremental responses.

stiffened by diagonal linear springs (Fig. 5.4), whose stiffness k_S is conveniently made dimensionless by introducing the parameter $\kappa = k_S l/A$. In

this configuration, the lattice is subject to a preload state defined by the axial forces P_1 and P_2, made dimensionless respectively as $p_1 = P_1 l^2/B_1$ and $p_2 = P_2 l^2/B_2$. Hence, a lattice configuration is completely defined by the parameter set $\{p_1, p_2, \Lambda_1, \Lambda_2, \kappa, \alpha\}$. Note also that the lattice structure considered includes the simpler case of a rectangular grid that has been analyzed in [19].

5.4.1 Macro and micro bifurcations as degeneracies of the dispersion relation

The effect of the diagonal reinforcement (springs labeled with S in Fig. 5.4) on the bifurcation of the lattice has been systematically investigated in Chapter 4 of this study, where it has been shown to play a fundamental role in determining the wavelength critical for bifurcation. Specifically, it has been demonstrated that an increase in the spring stiffness induces a transition of the critical bifurcation from macroscopic to microscopic, and in particular the bifurcation is characterized by an infinite wavelength when $\kappa = 0$.

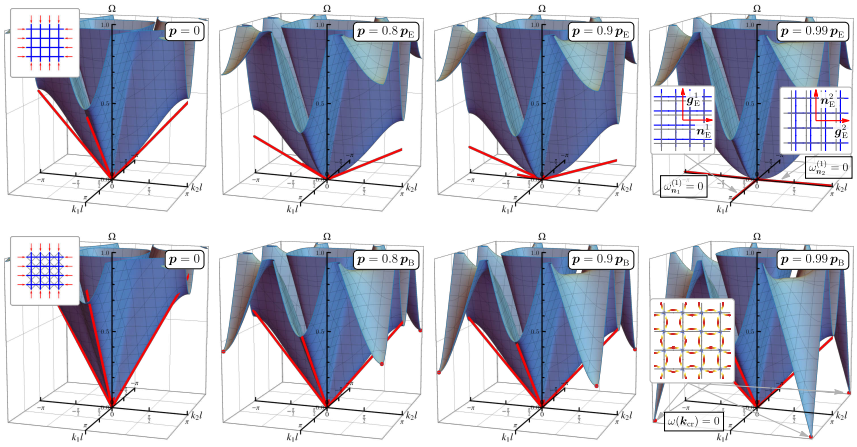

Fig. 5.5. The dispersion surfaces, computed for states of preload of increasing magnitude (from left to right), demonstrate the difference between macroscopic (upper part) and microscopic (lower part) bifurcations occurring in a square grid of elastic rods. The stiffness of the diagonal springs can be tuned to cause a switching of the critical bifurcation mode from macroscopic (low spring stiffness) to microscopic (high spring stiffness). The four surfaces reported in the upper part refer to equibiaxial compression of a square grid with $\Lambda_1 = \Lambda_2 = 10$ and not reinforced with springs, thus experiencing an infinite-wavelength bifurcation corresponding to the vanishing slope of the acoustic branches at the origin (when the preload reaches a critical value $\boldsymbol{p}_{\mathrm{E}} = \{-5.434, -5.434\}$). The four surfaces reported in the lower part refer to the same grid but reinforced with springs ($\kappa = 0.4$), which induces a 'stiffening' of the acoustic branches at the origin and therefore a critical bifurcation occurs, at a preload $\boldsymbol{p}_{\mathrm{B}} = \{-\pi^2, -\pi^2\}$, when the lowering of the dispersion surface causes the generation of a zero-frequency wave with non-null wave vector (corresponding to a finite wavelength buckling).

On the other hand, it can be argued that the dynamical setting formulated here may provide a more direct mechanical interpretation of the significant difference between macroscopic and microscopic bifurcation, compared to a static analysis. In fact, as the homogenization scheme introduced in Section 5.3 proves that the long-wavelength asymptotics for waves propagating in the lattice is governed by the acoustic tensor of the effective medium, Eq. (5.44), it becomes now clear that a macro-bifurcation in the lattice has to be equivalent to failure of ellipticity in its equivalent continuum. Hence, a macro-bifurcation occurs when the velocity of the acoustic long waves of the lattice vanishes along some directions. Moreover, a clear interpretation of short-wavelength bifurcations (micro-bifurcations) is also provided by the analysis of the dispersion relation of the lattice (5.18), interpreted now as a function of the preload state. The latter can be used to identify the condition of buckling in the lattice as the 'propagation' of a Bloch wave at vanishing frequency. In fact, regardless of the critical wavelength, macro and micro bifurcations can be visualized by plotting the evolution of the dispersion surfaces along a loading path up to loss of stability.

The essential difference between the two kinds of bifurcation is exemplified in Fig. 5.5 for two square grids ($\alpha = \pi/2$ and $\Lambda_1 = \Lambda_2 = 10$), one without diagonal springs (upper row in the figure) and the other with $\kappa = 0.4$ (lower row in the figure), subject to equibiaxial compression ($p_1 = p_2$) of increasing magnitude (from left to right in the figure).

The dispersion surfaces (plotted in the non-dimensional space $\{k_1 l, k_2 l, \Omega\}$ with $\Omega = \omega\, l\sqrt{\gamma/A}$ and $\gamma_r = 0$) show that *the macro-bifurcation in the grid without springs occurs with the progressive lowering, and eventually vanishing, of the slope of the acoustic branches at the origin, while the dispersion surface attains non-null frequency for every other wave vector*. On the contrary, the micro-bifurcation occurring in the grid reinforced with springs is characterized by non-vanishing slope of the acoustic branches at the origin, but instead the preload-induced lowering of the dispersion surface causes the generation of a zero-frequency wave with non-null wave vector (corresponding to a finite wavelength buckling). These dispersion surfaces can be considered the dynamic counterpart of the bifurcation surfaces presented in Chapter 4 of this study.

Failure of ellipticity and the consequent emergence of strain localization in the lattice is now investigated following the following steps:

(i) the acoustic tensor $\boldsymbol{A}^{(\mathbb{C})}(\boldsymbol{n})$ of the homogenized continuum is analytically calculated as an explicit function of the set of parameters $\{p_1, p_2, \Lambda_1, \Lambda_2, \kappa, \alpha\}$;

(ii) loss of ellipticity is analyzed for cubic, orthotropic, and completely anisotropic lattices by identifying the prestress states leading to a vanishing eigenvalue of the acoustic tensor, while the corresponding eigenvector identifies the localization mode;

(iii) the ellipticity domain in the $\{p_1, p_2\}$-space and its dependence on lattice parameters $\{\Lambda_1, \Lambda_2, \alpha\}$ is determined;

(iv) the predicted directions and modes of strain localization are compared with the maps of displacements resulting in the equivalent elastic material from the application of a concentrated pulsating force (the time-harmonic Green's function), thus following the so-called 'perturbative approach to localization' introduced in [89];

(v) the behaviour of the equivalent elastic solid is validated through numerical simulations (with finite elements) of the forced low-frequency response of the corresponding preloaded lattice.

5.4.2 Acoustic tensor, eigenvalues, eigenvectors, and ellipticity domain

With reference to the basis $\{\boldsymbol{e}_1, \boldsymbol{e}_2\}$, the acoustic tensor $\boldsymbol{A}^{(\mathbb{C})}(\boldsymbol{n})$ for the continuum equivalent to the homogenized response of the lattice shown in Fig. 5.4 is represented (in two-dimensions) as

$$\begin{aligned}\boldsymbol{A}^{(\mathbb{C})}(\boldsymbol{n}) = A_{11}^{(\mathbb{C})}(\boldsymbol{n})\,\boldsymbol{e}_1\otimes\boldsymbol{e}_1 + A_{12}^{(\mathbb{C})}(\boldsymbol{n})\,\boldsymbol{e}_1\otimes\boldsymbol{e}_2 + \\ + A_{21}^{(\mathbb{C})}(\boldsymbol{n})\,\boldsymbol{e}_2\otimes\boldsymbol{e}_1 + A_{22}^{(\mathbb{C})}(\boldsymbol{n})\,\boldsymbol{e}_2\otimes\boldsymbol{e}_2\,,\end{aligned} \tag{5.47}$$

where the components, computed via Eq. (5.44), are found to be

$$\begin{aligned}A_{11}^{(\mathbb{C})}(\boldsymbol{n}) &= \left(h_{1111}\,n_1^2 + h_{1112}\,n_1n_2 + h_{1122}\,n_2^2\right)A/l\,,\\ A_{12}^{(\mathbb{C})}(\boldsymbol{n}) = A_{21}^{(\mathbb{C})}(\boldsymbol{n}) &= \left(h_{1211}\,n_1^2 + h_{1212}\,n_1n_2 + h_{1222}\,n_2^2\right)A/l\,,\\ A_{22}^{(\mathbb{C})}(\boldsymbol{n}) &= \left(h_{2211}\,n_1^2 + h_{2212}\,n_1n_2 + h_{2222}\,n_2^2\right)A/l\,,\end{aligned}$$

where the components h_{ijkl} are function of the parameter set $\{p_1, p_2, \Lambda_1, \Lambda_2, \kappa, \alpha\}$. Using the same notation as in Chapter 4, the contribution of the rods' grid and the springs are denoted as h_{ijkl}^{G} and h_{ijkl}^{S}, respectively, so that

$$h_{ijkl}(p_1, p_2, \Lambda_1, \phi, \kappa, \alpha) = h_{ijkl}^{\mathrm{G}}(p_1, p_2, \Lambda_1, \phi, \alpha) + h_{ijkl}^{\mathrm{S}}(\kappa, \alpha) \tag{5.48}$$

where $\phi = B_2/B_1$ (note that $\Lambda_2 = \Lambda_1/\sqrt{\phi}$). The full expression for the functions h_{ijkl}^{G} and h_{ijkl}^{S} is the following

$$\begin{aligned}&h_{1111}^{\mathrm{G}}\\ &= \frac{1}{2d\sin\alpha}\left(\sinh\left(\frac{\sqrt{p_2}}{2}\right)\left(\sqrt{p_1}p_2\phi\cosh\left(\frac{\sqrt{p_1}}{2}\right)\left(4\Lambda_1^2\cos(2\alpha)+11\Lambda_1^2+\cos(4\alpha)\left(\Lambda_1^2-p_2\phi\right)+p_2\phi\right)\right.\right.\\ &\quad - 2\sinh\left(\frac{\sqrt{p_1}}{2}\right)\left(11\Lambda_1^2p_1 + 4\Lambda_1^2\cos(2\alpha)(p_1+p_2\phi) + \cos(4\alpha)\left(\Lambda_1^2p_1 + p_2\phi\left(\Lambda_1^2 - p_2\phi\right)\right) + \right.\\ &\quad \left.\left.\left. p_2\phi\left(11\Lambda_1^2 + p_2\phi\right)\right)\right) + p_1\sqrt{p_2}\sinh\left(\frac{\sqrt{p_1}}{2}\right)\cosh\left(\frac{\sqrt{p_2}}{2}\right)\left(4\Lambda_1^2\cos(2\alpha) + \right.\\ &\quad \left.\left. 11\Lambda_1^2 + \cos(4\alpha)\left(\Lambda_1^2 - p_2\phi\right) + p_2\phi\right)\right),\end{aligned}$$

$$
\begin{aligned}
h^{\mathrm{G}}_{1112} = \frac{4\cos\alpha}{d}\Bigg(&\sinh\left(\frac{\sqrt{p_2}}{2}\right)\Bigg(\sqrt{p_1}p_2\phi\cosh\left(\frac{\sqrt{p_1}}{2}\right)\left(\Lambda_1^2+\cos(2\alpha)\left(\Lambda_1^2-p_2\phi\right)+p_2\phi\right)\\
&-2\sinh\left(\frac{\sqrt{p_1}}{2}\right)\left(\Lambda_1^2p_1+\cos(2\alpha)\left(\Lambda_1^2p_1+p_2\phi\left(\Lambda_1^2-p_2\phi\right)\right)+p_2\phi\left(\Lambda_1^2+p_2\phi\right)\right)\Bigg)\\
&+p_1\sqrt{p_2}\sinh\left(\frac{\sqrt{p_1}}{2}\right)\cosh\left(\frac{\sqrt{p_2}}{2}\right)\left(\Lambda_1^2+\cos(2\alpha)\left(\Lambda_1^2-p_2\phi\right)+p_2\phi\right)\Bigg),\\
h^{\mathrm{G}}_{1122} = \frac{2\sin\alpha}{d}\Bigg(&\sinh\left(\frac{\sqrt{p_2}}{2}\right)\Bigg(\sqrt{p_1}p_2\phi\cosh\left(\frac{\sqrt{p_1}}{2}\right)\left(\Lambda_1^2+\cos(2\alpha)\left(\Lambda_1^2-p_2\phi\right)+p_2\phi\right)\\
&-2\sinh\left(\frac{\sqrt{p_1}}{2}\right)\left(\Lambda_1^2p_1+\cos(2\alpha)\left(\Lambda_1^2p_1+p_2\phi\left(\Lambda_1^2-p_2\phi\right)\right)+p_2\phi\left(\Lambda_1^2+p_2\phi\right)\right)\Bigg)\\
&+p_1\sqrt{p_2}\sinh\left(\frac{\sqrt{p_1}}{2}\right)\cosh\left(\frac{\sqrt{p_2}}{2}\right)\left(\Lambda_1^2+\cos(2\alpha)\left(\Lambda_1^2-p_2\phi\right)+p_2\phi\right)\Bigg),\\
h^{\mathrm{G}}_{1211} = \frac{4\cos\alpha}{d}\Bigg(&p_1\sqrt{p_2}\cos^2\alpha\sinh\left(\frac{\sqrt{p_1}}{2}\right)\cosh\left(\frac{\sqrt{p_2}}{2}\right)\left(\Lambda_1^2-p_2\phi\right)\\
&-\sinh\left(\frac{\sqrt{p_2}}{2}\right)\Bigg(\sqrt{p_1}p_2\phi\cos^2\alpha\cosh\left(\frac{\sqrt{p_1}}{2}\right)\left(p_2\phi-\Lambda_1^2\right)\\
&+\sinh\left(\frac{\sqrt{p_1}}{2}\right)\left(\cos(2\alpha)\left(\Lambda_1^2p_1+p_2\phi\left(\Lambda_1^2-p_2\phi\right)\right)+p_1\left(\Lambda_1^2-2p_2\phi\right)+p_2\phi\left(\Lambda_1^2-p_2\phi\right)\right)\Bigg)\Bigg),\\
h^{\mathrm{G}}_{1212} = \frac{4\sin\alpha}{d}\Bigg(&2p_1\sqrt{p_2}\cos^2\alpha\sinh\left(\frac{\sqrt{p_1}}{2}\right)\cosh\left(\frac{\sqrt{p_2}}{2}\right)\left(\Lambda_1^2-p_2\phi\right)\\
&+\sinh\left(\frac{\sqrt{p_2}}{2}\right)\Bigg(2\sqrt{p_1}p_2\phi\cos^2\alpha\cosh\left(\frac{\sqrt{p_1}}{2}\right)\left(\Lambda_1^2-p_2\phi\right)\\
&+2\sinh\left(\frac{\sqrt{p_1}}{2}\right)\left((p_1+p_2\phi)\left(-\left(\Lambda_1^2-p_2\phi\right)\right)-\cos(2\alpha)\left(\Lambda_1^2p_1+p_2\phi\left(\Lambda_1^2-p_2\phi\right)\right)\right)\Bigg)\Bigg),\\
h^{\mathrm{G}}_{1222} = \frac{-4\sin^2\alpha\cos\alpha}{d}\Bigg(&\sinh\left(\frac{\sqrt{p_2}}{2}\right)\Bigg(2\sinh\left(\frac{\sqrt{p_1}}{2}\right)\left(\Lambda_1^2p_1+p_2\phi\left(\Lambda_1^2-p_2\phi\right)\right)\\
&+\sqrt{p_1}p_2\phi\cosh\left(\frac{\sqrt{p_1}}{2}\right)\left(p_2\phi-\Lambda_1^2\right)\Bigg)+p_1\sqrt{p_2}\sinh\left(\frac{\sqrt{p_1}}{2}\right)\cosh\left(\frac{\sqrt{p_2}}{2}\right)\left(p_2\phi-\Lambda_1^2\right)\Bigg),\\
h^{\mathrm{G}}_{2211} =\ &\\
\frac{1}{2d\sin\alpha}\Bigg(&\sinh\left(\frac{\sqrt{p_2}}{2}\right)\Bigg(\sqrt{p_1}p_2\phi\cosh\left(\frac{\sqrt{p_1}}{2}\right)\left(\Lambda_1^2+8p_1+\cos(4\alpha)\left(p_2\phi-\Lambda_1^2\right)+4p_2\phi\cos(2\alpha)+3p_2\phi\right)\\
&-2\sinh\left(\frac{\sqrt{p_1}}{2}\right)\Bigg(8p_1^2-\cos(4\alpha)\left(\Lambda_1^2p_1+p_2\phi\left(\Lambda_1^2-p_2\phi\right)\right)+4p_2\phi\cos(2\alpha)(2p_1+p_2\phi)+\\
&p_1\left(\Lambda_1^2+8p_2\phi\right)+p_2\phi\left(\Lambda_1^2+3p_2\phi\right)\Bigg)\Bigg)+p_1\sqrt{p_2}\sinh\left(\frac{\sqrt{p_1}}{2}\right)\cosh\left(\frac{\sqrt{p_2}}{2}\right)\left(\Lambda_1^2+\\
&8p_1+\cos(4\alpha)\left(p_2\phi-\Lambda_1^2\right)+4p_2\phi\cos(2\alpha)+3p_2\phi\right)\Bigg),\\
h^{\mathrm{G}}_{2212}&\\
= \frac{-4\cos\alpha}{d}\Bigg(&\sinh\left(\frac{\sqrt{p_2}}{2}\right)\Bigg(2\sinh\left(\frac{\sqrt{p_1}}{2}\right)\left(-\cos(2\alpha)\left(\Lambda_1^2p_1+p_2\phi\left(\Lambda_1^2-p_2\phi\right)\right)+p_1\left(\Lambda_1^2+2p_2\phi\right)+\\
&p_2\phi\left(\Lambda_1^2+p_2\phi\right)\Bigg)-\sqrt{p_1}p_2\phi\cosh\left(\frac{\sqrt{p_1}}{2}\right)\left(\Lambda_1^2+\cos(2\alpha)\left(p_2\phi-\Lambda_1^2\right)+p_2\phi\right)\Bigg)\\
&-p_1\sqrt{p_2}\sinh\left(\frac{\sqrt{p_1}}{2}\right)\cosh\left(\frac{\sqrt{p_2}}{2}\right)\left(\Lambda_1^2+\cos(2\alpha)\left(p_2\phi-\Lambda_1^2\right)+p_2\phi\right)\Bigg),
\end{aligned}
$$

$$
\begin{aligned}
&h^{\mathrm{G}}_{2222}\\
&= \frac{-2\sin\alpha}{d}\left(\sinh\left(\frac{\sqrt{p_2}}{2}\right)\left(2\sinh\left(\frac{\sqrt{p_1}}{2}\right)\left(\Lambda_1^2 p_1 - \cos(2\alpha)\left(\Lambda_1^2 p_1 + p_2\phi\left(\Lambda_1^2 - p_2\phi\right)\right) + p_2\phi\left(\Lambda_1^2 + p_2\phi\right)\right)\right.\right.\\
&\qquad\left.\left. - \sqrt{p_1}p_2\phi\cosh\left(\frac{\sqrt{p_1}}{2}\right)\left(\Lambda_1^2 + \cos(2\alpha)\left(p_2\phi - \Lambda_1^2\right) + p_2\phi\right)\right)\right.\\
&\qquad\left. - p_1\sqrt{p_2}\sinh\left(\frac{\sqrt{p_1}}{2}\right)\cosh\left(\frac{\sqrt{p_2}}{2}\right)\left(\Lambda_1^2 + \cos(2\alpha)\left(p_2\phi - \Lambda_1^2\right) + p_2\phi\right)\right),
\end{aligned}
$$

where

$$
\begin{aligned}
d = e^{-\frac{1}{2}\left(\sqrt{p_1}+\sqrt{p_2}\right)}\Lambda_1^2\left(\left(e^{\sqrt{p_1}}\left(\sqrt{p_1}-2\right)+\sqrt{p_1}+2\right)\left(e^{\sqrt{p_2}}-1\right)p_2\phi - 2\left(e^{\sqrt{p_1}}-1\right)p_1\left(e^{\sqrt{p_2}}-1\right)\right.\\
\left. + \left(e^{\sqrt{p_1}}-1\right)p_1\left(e^{\sqrt{p_2}}+1\right)\sqrt{p_2}\right).
\end{aligned}
$$

The components h^{S}_{ijkl}, ruling the effect of diagonal springs, can be written as

$$
\begin{aligned}
&h^{\mathrm{S}}_{1111} = \kappa\frac{5+3\cos(2\alpha)}{4\sin\alpha}, \quad h^{\mathrm{S}}_{1112} = 2\kappa\cos\alpha, && h^{\mathrm{S}}_{1211} = \kappa\cos\alpha,\\
&h^{\mathrm{S}}_{1212} = \kappa\sin\alpha, && h^{\mathrm{S}}_{1122} = h^{\mathrm{S}}_{2211} = h^{\mathrm{S}}_{2222} = \frac{1}{2}\kappa\sin\alpha, \quad h^{\mathrm{S}}_{1222} = h^{\mathrm{S}}_{2212} = 0.
\end{aligned}
$$

An inspection of the above expressions shows that the dependence on the prestress state is quite complex for the components h^{G}_{ijkl} and that the limit for $\boldsymbol{p} \to \mathbf{0}$ yields the acoustic tensor of the unloaded grid

$$
\begin{aligned}
&\lim_{\boldsymbol{p}\to\mathbf{0}} h^{\mathrm{G}}_{1111} = 12\sin\alpha\cos^2\alpha \Big/ \left(\Lambda_1^2+\Lambda_2^2\right) + \csc(\alpha) + \cos^3\alpha\cot(\alpha),\\
&\lim_{\boldsymbol{p}\to\mathbf{0}} h^{\mathrm{G}}_{1112} = 2\sin^2\alpha\cos\alpha\left(\cot^2(\alpha)\left(\Lambda_1^2+\Lambda_2^2\right)+12\right) \Big/ \left(\Lambda_1^2+\Lambda_2^2\right),\\
&\lim_{\boldsymbol{p}\to\mathbf{0}} h^{\mathrm{G}}_{1122} = \sin^3\alpha\left(\cot^2(\alpha)\left(\Lambda_1^2+\Lambda_2^2\right)+12\right) \Big/ \left(\Lambda_1^2+\Lambda_2^2\right),\\
&\lim_{\boldsymbol{p}\to\mathbf{0}} h^{\mathrm{G}}_{1211} = \cos\alpha\left(\cos(2\alpha)\left(\Lambda_1^2+\Lambda_2^2-12\right)+\Lambda_1^2+\Lambda_2^2+12\right) \Big/ \left(2\Lambda_1^2+2\Lambda_2^2\right),\\
&\lim_{\boldsymbol{p}\to\mathbf{0}} h^{\mathrm{G}}_{1212} = \sin\alpha\left(\cos(2\alpha)\left(\Lambda_1^2+\Lambda_2^2-12\right)+\Lambda_1^2+\Lambda_2^2\right) \Big/ \left(\Lambda_1^2+\Lambda_2^2\right),\\
&\lim_{\boldsymbol{p}\to\mathbf{0}} h^{\mathrm{G}}_{1222} = \sin^2\alpha\cos\alpha\left(\Lambda_1^2+\Lambda_2^2-12\right) \Big/ \left(\left(\Lambda_1^2+\Lambda_2^2\right)\right.,\\
&\lim_{\boldsymbol{p}\to\mathbf{0}} h^{\mathrm{G}}_{2211} = \sin\alpha\left(\cos(2\alpha)\left(\Lambda_1^2+\Lambda_2^2-12\right)+\Lambda_1^2+\Lambda_2^2+12\right) \Big/ \left(2\Lambda_1^2+2\Lambda_2^2\right),\\
&\lim_{\boldsymbol{p}\to\mathbf{0}} h^{\mathrm{G}}_{2212} = \sin\alpha\sin(2\alpha)\left(\Lambda_1^2+\Lambda_2^2-12\right) \Big/ \left(\Lambda_1^2+\Lambda_2^2\right),\\
&\lim_{\boldsymbol{p}\to\mathbf{0}} h_{2222} = \sin\alpha\left(-\cos(2\alpha)\left(\Lambda_1^2+\Lambda_2^2-12\right)+\Lambda_1^2+\Lambda_2^2+12\right) \Big/ \left(2\Lambda_1^2+2\Lambda_2^2\right).
\end{aligned}
$$

For the special case of a square grid $\alpha = \pi/2$ and in the absence of prestress, the acoustic tensor can be further simplified into

$$\lim_{\boldsymbol{p}\to\boldsymbol{0}} \boldsymbol{A}^{(\mathbb{C})}(\boldsymbol{n})\big|_{\alpha=\pi/2} = \frac{A}{l}\left(n_1^2 + \frac{12n_2^2}{\Lambda_1^2+\Lambda_2^2}\right)\boldsymbol{e}_1\otimes\boldsymbol{e}_1 + \\ + \frac{A}{l}\frac{12n_1n_2}{\Lambda_1^2+\Lambda_2^2}(\boldsymbol{e}_1\otimes\boldsymbol{e}_2+\boldsymbol{e}_2\otimes\boldsymbol{e}_1) + \frac{A}{l}\left(\frac{12n_1^2}{\Lambda_1^2+\Lambda_2^2}+n_2^2\right)\boldsymbol{e}_2\otimes\boldsymbol{e}_2\,.$$

It is recalled that the homogenized Cauchy material is defined to be *strongly elliptic* (SE) when the acoustic tensor is positive definite,

$$\boldsymbol{g}\cdot\boldsymbol{A}^{(\mathbb{C})}(\boldsymbol{n})\,\boldsymbol{g} > 0, \quad \forall \boldsymbol{g}\neq\boldsymbol{0}, \quad \forall \boldsymbol{n}\neq\boldsymbol{0} \qquad \Longleftrightarrow \qquad \text{(SE)}\,, \tag{5.49}$$

while *ellipticity* is defined as the non-singularity of the acoustic tensor,

$$\det \boldsymbol{A}^{(\mathbb{C})}(\boldsymbol{n}) \neq 0, \quad \forall \boldsymbol{n}\neq\boldsymbol{0} \qquad \Longleftrightarrow \qquad \text{(E)}\,. \tag{5.50}$$

As shown in Section 5.3.3, the acoustic tensor resulting from homogenization is symmetric, which implies that its eigenvalues are always real. This means that, letting $\{c_1^2, c_2^2\}$ be the eigenvalues of a symmetric $\boldsymbol{A}^{(\mathbb{C})}(\boldsymbol{n})$, (SE) is equivalent to the strict positiveness of the eigenvalues, $c_1^2 > 0$, $c_2^2 > 0$, and (E) is equivalent to the condition of non-vanishing eigenvalues, $c_1^2 \neq 0$, $c_2^2 \neq 0$ (for all unit vectors $\boldsymbol{n}$).

Geometry	*Rods slenderness*	*Symmetry*	$\boldsymbol{p}_{\mathrm{E}}$	θ_{cr}
Square	$\Lambda_1 = \Lambda_2 = 10$	Cubic	$-5.434\,\{1,1\}$	$0°, 90°$
($\alpha = \pi/2$)	$\Lambda_1 = 7$, $\Lambda_2 = 15$	Orthotropic	$-2.071\,\{1,1\}$	$0°$
Rhombus	$\Lambda_1 = \Lambda_2 = 10$	Orthotropic	$-5.345\,\{1,1\}$	$88.2°, 151.8°$
($\alpha = \pi/3$)	$\Lambda_1 = 7$, $\Lambda_2 = 15$	Anisotropic	$-2.043\,\{1,1\}$	$151.4°$

Table 5.1. Loss of ellipticity for different geometric configurations of the preloaded grid-like lattice (Fig. 5.4) in the absence of diagonal springs ($\kappa = 0$). The symmetry class is referred to the unloaded configuration. The preload $\boldsymbol{p}_{\mathrm{E}}$ and the localization direction $\boldsymbol{n}_{\mathrm{E}} = \cos(\theta_{\mathrm{cr}})\boldsymbol{e}_1 + \sin(\theta_{\mathrm{cr}})\boldsymbol{e}_2$ are obtained by solving the loss of ellipticity condition (5.51) (assuming a radial path $\boldsymbol{p} = \{p_1, p_1\}$) and therefore identifies a material state on the elliptic boundary.

The objective is now to characterize *failure of (E)* by studying the eigenvalues of (5.47) as functions of the preload state applied to the grid-like lattice. To this end, solutions are sought for the following loss of ellipticity condition

$$c_1^2(\boldsymbol{n},\boldsymbol{p})\,c_2^2(\boldsymbol{n},\boldsymbol{p}) = 0\,, \tag{5.51}$$

where $\boldsymbol{n}$ is the usual unit vector defining the direction of propagation and $\boldsymbol{p} = \{p_1, p_2\}$ is a vector simply collecting the preload parameters. In Eq. (5.51) the dependence on the geometric parameters $\{\alpha, \Lambda_1, \Lambda_2\}$ is omitted for brevity and moreover, without loss of generality, it is assumed that $c_1^2 \leq c_2^2$. For

(a) $p_1 = p_2 = -5.434$, $\Lambda_1 = \Lambda_2 = 10$, $\alpha = \pi/2$ (b) $p_1 = p_2 = -2.071$, $\Lambda_1 = 7$, $\Lambda_2 = 15$, $\alpha = \pi/2$

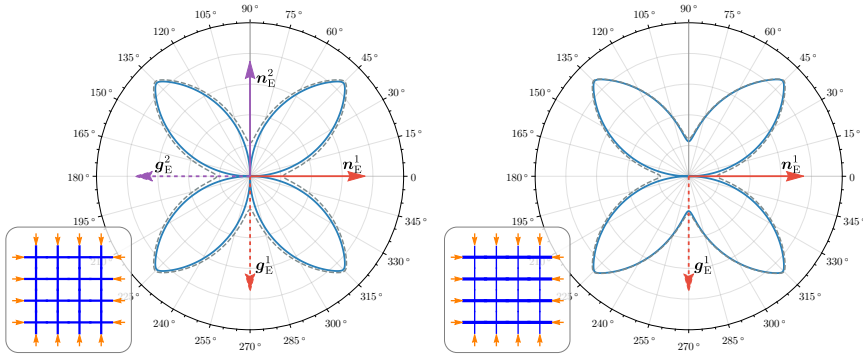

(c) $p_1 = p_2 = -5.345$, $\Lambda_1 = \Lambda_2 = 10$, $\alpha = \pi/3$ (d) $p_1 = p_2 = -2.043$, $\Lambda_1 = 7$, $\Lambda_2 = 15$, $\alpha = \pi/3$

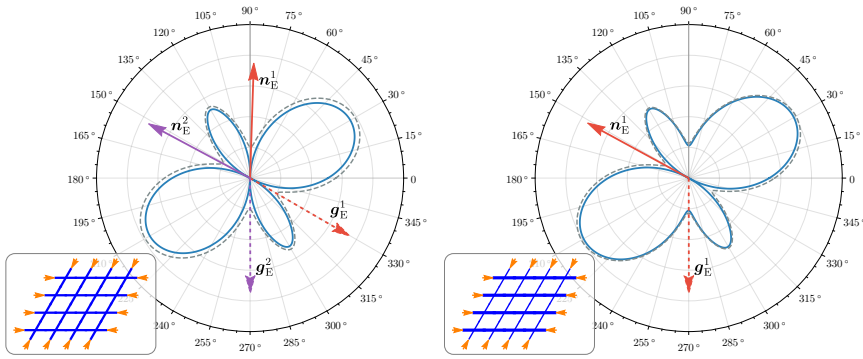

Fig. 5.6. Polar plots of the lowest eigenvalue of the acoustic tensor (5.47), for a prestress state at 50% (dashed gray line) and 100% (continuous blue line) of the limit value for ellipticity loss ($\boldsymbol{p}_E$ reported in Table 5.1). A square lattice and a rhombic lattice are considered with $\Lambda_1 = \Lambda_2 = 10$ and $\Lambda_1 = 7$, $\Lambda_2 = 15$. The prestress state for ellipticity loss is represented on the the elliptic boundary of Fig. 5.7 as the terminal point of the loading path (gray dashed arrow). In the orthotropic cases, both for squared and rhombic lattices, the loss of ellipticity is characterized by the vanishing of the eigenvalue of the acoustic tensor along two directions denoted as $\boldsymbol{n}_E^1$ and $\boldsymbol{n}_E^2$, with the associated wave amplitudes reported as $\boldsymbol{g}_E^1$ and $\boldsymbol{g}_E^2$. The fully anisotropic cases, displays the vanishing of the eigenvalue along a single direction $\boldsymbol{n}_E^1$. Note that for the rhombic lattice the relative orientation of $\boldsymbol{n}_E$ with respect to $\boldsymbol{g}_E$ shows that the mode of localization is neither a pure shear nor a pure expansion wave, but a mixing of the two. Conversely, the square lattice always reaches loss of ellipticity through the formation of pure shear bands.

every solution $\{\boldsymbol{n}_E, \boldsymbol{p}_E\}$ of Eq. (5.51), the eigenvector $\boldsymbol{g}_E = \boldsymbol{g}(\boldsymbol{n}_E)$ associated to the vanishing eigenvalue can be computed. Vectors $\boldsymbol{n}_E$ and $\boldsymbol{g}_E$ will be respectively referred as the *direction* (more precisely, the normal to) and *mode* of the strain localization band.

It can be directly verified that in the absence of preload, $\boldsymbol{p} \to \boldsymbol{0}$, the grid-like lattice considered has $c_1^2 > 0$ and $c_2^2 > 0$, so that (SE) holds, except in the case of an extreme material, where the stiffness of the the rods becomes vanishing small, as in [106]. Due to the symmetry of $\boldsymbol{A}^{(\mathbb{C})}(\boldsymbol{n})$, it follows

that, starting from the unloaded state $\boldsymbol{p} = \mathbf{0}$ with rods of finite stiffness and continuously varying the prestress, the material remains (SE) as long as (E) holds. Therefore, solutions of Eq. (5.51) are sought as pairs $\{\boldsymbol{n}_\mathrm{E}, \boldsymbol{p}_\mathrm{E}\}$ such that $\boldsymbol{p}_\mathrm{E}$ represents the terminal point of a path starting at $\boldsymbol{p} = \mathbf{0}$ and entirely contained in the (SE) domain; in other words, $\boldsymbol{p}_\mathrm{E}$ is on the boundary of the (SE) domain. The set of these points $\boldsymbol{p}_\mathrm{E}$ is referred as the *elliptic boundary*.

In order to explore loss of ellipticity for lattice configurations characterized by different symmetry classes, a square and a rhombic grid are considered, respectively with $\alpha = \pi/2$ and $\alpha = \pi/3$. For both examples, the following sets of slenderness values are selected $\Lambda_1 = \Lambda_2 = 10$, and $\Lambda_1 = 7$, $\Lambda_2 = 15$.

In Table 5.1, for each geometry considered, the first solution of Eq. (5.51) for equal prestress components $p_1 = p_2$ are reported together with the associated directions of localization, denoted as $\boldsymbol{n}_\mathrm{E} = \cos(\theta_\mathrm{cr})\boldsymbol{e}_1 + \sin(\theta_\mathrm{cr})\boldsymbol{e}_2$. Note that the symmetry class is referred here to the unloaded configuration, so that the symmetry of incremental response may change as an effect of loading. With the assumed values for grid angle α and slenderness, the cubic, orthotropic, and fully anisotropic cases (10 constants for planar elasticity) can be investigated.

In order to better visualize the direction $\boldsymbol{n}_\mathrm{E}$ and the associated mode $\boldsymbol{g}_\mathrm{E}$, a polar plot of the square root of the lowest eigenvalue $c_1(\boldsymbol{n}, \boldsymbol{p})$ is reported in Fig. 5.6, for the cases listed in Table 5.1, at two levels of preload, namely $0.5\,\boldsymbol{p}_\mathrm{E}$ (dashed gray line) and $\boldsymbol{p}_\mathrm{E}$ (continuous blue line). In Fig. 5.6a the square lattice with $\Lambda_1 = \Lambda_2 = 10$ is subject to a isotropic prestress in the two directions, $p_1 = p_2$, and therefore the cubic symmetry is maintained in the prestressed state. Owing to this symmetry, ellipticity is lost along two orthogonal directions $\boldsymbol{n}_\mathrm{E}^1$ and $\boldsymbol{n}_\mathrm{E}^2$. Moreover, the associated wave amplitudes $\boldsymbol{g}_\mathrm{E}^1$ and $\boldsymbol{g}_\mathrm{E}^2$ are perpendicular to the vector $\boldsymbol{n}_\mathrm{E}^1$ and $\boldsymbol{n}_\mathrm{E}^2$ respectively, hence indicating that the modes of localization are pure shear waves, the so-called *shear bands*.

For the orthotropic square lattice ($\Lambda_1 = 7$, $\Lambda_2 = 15$), the polar plot is given in Fig. 5.6b. In this case, owing to the orthotropy, waves propagating along the horizontal and vertical direction possess different velocities and therefore ellipticity is lost when the smallest of these velocities vanishes, leading to a single shear band (in this case with a normal $\boldsymbol{n}_\mathrm{E}^1$ aligned parallel to the horizontal direction).

Quite remarkably, *the shear wave responsible for the ellipticity loss is the one propagating along the direction of the 'stiffer' elastic link* (having the lowest slenderness), *while intuitively a 'shear mechanism' would be expected in the direction of the 'soft' elastic link*. This effect will be confirmed and explained further with the computation of the forced response in Section 5.5. Moreover, it is worth noting that the shear band directions for the square lattice, both cubic and orthotropic, are aligned parallel to the directions of the rods forming the lattice.

For the rhombic lattice with $\Lambda_1 = \Lambda_2 = 10$ and isotropic preload, shown in Fig. 5.6c, the mechanical behaviour is orthotropic and therefore two directions of localization are obtained. The associated wave amplitudes $\boldsymbol{g}_\mathrm{E}^1$

and $\boldsymbol{g}_{\mathrm{E}}^{2}$ both have respectively a component orthogonal and parallel to the vector $\boldsymbol{n}_{\mathrm{E}}^{1}$ and $\boldsymbol{n}_{\mathrm{E}}^{2}$, so that a 'mixture' of shear and compression waves is involved.

The fully anisotropic version for the rhombic lattice (Fig. 5.6d) can be obtained by changing the slenderness values ($\Lambda_1 = 7$, $\Lambda_2 = 15$), so that one of the two localizations is suppressed, while the other is preserved. It is also worth noting that, in contrast to the square case, the directions of localization for the rhombic lattice are not perfectly aligned parallel to the rods' normal, instead, they result slightly inclined, as will be confirmed by the computations reported in Section 5.5.

5.4.3 The effect of the prestress directionality on the ellipticity loss and localization directions

In the previous section, the loss of ellipticity has been determined for the four lattice's configurations reported Table 5.1, under the assumption of isotropic preload $p_1 = p_2$. This hypothesis is now removed to explore the influence of the 'directionality' of the preload state on the ellipticity loss, in terms of number and direction of strain localizations. The analysis is performed by computing the full set of solutions $\{\boldsymbol{n}_{\mathrm{E}}, \boldsymbol{p}_{\mathrm{E}}\}$ of Eq. (5.51), to determine the elliptic boundary in the $\{p_1, p_2\}$-space, for several values of rods' inclination α and slenderness $\lambda_{1,2}$.

Fig. 5.7a and 5.7b show the ellipticity domains computed, respectively, for the orthotropic ($\Lambda_1 = \Lambda_2 = 10$) and the anisotropic grid ($\Lambda_1 = 7$, $\Lambda_2 = 15$). The following observations can be drawn.

(i) The elliptic region is unbounded for tensile (positive) preload and bounded when at least one of the preloads is compressive (negative); this is an expected feature, as the contribution of a tensile preload to the potential energy, Eq. (5.8), is positive definite;

(ii) any deviation of the angle α from $\pi/2$ reduces the size of the elliptic region;

(iii) in the orthotropic case, the domain is symmetric with respect to the bisector $p_1 = p_2$ (Fig. 5.7a);

(iv) the elliptic boundary appears to be smooth everywhere except at a corner point;

(v) the anisotropy induced by different values of slenderness causes the corner to move; the elliptic region is reduced in size along the direction of the smallest slenderness.

In the same figure, the region of *positive definiteness* (PD) of the elastic tensor, $\boldsymbol{X} \cdot \mathbb{C}\boldsymbol{X} > 0 \ \forall \boldsymbol{X} \neq \boldsymbol{0}$, is also reported. Surprisingly, the (PD) region is found to be independent of the rods' angle α.

The directions of localization in terms of critical angle θ_{cr} are reported in Figs. 5.7c and 5.7d for different values of the lattice inclination α, with

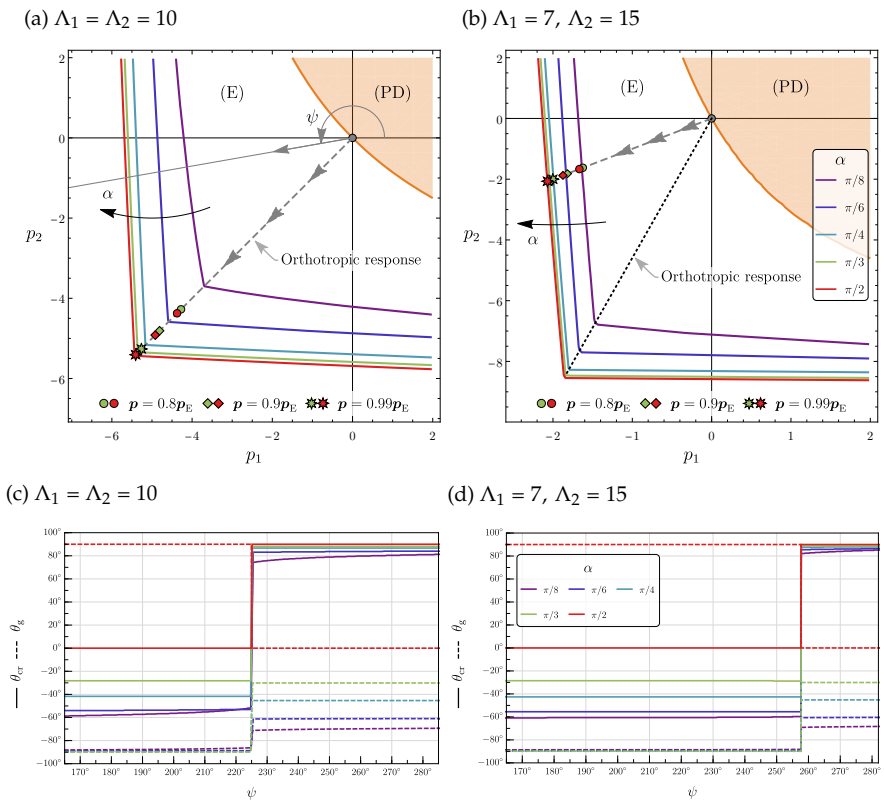

Fig. 5.7. Ellipticity domains for the grid-like lattice of preloaded elastic rods, computed for different values of rods' angle α and for both (a) orthotropy ($\Lambda_1 = \Lambda_2 = 10$) and (b) full anisotropy ($\Lambda_1 = 7$, $\Lambda_2 = 15$). The region of positive definiteness of the elasticity tensor $\mathbb{C}$ is also reported (orange region). The loading path (gray dashed arrow) refers to condition of isotropic preload $p_1 = p_2$ on which the markers (in red for the case $\alpha = \pi/2$ and green for $\alpha = \pi/3$) identify the preload levels used in the computation of the forced response (Section 5.5). Parts (c) and (d) report the relationship between the direction in the preload space (defined by the angle $\psi = \arctan(p_1, p_2)$, see part (a)) and the dyad $\boldsymbol{n}_E \otimes \boldsymbol{g}_E$ defined by the angles θ_{cr} and θ_g singling out, respectively, the direction of ellipticity loss and of the localization mode (i.e. $\boldsymbol{n}_E = \cos\theta_{cr}\boldsymbol{e}_1 + \sin\theta_{cr}\boldsymbol{e}_2$ and $\boldsymbol{g}_E = \cos\theta_g\boldsymbol{e}_1 + \sin\theta_g\boldsymbol{e}_2$). Notice that the case of localization along two directions (corresponding to the jumps visible in the graphs of part (c) and (d)) only occurs for a prestress state at the corner point of the elliptic boundary, which corresponds to an incrementally orthotropic material behaviour.

the purpose of quantifying the influence of the loading path (parameterized by means of the angle $\psi = \arctan(p_1, p_2)$). These plots show that only one localization occurs, except for a loading direction corresponding to a corner point on the elliptic boundary, where two simultaneous localizations occur. Even though this is expected for the orthotropic case (due to symmetry), the anisotropic grid can also exhibit a sort of 'orthotropic' response (displaying two localizations) when a proper value of preload $p_1 \neq p_2$ is applied (along the dashed black line of Fig. 5.7b). Furthermore, the angle between the

vectors $\boldsymbol{n}_{\mathrm{E}}^{1,2}$ and the horizontal axis (Fig. 5.7c and 5.7d), which identifies the direction of the localization bands, depends weakly on the prestress (except at the corner point of the elliptic boundary), namely, the directions of $\boldsymbol{n}_{\mathrm{E}}^{1,2}$ follow the orientations of the grid's ligaments, even if they result slightly misaligned.

5.5 Time-harmonic forced response near the elliptic boundary

The analysis of the homogenized continuum, equivalent to a preloaded grid of elastic rods (presented in Section 5.4) predicts that the incremental response can display strain localizations due to prestress-induced loss of ellipticity. In this section, the homogenization is validated through comparisons between the actual low-frequency forced response of the lattice (simulated numerically with a finite element technique) and the time-harmonic Green's function (which can be found in [119]) for the equivalent continuum, both computed at increasing levels of the preload, so that the elliptic boundary is approached. The comparison is performed for the four geometric configurations reported in Table 5.1 and for four prestress levels, namely $\{0, 0.8, 0.9, 0.99\}\, \boldsymbol{p}_{\mathrm{E}}$ (with $\boldsymbol{p}_{\mathrm{E}}$ being the prestress state leading to ellipticity loss), which are marked on the loading path of Fig. 5.7a and 5.7b.

The lattice response is numerically analyzed using the COMSOL Multiphysics® finite elements program in the frequency response mode. A square finite-size computational window with a width of 350 unit cells (of dimension $350 l_1$, with l_1 denoting the cell edge) is considered, with a perfectly matched layer (PML) along the boundaries, so that here waves are not reflected, rather absorbed, and the response of an infinite body is simulated.

A pulsating concentrated force, in-plane applied, is considered acting at the center of the computational domain. For a given load, the complex displacement field $\boldsymbol{u}(\boldsymbol{x})$, with horizontal and vertical components $u_1(x_1, x_2)$ and $u_2(x_1, x_2)$, is computed and the results are plotted in terms of the modulus of the displacement associated to its real part only, $\delta_R(x_1, x_2) = \sqrt{(\Re u_1)^2 + (\Re u_2)^2}$ (the plots of the imaginary part of the displacement is omitted for brevity).

In all the following analyses the frequency of the pulsating force is set to be $\Omega = \omega\, l \sqrt{\gamma/A} = 0.01$, a low value providing a reasonable match, in term of acoustic properties, between the effective continuum and the lattice. In fact, it is important to note that the mismatch between the two is different from zero for any non-vanishing frequency, even though vanishing in the limit $\Omega \to 0$. In particular, as the elliptic boundary is approached, this mismatch is expected to become wider for those waves propagating along the direction of ellipticity loss. This is easily explained by the fact that, as the *linear* term in the dispersion relation tends to vanish (in a direction

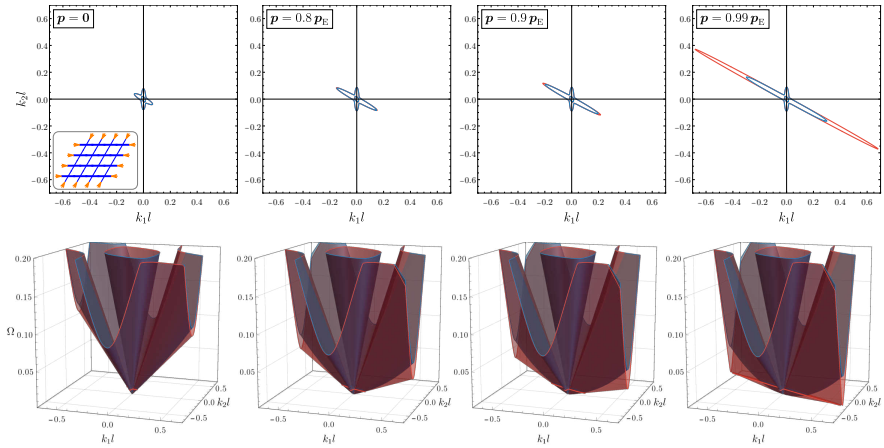

Fig. 5.8. Slowness contours and dispersion surfaces for a rhombic anisotropic lattice with $\Lambda_1 = 7$, $\Lambda_2 = 15$ (in blue) and for the effective Cauchy continuum (in red) at frequency $\Omega = 0.01$. The evolution of the contours and dispersion surfaces induced by a compressive preload of equal components $p_1 = p_2$ along two inclined directions (the considered loading path is depicted in Fig. 5.7b) demonstrates that the nonlinear dispersion of the lattice is negligible, except when the material is very close to the elliptic boundary, namely, for a prestress above $0.9\,\boldsymbol{p}_E$. The comparison between the behaviours of the lattice and its equivalent continuum shows a great agreement.

$\boldsymbol{n}_E$), the *nonlinear* dispersion of the lattice becomes non-negligible for any *non-vanishing* frequency.

By considering for instance the rhombic anisotropic grid ($\Lambda_1 = 7$, $\Lambda_2 = 15$), the deviation between the responses of the lattice (reported in blue in Fig. 5.8) and its equivalent continuum (reported in red in Fig. 5.8) can be visualized in terms of slowness contours computed at the frequency $\Omega = 0.01$. By comparing the contours for the four preload states, it can be appreciated that these are superimposed up $0.9\,\boldsymbol{p}_E$, so that the nonlinear dispersion of the lattice becomes non-negligible only when the material is very close to the elliptic boundary, namely, at a preload $0.99\,\boldsymbol{p}_E$, and only for waves close to the direction of ellipticity loss. It is also worth noting that when $\boldsymbol{p} \approx \boldsymbol{p}_E$, the slowness contour of the lattice (reported in blue) is always contained inside the contour of the continuum (reported in red), so that the nonlinear dispersion implies that waves speeds are slightly *higher* for the lattice than for the effective Cauchy medium.

5.5.1 Square lattice

Cubic and orthotropic square grids are considered, subject to a pulsating diagonal force (inclined at 45° with respect to the rods' axes), with the purpose of revealing the emergence of strain localizations aligned parallel and orthogonal to the rod axes.

The case of cubic symmetry ($\Lambda_1 = \Lambda_2 = 10$) is analyzed in Fig. 5.9, where the displacement field, numerically computed for the square grid (subject

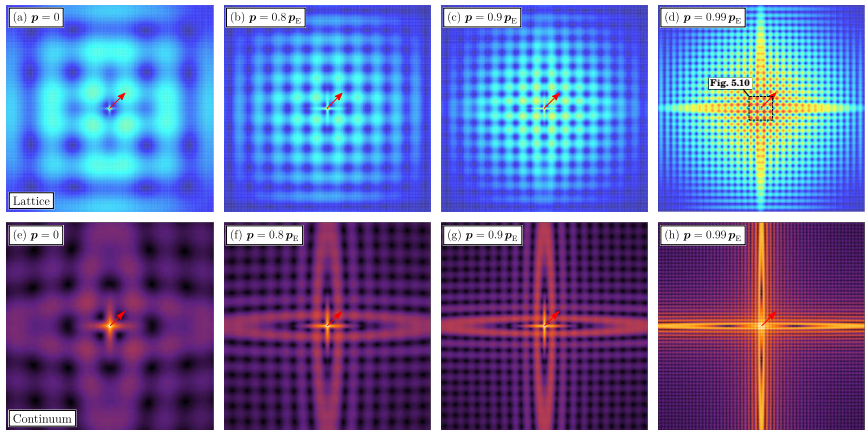

Fig. 5.9. The displacement field generated by a pulsating diagonal force (denoted with a red arrow and applied to the square lattice with cubic symmetry, $\Lambda_1 = \Lambda_2 = 10$) is simulated via f.e.m. [parts (a)–(d)] and compared to the response of the homogenized continuum [parts (e)–(h)] at different levels of prestress $\boldsymbol{p}$ (preload path shown in Fig. 5.7a). Note the emergence of two orthogonal shear bands, aligned parallel to the directions predicted at failure of ellipticity, see Fig. 5.6a.

to a pulsating concentrated force, upper row), is compared to the response of the homogenized continuum (analytically solved with applied the same concentrated force, lower row), for four values of prestress (increasing from left to right, $p_1 = p_2 = \{0, -3.347, -4.891, -5.380\}$). As the elliptic boundary is approached, the emergence of two strain localizations becomes evident and confirms the predicted vanishing of an eigenvalue (wave speed) reported in Fig. 5.6a.

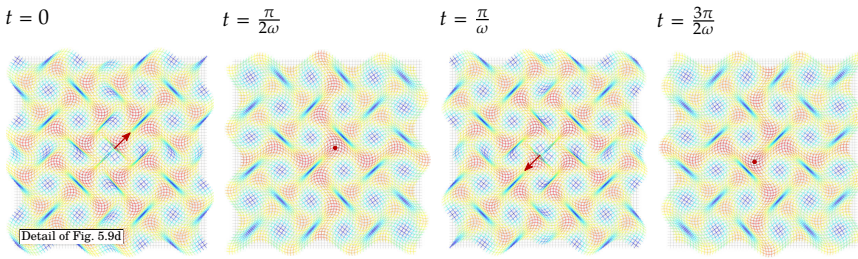

Fig. 5.10. Deformed configurations of a square lattice ($\Lambda_1 = \Lambda_2 = 10$) near (the zone is indicated in Fig. 5.9d) the point of application of a pulsating force (denoted with a red arrow) at a level of prestress close to the elliptic boundary ($\boldsymbol{p} = 0.99\,\boldsymbol{p}_{\mathrm{E}}$). The pattern shows a motion resulting from the superposition of two shear localizations induced by a pulsating diagonal load.

By taking different snapshots of the displacement map at different instants of time during the dynamic response of the grid and near the point of application of the pulsating force, it is possible to detect the actual localization mode activated by the applied diagonal force. In fact, deformed configurations calculated in the grid (the zone is indicated in Fig. 5.9d)

through a finite element simulation and plotted in Fig. 5.10 reveal a characteristic motion resulting from the superposition of two shear localizations emanating from the loading point.

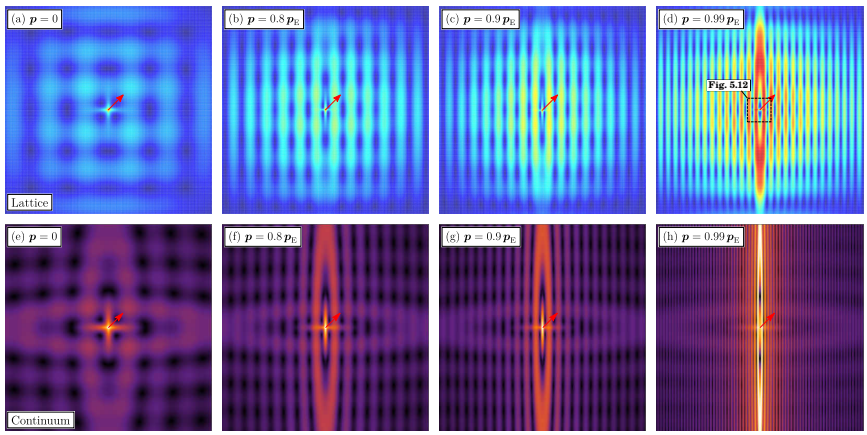

Fig. 5.11. The displacement field generated by a pulsating diagonal force (denoted with a red arrow and applied to the orthotropic square lattice, $\Lambda_1 = 7$, $\Lambda_2 = 15$) is simulated via f.e.m. [parts (a)–(d)] and compared to the response of the homogenized continuum [parts (e)–(h)] at different levels of prestress $\boldsymbol{p}$ (preload path shown in Fig. 5.7b). Note the emergence of a single vertical strain localization, actually a shear band, as predicted in Fig. 5.6b.

The square grid displays a strain localization into a *single* shear band when the slenderness values of the two orthogonal elastic links are set to be different, thus breaking the cubic symmetry, but preserving orthotropy. The response of the grid with $\Lambda_1 = 7$ and $\Lambda_2 = 15$ is reported in Fig. 5.11 for four preload states corresponding to $p_1 = p_2 = \{0, -1.657, -1.864, -2.050\}$. As already revealed by Fig. 5.6b, a single vertical shear band emerges, thus confirming the counter-intuitive result obtained in the previous section, namely that *the shear wave responsible for the ellipticity loss is the one propagating along the direction of the 'stiffest' elastic link* (which possesses the lowest slenderness). The mechanism underlying this effect is revealed by analyzing the actual deformed configuration of the grid reported in Fig. 5.12 (plotted at different instants of time and obtained via f.em. simulations). The figure, which refers to the zone indicated in Fig. 5.11d, reveals that the vertical strain localization emerges from a prevalent bending deformation of the 'soft' vertical links accompanied by an approximately rigid rotation of the 'stiff' horizontal rods, which is allowed by a large rotation at the nodes.

The comparison between the responses of the grid and of the homogenized continuum that has been presented in Figs. 5.9 and 5.11 shows an almost perfect agreement from low to high prestress levels, up to values close to the elliptic boundary. Nonetheless, the slowness contours reported in Fig. 5.8 shows a mismatch between the responses of the lattice and of the equivalent continuum, which becomes clearly visible when the lattice is close to the failure of ellipticity. This can be revealed by considering the

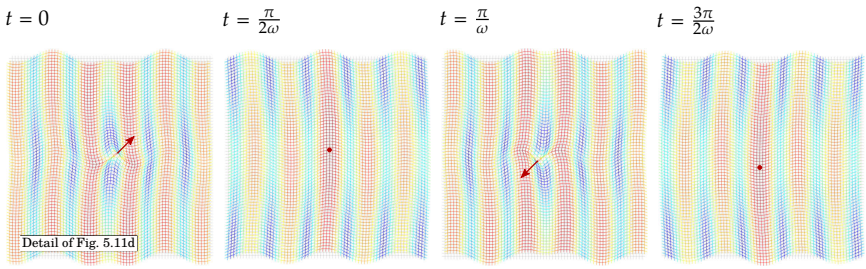

Fig. 5.12. Deformed configurations of the square lattice ($\Lambda_1 = 7$, $\Lambda_2 = 15$) near (the zone is indicated in Fig. 5.11d) the point of application of a pulsating concentrated force (denoted with a red arrow) at a level of prestress close to the elliptic boundary ($\boldsymbol{p} = 0.99\,\boldsymbol{p}_{\mathrm{E}}$). The pattern shows the characteristic motion of a single vertical shear band localization induced by the pulsating load. It can be noticed that the localization emerges from a prevalent bending deformation of the 'soft' vertical links and an approximately rigid rotation of the 'stiff' horizontal rods allowed by a significant rotation of the junctions.

(a) Cubic square lattice ($\Lambda_1 = \Lambda_2 = 10$) (b) Orthotropic square lattice ($\Lambda_1 = 7$, $\Lambda_2 = 15$)

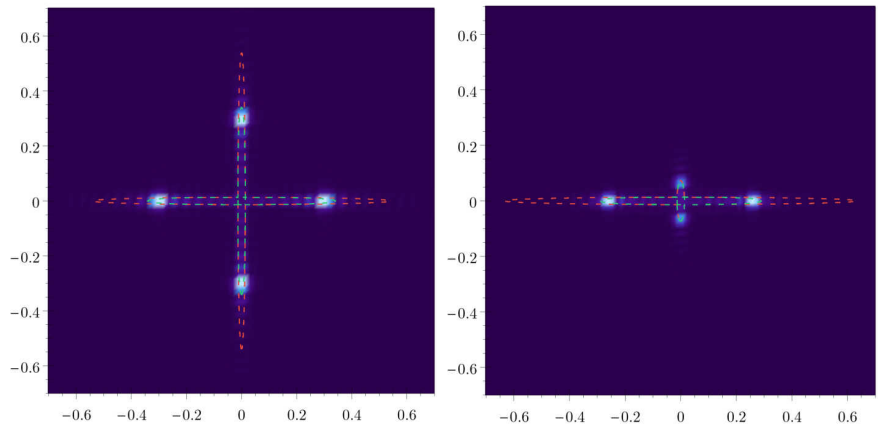

Fig. 5.13. Fourier transform of the complex displacement fields of the cubic (a) and orthotropic (b) square lattice subject to a diagonal force in the center and a prestress state of $\boldsymbol{p} = 0.99\,\boldsymbol{p}_{\mathrm{E}}$ (i.e. close to the elliptic boundary). The slowness contours of the lattice (dashed green) and the effective continuum (dashed red) are superimposed to highlight the Bloch spectrum of waves excited by the forcing source. Note that the strong focus of the spectrum indicates that few plane waves, namely those 'slow' waves that are close to cause the ellipticity loss, prevail on the response as it expected for a material near the elliptic boundary. In fact it is worth noting that for the orthotropic grid (b) the waves propagating vertically remains mostly inactivated compared to the ones propagating horizontally.

lattice's complex displacement field (reported in the last column of Figs. 5.9 and 5.11, prestressed at $\boldsymbol{p} = 0.99\,\boldsymbol{p}_{\mathrm{E}}$), computing its Fourier transform and superimposing this to the corresponding slowness contour. This is reported in Fig. 5.13, where the Fourier transform shows that, for both considered square grids, the Bloch spectrum of waves excited by the diagonal load matches the slowness contour of the lattice (reported in green) and is also

highly focused around the directions of ellipticity loss where it is at the maximum distance from the contour of the continuum (reported in red). It is worth noting that the strong focus of the spectrum confirms the fact that few plane waves, namely those 'slow' waves that are close to cause the ellipticity loss, prevail on the response, as it is expected for a material near the elliptic boundary.

5.5.2 Rhombic lattice

In the previous section, the square lattice was shown to display only localizations in the form of pure shear bands perfectly aligned parallel to the elastic ligaments. However, on the basis of the analysis performed in Section 5.4, the formation of localizations is expected along different directions and with different deformation modes when a rhombic grid is considered, $\alpha \neq \pi/2$.

In order to investigate the response of the orthotropic ($\Lambda_1 = \Lambda_2 = 10$) and anisotropic ($\Lambda_1 = 7$, $\Lambda_2 = 15$) rhombic lattices ($\alpha = \pi/3$), both horizontal and vertical concentrated forces will be considered, so to observe a dependence of the number of strain localizations on the loading orientation. Furthermore, in contrast to what happens in the square grid, the directions of localization are expected to occur with a slight misalignment with respect to the directions of the rods, as predicted in Figs. 5.6c and 5.6d.

In Fig. 5.14 the displacement field computed via f.e.m. for the orthotropic rhombic lattice (horizontally and vertically loaded with a pulsating force and reported on first and third row from the top of the figure) is compared to the response of the homogenized continuum (reported in the second and fourth row) at four values of preload (increasing from left to right) corresponding to $p_1 = p_2 = \{0, -4.276, -4.811, -5.292\}$. By comparing Figs. 5.14a–5.14d to Figs. 5.14e–5.14h and Figs. 5.14i–5.14l to Figs. 5.14m–5.14p, the agreement between the lattice response and its homogenized continuum becomes evident at each state of lattice's preload. With reference to a prestress state $\boldsymbol{p} = 0.99\,\boldsymbol{p}_{\mathrm{E}}$ (last column on the right of the figure), while two localization bands are activated by the vertical force, only one is generated by the horizontal force.

Note also that the slight misalignment between the localization direction and the rod angle remains hardly visible *until the material is close to elliptic boundary* (compare for example the case of vanishing prestress, Fig. 5.14a, to the case $\boldsymbol{p} = 0.99\,\boldsymbol{p}_{\mathrm{E}}$, Fig. 5.14d).

The localization modes are analyzed in Fig. 5.15 by inspecting the lattice deformation computed via f.e.m. at different temporal instants through snapshots taken in the neighbourhood of the loading point [two zones are considered, which do not include the concentrated force and are shown in Fig. 5.14 parts (d) and (l)]. By comparing the localization band induced by the horizontal load (upper row of Fig. 5.15) to the one generated by the vertical force (second row in Fig. 5.15), it is clear that the horizontal band is characterized by an almost perfectly straight wavefront, while the inclined band displays a periodic modulation along the front. This modulation is

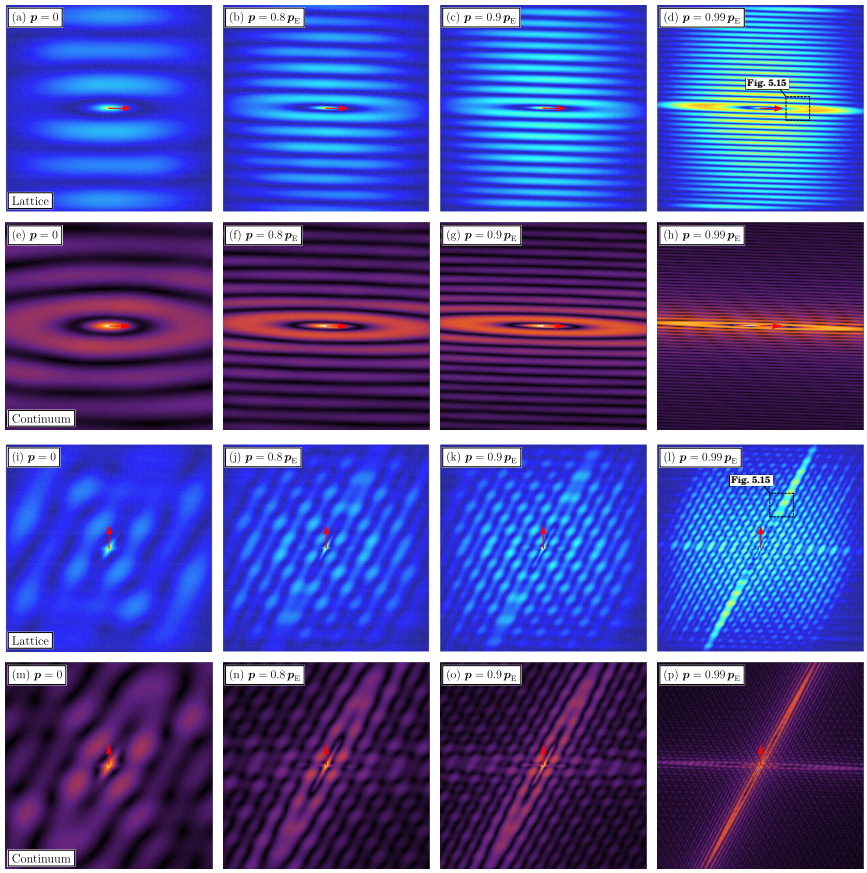

Fig. 5.14. The displacement field generated by a pulsating *horizontal* force (denoted with a red arrow and applied to the orthotropic rhombic lattice, $\Lambda_1 = \Lambda_2 = 10$) is simulated via f.e.m. [parts (a)–(d)] and compared to the response of the homogenized continuum [parts (e)–(h)] at different levels of prestress $\boldsymbol{p}$ (preload path shown in Fig. 5.7a). The same comparison is reported in parts (i)–(l) and (m)–(p) for a pulsating *vertical* force. Note that, even though ellipticity is lost along the two directions predicted in Fig. 5.6c, the activation of strain localization depends on the orientation of the load, so that two bands are activated by the vertical force, while only one is generated by the horizontal load. Furthermore, note that the directions of the localization bands (with angles of the normal equal to $\theta_{\mathrm{cr}} = 88.2°, 151.8°$) is slightly misaligned with respect to the rod's inclination.

due to the superposition of the two localization patterns that are activated by the vertical force, where the inclined band prevails on the almost horizontal one, as can be seen in Figs. 5.14l and 5.14p.

The relative contribution of the two localizations can be further investigated through a Fourier transform of the lattice response, to be compared with the Bloch spectrum generated by the forcing source. Fig. 5.16 shows the Fourier transform of the field generated in the rhombic grid when the material is close to the elliptic boundary ($\boldsymbol{p} = 0.99\,\boldsymbol{p}_{\mathrm{E}}$). Fig. 5.16a and 5.16b

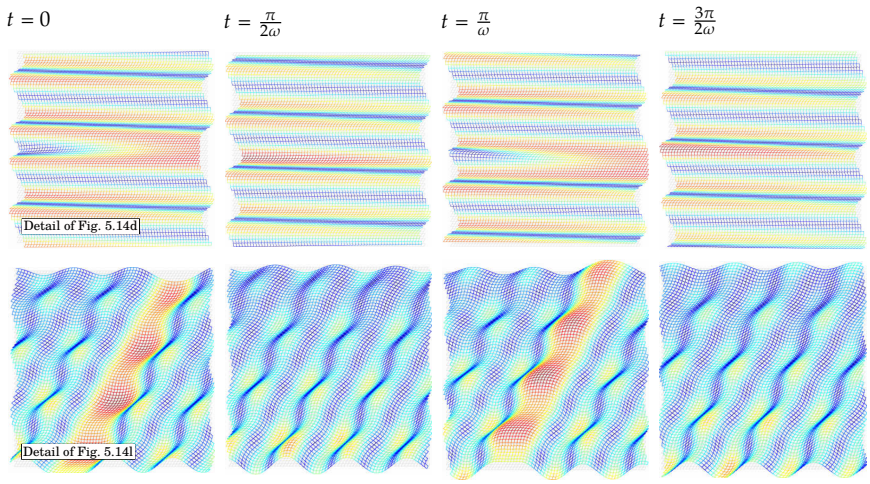

Fig. 5.15. Deformed configurations of the rhombic lattice ($\Lambda_1 = \Lambda_2 = 10$) near (the zones are indicated Fig. in 5.14 parts d and l) the point of application of a pulsating concentrated force, at a level of prestress close to the elliptic boundary ($\boldsymbol{p} = 0.99\,\boldsymbol{p}_{\mathrm{E}}$). The pattern on the first (the second) row shows the motion of the localization induced by the pulsating horizontal (pulsating vertical) load. Note that the effect of the load is the generation of bands almost parallel to each other and possessing almost constant amplitude, except for a modulation of the inclined localization (shown in the lower row). In both cases the deformation mode is mostly of shear-type even though an 'expansion' component is also present, as indicated by the vectors $\boldsymbol{g}_{\mathrm{E}}$, Fig. 5.6c.

correspond, respectively, to the Fourier transform of Fig. 5.14d and Fig. 5.14l. The two sharp peaks of Fig. 5.16a clearly show that the source is emanating pure plane waves propagating almost vertically ($\theta_{\mathrm{cr}} = 88.2°$) (the slight tilt exactly matches the sub-horizontal wavefronts of the response). Instead, the four peaks of Fig. 5.16b demonstrate that two families of plane waves are activated: the prevailing ones propagate along the inclined direction ($\theta_{\mathrm{cr}} = 151.8°$) while the vertically-propagating waves result dimmer (in agreement with the response of Fig. 5.14l).

Results obtained with the same setting used to generate Fig. 5.14 (relative to an orthotropic rhombic lattice) are reported in Fig. 5.17, which now refers to an *anisotropic* rhombic lattice ($\Lambda_1 = 7,\ \Lambda_2 = 15$), for four values of prestress, $p_1 = p_2 = 0, -1.634, -1.839, -2.023$.

For a complete anisotropic material only a single localization is expected to occur and in the case of the anisotropic grid considered the localization direction has been predicted in Fig. 5.6d to occur at an inclination $\theta_{\mathrm{cr}} = 151.4°$ of the band normal. However, similarly to the case of the orthotropic grid, the activation of the localization depends on the orientation of the perturbing force. This can be observed by comparing the lattice response generated by a horizontal and a vertical pulsating force, both reported in Fig. 5.17 and showing that strain localization is absent when a horizontal force is applied, regardless of the prestress level (see Figs. 5.17a–5.17h). On the other hand, the vertical concentrated force triggers an inclined localization when the

(a) Horizontal loading (b) Vertical loading

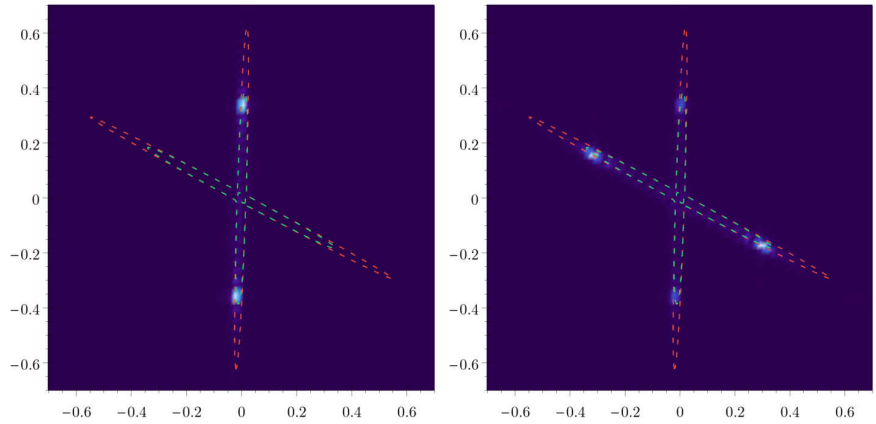

Fig. 5.16. Fourier transform of the complex displacement fields of the rhombic lattice (reported in Fig. 5.14 parts d and l, with $\Lambda_1 = \Lambda_2 = 10$) subject to an horizontal (a) and vertical (b) pulsating force applied at a prestress close to the elliptic boundary, $\boldsymbol{p} = 0.99\,\boldsymbol{p}_{\mathrm{E}}$. The slowness contours of the lattice (dashed green) and of the effective continuum (dashed red) are superimposed to highlight the Bloch spectrum of waves excited by the forcing source. Note that the sharp peaks are aligned to the directions of ellipticity loss as predicted in Fig. 5.6c. In part (a) the horizontal concentrated force only activates waves propagating at $\theta_{\mathrm{cr}} = 88.2°$, while in (b) the vertical concetrated force generates four peaks along the directions $\theta_{\mathrm{cr}} = 88.2°, 151.8°$. This is well in agreement with the responses reported in Figs. 5.14d and 5.14l.

material is brought close to ellipticity loss (see Figs. 5.17i–5.17p).

Results reported in Figs. 5.18 and 5.19, referred to the *anisotropic* rhombic lattice have been obtained with the same setting of Figs. 5.15 and 5.16, referring to the orthoptropic case.

Fig. 5.18 shows that, as only one localization band is present, the deformation pattern is characterized by the generation of essentially straight wavefronts propagating outwards from the localization band. The generation of these parallel waves is perfectly captured by the sharp peaks in the Fourier transform of the lattice response, reported in Fig. 5.19. Fig. 5.19a and 5.19b correspond, respectively, to the Fourier transform of Fig. 5.17d and Fig. 5.17l. The two sharp peaks of Fig. 5.19b, sitting at the long tips of the contour aligned parallel to the direction $\theta_{\mathrm{cr}} = 151.4°$, clearly shows that the response induced by the vertical force involves pure plane waves propagating with fronts inclined at $\theta_{\mathrm{cr}} = 151.4° - 90° = 61.4°$ with respect to the horizontal axis.

It is also important to note that waves do not propagate vertically when the load is vertical while these are the only waves composing the response triggered by a horizontal force (see the peaks on the short tips of the contour in Fig. 5.19a). This is in agreement with the fact that localization is not generated by the horizontal force and the 'slow waves' leading the homogenized continuum to ellipticity loss remain inactive.

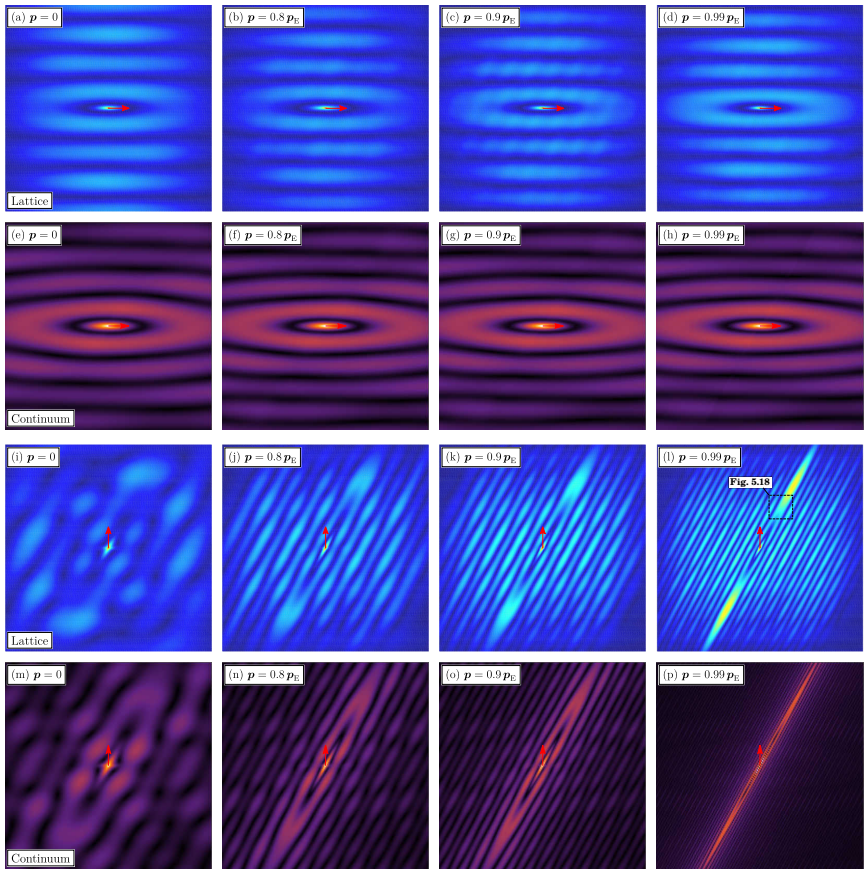

Fig. 5.17. As for Fig. 5.14, except that an *anisotropic* rhombic lattice ($\Lambda_1 = 7$, $\Lambda_2 = 15$) is considered, for four different levels of preload (the path is shown in Fig. 5.7b). Note that, even though ellipticity is lost along the direction predicted in Fig. 5.6d (with normal angle $\theta_{cr} = 151.4°$), the activation of the strain localization depends on the orientation of the applied pulsating force, so that the band is activated by the vertical force while localization is inhibited when the grid is loaded horizontally.

5.6 Conclusions

An analytic formulation has been developed for the dynamics of lattices of elastic rods (with distributed mass density and rotational inertia) subject to axial forces of arbitrary amount, incrementally loaded in the plane. This formulation leads, through an asymptotic expansion of Floquet-Bloch waves, to a low frequency approximation for an equivalent Cauchy elastic material which turns out to be coincident with that determined on the basis of an energy match (see Chapter 4 of this study).

The developed technique can be employed to systematically analyze

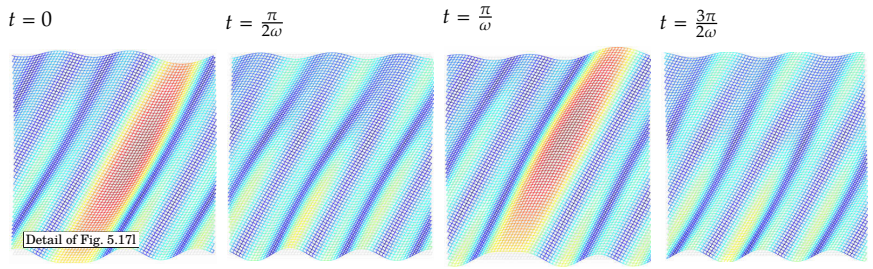

Fig. 5.18. As for Fig. 5.15, except that an *anisotropic* rhombic lattice ($\Lambda_1 = 7$, $\Lambda_2 = 15$) is considered, for four different levels of preload (the path is shown in Fig. 5.7b). The zone reported in the figure is shown in Fig. 5.17l. The pattern shows the motion of the localization induced by the pulsating vertical load, which generates waves emanating outwards from the localization band, parallel to each other, and possessing an almost constant amplitude. The deformation mode is mostly of shear-type even though an 'expansion' component is also present, as indicated by the vector $\boldsymbol{g}_{\mathrm{E}}$ reported in Fig. 5.6d.

(a) Horizontal loading (b) Vertical loading

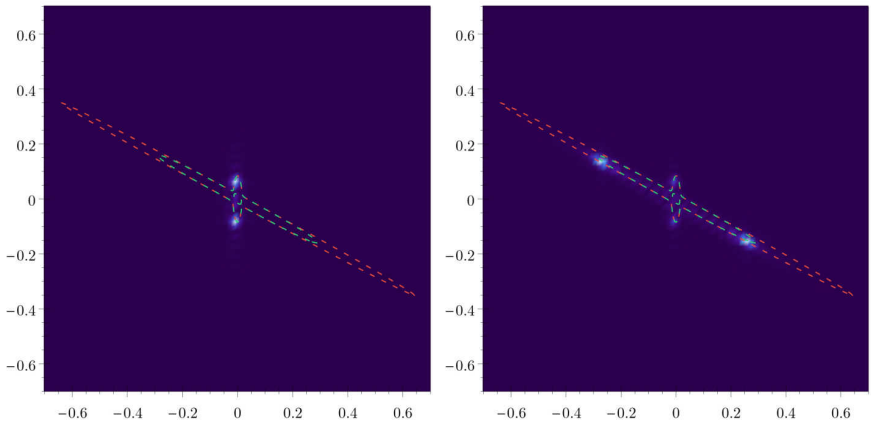

Fig. 5.19. As for Fig. 5.16, except that an *anisotropic* rhombic lattice ($\Lambda_1 = 7$, $\Lambda_2 = 15$) is considered and the Fourier transform refers to the displacement fields reported in Figs. 5.17d and 5.17l. Localization is absent when the pulsating force is horizontal, (a), as the waves sitting on the long tips of the contours remain inactive. The vertical force triggers two peaks along the direction $\theta_{\mathrm{cr}} = 151.4°$, which is in fact the direction normal to the localization band, (b). The Fourier transform is in perfect agreement with the responses shown in Figs. 5.17d and 5.17l.

arbitrary lattice geometries and preloaded configurations, therefore predicting both local and global material instabilities, in other words micro-buckling and strain localizations. Loss of ellipticity has been analyzed for a skewed grid-like lattice, to (i) explore cubic, orthotropic and fully anisotropic homogenized material responses, (ii) compute the elliptic domain of the homogenized continuum as a function of lattice parameters, (iii) analyse the structure of the acoustic branches close to ellipticity loss, and (iv) investigate forced vibrations (both in physical and Fourier spaces) revealing low-frequency wave localizations. The homogenization is proven

to yield a superb approximation to the behaviour of the rod's lattice, except when micro-buckling occurs, which remains undetected in the equivalent continuum.

A

Tuning a dynamic interface by designing its slenderness

This appendix presents a different strategy of obtaining the dynamic interfaces presented in Chapter 3. In fact, the effect of total reflection, negative refraction, and wave channeling can also be obtained without prestress, but through a proper choice of the slenderness λ of the beams. The drawback of this strategy is that the tunability of the system is lost, as the material domain has to be preconceived for a specific application, by assigning the appropriate slenderness to each structural element.

The results obtained with this strategy are reported in Fig. A.1, illustrating the case of total reflection, wave trapping, and negative refraction. Fig. A.1a shows how a signal induced by a moment (of out-of-plane axis), pulsating at the frequency $\Omega = 3.43$, applied to a lattice with beams of slenderness $\lambda = 10$ is totally reflected by a structured interface made of beams with slenderness $\lambda = 20$. Taking advantage of this total reflection effect, it is possible to channel waves along a path by applying a pulsating moment, inside of a layer of beams with slenderness $\lambda = 10$, embedded in a lattice of beams with $\lambda = 20$, as highlighted in Fig. A.1b.

By swapping the slenderness values of the ambient lattice and the structured interface of the above example, the negative refraction effect is obtained, at a frequency $\Omega = 2.5$, Fig. A.1c. Note that the dynamic response induced by a pulsating moment displays a strong localization along two preferential directions inclined at $\pm 45°$. Part of the generated waves is reflected by the interface and part is transmitted. It is possible to see how the refracted waves is essentially split into two channels: one with positive and the other with negative angle of refraction. The different angles of refraction are due to the different response of the single Bloch-wave components generated at the source. It can be noticed that the part of the signal that

is negatively refracted across the interface reconstructs a dim image of the source on the opposite side of the domain.

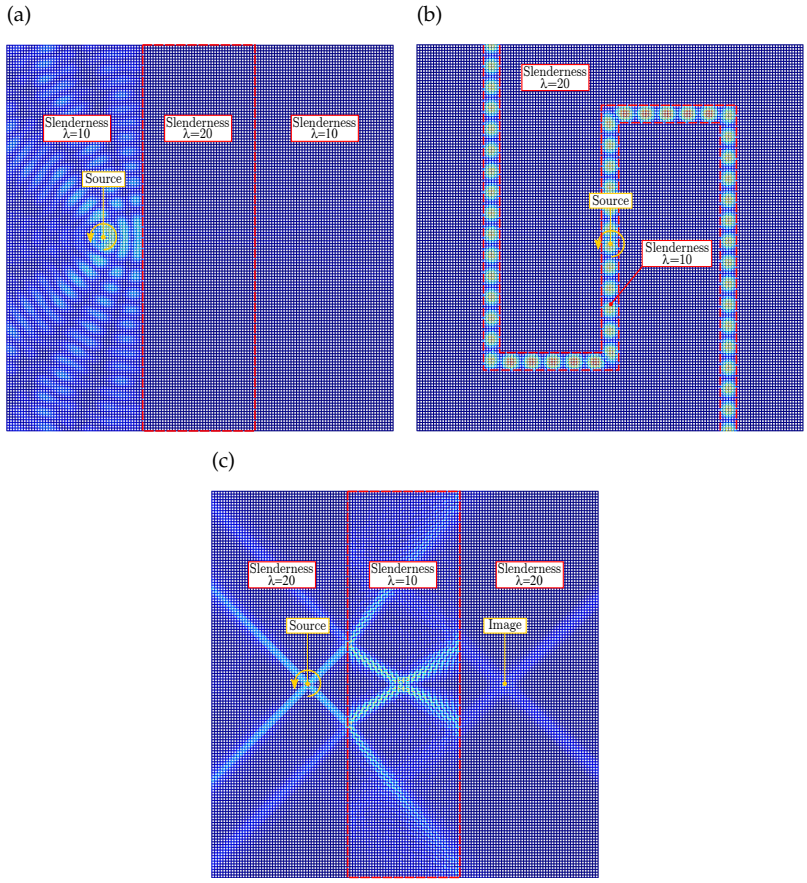

Fig. A.1. (a) Total reflection of a signal generated by a moment (which pulsates at the frequency $\Omega = 3.43$ and is applied to a lattice with beams of slenderness $\lambda = 10$) at a structured interface made of beams with slenderness $\lambda = 20$. (b) Trapping of a wave generated by an applied moment, located inside a narrow layer of beams of slenderness $\lambda = 10$ embedded in a lattice with slenderness $\lambda = 20$. (c) Negative refraction of a wave generated by an applied moment (pulsating at the frequency $\Omega = 2.5$), located inside a layer of beams of slenderness $\lambda = 10$, embedded in a lattice of beams with $\lambda = 20$.

B

Regime classification of the effective continuum

The mathematical classification of the PDE describing the incremental equilibrium of the equivalent solid provides valuable information on the number of localizations available on the elliptic boundary. In fact, the partial differential equations governing the equilibrium of the effective continuum, in the absence of body forces,

$$\operatorname{div} \mathbb{C}[\operatorname{grad} \boldsymbol{v}] = \mathbf{0}, \tag{B.1}$$

can be classified according to the following general criterion. Referring to a two-dimensional setting, a solution of the system (B.1) is selected in a wave form,

$$\boldsymbol{v} = \boldsymbol{g} \exp[i(x_1 + \Omega x_2)]\,, \tag{B.2}$$

where $\boldsymbol{g}$ is the wave amplitude and Ω a complex angular frequency. A substitution of (B.2) in the governing equation (B.1) yields the following linear algebraic system

$$\begin{bmatrix} \mathbb{C}_{1212}\Omega^2 + 2\mathbb{C}_{1112}\Omega + \mathbb{C}_{1111} & \mathbb{C}_{1222}\Omega^2 + (\mathbb{C}_{1122} + \mathbb{C}_{1221})\Omega + \mathbb{C}_{1111} \\ \mathbb{C}_{1222}\Omega^2 + (\mathbb{C}_{1122} + \mathbb{C}_{1221})\Omega + \mathbb{C}_{1111} & \mathbb{C}_{2222}\Omega^2 + 2\mathbb{C}_{2122}\Omega + \mathbb{C}_{2121} \end{bmatrix} \begin{Bmatrix} g_1 \\ g_2 \end{Bmatrix} = \begin{Bmatrix} 0 \\ 0 \end{Bmatrix}.$$

This system has non-trivial solutions if and only if the determinant of the coefficient matrix is equal to zero, a condition yielding the characteristic equation in the form of a quartic

$$a_4\Omega^4 + 2a_3\Omega^3 + a_2\Omega^2 + 2a_1\Omega + a_0 = 0\,, \tag{B.3}$$

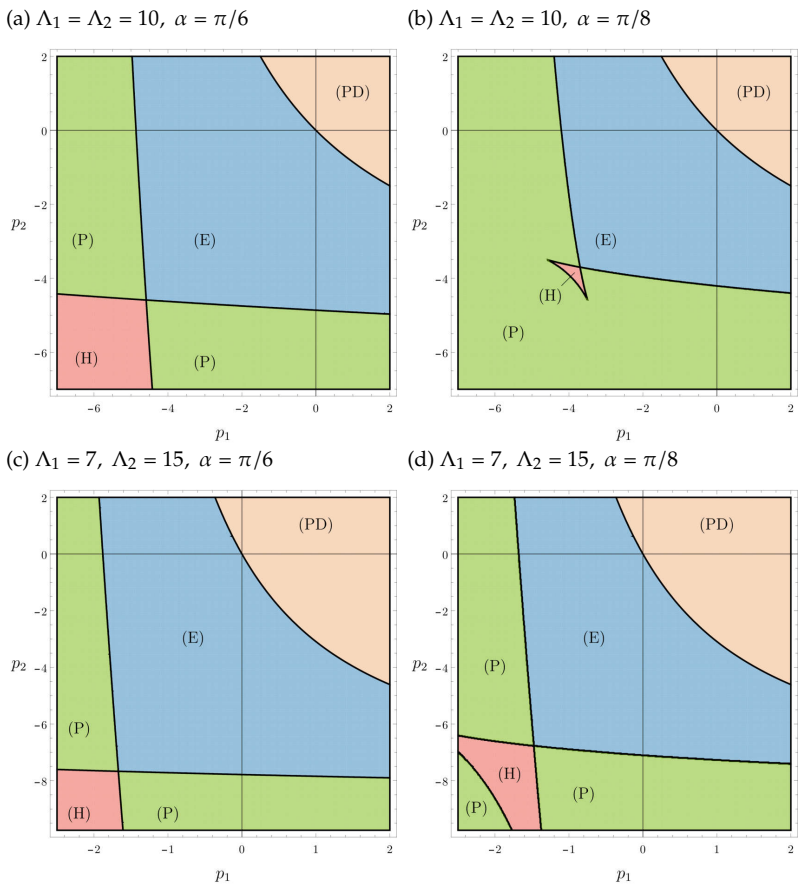

Fig. B.1. Regime classification of equilibrium PDE for the effective continuum equivalent of a rhombic elastic lattice as that sketched in Fig. 4.5 but without diagonal springs. The upper parts (a, b) refer to an orthotropic material ($\Lambda_1 = \Lambda_2 = 10$) material, while the lower parts (c, d) to a completely anisotropic material ($\Lambda_1 = 7,\ \Lambda_2 = 15$). The left parts (a, c) refer to a grid with inclination $\alpha = \pi/6$ and the right $\alpha = \pi/8$ (b, d). Note that the Hyperbolic and Elliptic regions 'touch' at a point.

where

$$
\begin{aligned}
a_4 &= \mathbb{C}_{1222}^2 - \mathbb{C}_{1212}\mathbb{C}_{2222}\,,\\
a_3 &= (\mathbb{C}_{1122} + \mathbb{C}_{1221})\,\mathbb{C}_{1222} - \mathbb{C}_{1212}\mathbb{C}_{2122} - \mathbb{C}_{1112}\mathbb{C}_{2222}\,,\\
a_2 &= (\mathbb{C}_{1122} + \mathbb{C}_{1221})^2 + 2\mathbb{C}_{1121}\mathbb{C}_{1222} - \mathbb{C}_{1212}\mathbb{C}_{2121} - 4\mathbb{C}_{1112}\mathbb{C}_{2122} - \mathbb{C}_{1111}\mathbb{C}_{2222}\,,\\
a_1 &= -\mathbb{C}_{1121}\,(\mathbb{C}_{1122} + \mathbb{C}_{1221}) + \mathbb{C}_{1112}\mathbb{C}_{2121} + \mathbb{C}_{1111}\mathbb{C}_{2122}\,,\\
a_0 &= \mathbb{C}_{1121}^2 - \mathbb{C}_{1111}\mathbb{C}_{2121}\,.
\end{aligned}
$$

The nature of the roots Ω_j of the quartic (B.3) defines the regime classification according to the following nomenclature [99, 124]:

- In the elliptical regime all the roots Ω_j are complex;

- In the hyperbolic regime all the roots Ω_j are real;
- In the parabolic regime two roots are real and two roots are complex.

According to this criterion, the regimes for the grid-like lattice of prestressed elastic rods have been classified and the results are shown in Fig. B.1 for both orthotropic ($\Lambda_1 = \Lambda_2 = 10$) and anisotropic ($\Lambda_1 = 7,\ \Lambda_2 = 15$) case. For the sake of brevity, only the case $\kappa = 0$ is reported.

Note that the elliptic region 'touches' the hyperbolic domain only at a point.

C

Linearized equations of motion of an axially pre-stretched rod

The linearized dynamics of an axially stretchable Rayleigh elastic rod can be obtained through a linearization (around a stretched equilibrium configuration) of the equations governing the dynamics of large deflections and flexure of an elastic rod.

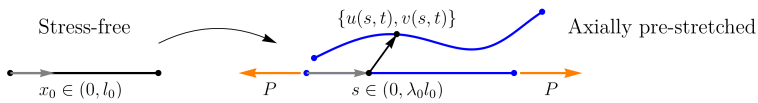

Fig. C.1. Stress-free and current stretched configurations of the rod model used in Chapter 4 and 5. The current configuration is assumed to be free from flexure and stretched by λ_0 under the action the axial load P. The pre-stretched equilibrium configuration is then assumed as reference in order to obtain the linearized equations of motion governing the incremental displacement fields $\{u(s,t), v(s,t)\}$. The rotation of the cross-section is not sketched, as it is assumed to be constrained by the unshearability condition (C.2).

Denoting the stress-free, straight configuration of the elastic rod with a local axial coordinate x_0 (see Fig. C.1), the potential energy and kinetic energy are defined in the reference configuration as

$$\mathcal{V} = \int_0^{l_0} \left(\psi_\lambda(\lambda) + \psi_\chi(\chi) - P\, u'(x_0, t) \right) dx_0 \,, \tag{C.1a}$$

$$\mathcal{T} = \frac{1}{2} \int_0^{l_0} \left(\gamma_0 \left(\dot{u}(x_0, t)^2 + \dot{v}(x_0, t)^2 \right) + \gamma_{r,0}\, \dot{\theta}(x_0, t)^2 \right) dx_0 \,, \tag{C.1b}$$

where l_0, γ_0, and $\gamma_{r,0}$ are the initial length, linear mass density, and rotational inertia, while ψ_λ and ψ_χ are strain-energy functions for, respectively, axial and flexural deformations. The axial and transverse displacement fields $\{u(x_0,t), v(x_0,t)\}$ are defined as sketched in Fig C.1, while the rotation of the cross-section is assumed to be constrained by the unshearability condition

$$\theta = \arctan\left(\frac{v'}{1+u'}\right) \tag{C.2}$$

The axial stretch λ and the curvature χ are defined by the kinematics of an extensible unshearable rod as

$$\lambda = (1+u'(x_0,t))\cos\theta(x_0,t) + v'(x_0,t)\sin\theta(x_0,t)\,, \tag{C.3a}$$

$$\chi = \theta'(x_0,t) = \frac{\partial}{\partial x_0}\left(\arctan\left(\frac{v'(x_0,t)}{1+u'(x_0,t)}\right)\right)\,, \tag{C.3b}$$

where in (C.3b) the unshearability constraint (C.2) has been explicitly substituted.

The linearized response around *straight, but axially stretched, configurations* can be obtained through the second-order expansion of the functionals (C.1) with respect to the independent displacement fields $\{u, v\}$ around the deformed configuration $\{u_0, v_0\} = \{(\lambda_0 - 1)x_0, 0\}$. Hence, by substituting (C.3) into (C.1) and neglecting an arbitrary constant term, the following expansion is obtained

$$\begin{aligned}\mathcal{V}(u_0+\delta u, v_0+\delta v) \sim &\int_0^{l_0}\left(\psi'_\lambda(\lambda_0) - P\right)\delta u'(x_0,t)dx_0 + \\ &+\frac{1}{2}\int_0^{l_0}\psi''_\lambda(\lambda_0)\delta u'(x_0,t)^2 dx_0 + \\ &+\frac{1}{2}\int_0^{l_0}\left(\frac{\psi'_\lambda(\lambda_0)}{\lambda_0}\delta v'(x_0,t)^2 + \frac{\psi''_\chi(0)}{\lambda_0^2}\delta v''(x_0,t)^2\right)dx_0\,,\end{aligned} \tag{C.4a}$$

$$\begin{aligned}&\mathcal{T}(u_0+\delta u, v_0+\delta v) \sim \\ &\qquad\frac{1}{2}\int_0^{l_0}\left(\gamma_0\left(\delta\dot{u}(x_0,t)^2 + \delta\dot{v}(x_0,t)^2\right) + \frac{\gamma_{r,0}}{\lambda_0^2}\delta\dot{v}'(x_0,t)^2\right)dx_0\,,\end{aligned} \tag{C.4b}$$

where it has been assumed that residual bending moment is absent in the unloaded configuration $\psi'_\chi(0) = 0$.

As the first-order term of (C.4a) has to vanish when the configuration $\{u_0, v_0\} = \{(\lambda_0 - 1)x_0, 0\}$ satisfies equilibrium, the prestretch λ_0 is the solution of the condition $\psi'_\lambda(\lambda_0) - P = 0$, indicating that the applied load P is indeed equal to the axial preload. Moreover, it is important to note that the second-order term of (C.4a) involves the strain energy functions only in terms of second derivatives, $\psi''_\lambda(\lambda_0)$ and $\psi''_\chi(0)$, evaluated on the straight

stretched configuration.

It is now instrumental to update the reference configuration from the stress-free configuration to the stretched configuration, so that the second-order functionals (C.4) can be adopted to govern the incremental response of the rod. This can be performed by changing the variable of integration from x_0 to the current stretched coordinate $s = \lambda_0 x_0$ and expressing the fields $\{u, v\}$ as functions of s. Thus, the second-order terms in eqs (C.4) become

$$\begin{aligned}\mathcal{V}(u_0+\delta u, v_0+\delta v) \sim & \frac{1}{2}\int_0^l \psi_\lambda''(\lambda_0)\lambda_0\,\delta u'(s,t)^2 ds + \\ & + \frac{1}{2}\int_0^l \left(P\delta v'(s,t)^2 + \psi_\chi''(0)\lambda_0\,\delta v''(s,t)^2\right) ds\,,\end{aligned} \tag{C.5a}$$

$$\begin{aligned}\mathcal{T}(u_0+\delta u, v_0+\delta v) \sim & \\ & \frac{1}{2}\int_0^l \left(\frac{\gamma_0}{\lambda_0}\left(\delta\dot{u}(s,t)^2 + \delta\dot{v}(s,t)^2\right) + \frac{\gamma_{r,0}}{\lambda_0}\delta\dot{v}'(s,t)^2\right) ds\,,\end{aligned} \tag{C.5b}$$

where $l = \lambda_0 l_0$ is the current rod's length and the symbol $'$ has to be understood as differentiation with respect to s[1]. It is worth noting that, as $\delta u'(s,t)$ and $\delta v''(s,t)$ are, respectively, the incremental axial strain and curvature, the corresponding coefficients are effectively the *current value of axial and bending stiffness*, so that they can be concisely denoted as $\psi_\lambda''(\lambda_0)\lambda_0 = A(\lambda_0)$ and $\psi_\chi''(0)\lambda_0 = B(\lambda_0)$, both functions of the current axial stretch λ_0.

As the second-order functionals (C.5) have been derived from the large deformation theory, they describe the correct incremental response of the rod superimposed upon a give pre-stretched state. Therefore, the correct form of the equations of motion governing the incremental displacements can be derived employing the following functionals

$$\begin{aligned}\mathcal{V}(u,v) = & \frac{1}{2}\int_0^l A(\lambda_0)\,u'(s,t)^2 ds + \\ & + \frac{1}{2}\int_0^l \left(Pv'(s,t)^2 + B(\lambda_0)\,v''(s,t)^2\right) ds\,,\end{aligned} \tag{C.6a}$$

$$\mathcal{T}(u,v) = \frac{1}{2}\int_0^l \left(\frac{\gamma_0}{\lambda_0}\left(\dot{u}(s,t)^2 + \dot{v}(s,t)^2\right) + \frac{\gamma_{r,0}}{\lambda_0}\dot{v}'(s,t)^2\right) ds\,, \tag{C.6b}$$

where now the fields $\{u(s,t), v(s,t)\}$ are the current incremental fields and the dependence of the current stiffnesses $A(\lambda_0)$ and $B(\lambda_0)$ on the current axial stretch is highlighted. Note that the linear mass density appears divided by the prestretch, indicating that the *current* density governs the incremental inertia of the rod, in fact the conservation of mass requires $\gamma_0/\lambda_0 = \gamma(\lambda_0)$, where γ is the current linear mass density of the stretched rod. Similarly, the *current* rotational inertia is denoted as $\gamma_{r,0}/\lambda_0 = \gamma_r(\lambda_0)$.

[1]Note that, with a little abuse of notation, the symbols for the functions $\{u, v\}$ have been maintained even though the independent variable has changed from x_0 to s.

The governing equations (5.3) used in Chapter 5 for the incremental dynamics of the rod are directly obtained through the application of Hamilton's principle on the Lagrangian $\mathcal{L} = \mathcal{T} - \mathcal{V}$ constructed using the second-order functionals (C.6). Similarly, the incremental equilibrium equations (4.2) employed in the static analysis of Chapter 4 are directly obtained from (C.6a) by imposing the first variation $\delta\mathcal{V}(u, v)$ to vanish.

C.1 Example of a rod made of incompressible hyperelastic material

The incremental potential (C.6a) has been derived with reference to a rod model defined by two arbitrary strain-energy functions governing the current stiffnesses $A(\lambda_0)$ and $B(\lambda_0)$. It is now shown that these two parameters can be evaluated explicitly for every incompressible elastic material selected to model the lattice's rods.

The incremental constitutive response of a rectangular block of incompressible material, deformed under plane strain and initially isotropic can be described (when a uniaxial stress state prevails in the current configuration) through [99]

$$\dot{S}_{11} = (2\mu_* - T_1)\frac{\partial u_1}{\partial x_1} + \dot{p}\,, \qquad \dot{S}_{22} = 2\mu_*\frac{\partial u_2}{\partial x_2} + \dot{p}\,,$$

where $\dot{S}_{ij}$ is the increment of the first Piola-Kirchhoff stress and u_i are the incremental displacements, μ_* the incremental modulus (corresponding to shearing inclined at 45° with respect to the axes), T_1 the current uniaxial Cauchy stress ($T_2 = 0$), and $\dot{p}$ the incremental Lagrange multiplier associated to the incompressibility constraint. Assuming that plane stress prevails incrementally, $\dot{S}_{22} = 0$, and using the incompressibility constraint, $\dot{p}$ can be eliminated to yield

$$\dot{S}_{11} = (4\mu_* - T_1)\frac{\partial u_1}{\partial x_1}\,. \tag{C.7}$$

By considering the incremental equilibrium along the x_1 direction

$$\frac{\partial \dot{S}_{11}}{\partial x_1} + \frac{\partial \dot{S}_{12}}{\partial x_2} = 0\,,$$

an integration over the current thickness h of the block and a subsequent substitution of Eq. (C.7) lead to

$$\int_{-h/2}^{h/2} \frac{\partial \dot{S}_{11}}{\partial x_1}\, dx_2 = (4\mu_* - T_1)\int_{-h/2}^{h/2} \frac{\partial^2 u_1}{\partial x_1^2}\, dx_2 = 0\,, \tag{C.8}$$

where the assumption of vanishing traction at $x_2 = \pm h/2$ has been used.

The incremental flexural equilibrium can also be retrieved. To this purpose, for a perturbation from the current unixial stress state, Biot [125] has

shown that the incremental equilibrium requires

$$\frac{\partial^2}{\partial x_1^2}\int_{-h/2}^{h/2} x_2\dot{S}_{11}\,dx_2 + T_1\frac{\partial^2}{\partial x_1^2}\int_{-h/2}^{h/2} u_2\,dx_2 = 0, \tag{C.9}$$

where the first integral can be recognized to be the incremental bending moment.

By adopting the incremental kinematics of an Euler-Bernoulli beam (satisfying the unshearability condition)

$$u_1(x_1,x_2) = u(x_1) - x_2\frac{\partial v(x_1)}{\partial x_1}\,, \qquad u_2(x_1,x_2) = v(x_1)\,, \tag{C.10}$$

and using (C.7), the axial and flexural equilibrium equations (C.8) and (C.9) become

$$(4\mu_* - T_1)h\frac{\partial^2 u(x_1)}{\partial x_1^2} = 0\,, \tag{C.11a}$$

$$(4\mu_* - T_1)\frac{h^3}{12}\frac{\partial^4 v(x_1)}{\partial x_1^4} - T_1 h\frac{\partial^2 v(x_1)}{\partial x_1^2} = 0\,. \tag{C.11b}$$

By noting that $T_1 h$ is the resultant axial load, so that $T_1 h = P$, the direct comparison between equations (C.11) and (4.2) provides the identification of the current stiffnesses $A(\lambda_0)$ and $B(\lambda_0)$ as

$$\begin{aligned} A(\lambda_0) &= (4\mu_*(\lambda_0) - T_1(\lambda_0))h(\lambda_0)\,,\\ B(\lambda_0) &= (4\mu_*(\lambda_0) - T_1(\lambda_0))h(\lambda_0)^3/12\,, \end{aligned} \tag{C.12}$$

where the explicit dependence on the current pre-stretch λ_0 has been highlighted. For instance, for a Mooney-Rivlin material $\mu_* = \mu_0(\lambda_0^2 + \lambda_0^{-2})/2$ and $T_1 = \mu_0(\lambda_0^2 - \lambda_0^{-2})$, and expressions (C.12) become

$$A(\lambda_0) = \mu_0(\lambda_0 + 3\lambda_0^{-3})h_0\,, \qquad B(\lambda_0) = \mu_0(\lambda_0^{-1} + 3\lambda_0^{-5})h_0^3/12\,.$$

with $h_0 = h/\lambda_0$ being the initial thickness, and μ_0 the initial shear modulus of the material.

Bibliography

[1] G. Bordiga, L. Cabras, D. Bigoni, and A. Piccolroaz. "Free and Forced Wave Propagation in a Rayleigh-Beam Grid: Flat Bands, Dirac Cones, and Vibration Localization vs Isotropization". In: *Int. J. Solids Struct.* 161 (2019), pp. 64–81. DOI: 10.1016/j.ijsolstr.2018.11.007.

[2] G. Bordiga, L. Cabras, A. Piccolroaz, and D. Bigoni. "Prestress Tuning of Negative Refraction and Wave Channeling from Flexural Sources". In: *Appl. Phys. Lett.* 114.4 (2019), p. 041901. DOI: 10.1063/1.5084258.

[3] G. Bordiga, L. Cabras, A. Piccolroaz, and D. Bigoni. "Incremental Constitutive Tensors and Strain Localization for Prestressed Elastic Lattices: Part I – Quasi-static Response". In: *J. Mech. Phys. Solids* (2020). arXiv: 2001.02096 [physics.class-ph]. *(under review)*.

[4] G. Bordiga, L. Cabras, A. Piccolroaz, and D. Bigoni. "Incremental Constitutive Tensors and Strain Localization for Prestressed Elastic Lattices: Part II – Incremental Dynamics". In: *J. Mech. Phys. Solids* (2020). arXiv: 2001.02151 [physics.class-ph]. *(under review)*.

[5] K. Bertoldi. "Harnessing Instabilities to Design Tunable Architected Cellular Materials". In: *Annu. Rev. Mater. Res.* 47.1 (2017), pp. 51–61. DOI: 10.1146/annurev-matsci-070616-123908.

[6] D. M. Kochmann and K. Bertoldi. "Exploiting Microstructural Instabilities in Solids and Structures: From Metamaterials to Structural Transitions". In: *Appl. Mech. Rev.* 69.5 (2017). DOI: 10.1115/1.4037966.

[7] A. Rafsanjani, L. Jin, B. Deng, and K. Bertoldi. "Propagation of Pop Ups in Kirigami Shells". In: *PNAS* 116.17 (2019), pp. 8200–8205. DOI: 10.1073/pnas.1817763116.

[8] B. H. Nguyen, X. Zhuang, H. S. Park, and T. Rabczuk. "Tunable Topological Bandgaps and Frequencies in a Pre-Stressed Soft Phononic Crystal". In: *J. Appl. Phys.* 125.9 (2019), p. 095106. DOI: 10.1063/1.5066088.

[9] P. Wang, F. Casadei, S. H. Kang, and K. Bertoldi. "Locally Resonant Band Gaps in Periodic Beam Lattices by Tuning Connectivity". In: *Phys. Rev. B* 91.2 (2015), p. 020103. DOI: 10.1103/PhysRevB.91.020103.

[10] P. Wang, L. Lu, and K. Bertoldi. "Topological Phononic Crystals with One-Way Elastic Edge Waves". In: *Phys. Rev. Lett.* 115.10 (2015), p. 104302. DOI: 10.1103/PhysRevLett.115.104302.

[11] G. Carta, I. S. Jones, N. V. Movchan, A. B. Movchan, and M. J. Nieves. ""Deflecting Elastic Prism" and Unidirectional Localisation for Waves in Chiral Elastic Systems". In: *Sci. Rep.* 7.1 (2017), p. 26. DOI: 10.1038/s41598-017-00054-6.

[12] D. Bigoni and P. A. Gourgiotis. "Folding and Faulting of an Elastic Continuum". In: *Proc. R. Soc. A* 472.2187 (2016). DOI: 10.1098/rspa.2016.0018.

[13] P. A. Gourgiotis and D. Bigoni. "Stress Channelling in Extreme Couple-Stress Materials Part II: Localized Folding vs Faulting of a Continuum in Single and Cross Geometries". In: *J. Mech. Phys. Solids* 88 (2016), pp. 169–185. DOI: 10.1016/j.jmps.2015.09.005.

[14] P. A. Gourgiotis and D. Bigoni. "The Dynamics of Folding Instability in a Constrained Cosserat Medium". In: *Philos. Trans. R. Soc. A* 375.2093 (2017), p. 20160159. DOI: 10.1098/rsta.2016.0159.

[15] J. T. B. Overvelde, J. C. Weaver, C. Hoberman, and K. Bertoldi. "Rational Design of Reconfigurable Prismatic Architected Materials". In: *Nature* 541.7637 (2017), pp. 347–352. DOI: 10.1038/nature20824.

[16] J. Shim, S. Shan, A. Košmrlj, S. H. Kang, E. R. Chen, J. C. Weaver, and K. Bertoldi. "Harnessing Instabilities for Design of Soft Reconfigurable Auxetic/Chiral Materials". In: *Soft Matter* 9.34 (2013), pp. 8198–8202. DOI: 10.1039/C3SM51148K.

[17] J.-P. Xia, D. Jia, H.-X. Sun, S.-Q. Yuan, Y. Ge, Q.-R. Si, and X.-J. Liu. "Programmable Coding Acoustic Topological Insulator". In: *Adv. Mater.* 30.46 (2018), p. 1805002. DOI: 10.1002/adma.201805002.

[18] G. Geymonat, S. Müller, and N. Triantafyllidis. "Homogenization of Nonlinearly Elastic Materials, Microscopic Bifurcation and Macroscopic Loss of Rank-One Convexity". In: *Arch. Ration. Mech. Anal.* 122.3 (1993), pp. 231–290. DOI: 10.1007/BF00380256.

[19] N. Triantafyllidis and W. C. Schnaidt. "Comparison of Microscopic and Macroscopic Instabilities in a Class of Two-Dimensional Periodic Composites". In: *J. Mech. Phys. Solids* 41.9 (1993), pp. 1533–1565. DOI: 10.1016/0022-5096(93)90039-I.

[20] P. Ponte Castañeda. "The Effective Mechanical Properties of Nonlinear Isotropic Composites". In: *J. Mech. Phys. Solids* 39.1 (1991), pp. 45–71. DOI: 10.1016/0022-5096(91)90030-R.

[21] W. J. Parnell. "Effective Wave Propagation in a Prestressed Nonlinear Elastic Composite Bar". In: *IMA J. Appl. Math.* 72.2 (2007), pp. 223–244. DOI: 10.1093/imamat/hxl033.

[22] J. R. Willis. "Exact Effective Relations for Dynamics of a Laminated Body". In: *Mech. Mater.* The Special Issue in Honor of Graeme W. Milton 41.4 (2009), pp. 385–393. DOI: 10.1016/j.mechmat.2009.01.010.

[23] R. V. Craster, J. Kaplunov, and A. V. Pichugin. "High-Frequency Homogenization for Periodic Media". In: *Proc. R. Soc. A* 466.2120 (2010), pp. 2341–2362. DOI: 10.1098/rspa.2009.0612.

[24] R. C. McPhedran, A. B. Movchan, N. V. Movchan, M. Brun, and M. J. A. Smith. "'Parabolic' Trapped Modes and Steered Dirac Cones in Platonic Crystals". In: *Proc. R. Soc. A* 471.2177 (2015). DOI: 10.1098/rspa.2014.0746.

[25] A. Piccolroaz, A. Movchan, and L. Cabras. "Dispersion Degeneracies and Standing Modes in Flexural Waves Supported by Rayleigh Beam Structures". In: *Int. J. Solids Struct.* 109 (2017), pp. 152–165. DOI: 10.1016/j.ijsolstr.2017.01.017.

[26] V. G. Veselago. "The Electrodynamics of Substances with Simultaneously Negative Values of ε and μ". In: *Sov. Phys. Usp.* 10.4 (1968), p. 509. DOI: 10.1070/PU1968v010n04ABEH003699.

[27] N. Triantafyllidis and B. N. Maker. "On the Comparison Between Microscopic and Macroscopic Instability Mechanisms in a Class of Fiber-Reinforced Composites". In: *J. Appl. Mech* 52.4 (1985), pp. 794–800. DOI: 10.1115/1.3169148.

[28] N. Triantafyllidis and M. W. Schraad. "Onset of Failure in Aluminum Honeycombs under General In-Plane Loading". In: *J. Mech. Phys. Solids* 46.6 (1998), pp. 1089–1124. DOI: 10.1016/S0022-5096(97)00060-4.

[29] M. D. Nestorović and N. Triantafyllidis. "Onset of Failure in Finitely Strained Layered Composites Subjected to Combined Normal and Shear Loading". In: *J. Mech. Phys. Solids* 52.4 (2004), pp. 941–974. DOI: 10.1016/j.jmps.2003.06.001.

[30] M. P. Santisi d'Avila, N. Triantafyllidis, and G. Wen. "Localization of Deformation and Loss of Macroscopic Ellipticity in Microstructured Solids". In: *J. Mech. Phys. Solids*. SI:Pierre Suquet Symposium 97 (2016), pp. 275–298. DOI: 10.1016/j.jmps.2016.07.009.

[31] P. Ponte Castañeda and A. J. M. Spencer. "The Overall Constitutive Behaviour of Nonlinearly Elastic Composites". In: *Proc. R. Soc. A* 422.1862 (1989), pp. 147–171. DOI: 10.1098/rspa.1989.0023.

[32] P. Ponte Castañeda. "Exact Second-Order Estimates for the Effective Mechanical Properties of Nonlinear Composite Materials". In: *J. Mech. Phys. Solids* 44.6 (1996), pp. 827–862. DOI: 10.1016/0022-5096(96)00015-4.

[33] P. Ponte Castañeda and P. Suquet. "Nonlinear Composites". In: *Advances in Applied Mechanics*. Ed. by E. van der Giessen and T. Y. Wu. Vol. 34. Elsevier, 1997, pp. 171–302. DOI: 10.1016/S0065-2156(08)70321-1.

[34] P. Ponte Castañeda. "Second-Order Homogenization Estimates for Nonlinear Composites Incorporating Field Fluctuations: II—Applications". In: *J. Mech. Phys. Solids* 50.4 (2002), pp. 759–782. DOI: 10.1016/S0022-5096(01)00098-9.

[35] P. Ponte Castañeda. "Second-Order Homogenization Estimates for Nonlinear Composites Incorporating Field Fluctuations: I—Theory". In: *J. Mech. Phys. Solids* 50.4 (2002), pp. 737–757. DOI: 10.1016/S0022-5096(01)00099-0.

[36] O. Lopez-Pamies and P. Ponte Castañeda. "On the Overall Behavior, Microstructure Evolution, and Macroscopic Stability in Reinforced Rubbers at Large Deformations: II—Application to Cylindrical Fibers". In: *J. Mech. Phys. Solids* 54.4 (2006), pp. 831–863. DOI: 10.1016/j.jmps.2005.10.010.

[37] O. Lopez-Pamies and P. Ponte Castañeda. "On the Overall Behavior, Microstructure Evolution, and Macroscopic Stability in Reinforced Rubbers at Large Deformations: I—Theory". In: *J. Mech. Phys. Solids* 54.4 (2006), pp. 807–830. DOI: 10.1016/j.jmps.2005.10.006.

[38] R. Avazmohammadi and P. Ponte Castañeda. "Macroscopic Constitutive Relations for Elastomers Reinforced with Short Aligned Fibers: Instabilities and Post-Bifurcation Response". In: *J. Mech. Phys. Solids*. SI:Pierre Suquet Symposium 97 (2016), pp. 37–67. DOI: 10.1016/j.jmps.2015.07.007.

[39] D. Bigoni and A. B. Movchan. "Statics and Dynamics of Structural Interfaces in Elasticity". In: *Int. J. Solids Struct.* 39.19 (2002), pp. 4843–4865. DOI: 10.1016/S0020-7683(02)00416-X.

[40] A. A. Kutsenko, A. J. Nagy, X. Su, A. L. Shuvalov, and A. N. Norris. "Wave Propagation and Homogenization in 2d and 3d Lattices: A Semi-Analytical Approach". In: *Q. J. Mechanics Appl. Math.* 70.2 (2017), pp. 131–151. DOI: 10.1093/qjmam/hbx002.

[41] O. Sigmund and J. S. Jensen. "Systematic Design of Phononic Band-Gap Materials and Structures by Topology Optimization". In: *Philos. Trans. R. Soc. A* 361.1806 (2003), pp. 1001–1019. DOI: 10.1098/rsta.2003.1177.

[42] Q. J. Lim, P. Wang, S. J. A. Koh, E. H. Khoo, and K. Bertoldi. "Wave Propagation in Fractal-Inspired Self-Similar Beam Lattices". In: *Appl. Phys. Lett.* 107.22 (2015), p. 221911. DOI: 10.1063/1.4936564.

[43] A. Bacigalupo, G. Gnecco, M. Lepidi, and L. Gambarotta. "Optimal Design of Low-Frequency Band Gaps in Anti-Tetrachiral Lattice Meta-Materials". In: *Compos. Part B-Eng.* Composite Lattices and Multiscale Innovative Materials and Structures 115 (2017), pp. 341–359. DOI: 10.1016/j.compositesb.2016.09.062.

[44] M. Lepidi and A. Bacigalupo. "Parametric Design of the Band Structure for Lattice Materials". In: *Meccanica* 53.3 (2018), pp. 613–628. DOI: 10.1007/s11012-017-0644-y.

[45] T. Antonakakis, R. V. Craster, and S. Guenneau. "Asymptotics for Metamaterials and Photonic Crystals". In: *Proc. R. Soc. A* 469.2152 (2013), p. 20120533. DOI: 10.1098/rspa.2012.0533.

[46] M. Brun, G. F. Giaccu, A. B. Movchan, and N. V. Movchan. "Asymptotics of Eigenfrequencies in the Dynamic Response of Elongated Multi-Structures". In: *Proc. R. Soc. A* 468.2138 (2012), pp. 378–394. DOI: 10.1098/rspa.2011.0415.

[47] M. Brun, A. B. Movchan, and I. S. Jones. "Phononic Band Gap Systems in Structural Mechanics: Finite Slender Elastic Structures and Infinite Periodic Waveguides". In: *J. Vib. Acoust.* 135.4 (2013), p. 041013. DOI: 10.1115/1.4023819.

[48] G. Carta, A. B. Movchan, L. P. Argani, and O. S. Bursi. "Quasi-Periodicity and Multi-Scale Resonators for the Reduction of Seismic Vibrations in Fluid-Solid Systems". In: *Int. J. Eng. Sci.* 109 (2016), pp. 216–239. DOI: 10.1016/j.ijengsci.2016.09.010.

[49] A. Colombi, D. Colquitt, P. Roux, S. Guenneau, and R. V. Craster. "A Seismic Metamaterial: The Resonant Metawedge". In: *Sci. Rep.* 6.1 (2016), pp. 1–6. DOI: 10.1038/srep27717.

[50] Y. Achaoui, T. Antonakakis, S. Brûlé, R. V. Craster, S. Enoch, and S. Guenneau. "Clamped Seismic Metamaterials: Ultra-Low Frequency Stop Bands". In: *New J. Phys.* 19.6 (2017), p. 063022. DOI: 10.1088/1367-2630/aa6e21.

[51] M. J. Leamy. "Exact Wave-Based Bloch Analysis Procedure for Investigating Wave Propagation in Two-Dimensional Periodic Lattices". In: *J. Sound Vib.* 331.7 (2012), pp. 1580–1596. DOI: 10.1016/j.jsv.2011.11.023.

[52] A. S. Phani, J. Woodhouse, and N. A. Fleck. "Wave Propagation in Two-Dimensional Periodic Lattices". In: *J. Acoust. Soc. Am.* 119.4 (2006), pp. 1995–2005. DOI: 10.1121/1.2179748.

[53] S. Gonella and M. Ruzzene. "Homogenization and Equivalent In-Plane Properties of Two-Dimensional Periodic Lattices". In: *Int. J. Solids Struct.* 45.10 (2008), pp. 2897–2915. DOI: 10.1016/j.ijsolstr.2008.01.002.

[54] A. Spadoni, M. Ruzzene, S. Gonella, and F. Scarpa. "Phononic Properties of Hexagonal Chiral Lattices". In: *Wave Motion* 46.7 (2009), pp. 435–450. DOI: 10.1016/j.wavemoti.2009.04.002.

[55] A. Piccolroaz, A. B. Movchan, and L. Cabras. "Rotational Inertia Interface in a Dynamic Lattice of Flexural Beams". In: *Int. J. Solids Struct.* 112 (2017), pp. 43–53. DOI: 10.1016/j.ijsolstr.2017.02.023.

[56] L. Cabras, A. B. Movchan, and A. Piccolroaz. "Floquet–Bloch Waves in Periodic Networks of Rayleigh Beams: Cellular System, Dispersion Degenerations, and Structured Connection Regions". In: *Mech. Solids* 52.5 (2017), pp. 549–563. DOI: 10.3103/S0025654417050107.

[57] M. Ruzzene, F. Scarpa, and F. Soranna. "Wave Beaming Effects in Two-Dimensional Cellular Structures". In: *Smart Mater. Struct.* 12.3 (2003), p. 363. DOI: 10.1088/0964-1726/12/3/307.

[58] H. Kolsky. *Stress Waves in Solids*. Dover Books on Physics. Dover Publications, 1963.

[59] A. Piccolroaz and A. B. Movchan. "Dispersion and Localisation in Structured Rayleigh Beams". In: *Int. J. Solids Struct.* 51.25 (2014), pp. 4452–4461. DOI: 10.1016/j.ijsolstr.2014.09.016.

[60] R. S. Langley. "The Response of Two-Dimensional Periodic Structures to Point Harmonic Forcing". In: *J. Sound Vib.* 197.4 (1996), pp. 447–469. DOI: 10.1006/jsvi.1996.0542.

[61] A. B. Movchan and L. I. Slepyan. "Resonant Waves in Elastic Structured Media: Dynamic Homogenisation versus Green's Functions". In: *Int. J. Solids Struct.* 51.13 (2014), pp. 2254–2260. DOI: 10.1016/j.ijsolstr.2014.03.015.

[62] A. L. Vanel, R. V. Craster, D. J. Colquitt, and M. Makwana. "Asymptotics of Dynamic Lattice Green's Functions". In: *Wave Motion* 67 (2016), pp. 15–31. DOI: 10.1016/j.wavemoti.2016.05.010.

[63] A. Bacigalupo and M. Lepidi. "Acoustic Wave Polarization and Energy Flow in Periodic Beam Lattice Materials". In: *Int. J. Solids Struct.* 147 (2018), pp. 183–203. DOI: 10.1016/j.ijsolstr.2018.05.025.

[64] L. J. Gibson and M. F. Ashby. *Cellular Solids: Structure & Properties*. 1. ed. International Series on Materials Science & Technology. OCLC: 16922914. Oxford: Pergamon Press, 1988.

[65] L. Brillouin. *Wave Propagation in Periodic Structures: Electric Filters and Crystal Lattices*. Courier Corporation, 1946.

[66] Pendry. "Negative Refraction Makes a Perfect Lens". In: *Phys. Rev. Lett.* 85.18 (2000), pp. 3966–3969. DOI: 10.1103/PhysRevLett.85.3966.

[67] N. Kaina, F. Lemoult, M. Fink, and G. Lerosey. "Negative Refractive Index and Acoustic Superlens from Multiple Scattering in Single Negative Metamaterials". In: *Nature* 525.7567 (2015), pp. 77–81. DOI: 10.1038/nature14678.

[68] R. V. Craster and S. Guenneau. *Acoustic Metamaterials: Negative Refraction, Imaging, Lensing and Cloaking*. Springer Science & Business Media, 2012.

[69] X. Zhang and Z. Liu. "Negative Refraction of Acoustic Waves in Two-Dimensional Phononic Crystals". In: *Appl. Phys. Lett.* 85.2 (2004), pp. 341–343. DOI: 10.1063/1.1772854.

[70] M. Brun, S. Guenneau, A. B. Movchan, and D. Bigoni. "Dynamics of Structural Interfaces: Filtering and Focussing Effects for Elastic Waves". In: *J. Mech. Phys. Solids* 58.9 (2010), pp. 1212–1224. DOI: 10.1016/j.jmps.2010.06.008.

[71] B. Morvan, A. Tinel, A.-C. Hladky-Hennion, J. Vasseur, and B. Dubus. "Experimental Demonstration of the Negative Refraction of a Transverse Elastic Wave in a Two-Dimensional Solid Phononic Crystal". In: *Appl. Phys. Lett.* 96.10 (2010), p. 101905. DOI: 10.1063/1.3302456.

[72] R. Zhu, X. N. Liu, G. K. Hu, C. T. Sun, and G. L. Huang. "Negative Refraction of Elastic Waves at the Deep-Subwavelength Scale in a Single-Phase Metamaterial". In: *Nat. Commun.* 5 (2014), p. 5510. DOI: 10.1038/ncomms6510.

[73] B. Liu, B. Ren, J. Zhao, X. Xu, Y. Feng, W. Zhao, and Y. Jiang. "Experimental Realization of All-Angle Negative Refraction in Acoustic Gradient Metasurface". In: *Appl. Phys. Lett.* 111.22 (2017), p. 221602. DOI: 10.1063/1.5004005.

[74] X. Lin, Y. Yang, N. Rivera, J. J. López, Y. Shen, I. Kaminer, H. Chen, B. Zhang, J. D. Joannopoulos, and M. Soljačić. "All-Angle Negative Refraction of Highly Squeezed Plasmon and Phonon Polaritons in Graphene–Boron Nitride Heterostructures". In: *PNAS* 114.26 (2017), pp. 6717–6721. DOI: 10.1073/pnas.1701830114.

[75] M. Farhat, S. Guenneau, S. Enoch, A. B. Movchan, and G. G. Petursson. "Focussing Bending Waves via Negative Refraction in Perforated Thin Plates". In: *Appl. Phys. Lett.* 96.8 (2010), p. 081909. DOI: 10.1063/1.3327813.

[76] M. Garau, G. Carta, M. J. Nieves, I. S. Jones, N. V. Movchan, and A. B. Movchan. "Interfacial Waveforms in Chiral Lattices with Gyroscopic Spinners". In: *Proc. R. Soc. A* 474.2215 (2018), p. 20180132. DOI: 10.1098/rspa.2018.0132.

[77] P. Celli and S. Gonella. "Tunable Directivity in Metamaterials with Reconfigurable Cell Symmetry". In: *Appl. Phys. Lett.* 106.9 (2015), p. 091905. DOI: 10.1063/1.4914011.

[78] X. Mao and T. C. Lubensky. "Maxwell Lattices and Topological Mechanics". In: *Annu. Rev. Condens. Matter Phys.* 9.1 (2018), pp. 413–433. DOI: 10.1146/annurev-conmatphys-033117-054235.

[79] J. Ma, D. Zhou, K. Sun, X. Mao, and S. Gonella. "Edge Modes and Asymmetric Wave Transport in Topological Lattices: Experimental Characterization at Finite Frequencies". In: *Phys. Rev. Lett.* 121.9 (2018), p. 094301. DOI: 10.1103/PhysRevLett.121.094301.

[80] M. Miniaci, R. K. Pal, B. Morvan, and M. Ruzzene. "Experimental Observation of Topologically Protected Helical Edge Modes in Patterned Elastic Plates". In: *Phys. Rev. X* 8.3 (2018), p. 031074. DOI: 10.1103/PhysRevX.8.031074.

[81] D. Bigoni, M. Gei, and A. B. Movchan. "Dynamics of a Prestressed Stiff Layer on an Elastic Half Space: Filtering and Band Gap Characteristics of Periodic Structural Models Derived from Long-Wave Asymptotics". In: *J. Mech. Phys. Solids* 56.7 (2008), pp. 2494–2520. DOI: 10.1016/j.jmps.2008.02.007.

[82] M. Gei, A. B. Movchan, and D. Bigoni. "Band-Gap Shift and Defect-Induced Annihilation in Prestressed Elastic Structures". In: *J. Appl. Phys.* 105.6 (2009), p. 063507. DOI: 10.1063/1.3093694.

[83] R. K. Pal, M. Ruzzene, and J. J. Rimoli. "Tunable Wave Propagation by Varying Prestrain in Tensegrity-Based Periodic Media". In: *Extreme Mech. Lett.* 22 (2018), pp. 149–156. DOI: 10.1016/j.eml.2018.06.005.

[84] A.-C. Hladky-Hennion, J. Vasseur, B. Dubus, B. Djafari-Rouhani, D. Ekeom, and B. Morvan. "Numerical Analysis of Negative Refraction of Transverse Waves in an Elastic Material". In: *J. Appl. Phys.* 104.6 (2008), p. 064906. DOI: 10.1063/1.2978379.

[85] X. N. Liu, G. K. Hu, G. L. Huang, and C. T. Sun. "An Elastic Metamaterial with Simultaneously Negative Mass Density and Bulk Modulus". In: *Appl. Phys. Lett.* 98.25 (2011), p. 251907. DOI: 10.1063/1.3597651.

[86] M. J. A. Smith, R. C. McPhedran, C. G. Poulton, and M. H. Meylan. "Negative Refraction and Dispersion Phenomena in Platonic Clusters". In: *Waves Random Complex Media* 22.4 (2012), pp. 435–458. DOI: 10.1080/17455030.2012.711495.

[87] K. H. Matlack, M. Serra-Garcia, A. Palermo, S. D. Huber, and C. Daraio. "Designing Perturbative Metamaterials from Discrete Models". In: *Nat. Mater.* 17.4 (2018), p. 323. DOI: 10.1038/s41563-017-0003-3.

[88] W. Jiao and S. Gonella. "Intermodal and Subwavelength Energy Trapping in Nonlinear Metamaterial Waveguides". In: *Phys. Rev. Applied* 10.2 (2018), p. 024006. DOI: 10.1103/PhysRevApplied.10.024006.

[89] D. Bigoni and D. Capuani. "Green's Function for Incremental Nonlinear Elasticity: Shear Bands and Boundary Integral Formulation". In: *J. Mech. Phys. Solids* 50.3 (2002), pp. 471–500. DOI: 10.1016/S0022-5096(01)00090-4.

[90] A. Bacigalupo and L. Gambarotta. "A Multi-Scale Strain-Localization Analysis of a Layered Strip with Debonding Interfaces". In: *Int. J. Solids Struct.* 50.13 (2013), pp. 2061–2077. DOI: 10.1016/j.ijsolstr.2013.03.006.

[91] S. D. Papka and S. Kyriakides. "In-Plane Compressive Response and Crushing of Honeycomb". In: *J. Mech. Phys. Solids* 42.10 (1994), pp. 1499–1532. DOI: 10.1016/0022-5096(94)90085-X.

[92] S. D. Papka and S. Kyriakides. "Experiments and Full-Scale Numerical Simulations of in-Plane Crushing of a Honeycomb". In: *Acta Mater.* 46.8 (1998), pp. 2765–2776. DOI: 10.1016/S1359-6454(97)00453-9.

[93] S. D. Papka and S. Kyriakides. "In-Plane Biaxial Crushing of Honeycombs—: Part II: Analysis". In: *Int. J. Solids Struct.* 36.29 (1999), pp. 4397–4423. DOI: 10.1016/S0020-7683(98)00225-X.

[94] W.-Y. Jang, S. Kyriakides, and A. M. Kraynik. "On the Compressive Strength of Open-Cell Metal Foams with Kelvin and Random Cell Structures". In: *Int. J. Solids Struct.* 47.21 (2010), pp. 2872–2883. DOI: 10.1016/j.ijsolstr.2010.06.014.

[95] A. Da Silva and S. Kyriakides. "Compressive Response and Failure of Balsa Wood". In: *Int. J. Solids Struct.* 44.25 (2007), pp. 8685–8717. DOI: 10.1016/j.ijsolstr.2007.07.003.

[96] M. Born and K. Huang. *Dynamical Theory of Crystal Lattices*. 1955.

[97] J. Willis. *Mechanics of Composites*. Ecole polytechnique, Département de mécanique, 2002.

[98] R. Hutchinson and N. Fleck. "The Structural Performance of the Periodic Truss". In: *J. Mech. Phys. Solids* 54.4 (2006), pp. 756–782. DOI: 10.1016/j.jmps.2005.10.008.

[99] D. Bigoni. *Nonlinear Solid Mechanics: Bifurcation Theory and Material Instability*. Cambridge: Cambridge University Press, 2012.

[100] R. Hill. "On Constitutive Macro-Variables for Heterogeneous Solids at Finite Strain". In: *Proc. R. Soc. A* 326.1565 (1972), pp. 131–147. DOI: 10.1098/rspa.1972.0001.

[101] E. Sanchez-Palencia and A. Zaoui, eds. *Homogenization Techniques for Composite Media*. Vol. 272. Lecture Notes in Physics. Berlin, Heidelberg: Springer Berlin Heidelberg, 1987. DOI: 10.1007/3-540-17616-0.

[102] L. Zhang and X. Mao. "Fracturing of Topological Maxwell Lattices". In: *New J. Phys.* 20.6 (2018), p. 063034. DOI: 10.1088/1367-2630/aac765.

[103] S. Pellegrino and C. R. Calladine. "Matrix Analysis of Statically and Kinematically Indeterminate Frameworks". In: *Int. J. Solids Struct.* 22.4 (1986), pp. 409–428. DOI: 10.1016/0020-7683(86)90014-4.

[104] S. Pellegrino. "Analysis of Prestressed Mechanisms". In: *Int. J. Solids Struct.* 26.12 (1990), pp. 1329–1350. DOI: 10.1016/0020-7683(90)90082-7.

[105] R. Hill. "Acceleration Waves in Solids". In: *J. Mech. Phys. Solids* 10.1 (1962), pp. 1–16. DOI: 10.1016/0022-5096(62)90024-8.

[106] P. A. Gourgiotis and D. Bigoni. "Stress Channelling in Extreme Couple-Stress Materials Part I: Strong Ellipticity, Wave Propagation, Ellipticity, and Discontinuity Relations". In: *J. Mech. Phys. Solids* 88 (2016), pp. 150–168. DOI: 10.1016/j.jmps.2015.09.006.

[107] G. S. Mishuris, A. B. Movchan, and L. I. Slepyan. "Localised Knife Waves in a Structured Interface". In: *J. Mech. Phys. Solids* 57.12 (2009), pp. 1958–1979. DOI: 10.1016/j.jmps.2009.08.004.

[108] D. Tallarico, N. V. Movchan, A. B. Movchan, and D. J. Colquitt. "Tilted Resonators in a Triangular Elastic Lattice: Chirality, Bloch Waves and Negative Refraction". In: *J. Mech. Phys. Solids* 103 (2017), pp. 236–256. DOI: 10.1016/j.jmps.2017.03.007.

[109] J. R. Willis. "Effective Constitutive Relations for Waves in Composites and Metamaterials". In: *Proc. R. Soc. A* 467.2131 (2011), pp. 1865–1879. DOI: 10.1098/rspa.2010.0620.

[110] J. R. Willis. "The Construction of Effective Relations for Waves in a Composite". In: *C. R. Mécanique*. Recent Advances in Micromechanics of Materials 340.4 (2012), pp. 181–192. DOI: 10.1016/j.crme.2012.02.001.

[111] S. Nemat-Nasser, J. R. Willis, A. Srivastava, and A. V. Amirkhizi. "Homogenization of Periodic Elastic Composites and Locally Resonant Sonic Materials". In: *Phys. Rev. B* 83.10 (2011), p. 104103. DOI: 10.1103/PhysRevB.83.104103.

[112] H. Nassar, Q. .-.-C. He, and N. Auffray. "Willis Elastodynamic Homogenization Theory Revisited for Periodic Media". In: *J. Mech. Phys. Solids* 77 (2015), pp. 158–178. DOI: 10.1016/j.jmps.2014.12.011.

[113] H. Nassar, X. C. Xu, A. N. Norris, and G. L. Huang. "Modulated Phononic Crystals: Non-Reciprocal Wave Propagation and Willis Materials". In: *J. Mech. Phys. Solids* 101 (2017), pp. 10–29. DOI: 10.1016/j.jmps.2017.01.010.

[114] A. N. Norris, A. L. Shuvalov, and A. A. Kutsenko. "Analytical Formulation of Three-Dimensional Dynamic Homogenization for Periodic Elastic Systems". In: *Proc. R. Soc. A* 468.2142 (2012), pp. 1629–1651. DOI: 10.1098/rspa.2011.0698.

[115] S. Meng and B. B. Guzina. "On the Dynamic Homogenization of Periodic Media: Willis' Approach versus Two-Scale Paradigm". In: *Proc. R. Soc. A* 474.2213 (2018), p. 20170638. DOI: 10.1098/rspa.2017.0638.

[116] B. B. Guzina, S. Meng, and O. Oudghiri-Idrissi. "A Rational Framework for Dynamic Homogenization at Finite Wavelengths and Frequencies". In: *Proc. R. Soc. A* 475.2223 (2019), p. 20180547. DOI: 10.1098/rspa.2018.0547.

[117] M. J. Nieves and M. Brun. "Dynamic Characterization of a Periodic Microstructured Flexural System with Rotational Inertia". In: *Philos. Trans. R. Soc. A* 377.2156 (2019), p. 20190113. DOI: 10.1098/rsta.2019.0113.

[118] D. Bigoni and D. Capuani. "Time-Harmonic Green's Function and Boundary Integral Formulation for Incremental Nonlinear Elasticity: Dynamics of Wave Patterns and Shear Bands". In: *J. Mech. Phys. Solids* 53.5 (2005), pp. 1163–1187. DOI: 10.1016/j.jmps.2004.11.007.

[119] A. Piccolroaz, D. Bigoni, and J. R. Willis. "A Dynamical Interpretation of Flutter Instability in a Continuous Medium". In: *J. Mech. Phys. Solids* 54.11 (2006), pp. 2391–2417. DOI: 10.1016/j.jmps.2006.05.005.

[120] R. S. Langley. "A Note on the Force Boundary Conditions for Two-Dimensional Periodic Structures with Corner Freedoms". In: *J. Sound Vib.* 167.2 (1993), pp. 377–381. DOI: 10.1006/jsvi.1993.1341.

[121] M. S. Elsayed and D. Pasini. "Analysis of the Elastostatic Specific Stiffness of 2D Stretching-Dominated Lattice Materials". In: *Mech. Mater.* 42.7 (2010), pp. 709–725. DOI: 10.1016/j.mechmat.2010.05.003.

[122] M. Bacca, D. Bigoni, F. Dal Corso, and D. Veber. "Mindlin Second-Gradient Elastic Properties from Dilute Two-Phase Cauchy-Elastic Composites Part II: Higher-Order Constitutive Properties and Application Cases". In: *Int. J. Solids Struct.* 50.24 (2013), pp. 4020–4029. DOI: 10.1016/j.ijsolstr.2013.08.016.

[123] H. Abdoul-Anziz and P. Seppecher. "Homogenization of Periodic Graph-Based Elastic Structures". In: *J. L'École Polytech. — Mathématiques* 5 (2018), pp. 259–288. DOI: 10.5802/jep.70.

[124] M. Renardy and R. C. Rogers. *An Introduction to Partial Differential Equations*. 2nd ed. Texts in Applied Mathematics. New York: Springer-Verlag, 2004.

[125] M. A. Biot. *Mechanics of Incremental Deformations: Theory of Elasticity and Viscoelasticity of Initially Stressed Solids and Fluids, Including Thermodynamic Foundations and Applications to Finite Strain*. Wiley, 1965.